Transport properties and proximity effect of topological hybrid structures

Dissertation zur Erlangung des
naturwissenschaftlichen Doktorgrades
der Julius-Maximilians-Universität Würzburg

vorgelegt von

Daniel Manfred Breunig

aus Kempten (Allgäu)

Würzburg, 2021

This document is licensed under the Creative Commons Attribution-ShareAlike 4.0 International License (CC BY-SA 4.0):
http://creativecommons.org/licenses/by-sa/4.0 This CC license does not apply to third party material (attributed to another source) in this publication.

Eingereicht am: ....
bei der Fakultät für Physik und Astronomie

1. Gutachter:
2. Gutachter:
3. Gutachter:

Vorsitzende(r): ....
1. Prüfer:
2. Prüfer:
3. Prüfer:
im Promotionskolloquium

Tag des Promotionskolloquiums: ....

Doktorurkunde ausgehändigt am: ....

Abstract

Over the last two decades, accompanied by their prediction and ensuing realization, topological non-trivial materials like topological insulators, Dirac semimetals, and Weyl semimetals have been in the focus of mesoscopic condensed matter research. While hosting a plethora of intriguing physical phenomena all on their own, even more fascinating features emerge when superconducting order is included. Their intrinsically pronounced spin-orbit coupling leads to peculiar, time-reversal symmetry protected surface states, unconventional superconductivity, and even to the emergence of exotic bound states in appropriate setups. This Thesis explores various junctions built from – or incorporating – topological materials in contact with superconducting order, placing particular emphasis on the transport properties and the proximity effect.

We begin with the analysis of Josephson junctions where planar samples of mercury telluride are sandwiched between conventional superconducting contacts. The surprising observation of pronounced excess currents in experiments, which can be well described by the Blonder-Tinkham-Klapwijk theory, has long been an ambiguous issue in this field, since the necessary presumptions are seemingly not met. We propose a resolution to this predicament by demonstrating that the interface properties in hybrid nanostructures of distinctly different materials yet corroborate these assumptions and explain the outcome. An experimental realization is feasible by gating the contacts. We then proceed with NSN junctions based on time-reversal symmetry broken Weyl semimetals and including superconducting order. Due to the anisotropy of the electron band structure, both the transport properties as well as the proximity effect depend substantially on the orientation of the interfaces between the materials. Moreover, an imbalance can be induced in the electron population between Weyl nodes of opposite chirality, resulting in a non-vanishing spin polarization of the Cooper pairs leaking into the normal contacts. We show that such a system features a tunable dipole character with possible applications in spintronics. Finally, we consider partially superconducting surface states of three-dimensional topological insulators. Tuning such a system into the so-called bipolar setup, this results in the formation of equal-spin Cooper pairs inside the superconductor, while simultaneously acting as a filter for non-local singlet pairing. The creation and manipulation of these spin-polarized Cooper pairs can be achieved by mere electronic switching processes and in the absence of any magnetic order, rendering such a nanostructure an interesting system for superconducting spintronics. The inherent spin-orbit coupling of the surface state is crucial for this observation, as is the bipolar setup which strongly promotes non-local Andreev processes.

Zusammenfassung

Seit nun gut zwei Jahrzehnten stehen Materialien wie Topologische Isolatoren, Dirac Halbmetalle und Weyl Halbmetalle im Fokus der Forschung der mesoskopischen Festkörperphysik. Diese topologisch nicht-trivialen Materialien weisen sich durch eine Vielzahl faszinierender Eigenschaften aus, insbesondere, wenn sie in Kombination mit supraleitender Ordnung untersucht werden. Die intrinsisch sehr stark ausgeprägte Spin-Bahn Kopplung führt zu charakteristischen Oberflächenzuständen, die durch die Zeitumkehrsymmetrie geschützt sind, zu unkonventioneller Supraleitung und sogar zur Ausbildung exotischer, gebundener Zustände in entsprechenden Strukturen. Diese Dissertation untersucht die Transporteigenschaften als auch den Proximity-Effekt in verschiedenen Kontakten aus topologischen Materialien und Supraleitern.

Zu Beginn befassen wir uns mit Josephson-Kontakten, in denen planare Proben aus Quecksilbertellurid in Kontakt mit konventionellen Supraleitern gebracht werden. In solchen Nanostrukturen wurden ausgeprägte Exzessströme gemessen, die zudem in guter Übereinstimmung mit der Blonder-Tinkham-Klapwijk Theorie stehen. Diese Beobachtungen sind jedoch kontraintuitiv, da die Voraussetzungen für den Formalismus scheinbar nicht gegeben sind. Wir zeigen anhand der Grenzflächeneigenschaften zwischen sich deutlich unterscheidenden Materialien, dass diese Annahmen dennoch korrekt sind und die Messergebnisse erklären. Dies lässt sich mit Hilfe von Seitenkontakten in einem Experiment nachweisen. Des Weiteren untersuchen wir Weyl Halbmetalle mit gebrochener Zeitumkehrsymmetrie und im Kontakt mit einem zentralen Supraleiter. Die Transporteigenschaften, wie auch der Proximity-Effekt, hängen wegen der Anisotropie der Bandstruktur stark von der Ausrichtung der Grenzflächen zwischen den Materialien ab. Zudem lässt sich ein Ungleichgewicht in der Elektronenpopulation zwischen Weylknoten unterschiedlicher Chiralität einstellen, was zu einer endlichen Spinpolarisation der Cooper-Paare führt, die in die normalleitenden Kontakte eindringen. Das System weist dann einen steuerbaren Dipolcharakter auf, welcher interessant für Anwendungen in der Spintronik ist. Schlussendlich analysieren wir den Oberflächenzustand eines dreidimensionalen topologischen Isolators, der lokal supraleitende Ordnung aufweist. Wird ein solches System in den sogenannten bipolaren Setup eingestellt, kann es zur Erzeugung und Manipulation von Triplet-Cooper-Paaren mit endlicher Spinpolarisation im Supraleiter verwendet werden. Gleichzeitig stellt es einen Filter für nicht-lokale Spin-Singlet-Paarung dar. Realisiert wird dies mit Hilfe elektrischer Spannung, und bedarf insbesondere keiner magnetische Ordnung zur Ausrichtung des Spin. Stattdessen verlassen wir uns auf die starke Spin-Bahn-Kopplung des Oberflächenzustands sowie den bipolaren Setup, welcher den nicht–lokalen Transport deutlich verstärkt.

Acronyms

1D/2D/3D	one-/two-/three-dimensional
Al	Aluminum
BCS	Bardeen-Cooper-Schrieffer
BdG	Bogoliubov-de Gennes
BHZ	Bernevig-Hughes-Zhang
BTK	Blonder-Tinkham-Klapwijk
CCP	Chiral chemical potential
DSM	Dirac semimetal
FSM	Fermi surface mismatch
CdTe	Cadmium telluride
HgTe	Mercury telluride
N/N'	*represents a normal-state domain*
S	*represents a superconducting-state domain*
SM	Semiconductor
TRS	Time-reversal symmetry
QW	Quantum well
WSM	Weyl semimetal

Table of contents

1

Introduction

Scattering theory is a powerful and comprehensive formalism to understand and predict the transport properties of particles and waves in heterogeneous systems, not only in acoustics and electrodynamics [1–3], but also, and in particular, in condensed matter physics. It provides a convenient framework to calculate experimental observables like the density of states, the differential conductance, and the current in hybrid nanostructures. Therefore, it extends similar, classical theories, like the famous Drude-model [4, 5] or the Drude-Sommerfeld-model [6], to the mesoscopic domain. From the mathematical perspective, it corresponds to solving a system of (usually) first- or second-order differential equations under certain initial or boundary conditions, imposed at the edges or the asymptotic limits of the system, as well as at the interfaces between different media. While, in electrodynamics, this system of differential equations is given by the Maxwell equations, it is the Schrödinger equation in the field of quantum mechanics [7]. The latter utilizes the Hamiltonian, an operator which incorporates the physical information of the underlying structure, and is usually approached algebraically as an eigenvalue problem. This allows expressing, for instance, electrons by means of wave functions, which are subsequently used to construct scattering states that describe the entire system appropriately. The matching of these states at the interfaces according to certain conditions (determined later in this work) then provides the necessary information to derive the above-mentioned observables. In this context, the scattering matrix has been introduced as a convenient quantity that relates the incoming to the outgoing states in a heterostructure or a material featuring local impurities. It is directly related to the Green function of the system, which is, formally, the inverse operator of the Hamiltonian. This is extremely useful, since it does not only allow to derive transport properties in continuous systems but also in discrete environments like crystalline lattices (the tight-binding model) or finite-size samples (described by the method of finite differences) [8]. Moreover, the Green function contains not only information about the transport in a nanostructure, but equally on the coupling and the pairing between different states, given that the system features several degrees of freedom (spin/sublattice/Nambu/...). As we will show in this Thesis, this inverse operator provides crucial information for our analysis and can be derived by either the scattering matrix or directly by the full set of scattering states associated with a given Hamiltonian.

In particular, we are going to consider heterojunctions built from a rather new type of materials, denoted by *topological insulators* (TIs), and its derivatives. A prime example is the Quantum Spin Hall Effect (QSHE). In the classical Hall effect [9], a voltage difference is applied to a metal or semiconductor, resulting in the conduction of electrons along the emerging electric field. A perpendicular magnetic field forces these moving charge carriers to one of the edges of the sample, resulting in a measurable transverse voltage (the *Hall voltage*). In a two-dimensional (2D) electron gas and at low temperatures, a similar experiment can be performed. Exposing such a setup to a strong magnetic field, this leads to a transverse voltage as well. The corresponding resistance is, however, quantized due to the emergence of Landau levels in the band structure [10], a phenomenon denoted by the (integer or fractional) *Quantum Hall Effect*. The observation of both effects depends, nonetheless, on strong magnetic fields. This raised the question if such physics, i.e., the emergence of charge-carrying edge states, can emerge in a system without the need to apply a magnetic flux. As a consequence, first suggestions for three-dimensional (3D) TIs have been proposed in 1985 [11] and 1987 [12], and concretized for 2D TIs in 2005 [13] and 2006 [14] as QSHE. The experimental verification in a mercury telluride (HgTe) quantum well (QW) has been achieved at the University of Würzburg in 2007 [15]. In the subsequent years, more elements have been identified as topological insulators, resulting in the establishment of a whole catalog of topological insulators [16].

TIs are bulk insulators with metallic surface states, which are protected by time-reversal symmetry (TRS) due to the non-trivial topology of their band structure (indicated by a topological invariant). And in contrast to the Hall effect and the Quantum Hall effect, which require strong magnetic fields, this phase of matter relies on pronounced spin-orbit coupling in the material. As a consequence, the one-dimensional (1D) edge states feature spin-momentum locking, severely suppressing the scattering at impurities and thus minimizing the electrical resistance in transport measurements. Moreover, their band structure is linear at the band crossing points and can be described by the massless Dirac Hamiltonian. All these features render them interesting materials to be studied, such that each chapter considers a junction where the underlying material, or at least the scattering domain, features topological nature.

The concept of topological order is, nonetheless, not limited to insulators or 2D systems. In fact, it has been shown that, in certain space groups, Dirac physics can emerge in metallic 3D bulk materials as well - featuring linear band crossings and topological order - which are known today as *Dirac semimetals* [17] (DSMs). More intriguingly, breaking time-reversal and/or inversion symmetry in a DSM, this splits single Dirac nodes (which are doubly degenerate bands that feature no handedness) into an even number of Weyl nodes with pairwise opposite chiralities [18, 19]. These *Weyl semimetals* (WSMs) feature band crossings, denoted by Weyl points, which can be described as monopole charges in k-space and lead to the emergence of the so-called Fermi surface arcs. These special representations of topological surface states were crucial in the experimental realization and detection of WSMs in 2015 [20], which are, since then, equally in the focus of solid-state research as TIs. While WSMs can be realized in different types in condensed matter systems (i.e., type-I WSMs with a point-like Fermi surface and type-II WSMs with a 'tilted' dispersion where the Weyl node separates electron and hole pockets [21]) and show a plethora of intriguing physics, we are particularly interested in type-I WSMs and the anisotropy of their band structure.

Even though topological materials are fascinating phenomena on their own, our aim is to bring them into contact with another interesting material, namely superconductors. Superconductivity was discovered by Heike Kamerlingh Onnes in 1911 [22] in metals at very low temperatures and shows, per definition, vanishing electrical resistance and the Meißner-Ochsenfeld-effect [23], i.e., the complete expelling of magnetic field lines from its interior. After its discovery, for several decades, superconductors were primarily studied from a phenomenological point of view, and a widely accepted, microscopic theory was only published by Bardeen, Cooper, and Schrieffer (BCS) in their seminal work in 1957 [24]. They showed theoretically that, at sufficiently low temperatures, electrons in a crystalline lattice overcome the Coulomb barrier due to phononic interactions, effectively resulting in an attractive potential between them. This leads to the formation of Cooper pairs – bosonic particles build from each two electrons – and results in a condensate described by a wave function that extends over the entire metal. Impurities in the lattice have a negligible effect on this condensate, such that the electrical resistance vanishes completely in the superconducting state. In the electron band structure of the metal, this is reflected by the emergence of a global gap around the Fermi energy, in which the density of states drops to zero.

This superconducting gap is a crucial ingredient throughout this Thesis since it enables peculiar scattering processes in normal metal-superconductor heterojunctions. An electron that approaches such an interface from the normal side and with an energy that lies inside the gap cannot enter the superconducting domain, since no corresponding states are available. Naively, one would think that the superconductor thus acts as a barrier and that the electron can only be reflected back into the metal. However, it has been demonstrated that, with a certain probability, the incident electron can also be reflected as a hole at the interface. This fascinating process has been discovered by Andreev in 1964 [25]. A single electron (i.e., the incident particle) cannot enter the superconductor on its own due to the absence of states. Nonetheless, it can form a Cooper pair with a second electron from the Fermi sea in the same domain, such that both are added to the condensate. This leaves behind a hole in the normal metal, propagating away from the interface, a process denoted by (local) *Andreev reflection*. A similar process can occur in normal metal-superconductor-normal metal (NSN) systems, with the distinction that the incident electron and the second electron from the Fermi sea could also stem from different sides of the superconductor, which is commonly denoted by *crossed Andreev reflection*. As we illustrate in the following chapters, both scattering processes have intriguing effects on the transport properties as well as on the pairing and the proximity effect in hybrid junctions.

While the theories and phenomena mentioned above are related to conventional, low-temperature superconductors like aluminum or niobium, more exotic types of superconductivity at higher temperatures have been discovered over the years [26]. Since these require distinct materials and more complex theories to be described, this work will focus on the former type of superconducting order.

This Thesis is structured as follows. In Chap. 2, we consider 2D heterojunctions of materials featuring distinctly different band structures and discuss the implications on the transport properties in the system. In particular, we show that a significant mismatch between the Fermi surfaces renders the interfaces as a directional filter for electrons and therefore keeps the equilibrium reservoirs well separated from the scattering region. This is an important requirement for the applicability of scattering theory to describe transport properties and derive observables like the differential conductance or the current. The chapter is rather technical and begins with the analysis of N'NN' or SNS (N and N' describe different normal-state domains, S describes a region featuring superconducting order) junctions described by quadratic Hamiltonians, followed by a setup where the central domain is described by a proper Hamiltonian for HgTe QWs. The extension to 3D is discussed. Furthermore, we introduce generalized wave matching conditions and definitions of the probability current in the methods section.

Chapter 3 concerns 3D homogeneous, TRS broken WSMs with two Weyl nodes in the Brillouin zone. A localized domain of such a sample shall become superconducting by means of the proximity effect, effectively separating the adjacent normal domains and enabling to gate them independently. Furthermore, the anisotropy of the WSM band structure allows us to choose an orientation of the axis separating the Weyl nodes with respect to the interfaces between the leads and the central domain. Both features do not only affect the transport properties in the junction, but also the superconducting order leaking from the superconductor into the WSMs, i.e., the proximity effect in the leads. We study the differential conductance as well as the pairing amplitudes for different orientations and gating voltages, with an emphasis on the equal-spin triplet amplitudes. The methodological section introduces the Scattering State Approach, based on which we determine the Green function, as well as the concept of outgoing boundary conditions and the Wronskian method.

Finally, in Chap. 4, we consider 2D surface states of 3D TIs, equally featuring superconducting order in a restricted domain. Using gating technology, this NSN system is transferred into the bipolar setup, where the electrochemical potentials in the normal leads have the same magnitude, but different signs. This results in intriguing effects on the transport properties, particularly the local and non-local differential conductance, as well as on the proximity effect in the normal leads. The breaking of spin-rotational invariance suggests the formation of equal-spin Cooper pairs, and we introduce a quantity that measures this net spin pumped into the superconductor when a bias is applied to the system. We evaluate this quantity and illustrate why the bipolar setup is a favorable configuration for applications in superconducting spintronics.

Each chapter starts with a motivational section which puts the work into context with current research and introduces the physical concepts thoroughly, which is followed by a methods part in Chap. 2 and Chap. 3. We then provide the mathematical and theoretical basis (in terms of Hamiltonians and the associated eigensystems) upon which we perform calculations and draw results. The latter are subsequently presented and discussed in detail, followed by a section that concludes the chapter.

Parts of this thesis have been published in journals associated to the *American Physical Society*. The publications are mentioned in the corresponding motivational sections and reprinted figures are explicitly highlighted in the captions.

2

Directional electron-filtering at superconductor-semiconductor interfaces

This chapter is based on the work *Directional electron-filtering at superconductor-semiconductor interfaces* by Daniel Breunig, Song-Bo Zhang, Björn Trauzettel and Teun M. Klapwijk (Phys. Rev. B **103**, 165414 (2021)).

2.1 Motivation

In 1982, Blonder, Tinkham, and Klapwijk (BTK) proposed their seminal transport theory for normal metal-superconductor (NS) microconstrictions [27], providing a powerful formalism to study electrical transport in a wide range of 1D systems. Crucial requirements for its applicability are ballistic transport and equilibrated reservoirs in contact with the scattering region. This is achieved by choosing an appropriate and experimentally realizable geometry, where a transmissive interface is placed in an orifice in an elsewise opaque screen, separating the electron systems of the two materials. This separation allows to apply a bias over the junction by setting the reservoirs to different chemical potentials, where the electron occupation can be described by equilibrium Fermi distribution functions $f_0(E)$ and $f_0(E-eV)$, respectively [28]. Initially designed for experimental setups that correspond to this orifice model, prime examples for such spatially bound geometries are break junctions [29] and quantum point contacts [30]. This formalism is employed frequently and has been extended to more complex scenarios [31–33].

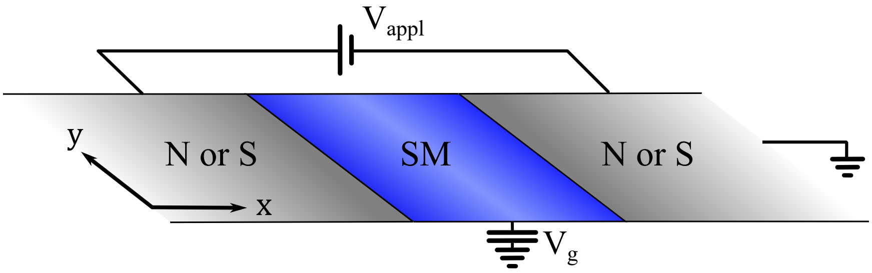

Fig. 2.1: Sketch of a 2D interface-junction considered in this work. A semiconductor (SM, blue) is brought into contact with a normal metal or an s-wave superconductor (N or S, gray). We assume two interfaces in x-direction, while the y-direction remains translational invariant. *Reprinted figure with permission from [34]. Copyright (2021) by the American Physical Society.*

The recent prediction and experimental confirmation of topological insulators [35, 36] motivated numerous experiments on Josephson junctions of 2D materials with rather dissimilar electronic properties. While, for a theoretical approach, the BTK formalism is well suited to describe Josephson junctions of homogeneous materials that comply with the orifice model [37, 38], this is not a priori true for planar systems that do not form any kind of constriction, as, for instance, illustrated in Fig. 2.1. Instead, one could assume interfaces with very low transparency. This would shift the system into the tunneling regime, effectively separating the reservoirs from each other, such that they remain equilibrated. However, recent measurements in Josephson junctions suggest intermediate to high interface transparencies [39–43], while still being in accordance with BTK theory. This invalidates the former argument. Local equilibria are crucial for Josephson junctions, which are intrinsically two-terminal devices where a bias is applied over the same contacts that serve as source and drain for the current [30, 44, 45], hence the question arises which mechanism guarantees their existence.

In this chapter, we demonstrate that, while the precondition of equilibrium reservoirs is usually implicitly presumed, a more detailed analysis of the interface characteristics – with respect to the different electronic properties in the metals and the semiconductor – is required to justify this assumption [46–49]. This is particularly interesting since the electronic properties of a semiconductor can be tuned by a gate-voltage, which changes the Fermi level and directly affects the interface properties. Insights on these features provide an understanding of the voltage-carrying state in ballistic Josephson junctions, as well as of the Andreev bound states in the zero-bias limit due to the effect on the boundary conditions [50].

We focus specifically on measurements of the so-called excess current, i.e., the offset between normal-state and superconducting-state current at biases much larger than the order parameter. It can be attributed to strong contributions from energies in proximity to the superconducting gap, which are mediated by Andreev reflection processes at the interface between a normal material and a superconductor [27]. Typical experimental setups are Josephson junctions based on mercury telluride (HgTe) heterostructures in contact with superconductors like aluminum (Al), niobium (Nb), and molybdenum-rhenium (MoRe) [36, 39, 51] with large cross-sectional areas of a few microns by 10 to 80 nanometers. The S domains are induced via superconducting top electrodes on the surface of a HgTe-layer by the proximity effect, or realized as side contacts in mesa-structures [52] as it has been done for graphene [42] and indium antimonide (InSb) [53]. In all of these setups, pronounced excess currents related to apparently substantial interface transparencies have been observed, even though the dimensions of the samples are not to any extent in agreement with the orifice model. Our aim is to resolve this seemingly contradictory observation by means of a mechanism denoted by *Fermi surface mismatch* (FSM). We study its effects on the electronic interface properties as well as on the transport in the system, with emphasis on the differential conductance and the current. While our analysis focuses on the properties of one single interface, we argue that the results can be applied to a Josephson junction as well.

The remainder of this chapter is structured as follows. In Sec. 2.2, we discuss FSM and its implications as a k-space orifice, separating the reservoirs in the presence of an elsewise transparent interface in planar junctions. Methods used to obtain our results as well as the derivation of physical observables are presented in Sec. 2.3, whereas in Sec. 2.4, we introduce the NS system on which we perform our analysis, including the theoretical background. The results are presented in detail in Sec. 2.5, where we first study an NN' junction in which both metals are in the normal state, followed by an NS system. In Sec. 2.6, we add more complexity to the system by describing the central region with the BHZ-Hamiltonian, and conclude with the extension of the BTK-Kastalsky-Beenakker formula to a system featuring FSM in Sec. 2.7.

This work has partially been published as a regular article in the journal *Physical Review B* [34]. Similarities in the text are unavoidable. The copyright (2021) belongs to the American Physical Society. All licenses to use the content in this Thesis have been obtained. Reprinted or adapted figures are distinctly marked.

2.2 Fermi surface mismatch

When superconductivity is induced by the proximity-effect in an elsewise homogeneous material, the underlying Hamiltonian is the same for the whole system, except for a localized pairing potential. This is no longer the case if a semiconductor, like HgTe, is interfaced with superconducting side contacts from a different material, e.g. Al. Then, the electronic properties are rather distinct, since both materials feature, for instance, dissimilar effective masses, degrees of freedom, or potentials. The underlying Hamiltonians are fundamentally different. If we want to study such a hybrid nanostructure by means of scattering theory, this has an essential effect on the electronic properties, denoted by *Fermi surface mismatch*. We want to introduce this concept at hand of a simple example.

Let us consider a system in which two metals, described by the model of the quasi-free electron gas, are brought into contact with each other, see Fig. 2.2. Then, their Hamiltonian is of the form

$$\mathcal{H} = \frac{\hbar^2 k^2}{2m^*} - \mu, \qquad\qquad k = |\boldsymbol{k}| = \sqrt{k_x^2 + k_y^2}, \tag{2.1}$$

where $\hbar\boldsymbol{k} = (\hbar k_x, \hbar k_y)$ is the momentum operator (k_x and k_y are the wavenumbers in x- and y-direction, respectively) with $\hbar$ the reduced Planck constant, m^* is the effective mass and μ the chemical potential. When the effective masses in N and N' deviate from each other, this means that their dispersions feature different curvatures, *cf.* Fig. 2.2, which leads to a mismatch of the Fermi surfaces. As we will see, this inevitably limits the transmissivity of the system.

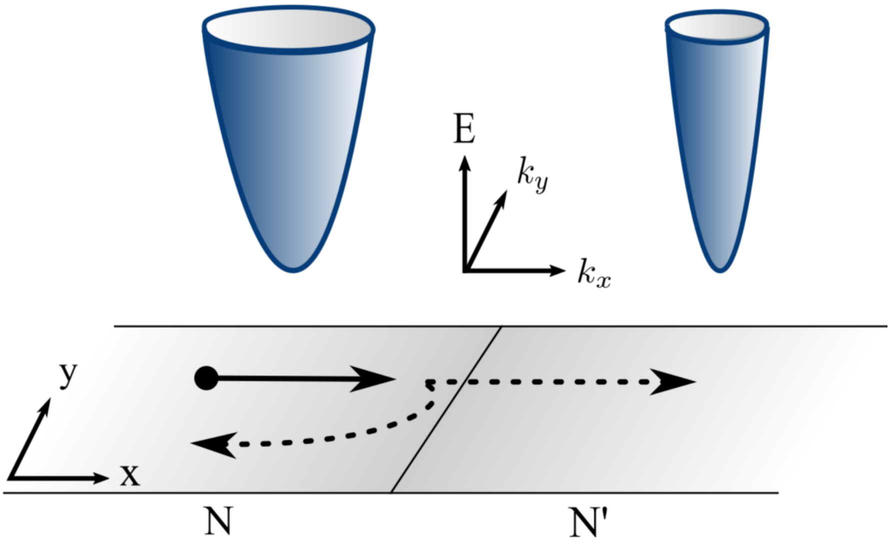

Fig. 2.2: Bottom: Junction of two normal metals N and N'. The solid arrow represents an incident electron in N approaching the interface, while the dashed arrows indicate possible scattering processes - reflection and transmission. Note that the y-direction is assumed to be translational invariant. **Top**: Schematic illustration of the dispersion in each material. Here, we assume different effective masses in N and N', leading to different curvatures.

The Fermi surface in a 2D material is the intersection of its dispersion with a plane of constant energy in k-space, i.e., a circle of radius k (k') in N (N'). If these radii differ from each other, $k \neq k'$, this has an interesting consequence, as we illustrate in Fig. 2.3. Considering an excitation in N that approaches the interface (solid arrow in Fig. 2.2, corresponding to a right moving particle with $k_x > 0$), there are, in general, two scattering processes that can occur. The electron can be reflected back into N, or it can be transmitted across the interface into N' (dashed arrows). This is, however, only possible if a corresponding state is available in N or N'. When we assume the system to be translational invariant in y-direction, then k_y (which parameterizes the transverse modes [8]) is conserved in a scattering event. Consequently, there are states in N that cannot undergo transmission due to the absence of corresponding states in N' (indicated by the red sectors in Fig. 2.3). In contrast, reflection can happen for any k_y, since there is always a state on the other side of the Fermi surface ($k_x \to -k_x$) in N. Therefore, only the modes in N indicated by the blue sector in Fig. 2.3 can be transmitted across the junction and thus contribute to the transport in the system. This is explicitly illustrated in Fig. 2.4 for an electron with scattering states in both N and N' (blue) as well as for an electron with a scattering state in N only (gray). We label the critical angle between the states that can undergo transmission and those that cannot as θ_c.

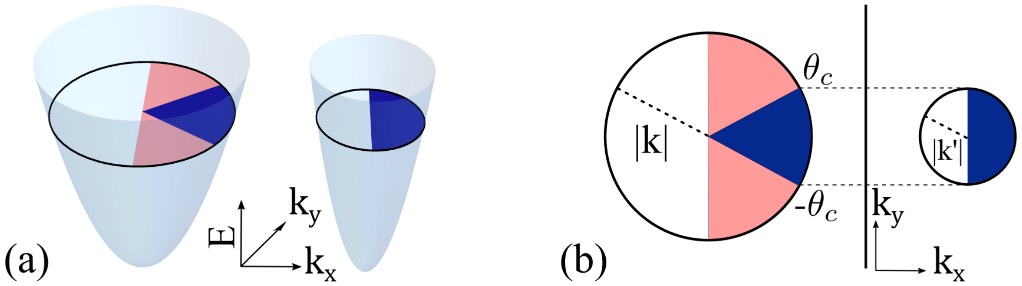

Fig. 2.3: (a) 3D and (b) top view of the Fermi surfaces at a constant energy E. Since they have different radii $|k|$ and $|k'|$ in N and N', respectively, there are states in N that have no counterpart in N', such that transmission cannot happen (indicated by the red sectors). Note that k_y is conserved in a scattering process since we assume the system to be translational invariant in y-direction. *Reprinted figure with permission from [34]. Copyright (2021) by the American Physical Society.*

As we can see, the interface of such a junction performs as a directional filter for incident electrons due to this mismatch between the Fermi surfaces. Only those with a small enough angle have a chance to be transmitted across the junction (determined by the intrinsic transmissivity of the interface) and contribute to the differential conductance and the current in the system, while all other modes are reflected with unit probability. The latter do not change the occupation in N and thus do not affect its Fermi distribution function. Therefore, if FSM is large enough, i.e., by creating an 'orifice in k-space', this perturbation becomes negligible and N can be interpreted as an equilibrated reservoir.

Evidently, this argumentation does not hold for an electron excited in the right metal. For any mode k_y in N', we find a corresponding mode in N, which essentially enables transmission across the interface for all angles of incidence. N' can thus not be assumed to be equilibrated. Instead, we argue that two of such interfaces need to be combined in series to form a junction as illustrated in Fig. 2.1. Then, the normal metals would perform as the reservoirs where we can define equilibrated incoming and outgoing populations (the fundamental assumption of BTK) and which we can set to different chemical potentials, while the semiconductor represents the scattering region where such an assumption (i.e., an equilibrium Fermi distribution) is not required.

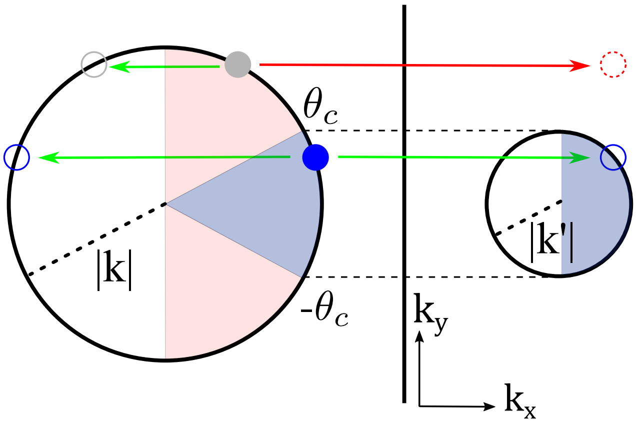

Fig. 2.4: Illustration of FSM. If the angle of incidence of an electron in N is smaller than θ_c, both reflection and transmission can occur, since the states are available for these processes (blue state). This is no longer true for an electron with an angle of incidence larger than θ_c, since there is no state available in N' (gray state).

In a hybrid junction of HgTe and, for instance, Al, FSM is very pronounced (*cf.* Sec. 2.6), which partially explains the observations in the experiments mentioned above. What remains is the question of how FSM affects the interface transmissivity and what currents are to be expected. This chapter is supposed to give an explicit answer to this question.

In order to quantify FSM, we introduce the ratio r between the radius of the smaller Fermi surface and that of the larger one. For instance, in the context of Fig. 2.3, this ratio would be defined as $r = |k'| / |k|$. It can attain values $0 < r \leq 1$, where $r = 1$ corresponds to a homogeneous system with equal Fermi surfaces and the limit $r \to 0$ to a point-like Fermi surface in one of the materials (not explicitly considered in this work). The reciprocal definition is possible as well, where the ratio attains values $1 \leq r < \infty$. Our choice, however, explores the same extend of FSM in a conveniently compact range of the ratio r.

Finally, we define the electron modes that can be transmitted across the interface as the *propagating modes*, whereas those that are reflected with unit probability are denoted *reflected modes*, see the inset of Fig. 2.5. This plot furthermore illustrates the number of propagating modes in relation to all incident modes[1], which decreases nearly linearly with increasing FSM, except for choices of r that are close to the homogeneous setup. As a last note, we emphasize that a large FSM corresponds to a small ratio r, and vice versa.

---

[1] Note that only half the circle in, e.g., Fig. 2.3 corresponds to incident modes, the other half describes an electron that moves away from the interface.

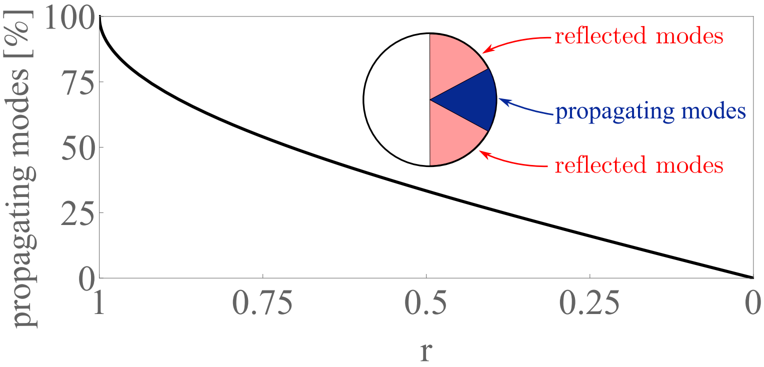

Fig. 2.5: Number of available electron modes for transmission (propagating modes) as a function of FSM. The inset illustrates the definitions of propagating and reflected modes. *Reprinted figure with permission from [34]. Copyright (2021) by the American Physical Society.*

2.3 Methods and derivations

2.3.1 Generalized wave matching conditions

In order to calculate transport properties in junctions with spatially varying parameters (without loss of generality, we choose the spatial variable along which the parameters vary to be x), we need to find the appropriate wave matching conditions at the interfaces. This is straightforward if we assume a homogeneous material where the spatial dependence appears only in the potential term of the Hamiltonian, and can be achieved by real space integration of the Schrödinger equation. A position-dependent effective mass $m(x)$, however, is more complicated, since it appears as a reciprocal coefficient of the second order of the momentum operator, $\hat{p}_x = -i\hbar\partial_x (= \hbar\hat{k}_x)$, but does not commute with the latter (in contrast to a constant effective mass), $\left[\hat{p}_x^2, m^{-1}(x)\right] \neq 0$. As a consequence, we cannot simply write the Hamiltonian in the form $\mathcal{H} \propto m^{-1}(x)\,\hat{p}_x^2$, since this term is not hermitian,

$$\left(m^{-1}(x)\,\hat{p}_x^2\right)^\dagger = \hat{p}_x^2\, m^{-1}(x) \neq m^{-1}(x)\,\hat{p}_x^2. \tag{2.2}$$

Thus, we need an expression that is both hermitian and well defined. The same issue arises if we want to consider position-dependent electron velocities, which are coefficients of the first order of the momentum operator. In order to provide wave matching conditions that are valid in a wide range of systems with spatially dependent parameters, let us introduce a rather general model Hamiltonian. For the time being, we assume that (i) the system is 1D (ii) the position-dependence appears solely in the form of step-functions or delta-functions, and (iii) only one interface is present. This simplifies the derivation of the wave matching conditions, but does not affect the results, as we will discuss later. Then, such a general, well defined and hermitian Hamiltonian [54, 55] is given by

$$\mathcal{H}(x) = \hat{p}_x\mathcal{A}(x,x_0)\hat{p}_x + \frac{1}{2}\left[\mathcal{B}(x,x_0)\hat{p}_x + \hat{p}_x\mathcal{B}(x,x_0)\right] + \mathcal{C}(x,x_0) + \mathcal{D}(x,x_0) \tag{2.3}$$

with x_0 the position of the interface. The quantities $\mathcal{A}$, $\mathcal{B}$, $\mathcal{C}$ and $\mathcal{D}$ are hermitian $(n \times n)$-matrices, with n the degrees of freedom of the system (e.g., spin, orbital, ...). In a condensed matter system, $\mathcal{A}$ is related to the reciprocal effective mass of the particles, $\mathcal{B}$ to their velocities and $\mathcal{C}$ and $\mathcal{D}$ are potentials. Explicitly, the position-dependence of these parameters shall read as

$$\Lambda(x) = \Lambda_l\,\Theta(x_0 - x) + \Lambda_r\,\Theta(x - x_0), \qquad \Lambda \in \{\mathcal{A},\mathcal{B},\mathcal{C}\} \tag{2.4a}$$

$$\mathcal{D}(x) = \mathcal{D}\,\delta(x - x_0), \tag{2.4b}$$

where $\Theta(\cdot)$ and $\delta(\cdot)$ are the Heaviside and Dirac Delta function, respectively, while l and r denote the domain left $(x < x_0)$ and right $(x > x_0)$ of the interface. Here, $\Lambda_{l/r}$ and $\mathcal{D}$ are no longer position-dependent. Note that the reasoning behind splitting up the potential in Eq. (2.3) into $\mathcal{C}(x)$ and $\mathcal{D}(x)$ is solely to distinguish step-like potentials from delta barriers.

We are now able to derive the generalized wave matching conditions for a Hamiltonian as introduced in Eq. (2.3). Since its eigenstates $\phi(x)$ are associated with one-particle probability distributions in real space, it is physically reasonable to assume that they are continuous for all x, and in particular at the interface, i.e.,

$$\lim_{\varepsilon\to 0^+}\phi(x_0+\varepsilon)=\lim_{\varepsilon\to 0^+}\phi(x_0-\varepsilon). \tag{2.5}$$

This provides a first condition. However, since Eq. (2.3) gives rise to a second-order system of differential equation(s), Eq. (2.5) alone is not sufficient. Therefore, we integrate the Schrödinger equation

$$\mathcal{H}\phi(x)=E\phi(x), \tag{2.6}$$

with E the energy eigenvalues, over a small domain around the interface at $x=x_0$ (we drop the argument x_0 in the following for compactness),

$$\int\limits_{x_0-\varepsilon}^{x_0+\varepsilon}\left[-\partial_x\left(\mathcal{A}(x)\phi'(x)\right)-\frac{i}{2}\left[\mathcal{B}(x)\phi'(x)+\partial_x\left(\mathcal{B}(x)\phi(x)\right)\right]+\left(\mathcal{C}(x)+\mathcal{D}(x)-E\right)\phi(x)\right]\mathrm{d}x=0. \tag{2.7}$$

We may evaluate each term of this integral separately. With $\Lambda'(x)=(\Lambda_r-\Lambda_l)\,\delta(x-x_0)$ and Eq. (2.5), we obtain

$$\int\limits_{x_0-\varepsilon}^{x_0+\varepsilon}\partial_x\left(\mathcal{A}(x)\phi'(x)\right)\mathrm{d}x=\left[\mathcal{A}(x)\phi'(x)\right]_{x_0-\varepsilon}^{x_0+\varepsilon}=\mathcal{A}_r\phi'(x_0+\varepsilon)-\mathcal{A}_l\phi'(x_0-\varepsilon), \tag{2.8}$$

$$\int\limits_{x_0-\varepsilon}^{x_0+\varepsilon}\mathcal{B}(x)\phi'(x)\mathrm{d}x=\left[\mathcal{B}(x)\phi(x)\right]_{x_0-\varepsilon}^{x_0+\varepsilon}-\int\limits_{x_0-\varepsilon}^{x_0+\varepsilon}\mathcal{B}'(x)\phi(x)\mathrm{d}x \tag{2.9a}$$

$$=\mathcal{B}_r\phi(x_0+\varepsilon)-\mathcal{B}_l\phi(x_0-\varepsilon)-\left(\mathcal{B}_r-\mathcal{B}_l\right)\phi(x_0)\overset{\varepsilon\to 0^+}{\longrightarrow}0, \tag{2.9b}$$

$$\int\limits_{x_0-\varepsilon}^{x_0+\varepsilon}\partial_x\left(\mathcal{B}(x)\phi(x)\right)\mathrm{d}x=\left[\mathcal{B}(x)\phi(x)\right]_{x_0-\varepsilon}^{x_0+\varepsilon}=\mathcal{B}_r\phi(x_0+\varepsilon)-\mathcal{B}_l\phi(x_0-\varepsilon)\overset{\varepsilon\to 0^+}{\longrightarrow}\left(\mathcal{B}_r-\mathcal{B}_l\right)\phi(x_0), \tag{2.10}$$

$$\int\limits_{x_0-\varepsilon}^{x_0+\varepsilon}\mathcal{C}(x)\phi(x)\mathrm{d}x=\mathcal{C}_l\int\limits_{x_0-\varepsilon}^{x_0}\phi(x)\mathrm{d}x+\mathcal{C}_r\int\limits_{x_0}^{x_0+\varepsilon}\phi(x)\mathrm{d}x\overset{\varepsilon\to 0^+}{\longrightarrow}0, \tag{2.11}$$

$$\int\limits_{x_0-\varepsilon}^{x_0+\varepsilon}\mathcal{D}(x)\phi(x)\mathrm{d}x=\mathcal{D}\int\limits_{x_0-\varepsilon}^{x_0+\varepsilon}\delta(x-x_0)\phi(x)\mathrm{d}x=\mathcal{D}\phi(x_0), \tag{2.12}$$

$$\int\limits_{x_0-\varepsilon}^{x_0+\varepsilon}E\phi(x)\mathrm{d}x\overset{\varepsilon\to 0^+}{\longrightarrow}0. \tag{2.13}$$

We thus arrive at the second wave matching condition, which reads

$$\lim_{\varepsilon\to 0^+}\left[\mathcal{A}_r\phi'(x_0+\varepsilon)-\mathcal{A}_l\phi'(x_0-\varepsilon)\right]=\left[\mathcal{D}-\frac{i}{2}\left(\mathcal{B}_r-\mathcal{B}_l\right)\right]\phi(x_0). \tag{2.14}$$

To summarize, the wave function itself is continuous, while its derivative features a jump if $\mathcal{B}_{l/r}$ or $\mathcal{D}$ is finite. This equation reduces to the well known condition for Delta potentials if $\mathcal{A}(x) \equiv \mathcal{A}$ and $\mathcal{B}(x) = \mathcal{B}$ (i.e., $\mathcal{A}_l = \mathcal{A}_r$ and $\mathcal{B}_l = \mathcal{B}_r$),

$$\lim_{\varepsilon \to 0^+} \left[\phi'(x_0 + \varepsilon) - \phi'(x_0 - \varepsilon)\right] = \mathcal{A}^{-1}\mathcal{D}\, \phi(x_0). \tag{2.15}$$

and to the continuity condition of the derivative if, additionally, $\mathcal{D} = 0$,

$$\lim_{\varepsilon \to 0^+} \left[\phi'(x_0 + \varepsilon) - \phi'(x_0 - \varepsilon)\right] = 0. \tag{2.16}$$

Notably, Eq. (2.14) depends neither on $\mathcal{C}_{l/r}$ nor the energy eigenvalues E.

Note that, as soon as any of the terms $(\mathcal{B}_r - \mathcal{B}_l)$ or $\mathcal{D}$ is non-zero, Eq. (2.14) is, mathematically speaking, only valid if at least one of the terms related to the effective mass, $\mathcal{A}_{l/r}$, is finite. Else, the condition reduces to $\phi(x_0) = 0$, which cannot be fulfilled for an arbitrary x_0. Physically speaking, this would mean that a junction of Dirac materials could not feature a Dirac potential or different Fermi velocities across an interface. We can resolve this by arguing that Dirac Hamiltonians in condensed matter theory are obtained by approximating a quadratic Hamiltonian in an energy domain in which the parameters $\mathcal{A}_{l/r}$ are rather small (i.e., the effective masses are very large), but do, strictly speaking, not vanish. Furthermore, a Dirac barrier can always be modeled by a potential of finite length d and performing the limit $d \to 0$, while keeping the barrier strength finite [56].

To arrive at Eq. (2.14), we made several assumptions that restrict the generality of our wave matching conditions. In fact, we are able to loosen these assumptions, whose primary purpose was the simplification of the derivation above. Let us resolve them one by one.

(i) The Hamiltonian needs not to be 1D for us to arrive at Eq. (2.14). It suffices if we can reduce a, e.g., 3D Hamiltonian $\mathcal{H}(x, y, z)$ to a quasi-1D operator. This is possible if the parameters vary in one spatial direction only, while the other two dimensions remain translational invariant. Then, we may perform Fourier transformations and obtain $\mathcal{H}(x, y, z) \to \mathcal{H}(x, k_y, k_z)$, where $k_{y/z}$ are the wavenumbers in y- and z-direction, representing good quantum numbers. All terms proportional to $k_{y/z}$ can be absorbed into the term $C(x)$ in Eq. (2.3), and the result in Eq. (2.14) is not affected. (ii) In principle, it is not necessary to restrict ourselves to step-like potentials. We can always separate a system with varying parameters into domains where they are nearly constant. This, however, may be cumbersome in an analytical calculation. (iii) Due to the linearity of the integral, Eq. (2.14) can be applied to any number of interfaces, as long as the Hamiltonian can be reduced to a quasi-1D operator. This means the interfaces need to appear along the same spatial direction (e.g., x).

2.3.2 Generalized probability current

While the wave matching conditions in Eqs. (2.5) and (2.14) provide relations to determine the scattering coefficients in a hybrid nanostructure, the actual transport properties depend on the corresponding probability current density. From the equation of continuity,

$$\frac{\partial \rho}{\partial t} + \partial_x j = 0, \qquad\qquad \rho = |\phi(x,t)|^2\,, \tag{2.17}$$

as well as the time-dependent Schrödinger equation,

$$i\frac{\partial}{\partial t}\phi(x,t) = \mathcal{H}\phi(x,t) \qquad \Rightarrow \qquad \frac{\partial}{\partial t}\phi(x,t) = -i\mathcal{H}\phi(x,t), \tag{2.18}$$

we are able to derive an equally general expression (related to Hamiltonians $\mathcal{H}$ of the form introduced in Eq. (2.3)) for the probability current density. We find (for the sake of clarity, we drop all variable-dependencies)

$$
\begin{aligned}
\frac{\partial\rho}{\partial t} &= \partial_t\phi^\dagger\phi + \phi^\dagger\partial_t\phi = \left(-i\mathcal{H}\phi\right)^\dagger\phi + \phi^\dagger\left(-i\mathcal{H}\phi\right) && \text{(2.19a)}\\
&= i\left[\phi^\dagger\mathcal{A}\phi'' + \phi^\dagger\mathcal{A}'\phi' - (\phi^\dagger)''\mathcal{A}\phi + (\phi^\dagger)'\mathcal{A}'\phi\right] - \left(\phi^\dagger\mathcal{B}\phi' + (\phi^\dagger)'\mathcal{B}\phi + \phi^\dagger\mathcal{B}'\phi\right) && \text{(2.19b)}\\
&= -\partial_x\left[i\left((\phi^\dagger)'\mathcal{A}\phi - \phi^\dagger\mathcal{A}\phi'\right) + \phi^\dagger\mathcal{B}\phi\right] = -\partial_x\left[2\,\mathrm{Im}\left(\phi^\dagger\mathcal{A}\phi'\right) + \phi^\dagger\mathcal{B}\phi\right], && \text{(2.19c)}
\end{aligned}
$$

such that the probability current density of a given eigenstate $\phi(x)$ reads

$$
j\left[\phi(x)\right] = 2\,\mathrm{Im}\left(\phi^\dagger(x)\mathcal{A}(x)\phi'(x)\right) + \phi^\dagger(x)\mathcal{B}(x)\phi(x). \tag{2.20}
$$

Note that this quantity depends only on the effective mass and the velocity of the electrons, but not on the potential terms in our model Hamiltonian.

2.3.3 Derivation of the current

With the probability amplitudes at hand, we are now able to derive an explicit relation for the bias-dependent current in the system. We start from the single-mode expression,

$$
I(k_y) = 2e\int\limits_{-\infty}^{\infty} N_{k_y}(E)v_{k_y}(E)\left[f_{k_y,\rightarrow}(E) - f_{k_y,\leftarrow}(E)\right]\mathrm{d}E \tag{2.21}
$$

with $N_{k_y}(E)$, $v_{k_y}(E)$ and $f_{k_y,\leftrightarrows}(E)$ the density of states, group velocity and distribution functions (the arrows indicating incoming and outgoing states) for each 1D mode, indexed by k_y, at energy E, respectively. The relation $N_{k_y}(E) = 1/\left[2\pi\hbar v_{k_y}(E)\right]$ allows us to further simplify this expression, and we obtain

$$
I(k_y) = \frac{2e}{h}\int\limits_{-\infty}^{\infty}\left[f_{k_y,\rightarrow}(E) - f_{k_y,\leftarrow}(E)\right]\mathrm{d}E. \tag{2.22}
$$

Under the assumption of local equilibria on the left and right hand side of the interface, we may write [27]

$$
\begin{aligned}
f_{k_y,\rightarrow}(E) &= f_0(E - eV), && \text{(2.23a)}\\
f_{k_y,\leftarrow}(E) &= A(E,k_y)\left[1 - f_{k_y,\rightarrow}(-E)\right] + B(E,k_y)f_{k_y,\rightarrow}(E) + \left[C(E,k_y) + D(E,k_y)\right]f_0(E), && \text{(2.23b)}
\end{aligned}
$$

where V is the bias applied to the system and A, B, C and D are probability current densities related to reflection (A, B) and transmission (C, D) scattering processes. We explain them in detail later in this chapter. With Eq. (2.23) as well as the relations $A(-E,k_y) = A(E,k_y)$ and $f_0(-E) = 1 - f_0(E)$, Eq. (2.22) evaluates to

$$
I(V,k_y) = \frac{2e}{h}\int\limits_{-\infty}^{\infty}\left[f_0(E - eV) - f_0(E)\right]\left[1 + A(E,k_y) - B(E,k_y)\right]\mathrm{d}E. \tag{2.24}
$$

As stated above, this is a single-mode expression under the assumption of translational invariance in y-direction. Therefore, the general current is given by the sum over all modes k_y,

$$
I(V) = \frac{2e}{h}\sum_{k_y}\int\limits_{-\infty}^{\infty}\left[f_0(E - eV) - f_0(E)\right]\left[1 + A(E,k_y) - B(E,k_y)\right]\mathrm{d}E. \tag{2.25}
$$

2.4 Setup and Hamiltonian

2.4.1 General definitions and calculations

While the system in Fig. 2.1 consists of two N(or S)-SM interfaces in series, we study the electronic properties and the scattering processes of only one of them. The full system can then be described by the formalism introduced by Octavio *et al.*, which allows to combine two single-interface setups to a joined system [57]. Without loss of generality, we choose the interface to be located at $x_0 = 0$. For simplicity and pedagogical reasons, we continue to employ the model of the quasi-free electron gas from Sec. 2.2 and assume s-wave pairing in the superconductor. A more sophisticated analysis on HgTe is given in Sec. 2.6. The Bogoliubov-de Gennes (BdG) framework [58] is a suitable formalism to deal with such a system, and we introduce the kernel Hamiltonian in the Nambu basis $(\hat{c},\, \hat{c}^\dagger)^T$ as

$$\mathcal{H}_{\mathrm{BdG}}(x) = \Big(\hat{k}_x \frac{\hbar^2}{2m(x)} \hat{k}_x + \frac{\hbar^2 k_y^2}{2m(x)} - \mu(x) + H\delta(x)\Big)\tau_z + \Delta(x)\tau_x, \tag{2.26}$$

where $\hat{c}^\dagger$ is the creation operator of an electron and $\tau_{0,x,y,z}$ are unit and Pauli matrices in Nambu space. Furthermore, $m(x)$ is the effective mass and $\mu(x)$, $\Delta(x)$ and H are the electrochemical potential, the superconducting order parameter and a repulsive scattering potential at the interface, respectively. Note that $\mathcal{H}_{\mathrm{BdG}}$ is of the form as introduced in Eq. (2.3) with

$$\mathcal{A}(x) = \frac{1}{2m(x)}\tau_z, \qquad \mathcal{B}(x) = 0, \qquad \mathcal{C}(x) = \left(\frac{\hbar^2 k_y^2}{2m(x)} - \mu(x)\right)\tau_z + \Delta(x)\tau_x, \qquad \mathcal{D} = H\tau_z, \tag{2.27}$$

and a quasi-1D operator since we assume the y-direction to be translational invariant. k_y is thus a good quantum number parameterizing the transverse modes.

In the domain left (L) and right (R) of the interface, we assume constant effective masses m_l and m_r, which shall be, in general, distinct from each other. Similarly, we assume the order parameter to be finite and constant in S only, while the electrochemical potential attains a global value. The potentials thus read, explicitly,

$$m(x) = m_l\Theta(-x) + m_r\Theta(x), \qquad \Delta(x) = \Delta_0\Theta(x), \qquad \mu(x) = \mu. \tag{2.28}$$

The step-wise variation of these parameters is justified if the Fermi wave lengths are large in both L and R. Solving the BdG equations

$$\mathcal{H}_{\mathrm{BdG}}(x)\psi(x) = E\psi(x), \tag{2.29}$$

this yields the eigenenergies deep inside the bulk materials,

$$E^\pm\big|_{x\ll x_0} = \pm\left(\frac{\hbar^2 k^2}{2m_l} - \mu\right), \qquad E^\pm\big|_{x\gg x_0} = \pm\sqrt{\left(\frac{\hbar^2 k^2}{2m_r} - \mu\right)^2 + \Delta_0^2} \tag{2.30}$$

with $k = \sqrt{k_x^2 + k_y^2}$. We obtain two bands each since we consider both electron and hole excitations, and the excitation energy is measured from the Fermi level inside S (here, $E = 0$). The associated (unnormalized) energy eigenstates read

$$|E^+\rangle = (1,0)^T, \qquad |E^-\rangle = (0,1)^T \tag{2.31}$$

in L and

$$|E^\pm\rangle = \begin{pmatrix} \dfrac{\left(k^2 - \kappa_r^2\right)\hbar^2 \pm \sqrt{\left(k^2 - \kappa_r^2\right)^2\hbar^4 + 4m_r^2\Delta_0^2}}{2m_r\Delta_0} \end{pmatrix} \tag{2.32}$$

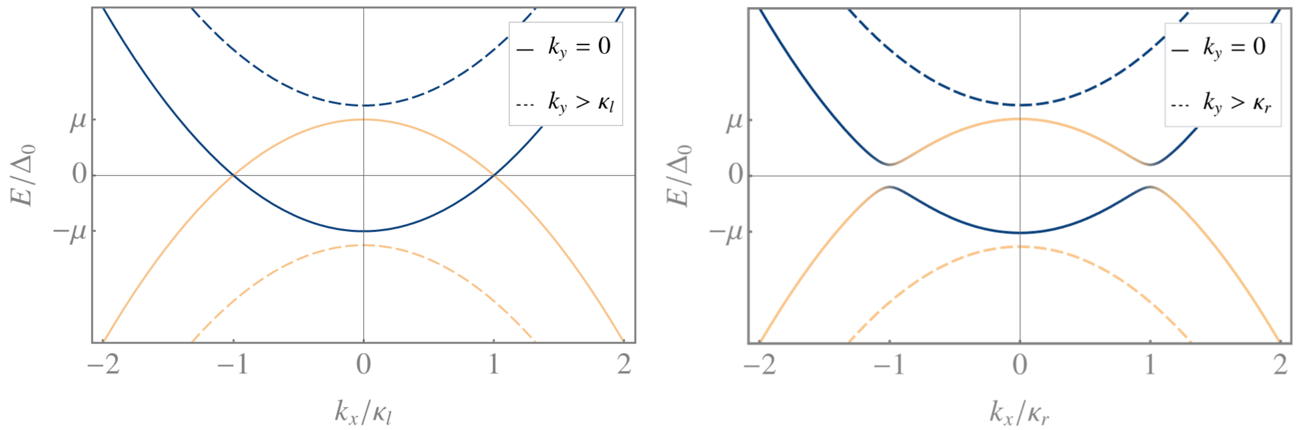

(a) $E\big|_{x\ll x_0}$ **(b)** $E\big|_{x\gg x_0}$

Fig. 2.6: Energy dispersion of the bulk materials far **(a)** left and **(b)** right of the interface as a function of k_x. Electron bands are given in dark blue, hole bands in orange. We consider the zero-mode (solid lines), where the electron band and the hole band are degenerate at the Fermi energy, and a mode which exceeds the Fermi wavenumbers $\kappa_{l/r}$ (dashed), where a partial gap opens up between the bands.

in R. The dispersions are plotted in Fig. 2.6, where the Fermi wavenumbers are given by $\kappa_{l/r} = \sqrt{2m_{l/r}\mu}/\hbar$ in L/R. For a finite (and positive) electrochemical potential, the bands intersect with each other at $k = \kappa_{l/r}$, i.e., the electron and hole states are degenerate at the Fermi energy, see Fig. 2.6(a) (here, $k_y = 0$). If $\Delta_0 > 0$, the superconducting gap opens around this energy, such that no electron or hole states exist in the domain $|E| \leq \Delta_0$, see Fig. 2.6(b) (here, $k_y = 0$). As a consequence, the bands change their particle nature around $k_x = \kappa_r$, which is indicated by the color code. For instance, $E^+\big|_{x\gg x_0}$ is electron-like (dark blue) for $|k_x| > \kappa_r$ and hole-like (orange) for $|k_x| < \kappa_r$. We can determine this particle nature by calculating the charge of the eigenstates in Eqs. (2.31) and (2.32) by means of the charge operator $\hat{\mathcal{C}} = \tau_z$,

$$Q_C = \frac{\langle E^\pm|\,\hat{\mathcal{C}}\,|E^\pm\rangle}{\langle E^\pm|E^\pm\rangle}. \tag{2.33}$$

Note that, by increasing the mode parameter k_y, we shift the electron (hole) dispersion to positive (negative) energies. This opens a partial gap between the bands if k_y is larger than the respective Fermi wavenumber $\kappa_{l/r}$, see the dashed lines in Fig. 2.6. As a consequence, elastic interband scattering processes can no longer occur and no S gap opens up for this choice of parameters. This is an important point which we discuss in detail later in this chapter. The same physics occurs if we choose μ to be negative, for all values of k_y (i.e., the dispersions are all similar to the dashed lines in Fig. 2.6, independent of k_y). Since this case is not relevant for us, we presume $\mu > 0$ in what follows.

In order to deal with the interface, the bulk eigenstates in Eqs. (2.31) and (2.32) are not sufficient since translational invariance is broken in x-direction. Therefore, $\hat{k}_x$ must be expressed in operator form, $\hat{k}_x = -i\partial_x$, and we obtain the eigenstates in a mixed energy-position representation as

$$\psi_e^\pm(x) = \begin{pmatrix}1\\0\end{pmatrix} e^{\pm ik_e x}, \quad \psi_h^\pm(x) = \begin{pmatrix}0\\1\end{pmatrix} e^{\mp ik_h x}, \quad \psi_{eq}^\pm(x) = \begin{pmatrix}u\\v\end{pmatrix} e^{\pm ik_{eq} x}, \quad \psi_{hq}^\pm(x) = \begin{pmatrix}v\\u\end{pmatrix} e^{\mp ik_{hq} x}. \tag{2.34}$$

Here, the superscripts ± indicate the sign of the group velocity in x-direction and the subscripts distinguish electrons (e) from holes (h) in L as well as electron-like (eq) from hole-like (hq) particles in R. The BCS coefficients are given by

$$u^2 = 1 - v^2 = \frac{1}{2}\left(1 + \frac{\Omega}{E}\right), \qquad \text{with} \qquad \Omega = \sqrt{E^2 + \Delta_0^2}, \tag{2.35}$$

and the wavenumbers read

$$k_e = \kappa_l \sqrt{1 + \frac{E}{\mu} - \left(\frac{k_y}{\kappa_l}\right)^2}, \qquad k_h = \xi_h \kappa_l \sqrt{1 - \frac{E}{\mu} - \left(\frac{k_y}{\kappa_l}\right)^2}, \tag{2.36a}$$

$$k_{eq} = \kappa_r \sqrt{1 + \frac{\Omega}{\mu} - \left(\frac{k_y}{\kappa_r}\right)^2}, \qquad k_{hq} = \xi_{hq} \kappa_r \sqrt{1 + \frac{\Omega}{\mu} - \left(\frac{k_y}{\kappa_r}\right)^2}. \tag{2.36b}$$

Finally, the factors

$$\xi_h = \operatorname{sgn}\left[\mu\left(1 - \left(\frac{k_y}{\kappa_l}\right)^2\right) - E\right], \qquad \xi_{hq} = \operatorname{sgn}\left[\sqrt{\mu^2\left(1 - \left(\frac{k_y}{\kappa_r}\right)^2\right)^2 + \Delta_0^2} - E\right] \tag{2.37}$$

guarantee the appropriate asymptotic behavior of the wave functions when $\psi_h^\pm(x)$ or $\psi_{hq}^\pm(x)$ describe evanescent waves. The explicit group velocities associated to each of the states in Eq. (2.34) can be obtained by the relation

$$v_g = \left(\frac{\hbar \partial k}{\partial E}\right)^{-1} \tag{2.38}$$

and read

$$v_{e/h} = \frac{\hbar k_{e/h}}{m_l}, \qquad v_{eq/hq} = \frac{\hbar k_{eq/hq}}{m_r}\left(|u|^2 - |v|^2\right). \tag{2.39}$$

Note that the BCS coefficient are complex conjugates of each other if $|E| < \Delta_0$, such that $v_{eq/hq}$ vanish at subgap energies. This captures the underlying physics appropriately, since there are no propagating states in this regime.

We are now able to define the scattering state for the NS-junction. Assuming an electron excited in N and moving towards the interface, it reads

$$\phi(x) = \begin{cases} \psi_e^+(x) + a\,\psi_h^-(x) + b\,\psi_e^-(x), & x < 0 \\ c\,\psi_{eq}^+(x) + d\,\psi_{hq}^+(x), & x > 0 \end{cases}. \tag{2.40}$$

This process is schematically illustrated in Fig. 2.7. When the incident electron (blue point) approaches the interface, it can either be reflected as an electron (normal reflection, b) on the other side of the Fermi surface or as a hole (Andreev reflection [25], a) on the same side of the Fermi surface. Likewise, it can be transmitted across the interface into S as an electron-like particle (transmission without branch crossing, c) or as a hole-like particle (transmission with branch crossing, d). Here, a, b, c and d are scattering coefficients, which are related to the probability amplitudes for each of their associated processes.

Note that, in total, there are four scattering states corresponding to *outgoing boundary conditions* (we elucidate this concept in detail in the next two chapters). While $\phi(x)$ describes an electron excited in N, we can equally assume that an electron-like particle is excited in S. In a setup with a single interface, the results are the same as those we obtain from $\phi(x)$, which is why we do not consider it separately. Furthermore, the scattering state for a hole excited in N (a hole-like particle excited in S) is related to that of an electron excited in N (an electron-like particle excited in S) by the intrinsic BdG particle-hole symmetry, given by

$$\mathcal{U}_{\mathrm{BdG}} \mathcal{H}_{\mathrm{BdG}} \mathcal{U}_{\mathrm{BdG}}^\dagger = -\mathcal{H}_{\mathrm{BdG}}, \tag{2.41}$$

where $\mathcal{U}_{\mathrm{BdG}} = -i\tau_y \mathcal{K}$ and $\mathcal{K}$ is the operator of complex conjugation. The full set of scattering states is not required to determine the current and the differential conductance of the junction, which is why we focus our studies on $\phi(x)$ as defined above. It is, however, necessary for the subsequent two chapters, which is why we put an emphasis on the *full set of states*.

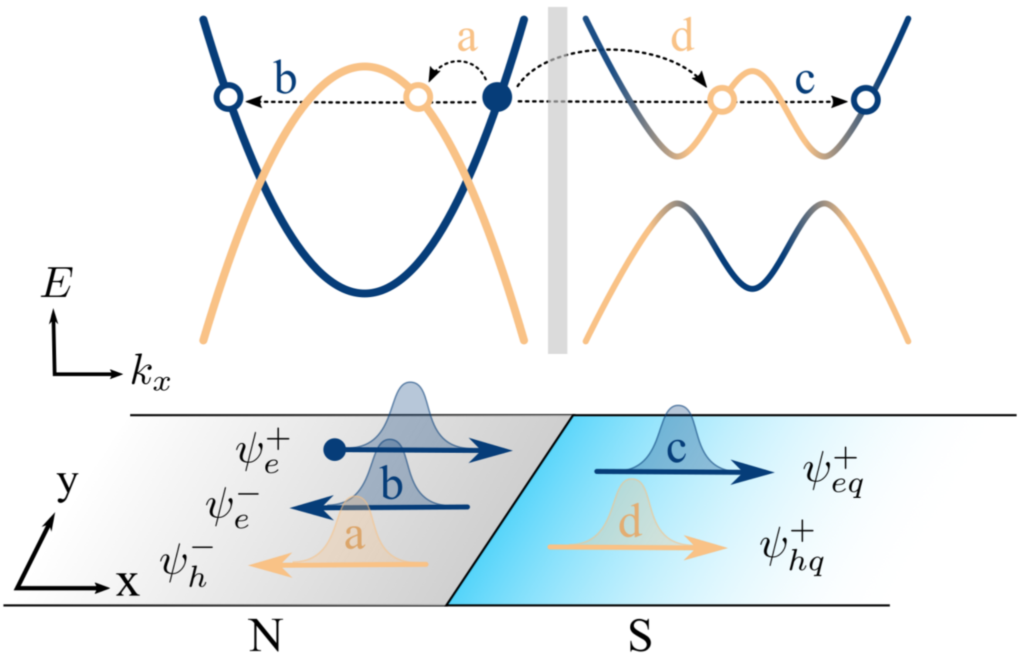

Fig. 2.7: Schematic illustration of the scattering state $\phi(x)$ from (**top**) a spectral and (**bottom**) a real-space point of view (for a fixed mode k_y). An electron is excited in N and approaches the interface (blue point). There, it can be reflected as either an electron or a hole, or it can be transmitted into S as either an electron-like or a hole-like particle.

2.4.2 The Andreev approximation

So far, the quantities introduced in Sec. 2.4.1 are derived without any approximation on the parameters in $\mathcal{H}_{\text{BdG}}$. Usually, however, the electrochemical potential μ, which is related to the carrier density, is rather large in metals and semiconductors, compared to the excitation energy and the order parameter. This so-called Andreev approximation, i.e., $\mu \gg E, \Delta_0$, significantly simplifies the following calculations, while the qualitative findings are merely affected. Explicitly, we have

$$\frac{E}{\mu} = \frac{\Omega}{\mu} \approx 0, \tag{2.42}$$

such that the wavenumbers in Eq. (2.36) simplify to

$$k_e = k_h \approx \kappa_l \cos\theta_l \equiv k_l, \qquad k_{eq} = k_{hq} \approx \kappa_r \cos\theta_r \equiv k_r \tag{2.43}$$

with

$$\theta_l = \arcsin\left(\frac{k_y}{\kappa_l}\right), \qquad \theta_r = \arcsin\left(\frac{k_y}{\kappa_r}\right). \tag{2.44}$$

These angles are well defined since we assume $|k_y| \leq \kappa_l$ in L and $|k_y| \leq \kappa_r$ in R. With Eq. (2.43), the group velocities simplify similarly,

$$v_e = v_h = \frac{\hbar k_l}{m_l} \equiv v_l, \qquad v_{eq} = v_{hq} = \frac{\hbar k_r}{m_r}\left(|u|^2 - |v|^2\right) \equiv v_r\left(|u|^2 - |v|^2\right). \tag{2.45}$$

and the eigenstates read as

$$\psi_e^\pm(x) = \begin{pmatrix}1\\0\end{pmatrix} e^{\pm ik_l x}, \quad \psi_h^\pm(x) = \begin{pmatrix}0\\1\end{pmatrix} e^{\mp ik_l x}, \quad \psi_{eq}^\pm(x) = \begin{pmatrix}u\\v\end{pmatrix} e^{\pm ik_r x}, \quad \psi_{hq}^\pm(x) = \begin{pmatrix}v\\u\end{pmatrix} e^{\mp ik_r x}. \tag{2.46}$$

Note that the approximation in Eq. (2.42) seems rather crude, especially since Ω features a complex phase if $|E| < \Delta_0$. Nevertheless, this does not affect the transport properties, since the latter is encoded in the BCS coefficients, u and v, as well.

2.5 Results

In order to study the electronic properties of the interface, we consider the transmission coefficient for electrical current, as denoted by BTK [27]. Under the presumption of local equilibria left and right of the junction, which we assume is justified by a sufficiently large FSM, it is given by

$$T(E, k_y) = 1 + A(E, k_y) - B(E, k_y), \tag{2.47a}$$

$$T(E, \theta_l) = 1 + A(E, \theta_l) - B(E, \theta_l), \tag{2.47b}$$

where the second definition via θ_l is appropriate for the scattering state $\phi(x)$ as introduced in Eq. (2.40) under the Andreev approximation[2]. This is a single-mode expression, while, in an experiment, distinct angles of incidence (i.e., transverse modes) are difficult to realize. Therefore, we introduce the *full transmission coefficient*, which is the sum over all modes of the expression in Eq. (2.47), as

$$T(E) \equiv \sum_{k_y} T(E, k_y) \rightarrow \frac{W}{2\pi} \int\limits_{-\kappa_l}^{\kappa_l} T(E, k_y) \mathrm{d}k_y, \tag{2.48a}$$

$$T(E) \equiv \sum_{\theta_l} T(E, \theta_l) \rightarrow \frac{W\kappa_l}{2\pi} \int\limits_{-\pi/2}^{\pi/2} T(E, \theta_l) \cos\theta_l \mathrm{d}\theta_l, \tag{2.48b}$$

where we replace the sum by a k-space integral in the continuous limit and W is the width of the junction.

In Eq. (2.47), A and B are the probability currents for Andreev and normal reflection, respectively. They can be derived from the scattering state $\phi(x)$ and the relation in Eq. (2.20) and read (we omit dependencies for the sake of clarity)

$$A = \frac{\mathrm{Re}(v_h)}{v_e} |a|^2, \qquad B = |b|^2, \qquad C = \frac{\mathrm{Re}(v_{eq})}{v_e} |c|^2, \qquad D = \frac{\mathrm{Re}(v_{hq})}{v_e} |d|^2, \tag{2.49}$$

where C and D are, additionally, the probabilities for transmission without and with branch crossing, respectively. Note that, since the probability current needs to be conserved, these amplitudes are related to each other by the equation

$$A + B + C + D = 1. \tag{2.50}$$

The scattering coefficients a, b, c, d are determined by matching the waves at the interface, $x_0 = 0$, according to the relations in Eqs. (2.5) and (2.14). Considering $\mathcal{H}_{\mathrm{BdG}}$ in Eq. (2.26), this yields the conditions

$$\lim_{\varepsilon \to 0} \left(\phi(0+\varepsilon) - \phi(0-\varepsilon)\right) = 0, \tag{2.51a}$$

$$\lim_{\varepsilon \to 0} \left(\frac{\phi'(0+\varepsilon)}{m_r} - \frac{\phi'(0-\varepsilon)}{m_l} \right) = \frac{2H}{\hbar^2} \phi(0). \tag{2.51b}$$

With this, we are now able to study the electronic properties of the interface.

2.5.1 Normal-state transmission

We start our analysis by setting the order parameter globally to zero, $\Delta(x) = 0$, such that we are left with an NN' junction. As we will show, significant results and conclusions on the transport properties that we can draw for an NS junction can already be found in a similar form in such a reduced model.

---

[2] Note that, since k_y is assumed to be conserved in a scattering process due to the translational invariance in y-direction, θ_r is directly related to θ_l

The simplified expressions provide a convenient starting point to understand the underlying physics of the problem, which can then be transferred and extended to the more complex superconducting case.

As a first consequence of this choice, the probability currents for Andreev reflection and transmission with branch crossing vanish, $A = D = 0$, i.e., all electron-hole conversion processes are suppressed due to the absence of coupling by the superconductor. Then, the transport coefficient evaluates (without any approximations for now) to

$$T(E,k_y) = 1 - B(E,k_y) = C(E,k_y) = \frac{4m_l m_r \hbar^4 \mathrm{Re}(k_e)\mathrm{Re}(k_{eq})}{4H^2 m_l^2 m_r^2 + \hbar^4 \left(m_r k_e + m_l k_{eq}\right)^2}. \tag{2.52}$$

In the NN' setup, k_{eq} describes the wavenumber of an electron, similar to k_e, so both can either be purely real or purely imaginary, *cf.* Eq. (2.36). This allows us to simplify the above expression to

$$T(E,k_y) = \frac{4\hbar^2 v_e v_{eq}}{4H^2 + \hbar^2 \left(v_e + v_{eq}\right)^2}\Theta(\kappa_l - |k_y|)\Theta(\kappa_r - |k_y|). \tag{2.53}$$

The Heaviside functions corroborate the underlying physics of the scattering process - if $|k_y| > \kappa_l$, the incident wave is described by an evanescent state which cannot propagate in the first place, while for $|k_y| > \kappa_r$, an incident electron in N has no corresponding state in N' and is always reflected (note that this is directly related to FSM). In both cases, T vanishes and we have no transport across the junction.

The Andreev approximation allows us to further simplify the transport coefficient. Assuming $m_l > m_r$, *cf.* Fig. 2.3 and rescaling $H \to Z\sqrt{(\kappa_l \kappa_r)/(m_l m_r)}\hbar^2$, we obtain an expression which is independent of the energy,

$$T(E,k_y) \approx T(k_y) = T(\theta_l) = \frac{4r\cos\theta_l \cos\theta_r\ \Theta(\theta_c - |\theta_l|)}{4rZ^2 + (r\cos\theta_l + \cos\theta_r)^2}, \qquad \cos\theta_r = r^{-1}\sqrt{r^2 - \sin^2\theta_l}. \tag{2.54}$$

Here, $\theta_c = \arcsin(\kappa_r/\kappa_l)$ is the critical angle as introduced in Fig. 2.3. For larger angles of incidence, $|\theta_l| > \theta_c$, transmission from N to N' is no longer possible due to the absence of states.

We proceed our analysis by first considering the dependence of T on the two relevant parameters, barrier strength Z and FSM r, separately. This aids in the understanding of the behavior if both an repulsive interface potential as well as a mismatch are present.

Dependence on the interface barrier Z

Assuming homogeneous materials ($\kappa_l = \kappa_r \Leftrightarrow r = 1$) and a finite Z-parameter, the transport coefficient simplifies to

$$T(\theta_l) = \frac{1}{\frac{Z^2}{\cos^2\theta_l} + 1}, \tag{2.55}$$

which reduces further to the well-known [27] 1D expression

$$T_0 \equiv T(\theta_l = 0) = \frac{1}{Z^2 + 1}, \tag{2.56}$$

at perpendicular incidence. This zero-mode value corresponds to the maximum of $T(\theta_l)$, while reflection becomes more favorable for increasing angles of incidence $|\theta_l| > 0$. We plot this behavior in Fig. 2.8(a). For a vanishing barrier strength $Z = 0$, transmission occurs with unit probability at all angles, since the interface is practically non-existing and we are left with a homogeneous material. Increasing Z reduces the zero-mode value T_0, see Fig. 2.8, which in turn diminishes the overall probability for transmission across the junction. At $\theta_l = \pm\pi/2$, $T(\theta_l)$ vanishes since the incident electron moves parallel to the interface.

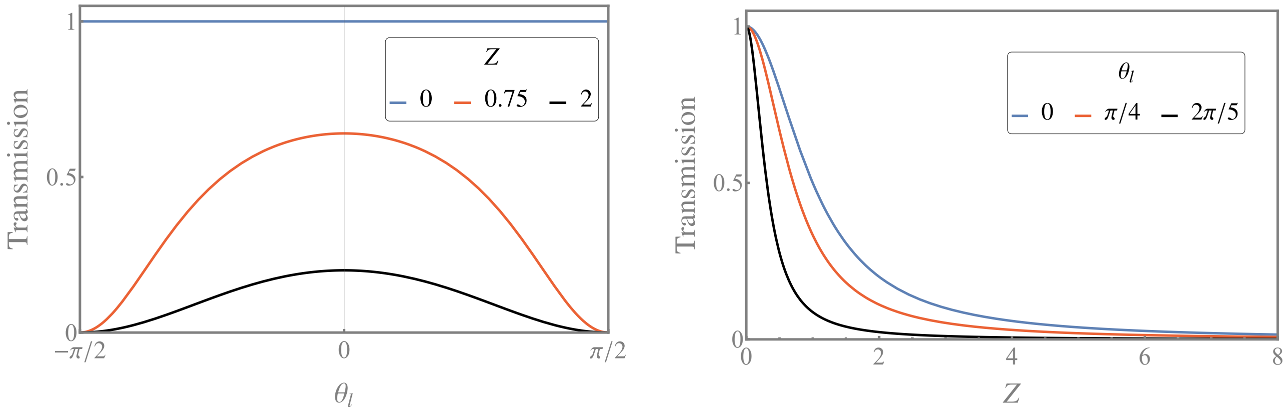

(a) Angle-dependence **(b)** Barrier-dependence

Fig. 2.8: Transmission coefficient T as a function of **(a)** the angle of incidence θ_l and **(b)** the barrier strength Z. Electrons are always transmitted from N to N' if the interface is clean, $Z = 0$. For a finite repulsive potential, T decreases from its zero-mode value, T_0, with increasing θ_l. *Reprinted figure with permission from [34]. Copyright (2021) by the American Physical Society.*

We can understand the increasing chance for reflection at finite angles if we rewrite Eq. (2.55) in terms of the group velocities, which yields

$$T(\theta_l) = \frac{v_l^2}{H^2/\hbar^2 + v_l^2}. \tag{2.57}$$

For larger angles of incidence, v_l – the group velocity normal to the interface – becomes smaller, *cf.* Eqs. (2.43) and (2.45), as does the transmission coefficient. As a consequence, electrons with a smaller group velocity in x-direction ($|\theta_l| > 0$) are more likely to be reflected at the interface than those with a larger group velocity ($\theta_l \approx 0$). Or, to put it differently, the former experience an apparently larger barrier strength than the latter, and we could write

$$T(\theta_l) = \frac{1}{\bar{Z}^2(\theta_l) + 1}, \qquad \text{with} \qquad \bar{Z}(\theta_l) = \frac{Z}{\cos\theta_l}, \tag{2.58}$$

where the mode is absorbed into the barrier strength. This allows us to write $T(\theta_l)$ in a form similar to T_0.

While an NN' junction made from a homogeneous material and a repulsive interface potential yields no surprising insights, the results for a system featuring FSM are more interesting, as we will show now.

Dependence on Fermi surface mismatch

Assuming a clean interface, but different effective masses m_l and m_r in L and R, respectively, the transmission coefficient for electrical current becomes

$$T(\theta_l) = \frac{4r\cos\theta_l\cos\theta_r}{(r\cos\theta_l + \cos\theta_r)^2}\Theta\left(\theta_c - |\theta_l|\right). \tag{2.59}$$

Blonder *et al.* [46] have studied FSM in 1D systems and concluded that this mismatch can be interpreted as an effective interface potential Z_{eff}. This becomes apparent when we consider Eq. (2.59) at perpendicular incidence, which yields

$$T(\theta_l = 0) = \frac{4r}{(1+r)^2}. \tag{2.60}$$

This expression is constant, and we are inclined to write this, once again, in the form of Eq. (2.56). By defining

$$Z_{\text{eff}} = \frac{1-r}{2\sqrt{r}}, \tag{2.61}$$

we obtain

$$T(\theta_l = 0) = \frac{1}{Z_{\text{eff}}^2 + 1}, \tag{2.62}$$

and one is lead to the seemingly convenient interpretation of FSM as an effective, repulsive potential which enables reflection at the interface of a 1D system. The physics in a planar setup is, however, more complicated.

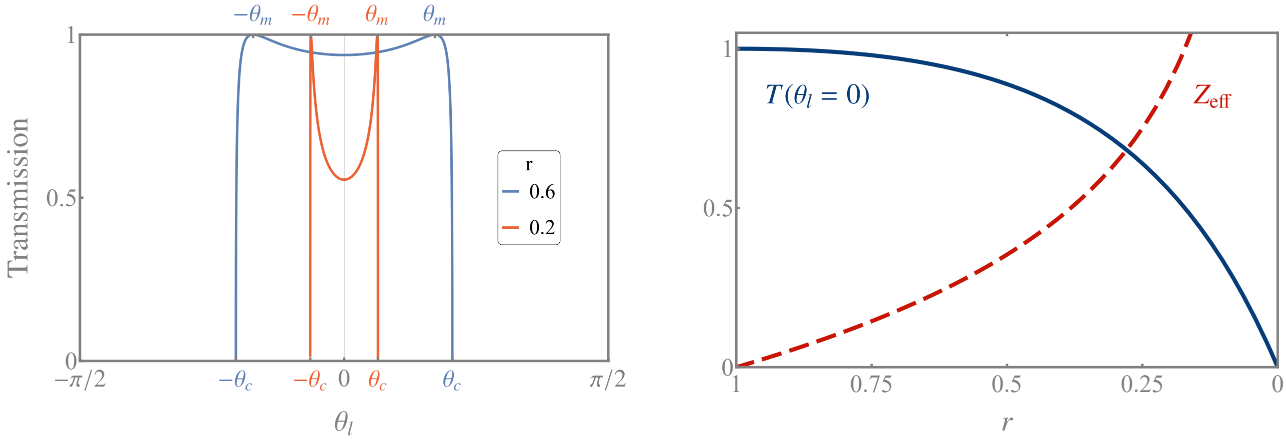

(a) Angle-dependence

(b) r-dependence

Fig. 2.9: (a) Transmission coefficient T as a function of the angle of incidence θ_l for different degrees of r. In contrast to a homogeneous system with an interface barrier, T increases from its zero-mode value and becomes unity at $\theta_l = \pm\theta_m$. Due to the mismatch, electrons with $|\theta_l| > \theta_c$ are always reflected. **(b)** FSM-dependence of the zero-mode value (blue) and the effective barrier strength (red). *Reprinted figure with permission from [34]. Copyright (2021) by the American Physical Society.*

We plot the transmission coefficient $T(\theta_l)$ as a function of the angle of incidence and for two different degrees of FSM in Fig. 2.9(a). As indicated by the step functions, the curves features a sharp cut-off at the critical angle $\theta_c = \arcsin(r)$, such that the probability for transmission is finite only for smaller angles of incidence. Incident modes with $\theta_c < |\theta_l| < \pi/2$ do not have a corresponding mode in R and are reflected with unit probability. Furthermore, the zero-mode transmission decreases with increasing FSM, see Fig. 2.9(b), in accordance with Eqs. (2.61) and (2.62). Intriguingly, however, $T(\theta_l)$ does *not* decrease when θ_l deviates from zero. Instead, it increases and even reaches a maximum at

$$|\theta_l| = \theta_m \equiv \arcsin\left(\frac{r}{\sqrt{1+r^2}}\right) < \theta_c. \tag{2.63}$$

The last inequality indicates that this maximum is reached for any choice of r. For $|\theta_l| > \theta_m$, $T(\theta_l)$ quickly decreases and vanishes at $\theta_l = \pm\theta_c$.

As we can see, the angular dependence behaves rather differently in a system featuring FSM and a clean interface than in a homogeneous material with a local repulsive potential. Evidently, FSM cannot be interpreted as an effective interface barrier in a planar setup. This has an interesting consequence for the full transmission coefficient, *cf.* Eq. (2.48), which is directly related to the differential conductance and thus the current in the system – while a large FSM reduces the angular range over which transport across the junction can occur, i.e., $|\theta_l| < \theta_c \ll \pi/2$, it still enables a strong contribution from the propagating modes, since it does not further decrease the probability for transmission. This can lead to an observable excess current, as we will show later in this chapter.

The reason for the observation of these maxima and the increasing transmission probability is related to the group velocity of the states in L and R, see Fig. 2.10. Mismatching dispersions left and right of the interface lead to generally different group velocities of the electrons. For perpendicular incidence, $v_{l/r}$ as well as their difference $|v_l - v_r|$ are maximal, which is why the transmission is lowest at $\theta_l = 0$ (in the range $|\theta_l| < \theta_m$). Increasing the angle reduces the velocities, v_r (which is finite and real only for $|\theta_l| < \theta_c$ due to FSM), however, at a larger rate than v_l. As a consequence, there exists an angle at which the two of them coincide, which is given by θ_m in Eq. (2.63), i.e., $v_l|_{\theta_l=\pm\theta_m} = v_r|_{\theta_l=\pm\theta_m}$. This is the optimal condition for perfect transmission in the absence of a barrier, and we have

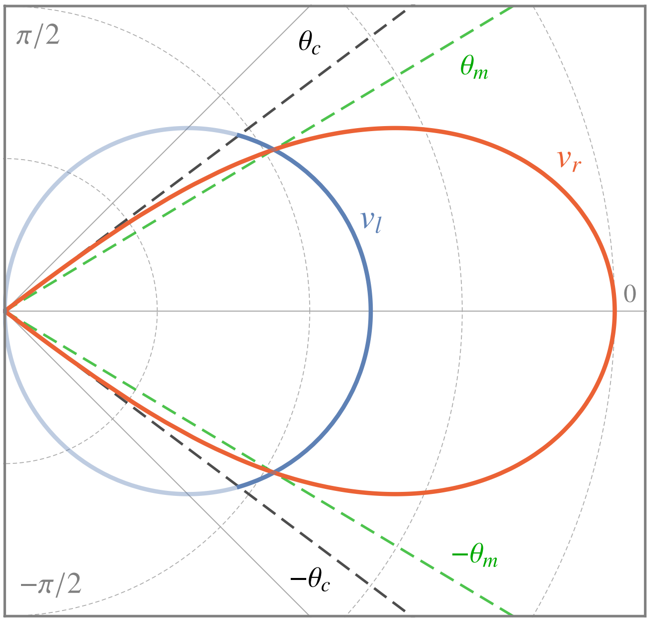

Fig. 2.10: Angular dependence of v_l and v_r in an NN' junction with $r = 0.6$. In a system featuring FSM, the group velocities are, in general, different from each other, but coincide at $\theta_l = \theta_m$, where the transmission probability becomes unity. Note that v_r is finite only for $|\theta_l| < \theta_c$. The velocities $v_l(|\theta_l| > \theta_c)$ of incident electrons that are reflected with unit probability are indicated by a reduced opacity.

$$T\left(\theta_l = \pm\theta_m\right) = 1. \tag{2.64}$$

The equivalence of the group velocities is a necessary condition for T to be maximized, which becomes apparent when we rewrite Eq. (2.59) in terms of the group velocities,

$$T(\theta_l) = \frac{4\tilde{v}}{(1+\tilde{v})^2} \qquad \text{with} \qquad \tilde{v} = \frac{v_r}{v_l}. \tag{2.65}$$

The differential $\partial_{\tilde{v}} T(\theta_l)$ vanishes for $\tilde{v} = 1$, i.e., when the group velocities are equal.

As a final remark on Fig. 2.9, we note that θ_m approaches the value of θ_c for $r \ll 1$, i.e., a large FSM. As a consequence, $T(\theta_l)$ features sharp peaks at these maxima $|\theta_l| = \theta_m \approx \theta_c$ for quasi-perpendicular incidence.

Competition between the parameters r and Z

In an experimental setup, perfectly clean interfaces are hard to obtain (e.g., due to oxide layers or similar impurities), i.e., $Z = 0$ is not a realistic assumption. Hence, we now study the full expression for T,

$$T(\theta_l) = \frac{4r\cos\theta_l\cos\theta_r}{4rZ^2 + (r\cos\theta_l + \cos\theta_r)^2}\Theta(\theta_c - |\theta_l|), \qquad \cos\theta_r = r^{-1}\sqrt{r^2 - \sin^2\theta_l}, \tag{2.66}$$

where both FSM and a finite interface barrier are taken into account. For perpendicular incidence, this expression reduces to

$$T(\theta_l = 0) = \frac{4r}{4rZ^2 + (r+1)^2} \tag{2.67}$$

and can be rewritten in the form of Eq. (2.56), as we have done it for T in Eq. (2.60), by introducing an effective barrier,

$$Z_{\text{eff}} = \frac{\sqrt{4rZ^2 - (1-r)^2}}{2\sqrt{r}} \quad \Rightarrow \quad T(\theta_l = 0) = \frac{1}{Z_{\text{eff}}^2 + 1}, \tag{2.68}$$

such that FSM apparently increases the barrier strength Z. This is, of course, only true for the zero-mode, as explained in the previous section. However, this raises the question which parameter, Z or r, governs the angle-resolved behavior of the transmission coefficient. We plot $T(\theta_l)$ in Fig. 2.11 for different values of the delta potential strength Z. For a rather small barrier (blue curve), we observe a similar behavior as in Fig. 2.9(a), where the transmission coefficient increases from its zero-mode value and reaches a maximum in the range $|\theta_l| < \theta_c$. Here, FSM apparently dictates the transport. In contrast, $T(\theta_l)$ decreases monotonously with increasing $|\theta_l|$ if we choose Z to be rather large (black curve), and the behavior, similar to that in Fig. 2.8(a), is governed by the barrier. In order to provide a quantitative distinction between the two regimes, we determine the position of the maximum when both FSM and an interface barrier are present. The differential of $T(\theta_l)$ with respect to the angle of incidence vanishes at

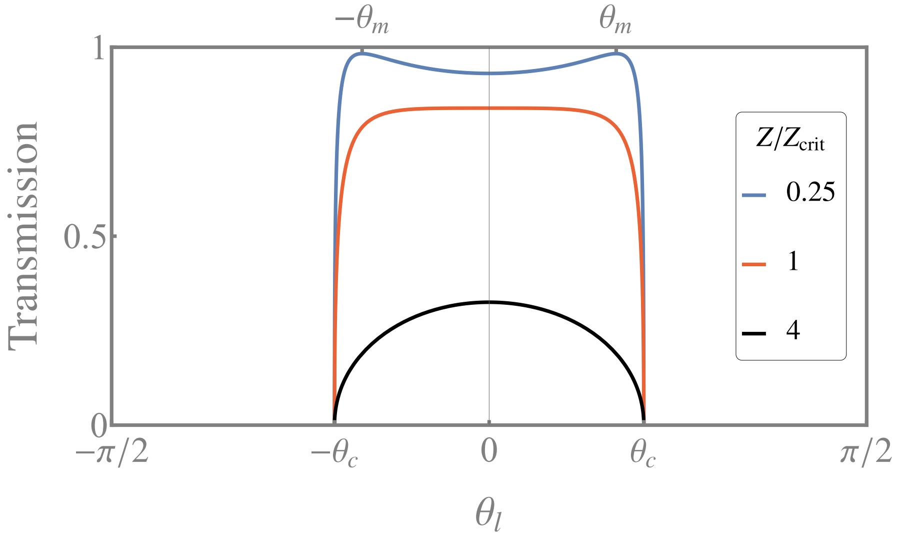

Fig. 2.11: Transmission coefficient T as a function of the angle of incidence θ_l in a system featuring FSM and different barrier strengths Z. The critical barrier strength Z_{crit} defines the behavior of $T(\theta_l)$. We choose $r = 0.6$. *Reprinted figure with permission from [34]. Copyright (2021) by the American Physical Society.*

$$\theta_l = \pm \arcsin\left(\frac{r\sqrt{(1-r^2)^2 - 4r(1+r^2)Z^2}}{\sqrt{(1-r^2)^2(1+r^2) - 8r^3Z^2}}\right) \equiv \theta_m, \tag{2.69}$$

as well as at $\theta_l = 0$. Note that this expression reduces to θ_m as defined in Eq. (2.63) for a clean interface. From Eq. (2.69), we can extract a critical barrier strength given by

$$Z_{\text{crit}} = \frac{1-r^2}{2\sqrt{r(1+r^2)}}. \tag{2.70}$$

For $Z < Z_{\text{crit}}$, the position of the extrema θ_m is real-valued, while it shifts into the complex plane for $Z > Z_{\text{crit}}$. As a consequence, FSM governs the transport in the former case, while it is the delta potential in the latter situation. If the barrier strength is equal to the critical value (red curve in Fig. 2.11), $T(\theta_l)$ is flat and constant over most of the range $|\theta_l| < \theta_c$ and decreases only in close proximity to the critical angle θ_c.

Considering the fact that the area under the curves corresponds to the full transmission coefficient, *cf.* Eq. (2.48), (and thus to the differential conductance and the current), this provides intriguing insight for an experimental setup – while a (strong) mismatch facilitates local equilibria by performing as a directional filter, it is essential that the contact between the metal and the semiconductor (i.e., the interface) remains rather clean and free of impurities. Otherwise, the transport across the junction is strongly suppressed.

While Z_{crit} indicates which quantity, r or Z, governs the angle-resolved dependence of the transmission coefficient, each regime is yet affected by the subordinate parameter. A strong barrier ($Z > Z_{\text{crit}}$) leads to a monotonously decreasing transmission, while the domain over which the latter is finite is restricted to the range $|\theta_l| < \theta_c$ by FSM. This is different from a homogeneous material with a local repulsive potential where T is finite for all $|\theta_l| < \pi/2$. Likewise, the FSM-governed transport features maxima for finite angles of incidence, yet those do no longer amount to unity, but to reduced transmission probabilities.

With this, we conclude our analysis of the normal state transmission and direct our attention to a system where the metal is in the superconducting state.

2.5.2 NS transmission

Let us presume the order parameter Δ_0 is finite in R. Then, Eq. (2.47) evaluates to

$$T(E,\theta_l) = \begin{cases} \frac{8r^2\cos^2\theta_l\cos^2\theta_r\,\Theta(\theta_c-|\theta_l|)}{(4rZ^2+r^2\cos^2\theta_l+\cos^2\theta_r)^2-\frac{E^2}{\Delta_0^2}\left((4rZ^2+\cos^2\theta_r)^2+2r^2\cos^2\theta_l(4rZ^2-\cos^2\theta_r)+r^4\cos^4\theta_l\right)}, & E < \Delta_0 \\ \frac{4r\cos\theta_l\cos\theta_r\,\Theta(\theta_c-|\theta_l|)}{(4rZ^2+r^2\cos\theta_l+\cos^2\theta_r)(u^2-v^2)+2r\cos\theta_l\cos\theta_r}, & E > \Delta_0 \end{cases}. \tag{2.71}$$

under the Andreev approximation $\mu \gg E, \Delta_0$. This expression is energy-dependent, in particular for subgap energies $0 \leq E < \Delta_0$ (for $E \gg \Delta_0$, the energy-dependent term $u^2 - v^2$ evaluates to unity, i.e., T approaches a constant asymptotic value). Since the angular dependence is qualitatively the same for any energy, and in order to compare the NS to the NN' transmission coefficient for electrical current, *cf.* Eq. (2.66), we study Eq. (2.71) at the Fermi energy, $E = 0$, and obtain

$$T(E=0,\theta_l) = \frac{8r^2\cos^2\theta_l\cos^2\theta_r}{\left(4rZ^2+r^2\cos^2\theta_l+\cos^2\theta_r\right)^2}\Theta(\theta_c-|\theta_l|), \qquad \cos\theta_r = r^{-1}\sqrt{r^2-\sin^2\theta_l}. \tag{2.72}$$

Since a superconductor couples electrons and holes, this enables Andreev reflection in the system and opens a second transport channel. As a consequence, T can be twice its normal-state counterpart, incorporated in the doubled numerical factor in the numerator of Eq. (2.72). For normal incidence, this expression reduces to

$$T(E=0,\theta_l=0) = \frac{8r^2}{\left(4rZ^2+r^2+1\right)^2}, \tag{2.73}$$

which, likewise, amounts up to twice the transmission in Eq. (2.67). A further distinction from the normal-state results is that Z enters the denominators in Eqs. (2.72) and (2.73) in fourth order, and not in second order as in Eqs. (2.66) and (2.67). This indicates that T is more sensitive to a dirty interface when one of the metals features superconducting order. We illustrate this in Fig. 2.12(a), where we plot the NN' (dashed) as well as the NS (solid) transmission coefficient as a function of Z and normalized to the clean-interface limit, $T(\theta_l)|_{Z=0}$ and $T(E=0,\theta_l)|_{Z=0}$, respectively. We clearly

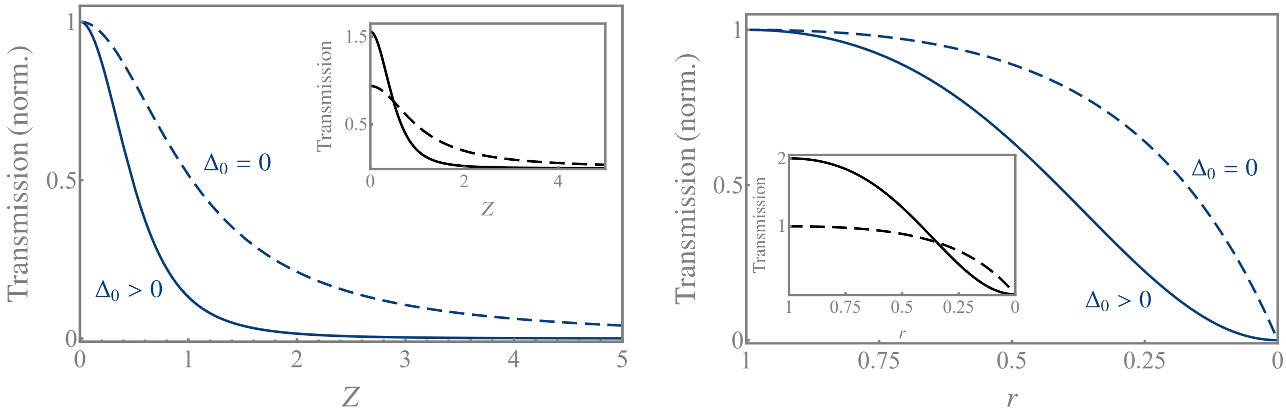

(a) Z-dependence

(b) r-dependence

Fig. 2.12: Normalized transmission coefficient at $E = \theta_l = 0$ as a function of the **(a)** barrier strength Z and **(b)** FSM r. Note that, while the NS transmission is noticeably more sensitive to the barrier strength than in an NN' junction, the r-dependence is not as drastic in comparison. Inset: non-normalized transmission. We choose **(a)** $r = 0.6$ and **(b)** $Z = 0$.

observe a stronger suppression of the probability amplitude in the NS junction, quickly exceeded by the NN' transmission for strong Z (see inset of Fig. 2.12(a)) and despite the additional hole channel.

The superconducting order in R similarly affects the r-dependence, such that the transmission decreases faster with increasing FSM than its normal-state counterpart, see Fig. 2.12(b). Here, we normalize to the homogeneous limit, $T(\theta_l)|_{r=1}$ and $T(E = 0, \theta_l)|_{r=1}$, respectively. Nevertheless, the effect is not as drastic as for the barrier-dependence, and the NN'-transmission exceeds that of the NS setup only for a rather large r (see inset of Fig. 2.12(b)). We can explain this by means of Eqs. (2.66) and (2.72) – $T(\theta_l)$ is of the order $\propto r^{-1}$, while it is $\propto r^{-2}$ in $T(E = 0, \theta_l)$.

At the beginning of this chapter, we argued that the qualitative findings of the angle-resolved transmission coefficient are very much alike in an NN' and an NS junction, which is why we started our analysis on the normal state transport. In Fig. 2.13, we validate this statement. In a homogeneous NS junction, $T(E = 0, \theta_l)$ is maximal for the zero-mode and decreases with increasing angle of incidence, except for the clean interface where Andreev reflection happens with unit probability[3] ($A = 1 \Rightarrow T = 2$). Correspondingly, the transmission coefficient features maxima at finite angles, after increasing from its zero-mode value, as well as a sharp cut-off at $\theta_l = \pm\theta_c$ in a system featuring FSM and a clean interface. Except for the quantitative deviation due to the additional hole channel and the increased sensitivity to the Z and r parameters, this behavior is comparable to the one we observed in the NN'-junction.

At first sight, however, the cut-off at $\pm\theta_c$ appears rather counter-intuitive. From Figs. 2.6(a) and 2.7(**top**), we can convince ourselves that the Fermi surfaces for the incident electron and a reflected hole in L are equivalent at the Fermi energy and comparable for all subgap-energies (in particular under the Andreev approximation). This means that, for any incident electron mode in L, there exists a corresponding hole mode, also in L, and Andreev reflection can, theoretically, occur for any $|\theta_l| < \pi/2$. Instead, this process is suppressed for angles larger than the critical angle. We can understand this phenomenon from our discussion in the context of Fig. 2.6(b). A superconducting gap opens up around $E = 0$, coupling electrons and holes at the Fermi wave vector κ_r (if the bands intersect with each other at the Fermi level for $\Delta_0 = 0$). Increasing k_y, however, shifts the bands to opposite energies, and the overlap vanishes for $|k_y| > \kappa_r$. For these modes, Andreev reflection is not possible since the superconductor does no longer provide the necessary coupling for interband scattering. Consequently, $T(E = 0, \theta_l)$ vanishes for $|k_y| > \kappa_r$, which is equivalent to the condition $|\theta_l| > \theta_c$. This explains why the transmission coefficient vanishes for angles of incidence larger than the critical angle, even though

---

[3] This is a consequence of the Andreev approximation, which suppresses normal reflection in the absence of a barrier.

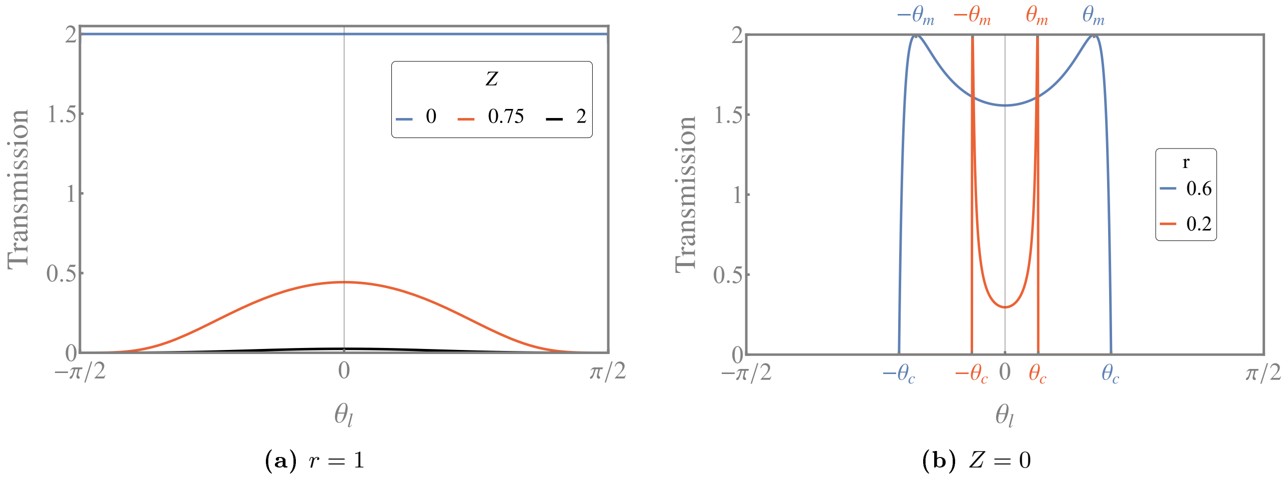

(a) $r = 1$ **(b)** $Z = 0$

Fig. 2.13: Transmission coefficient T as a function of θ_l for **(a)** a homogeneous system with a finite interface barrier and **(b)** a setup featuring FSM and a clean interface. Qualitatively, the results are not different from the normal-state transmission coefficient. *Reprinted figure with permission from [34]. Copyright (2021) by the American Physical Society.*

hole states are available in L for Andreev reflection at modes beyond θ_c.

Finally, we find exactly the same competition between the parameters r and Z for a finite Δ_0 as we observed it in the NN' junction, see Fig. 2.14. The angle θ_m at which the maximum occurs, *cf.* Eq. (2.69), is not affected by the order parameter, neither is the critical barrier strength, *cf.* Eq. (2.70). The regimes are thus governed by the parameters as we explained it in the previous section.

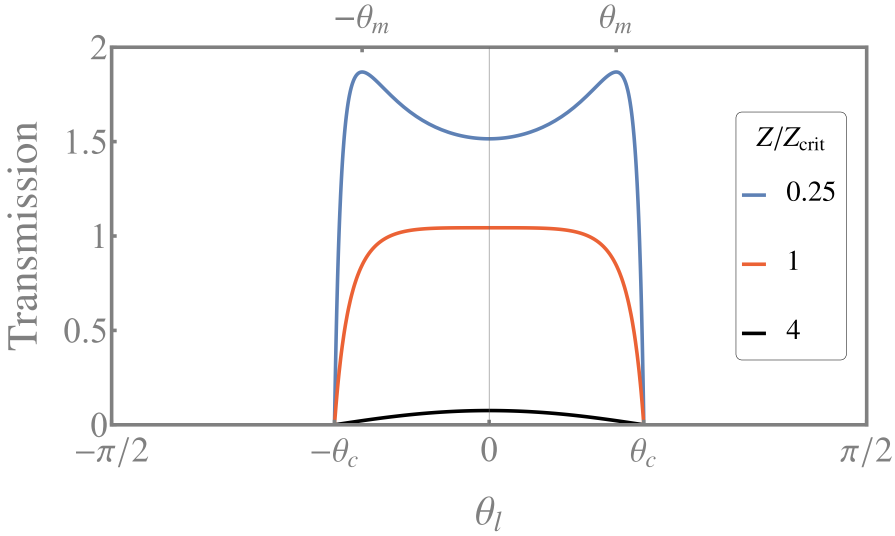

Fig. 2.14: Transmission coefficient T as a function of the angle of incidence θ_l in a system featuring FSM and different barrier strengths Z. The critical barrier strength Z_{crit} defines the behavior of $T(\theta_l)$. We choose $r = 0.6$. *Reprinted figure with permission from [34]. Copyright (2021) by the American Physical Society.*

While the qualitative findings are similar to the NN' setup, the quantitative results are noticeably affected by the fact that R features superconducting order. For a small barrier strength, the transmission coefficient is enhanced due to the additional hole channel and can attain twice the normal-state value, see the blue curves in Figs. 2.11 and 2.14. At the same time, this increases the conductance and the current in the system. However, T is more sensitive to Z and decreases significantly with increasing barrier strength. Apparently, it is stronger affected by impurities at the interface than in a system without superconducting order, see the black curves in Figs. 2.11 and 2.14.

From these findings, we conclude that FSM provides a mechanism that supports the assumption of local equilibria by directional filtering while, at the same time, allowing for strong contributions to the transmission coefficient for electrical current from the propagating modes. Superconductivity enhances T if a rather clean interface with a low opacity is provided. Else, transmission across the junction can be severely suppressed due to the repulsive potential. The angle-resolved features are comparable for any excitation energy, and we have the necessary understanding at our disposal to analyze the differential conductance as well as the currents in the junction.

2.5.3 Differential conductance and current

From our definition of the transmission coefficient for electrical current, *cf.* Eq. (2.47), the expression in Eq. (2.25) reduces to

$$I(V) = \frac{2e}{h} \sum_{k_y} \int_{-\infty}^{\infty} \left[f_0(E - eV) - f_0(E) \right] T(E, k_y) \mathrm{d}E, \tag{2.74}$$

and we can express the sum in the continuum limit and in accordance with Eq. (2.48) by an integral,

$$I(V) = \frac{2e}{h} \frac{W}{2\pi} \int_{-\kappa_l}^{\kappa_l} \mathrm{d}k_y \int_{-\infty}^{\infty} \left[f_0(E - eV) - f_0(E) \right] T(E, k_y) \mathrm{d}E, \tag{2.75a}$$

$$I(V) = \frac{2e}{h} \frac{W \kappa_l}{2\pi} \int_{-\pi/2}^{\pi/2} \mathrm{d}\theta_l \cos\theta_l \int_{-\infty}^{\infty} \left[f_0(E - eV) - f_0(E) \right] T(E, \theta_l) \mathrm{d}E. \tag{2.75b}$$

The first term is the general expression for quasi-1D junctions connected to equilibrium reservoirs, while the second one holds under the Andreev approximation. From our discussion in the context of the transmission coefficient, we can convince ourselves that the limits of the θ_l-integral can be replaced by $\pm\theta_c$ due to the sharp cut-off in the transport characteristics. The differential conductance can be derived from Eq. (2.75) by calculating the partial derivative of $I(V)$ with respect to the bias V,

$$G(V) = \frac{\partial I}{\partial V}(V) \xrightarrow{\mathrm{T} \to 0} \frac{2e^2}{h} T(E = eV), \tag{2.76}$$

where the last expression is obtained in the thermodynamic limit of a vanishing temperature, $\mathrm{T} \to 0$. With this, we are now able to calculate experimental observables of the junction.

A large electrochemical potential, $\mu \gg E$, in a system without superconducting order results in a transmission coefficient independent of the energy, *cf.* Eq. (2.53), and hence in a constant conductance and a linear current. We can thus define a normal-state resistance for a fixed choice of the parameters r and Z,

$$R_N \equiv G_{NN'}^{-1}, \qquad G_{NN'} \equiv G(V = 0)|_{\Delta_0 = 0}, \tag{2.77}$$

which serves as a normalization factor for the NS observables. Finally, the excess current is defined as the offset between the NS and the NN' current,

$$I_{\text{exc}}(V) = \underbrace{I(V)\big|_{\Delta_0 > 0}}_{\equiv I_{NS}} - \underbrace{I(V)\big|_{\Delta_0 = 0}}_{\equiv I_{NN'}}, \qquad I_{\text{exc}} \equiv \lim_{V \to \infty} I_{\text{exc}}(V). \tag{2.78}$$

Note that, here, we explicitly distinguish between the bias-dependent excess current $I_{\text{exc}}(V)$ and the standard definition of the excess current I_{exc} at large biases. To study the observables, we evaluate Eqs. (2.75) and (2.76) numerically in the following.

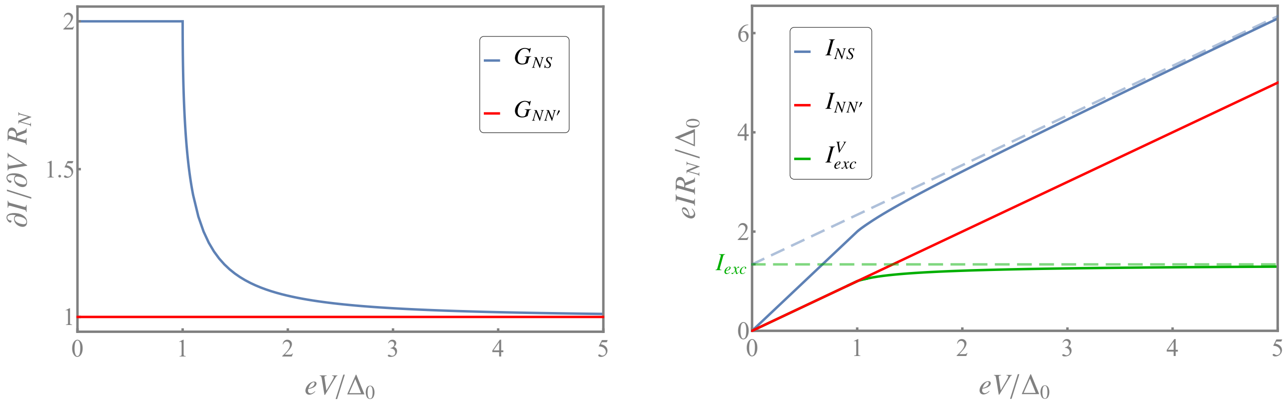

(a) Differential conductance

(b) Current

Fig. 2.15: (a) Conductance and **(b)** current as a function of the bias V in a homogeneous junction ($r = 1$) with no barrier ($Z = 0$). I_{exc}^V is the bias-dependent excess current.

In a homogeneous junction with a clean interface, we obtain the conductance and current as shown in Fig. 2.15. At subgap energies, I_{NS} is solely carried by Andreev reflection and twice the normal-state current. For $eV > \Delta_0$, the probability for Andreev reflection decreases quickly, such that $G_{NS} \equiv \partial I/\partial V\big|_{\Delta_0>0}$ approaches its normal-state value, $G_{NN'}$. While I_{NS} and $I_{NN'}$ feature the same slope at large biases, i.e.,

$$G_{NN'}\big|_{eV\gg\Delta_0} = G_{NS}\big|_{eV\gg\Delta_0}, \tag{2.79}$$

the contributions from biases $eV \approx \Delta_0$ lead to an offset between the currents, the so-called excess current. From the bias-dependent $I_{\text{exc}}(V)$, we can clearly observe that the main contribution to its asymptotic value I_{exc}, which is finite and rather large in this example, stems from this voltage domain. However, the underlying choice of parameters does not justify the assumption of local equilibria right and left of the interface in a planar junction, and thus the application of Eq. (2.75). In a system with both FSM and a repulsive, localized potential, we obtain the results as shown in Fig. 2.16. The barrier enables normal reflection, in particular in the subgap-regime, and thus reduces the differential conductance. The resonance at $eV = \Delta_0$, where G_{NS} exceeds $G_{NN'}$ significantly, is a well known feature of NS junctions with a dirty interface [27].

For an intermediate FSM and a comparably small barrier strength (in comparison to Z_{crit}), the NS conductance remains enhanced compared to its normal-state counterpart, and we observe an excess current similar to that of the homogeneous setup without barrier. A strong barrier (at the same FSM), however, significantly suppresses the subgap contribution, and I_{exc} nearly vanishes. Note that $I_{\text{exc}}(V)$ even becomes negative for biases $eV \approx \Delta_0$. We obtain a similar result for a strong FSM and a rather clean interface, while the excess current remains finite, yet small. It is, however, completely suppressed if the barrier is too strong. Then, no current flows for biases smaller than the superconducting order parameter, while the supragap current approaches its normal-state counterpart only slowly, and no offset can be observed.

From these observations, we can come to the conclusion that, while the excess current is apparently affected by a Fermi surface mismatch (in particular for a rather large FSM), the effect is not as drastic as it is for a strong interface barrier. This is in agreement with our analysis of the angle-resolved transmission coefficient and the competition between r and Z – if FSM governs the transport at a given energy, this leads to strong contributions to the full transmission coefficient, *cf.* Eq. (2.48), while it is rather small for a barrier-governed setup.

Fig. 2.17, where we plot I_{exc} (in the large bias limit) as a function of FSM as well as the barrier strength, illustrates this behavior in detail. While the homogeneous junction with the clean interface provides the strongest excess current, it decreases quickly for an increasing barrier strength, even for

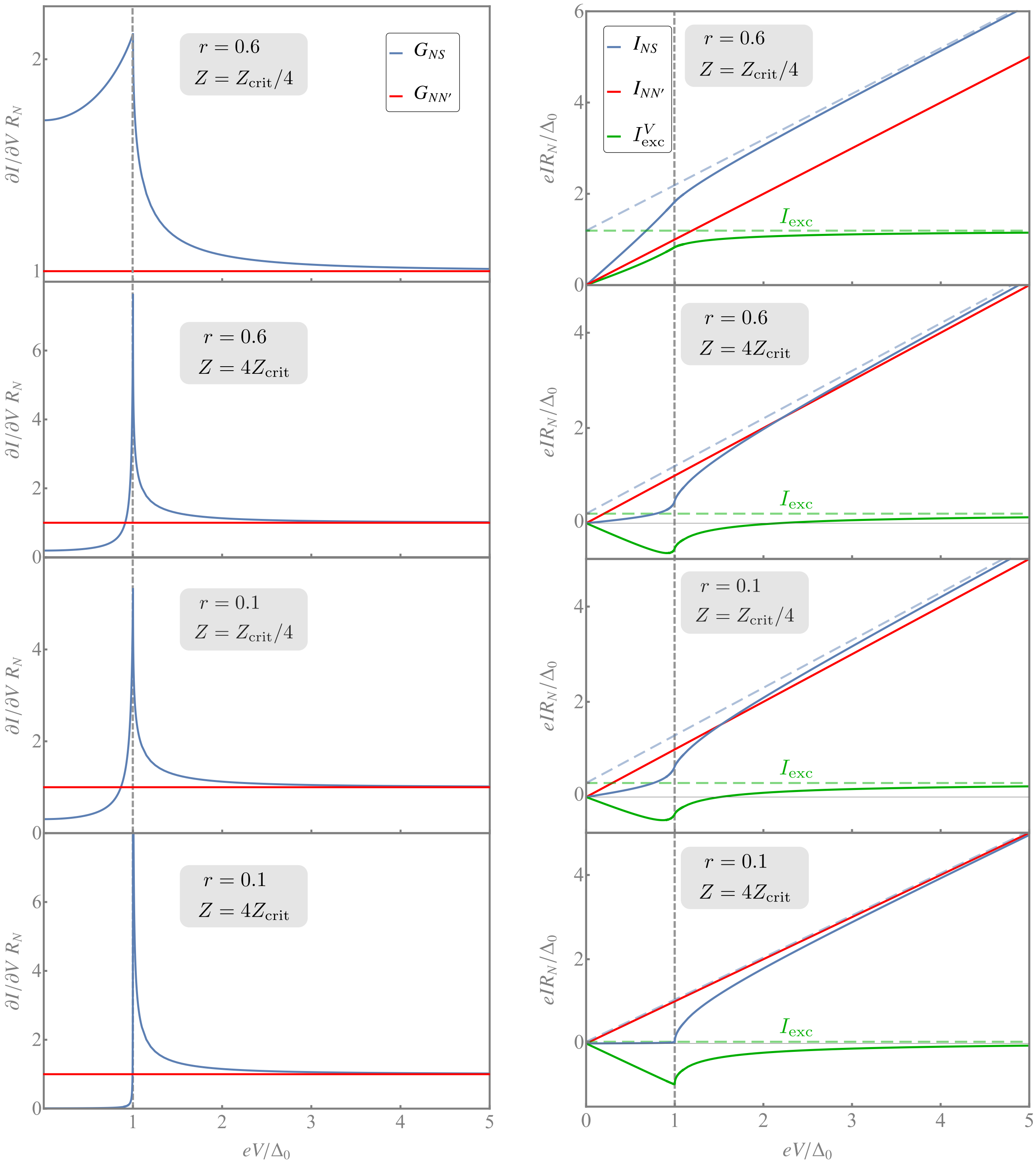

(a) Differential conductance.

(b) Current

Fig. 2.16: **(a)** Conductance and **(b)** current as a function of the bias V for various choices of the parameters r and Z. I^V_{exc} is the bias-dependent excess current. *Reprinted figure with permission from [34]. Copyright (2021) by the American Physical Society.*

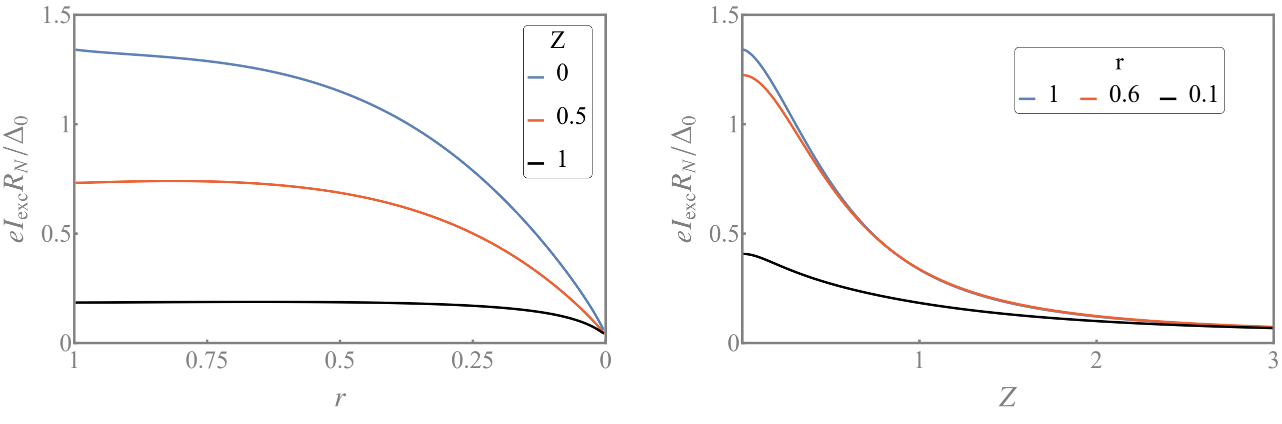

(a) r-dependence **(b)** Z-dependence

Fig. 2.17: Dependence of the excess current (in the large bias limit) as a function of **(a)** FSM and **(b)** the barrier strength. While I_{exc} is rather sensitive to Z and decreases quickly with increasing barrier strength, the excess current remains (approximately) constant over a wide range of r and decays only slowly for large FSM.

large FSM (i.e., a small r). In contrast, I_{exc} remains approximately constant when we introduce FSM to the system, in particular when a finite barrier is present. A decrease can be observed only at larger mismatches. This is an intriguing observation since the number of propagating modes is reduced continuously with increasing FSM, whereas the excess current is not affected immediately. We can understand this from the quantity Z_{crit} - considering a fixed and finite barrier strength Z, this reduces the excess current in the homogeneous setup ($r = 1$) from its maximum value. By increasing FSM (i.e., decreasing r), we equally increase Z_{crit} and the ratio Z/Z_{crit} is reduced, meaning that we transition from the Z-governed regime into the FSM-governed regime. As a consequence, the full transmission coefficient (at a fixed energy) grows, which counteracts the smaller number of propagating modes such that I_{exc} remains approximately constant over a wide range of FSM. However, when r is so small that $Z < Z_{\mathrm{crit}}$ holds, then $T(E)$ does no longer increase sufficiently (if at all) to neutralize the strongly reduced number of propagating modes. At this point, I_{exc} starts to decrease noticeably. This can be observed best from the blue curve in Fig. 2.17(a), i.e., the homogeneous setup, where $Z_{\mathrm{crit}} = 0$ and the excess current decreases monotonously for all r (albeit rather slowly for small FSM).

With this, we finish our analysis of the transmission coefficient as well as the differential conductance and the current (in particular, the excess current) of NS junctions based on the rather simple quasi-free electron Hamiltonian. We find that a mismatch in the electron band structure between the materials supports the assumption of local equilibria left and right of the interface by acting as a directional filter while allowing the observation of finite excess currents. Nonetheless, a rather clean interface is necessary.

2.6 Excess current in an Al-HgTe-Al junction

The Hamiltonian in Eq. (2.26) provides a convenient starting point for the analysis of the interface properties in systems featuring FSM. The model of the quasi-free electron gas is, however, rather simplistic, and recent experiments in solid-state physics, particularly in Würzburg, study transport features in junctions consisting of HgTe (to be precise, HgTe/CdTe, where CdTe is cadmium telluride) samples. Therefore, we consider a planar Josephson junction build from a HgTe QW sandwiched between two Al contacts in this section.

2.6.1 Model and preliminary calculations

Aluminum is a metal well known for being a conventional superconductor at temperatures below 1.2 K [59] and can be described appropriately by Eq. (2.1). Instead, HgTe, in which the QSHE and thus topological edge states were first discovered [15], is more complex and can be modeled by the Bernevig-Hughes-Zhang (BHZ) Hamiltonian [60, 61]. Since we consider a junction with superconducting order, we write it as a BdG-Hamiltonian in the Nambu spinor basis

$$\boldsymbol{\Psi} = \left(s_\uparrow,\, p_\uparrow,\, s_\downarrow,\, p_\downarrow, s_\uparrow^\dagger,\, p_\uparrow^\dagger,\, s_\downarrow^\dagger,\, p_\downarrow^\dagger\right)^T, \tag{2.80}$$

where $s_\sigma^\dagger (p_\sigma^\dagger)$ is the creation operator of an electron in the $s(p)$-orbital with spin $\sigma =\uparrow, \downarrow$ and obtain

$$\mathcal{H}_{\mathrm{BHZ}} = A\left(k_x s_z \sigma_x - k_y \tau_z \sigma_y\right) - \left(Bk^2 - M\right)\tau_z\sigma_z + \left(C - Dk^2\right)\tau_z, \tag{2.81}$$

where $k^2 = k_x^2 + k_y^2$ and τ_l, s_l and σ_l with $l \in \{0, x, y, z\}$ are unit and Pauli matrices in Nambu, spin and orbital space, respectively. Due to the additional degrees of freedom, the Hamiltonian in Eq. (2.1) needs to be extended in order to describe a hybrid junction and thus reads

$$\mathcal{H}_{\mathrm{Al}} = \left(\frac{\hbar^2 k^2}{2m} - \mu\right)\tau_z - \Delta_0 \tau_y s_y. \tag{2.82}$$

We now calculate the eigenstates from the Schrödinger equation. Defining $\boldsymbol{e}_{1\ldots 8}$ as the canonical unit vectors in the vector space $\mathbb{R}^8$, we have

$$\psi^{\pm}_{eq,s,\uparrow}(x) = \left(u\,\boldsymbol{e}_1 + v\,\boldsymbol{e}_7\right)e^{\pm i k_{eq} x}, \qquad \psi^{\pm}_{eq,p,\uparrow}(x) = \left(u\,\boldsymbol{e}_2 + v\,\boldsymbol{e}_8\right)e^{\pm i k_{eq} x}, \tag{2.83a}$$

$$\psi^{\pm}_{eq,s,\downarrow}(x) = \left(u\,\boldsymbol{e}_3 - v\,\boldsymbol{e}_5\right)e^{\pm i k_{eq} x}, \qquad \psi^{\pm}_{eq,p,\downarrow}(x) = \left(u\,\boldsymbol{e}_4 - v\,\boldsymbol{e}_6\right)e^{\pm i k_{eq} x}, \tag{2.83b}$$

$$\psi^{\pm}_{hq,s,\uparrow}(x) = \left(v\,\boldsymbol{e}_1 + u\,\boldsymbol{e}_7\right)e^{\mp i k_{hq} x}, \qquad \psi^{\pm}_{hq,p,\uparrow}(x) = \left(v\,\boldsymbol{e}_2 + u\,\boldsymbol{e}_8\right)e^{\mp i k_{hq} x}, \tag{2.83c}$$

$$\psi^{\pm}_{hq,s,\downarrow}(x) = \left(v\,\boldsymbol{e}_3 - u\,\boldsymbol{e}_5\right)e^{\mp i k_{hq} x}, \qquad \psi^{\pm}_{hq,p,\downarrow}(x) = \left(v\,\boldsymbol{e}_4 - u\,\boldsymbol{e}_6\right)e^{\mp i k_{hq} x}, \tag{2.83d}$$

in Al, where the superscripts ± and subscripts eq, hq are defined as those in the context of Eq. (2.34), while s, p label the orbital and $\uparrow, \downarrow$ the spin of the particle. The BCS coefficients u, v are introduced in Eq. (2.35). In the QW, the propagating eigenstates are given by

$$\psi^{\pm}_{e,\uparrow}(x) = \left(\left[(E-C) + M - (B-D)\left(k_e^2 + k_y^2\right)\right]\boldsymbol{e}_1 \pm A\left(k_e \mp i k_y\right)\boldsymbol{e}_2\right)e^{\pm i k_e x}, \tag{2.84a}$$

$$\psi^{\pm}_{e,\downarrow}(x) = \left(\left[(E-C) + M - (B-D)\left(k_e^2 + k_y^2\right)\right]\boldsymbol{e}_3 \mp A\left(k_e \pm i k_y\right)\boldsymbol{e}_4\right)e^{\pm i k_e x}, \tag{2.84b}$$

$$\psi^{\pm}_{h,\uparrow}(x) = \left(\left[-(E+C) + M - (B-D)\left(k_h^2 + k_y^2\right)\right]\boldsymbol{e}_7 \mp A\left(k_h \pm i k_y\right)\boldsymbol{e}_8\right)e^{\mp i k_h x}, \tag{2.84c}$$

$$\psi^{\pm}_{h,\downarrow}(x) = \left(\left[-(E+C) + M - (B-D)\left(k_h^2 + k_y^2\right)\right]\boldsymbol{e}_5 \pm A\left(k_h \mp i k_y\right)\boldsymbol{e}_6\right)e^{\mp i k_h x}, \tag{2.84d}$$

where $e(h)$ is an electron (hole) state, while $\mathcal{H}_{\mathrm{BHZ}}$ features a set of evanescent waves as well,

$$\psi^{\pm}_{\tilde{e},\uparrow}(x) = \left(\left[(E-C) + M + (B-D)\left(q_e^2 - k_y^2\right)\right]\boldsymbol{e}_1 \pm iA\left(q_e \mp k_y\right)\boldsymbol{e}_2\right)e^{\mp q_e x}, \tag{2.85a}$$

$$\psi^{\pm}_{\tilde{e},\downarrow}(x) = \left(\left[(E-C) + M + (B-D)\left(q_e^2 - k_y^2\right)\right]\boldsymbol{e}_3 \mp iA\left(q_e \pm k_y\right)\boldsymbol{e}_4\right)e^{\mp q_e x}, \tag{2.85b}$$

$$\psi^{\pm}_{\tilde{h},\uparrow}(x) = \left(\left[(E+C) - M - (B-D)\left(q_h^2 - k_y^2\right)\right]\boldsymbol{e}_7 \mp iA\left(q_h \mp k_y\right)\boldsymbol{e}_8\right)e^{\mp q_h x}, \tag{2.85c}$$

$$\psi^{\pm}_{\tilde{h},\downarrow}(x) = \left(\left[(E+C) - M - (B-D)\left(q_h^2 - k_y^2\right)\right]\boldsymbol{e}_5 \pm iA\left(q_h \pm k_y\right)\boldsymbol{e}_6\right)e^{\mp q_h x}. \tag{2.85d}$$

Here, the subscripts distinguish decaying electron ($\tilde{e}$) from hole ($\tilde{h}$) states, and the superscripts indicate in which direction, with respect to the x-axis, the state decays. Note that we need to consider both the propagating and evanescent waves in the QW to obtain the correct results.

The wavenumbers $k_{eq/hq}$ in AL are already defined in Eq. (2.35), whereas those in the HgTe sample are given by

$$k_e = \sqrt{\left(BM + D\left(E-C\right) - A^2/2 + k_e^0\right)/\left(B^2-D^2\right) - k_y^2}, \tag{2.86a}$$

$$k_h = \xi_h\sqrt{\left(BM - D\left(E+C\right) - A^2/2 + k_h^0\right)/\left(B^2-D^2\right) - k_y^2}, \tag{2.86b}$$

$$q_e = \sqrt{\left(A^2/2 - BM - D\left(E-C\right) + k_e^0\right)/\left(B^2-D^2\right) + k_y^2}, \tag{2.86c}$$

$$q_h = \sqrt{\left(A^2/2 - BM + D\left(E+C\right) + k_e^0\right)/\left(B^2-D^2\right) + k_y^2}, \tag{2.86d}$$

with

$$k_e^0 = \sqrt{\left(BM + D\left(E-C\right) - A^2/2\right)^2 - \left(B^2-D^2\right)\left(M^2 - \left(E-C\right)^2\right)}, \tag{2.87a}$$

$$k_h^0 = \sqrt{\left(BM - D\left(E-C\right) - A^2/2\right)^2 - \left(B^2-D^2\right)\left(M^2 - \left(E+C\right)^2\right)}, \tag{2.87b}$$

$$\xi_h = -\operatorname{sgn}\left(E + C - Dk_y^2 + \sqrt{A^2k_y^2 + \left(M - Bk_y^2\right)^2}\right). \tag{2.87c}$$

These definitions guarantee the correct behavior of the wave functions in a scattering state.

As in the previous section, we consider only one of the interfaces of the Al-HgTe-Al Josephson junction and study its electronic properties, while reminding ourselves that we can combine two of those by means of the formalism introduced by Octavio [57]. We choose it to be located at $x_0 = 0$, such that the scattering states read

$$\phi_s(x) = \begin{cases} \psi_{e,s}^+(x) + \sum\limits_{\tau}\sum\limits_{s'=\uparrow,\downarrow} r_{e\to\tau,s\to s'}\,\psi_{\tau,s'}^-(x), & x<0 \\ \sum\limits_{\tau}\sum\limits_{\sigma=s,p}\sum\limits_{s'=\uparrow,\downarrow} t_{e\to\tau,\sigma,s\to s'}\psi_{\tau,\sigma,s'}^+(x), & x>0 \end{cases}, \tag{2.88}$$

where $\tau\in\{e,h,\tilde{e},\tilde{h}\}$ in HgTe and $\tau\in\{eq,hq\}$ in Al. Here, we need to consider the scattering states for both an incident electron with spin ↑ and an incident electron with spin ↓. While the two projections are neither coupled in $\mathcal{H}_{\mathrm{BHZ}}$ nor in $\mathcal{H}_{\mathrm{Al}}$, a finite term A in the QW Hamiltonian leads to an asymmetry in the k_y-dependence of the transmission coefficient. Therefore, we take both $\phi_\uparrow(x)$ and $\phi_\downarrow(x)$ into account, which naturally doubles the maximum value T can attain.

To obtain the scattering coefficients $r_{e\to\tau,s\to s'}$ and $t_{e\to\tau,\sigma,s\to s'}$, we write the full system Hamiltonian in the form of Eq. (2.3) by identifying (we consider a clean interface)

$$\mathcal{A}(x) = \frac{\hbar^2}{2m^*}\tau_z\Theta(x) - \left(B+D\right)\tau_z\sigma_z\Theta(-x), \tag{2.89a}$$

$$\mathcal{B}(x) = As_z\sigma_x\Theta(-x), \tag{2.89b}$$

$$\mathcal{C}(x) = -\left(\mu\,\tau_z + \Delta_0\,\tau_y s_y\right)\Theta(x) + \left[\left(M - Bk_y^2\right)\tau_z\sigma_z + \left(C - Dk_y^2\right)\tau_z - Ak_y\tau_z\sigma_y\right]\Theta(-x), \tag{2.89c}$$

$$\mathcal{D}(x) = 0, \tag{2.89d}$$

and we obtain the wave matching conditions according to Eqs. (2.5) and (2.14) as

$$\lim_{\varepsilon\to0}\left(\phi_s(0+\varepsilon) - \phi_s(0-\varepsilon)\right) = 0, \tag{2.90a}$$

$$\lim_{\varepsilon\to0}\left(\frac{\hbar^2}{2m^*}\tau_z\phi_s'(0+\varepsilon) + \left(B+D\right)\tau_z\sigma_z\phi_s'(0-\varepsilon)\right) = \frac{i}{2}As_z\sigma_x\phi_s(0). \tag{2.90b}$$

Finally, we obtain the transmission coefficient for electrical current from Eq. (2.47a) and the definition of the probability current density in Eq. (2.20) as

$$T(E,k_y) = 2 - \sum_{s=\uparrow,\downarrow}\sum_{s'=\uparrow,\downarrow}\left|r_{e\to e,s\to s'}\right|^2 + \frac{j_h}{j_e}\sum_{s=\uparrow,\downarrow}\sum_{s'=\uparrow,\downarrow}\left|r_{e\to h,s\to s'}\right|^2 \tag{2.91}$$

with

$$j_e = \frac{2k_e}{\hbar}\left[A^2\left(E-C+M\right)-\left(B+D\right)\left(E-C+M-\left(B-D\right)\left(k_e^2+k_y^2\right)\right)^2\right], \tag{2.92a}$$

$$j_h = -\frac{2\mathrm{Re}(k_h)}{\hbar}\left[A^2\left(E+C-M\right)-\left(B+D\right)\left(E+C-M+\left(B-D\right)\left(k_e^2+k_y^2\right)\right)^2\right]. \tag{2.92b}$$

Note that, in Eq. (2.91), the term 2 is due to the fact that we consider both scattering states for spin ↑ and spin ↓ electrons, while the evanescent states are not represented since they carry no current.

2.6.2 Mode-dependence of the transmission coefficient

Due to the complexity of the problem, a compact analytical expression of Eq. (2.91) cannot be obtained, such that we evaluate it numerically and compare the results to our findings in the previous section. In fact, the definitions of the eigenstates in Eq. (2.85) and the wavenumbers in Eq. (2.86) are only valid for a definite set of parameters. The eigensystem of $\mathcal{H}_{\mathrm{BHZ}}$ is rather complicated and a proper definition of theses quantities is a tedious task for arbitrary parameters A, B, D and M. Therefore, we choose the QW to be in the inverted, i.e., topological, regime with a thickness of 7 nm, which is described by [15,61] $A = 364.5\,\mathrm{meV\,nm}$, $B = -686\,\mathrm{meV\,nm}^2$, $D = -512\,\mathrm{meV\,nm}^2$ and $M = -10\,\mathrm{meV}$. For Al, we assume an effective mass [62] $m^* = 1.16m_e$, with m_e the mass of a free electron, and obtain (rounded up) $\hbar^2/(2m^*) = 40\,\mathrm{meV\,nm}^2$ for the prefactor in $\mathcal{H}_{\mathrm{Al}}$.

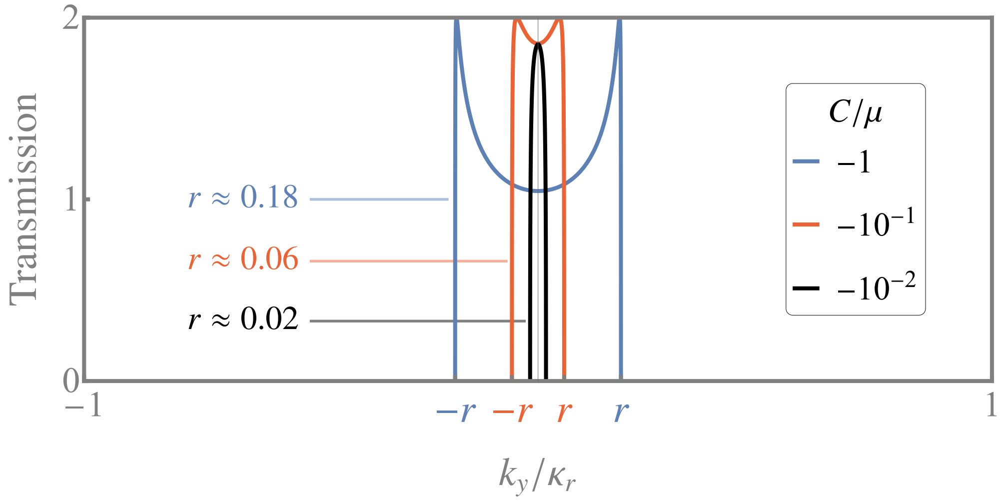

Fig. 2.18: Normal-state transmission coefficient T as a function of the mode k_y at different filling factors. We choose $E = 0$.

So far, we have not defined the electrochemical potentials, μ and C, in Al and HgTe, respectively. For the superconducting metal, we assume it to be much larger than E and Δ_0 and set it to $\mu = 10^5\Delta_0$. The filling factor C can be tuned by a gate voltage and is usually chosen to be equal to the Fermi energy of the superconductor ($C = 0$). With this, one can probe the surface states emerging in HgTe in its topological state [63]. However, since we assume the y-direction to be translational invariant, i.e, extending infinitely, our system features no boundaries and the surface states cannot emerge. With HgTe being a semimetal/semiconductor, we thus choose C to be finite and smaller than μ for the analysis of the differential conductance and the current in the system.

First, we consider the mode-resolved dependence of the transmission coefficient, parameterized by k_y[4]. For our choice of parameters, Al features the large Fermi surface with radius $\kappa_r = \sqrt{2m^*\mu}/\hbar$, while it is $\kappa_l = \sqrt{\left(BM + D\left(E-C\right) - A^2/2 + k_e^0\right)/\left(B^2-D^2\right)}$ for HgTe. FSM is given by the ratio

---

[4] While θ_l is a convenient parameterization indicating the angle of incidence, we resort to k_y in this section since FSM is generally rather large between Al and HgTe. This improves the illustrations. Note that k_y is normalized to κ_r in the figures, i.e., the range indicates all possible incident electron modes.

of the Fermi wavenumbers, $r = \kappa_l/\kappa_r$, which is now not only dependent on the ratio of the effective masses but on all of the parameters in HgTe. Eventually, this leads to a slight modification of the behavior if we compare it to the previous section. We plot $T(E=0,k_y)$ at the Fermi energy of the superconductor and a vanishing order parameter, $\Delta_0 = 0$, (i.e., Al is in its normal state) as a function of the mode in Fig. 2.18.

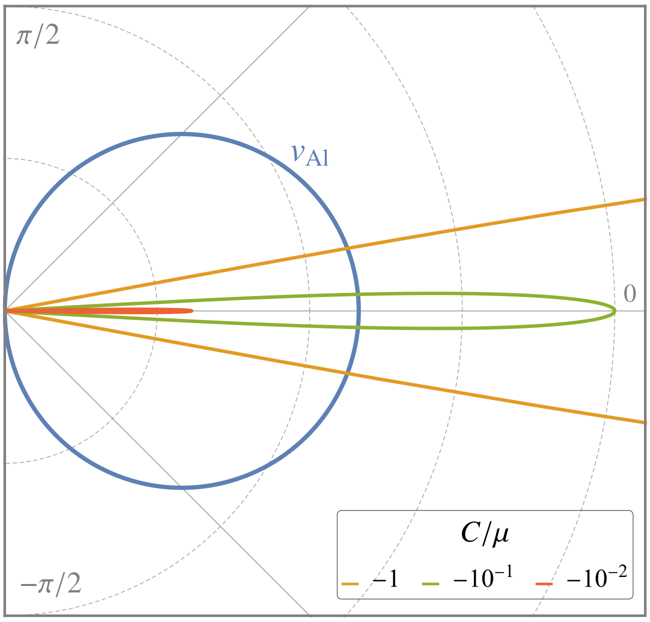

Fig. 2.19: Angular dependency of the group velocities of electrons in Al and HgTe for different values of the filling factor. In contrast to a variation of the effective mass, changing the electrochemical potential results in a reduction of the group velocity in the quantum well. We choose $E = 0$.

The behavior for filling factors comparable to μ in magnitude (blue and red curves) is similar to what we have observed before – T increases from its zero-mode value, $T(E=0,k_y=0)$, and reaches a maximum (which is equal to the number of channels) before it features a sharp cut-off at $k_y = \pm r\kappa_r$ (related to θ_c in the previous section). However, if $-C \ll \mu$ (black curve), the maxima at finite modes vanish, even though no interface barrier is present. Nevertheless, this is compensated by the fact that the zero-mode value, $T(E=0,k_y=0)$, increases with larger FSM, which equally differs from our observations in the simple model. This is due to the fact that, here, we vary FSM by means of the electrochemical potential (in HgTe) and not the effective mass, such that the group velocity of the electrons is affected differently. We illustrate this behavior in Fig. 2.19. If $C = -\mu$, the difference between the group velocities for perpendicular incidence is huge (orange line), and T deviates significantly from its maximum value. Nonetheless, they coincide for some k_y[5], such that T increases from its zero-mode value until it reaches its maximum there. For larger modes, it quickly decreases and vanishes after the cut-off, $k_y/\kappa_r > r$. When we reduce $|C|$ from the value of the electrochemical potential (green line), this decreases the zero-mode group velocity in HgTe as well as the difference between the velocities in the two materials. Consequently, $T(E,k_y=0)$ increases compared to the former choice of C, while the general behavior is the same. If we reduce C even further, the group velocity of the electrons in HgTe becomes smaller than that in Al (red line), and there exists no longer a mode k_y where they coincide. Then, T decreases from its zero-mode value, and the peaks vanish. Nonetheless, this zero-mode value can be rather pronounced, *cf.* Fig. 2.18. As a consequence, the propagating modes in an Al-HgTe-Al junction contribute significantly to the full transmission coefficient, even if FSM between the metals and the semiconductor is large.

We observe a similar behavior when Al features superconducting order, $\Delta_0 > 0$, see Fig. 2.20. Consistent with our observations in Sec. 2.5, the zero-mode transmission coefficient is more sensitive

---

[5] The expression for this maximum mode is too complicated to be given explicitly here.

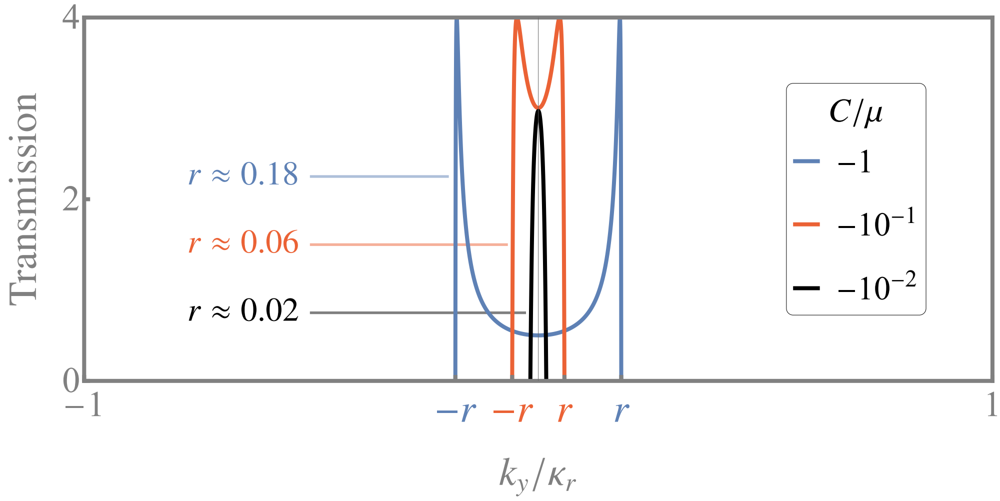

Fig. 2.20: Superconducting-state transmission coefficient T as a function of the mode k_y at different filling factors. We choose $E = 0$.

to r than its normal-state counterpart. Nonetheless, the probability amplitudes are enhanced for large FSM if the semiconductor is a HgTe sample instead of a quasi-free electron gas. While, in the latter case, the excess current becomes rather small for a significant mismatch, *cf.* Fig. 2.16 with $r = 0.1$, we now anticipate stronger contributions to this observable.

2.6.3 Differential conductance and current

From Eq. (2.91) and the definition in Eq. (2.48) we calculate the full transmission coefficient for the HgTe-Al interface junction and thus the differential conductance and the current by means of Eq. (2.25). We normalize the latter quantities to the normal-resistance R_N as defined in the context of Eq. (2.77), which is now bias-dependent,

$$R_N \equiv \frac{4e^2}{h} T(E = eV)\big|_{\Delta_0 = 0}. \tag{2.93}$$

The factor 4 stems from the spin and orbital degrees of freedom in $\mathcal{H}_{\mathrm{BHZ}}$. We plot the results in Fig. 2.21, where we choose a filling factor $C = -2 \cdot 10^{-3}\mu$. This results in a FSM of $r \approx 0.02$.

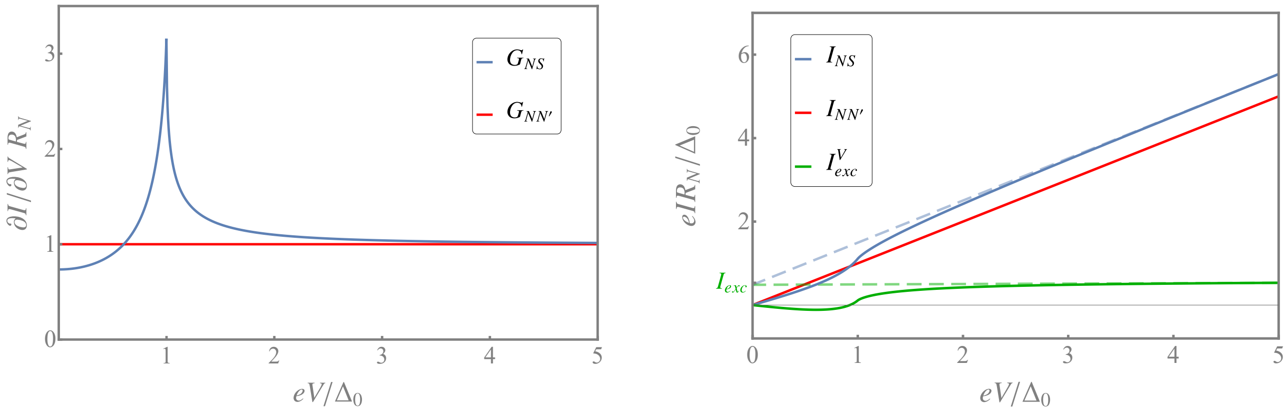

(a) Differential conductance

(b) Current

Fig. 2.21: **(a)** Conductance and **(b)** current as a function of the bias V in a HgTe-Al junction. I^V_{exc} is the bias-dependent excess current. We choose $C = -2 \cdot 10^{-3}\mu$.

The differential conductance features the characteristic resonance at $eV = \Delta_0$ and approaches its normal-state value at $eV \gg \Delta_0$. The associated current is comparable to the normal-state current in the subgap-regime, while we observe a noticeable offset for biases larger than the order parameter. This results in a finite excess current, which is larger than those we computed in Sec. 2.5 for significant FSM and negligible barrier strengths, *cf.* Fig. 2.16. As a consequence, we can expect measurable excess currents in S-N-S junctions where the normal domain is a HgTe/CdTe QW and the superconductors are normal metals like Al, even though FSM is very pronounced.

By applying a gate voltage to the semiconductor, this allows us to tune the filling factor C of the sample. Doing so equally affects FSM, *cf.* Figs. 2.18 and 2.20, and we expect the excess current to increase by increasing the magnitude of C as well. This is confirmed and illustrated in Fig. 2.22, where we plot I_{exc} in the large bias-limit as a function of the filling factor. As anticipated, the excess current (represented by the blue ordinate) increases as we increase $|C|$, or, as we can determine from the top scale, as we decrease FSM (i.e., increase r). The latter scale is not linear since r is directly related to C, as illustrated by the red dashed curve (represented by the red ordinate). This dependence of I_{exc} on r suggests a convenient setup for an experiment where FSM between the HgTe sample and a normal metal like Al can be probed by measuring the excess current while varying the gate voltage applied to the semiconductor. To comply with the assumption of equilibrium reservoirs left and right of the junction, this requires two interfaces, i.e., an Al-HgTe/CdTe-Al hybrid nanostructure. With this, we conclude our analysis of the mercury telluride system.

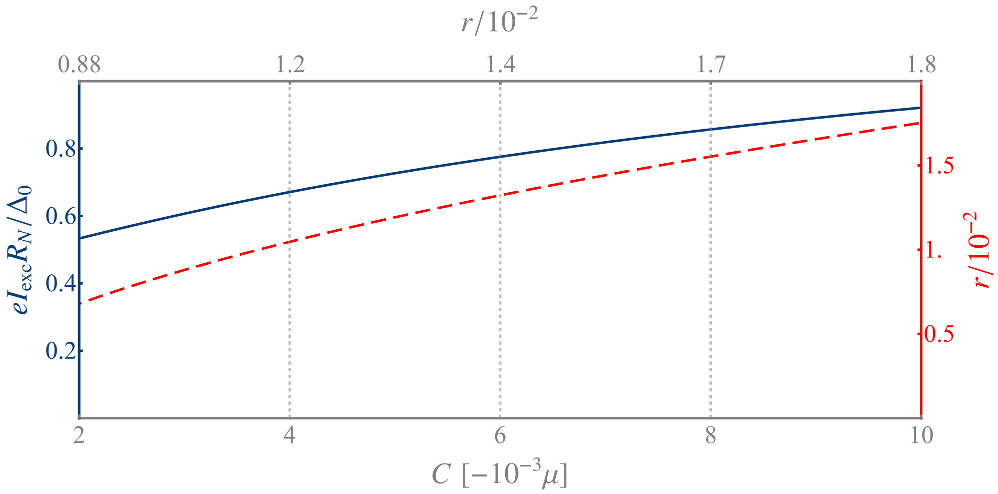

Fig. 2.22: Excess current I_{exc} as a function of the filling factor.

2.7 The BTK-Kastalsky-Beenakker formula

As the last point, we briefly study a practical formula that relates the differential conductance of NS-junctions to its normal-state expression in the so-called linear regime ($E = 0$) and extend it to planar systems featuring FSM. This relation, which, e.g., allows to calculate the gate-dependence of $G_{NS}(eV = 0)$ from $G_{NS}(eV \gg \Delta_0) \approx G_{NN'}$ rather conveniently [64], is based on BTK and was first written down by Kastalsky [65] and derived explicitly by Beenakker [66] shortly after.

2.7.1 Derivation of the formula

The system we consider is illustrated in Fig. 2.23. A normal metal with a disordered domain (illustrated in gray) is in contact with an s-wave superconductor. The interface between N and S is assumed to be perfectly clean, as are the domains N_1, N_2, and S. Thus, scattering due to impurities, constrictions, FSM, or similar only happens in the disordered region. As a consequence, Andreev reflection occurs with unit probability at the N_2-S interface if $\mu \gg E, \Delta_0$. The relation can be conveniently derived by means of the scattering matrix formalism [8], which relates outgoing propagating states (labeled 'b') to the incoming propagating states (labeled 'a'). Let us assume the excitation energy to be smaller

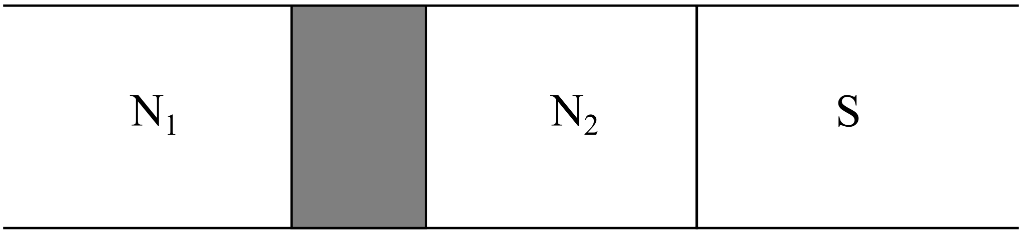

Fig. 2.23: Illustration of a planar metal-superconductor junction as considered in this analysis. The normal domains N_1 and N_2 as well as the superconductor are assumed to be perfectly clean, while the gray area may contain impurities, constrictions or similar kind of disorder. Moreover, we assume a perfect interface between N_2 and S.

than the superconducting gap Δ. Then, there are no outgoing states in S and we may consider the disordered domain, N_2 and S, as a 'black box', since all states relevant for the S-matrix lie in N_1, see Fig. 2.24. It is then defined by

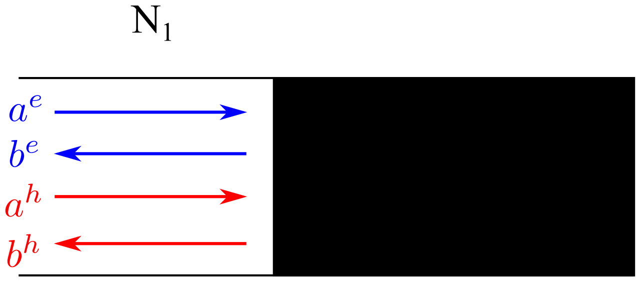

Fig. 2.24: 'Black box' simplification of Fig. 2.23.

$$\begin{pmatrix} b^e \\ b^h \end{pmatrix} = \begin{pmatrix} s_{ee} & s_{he} \\ s_{eh} & s_{hh} \end{pmatrix} \begin{pmatrix} a^e \\ a^h \end{pmatrix} \tag{2.94}$$

with $s_{ee/hh}$ and $s_{eh/he}$ the normal and Andreev reflection amplitudes, respectively. Note that, for the correct definition of the S-matrix, $a^{e/h}$ and $b^{e/h}$ need to carry the same current, which can be achieved by an appropriate normalization. Since $E < \Delta_0$, the conductance of the system can be determined according to the formula

$$G_{NS} = \frac{4e^2}{\hbar} \left| s_{eh} \right|^2 , \tag{2.95}$$

which we would like to relate to the normal-state conductance, as in [65, 66]. To this end, we employ a useful feature of this formalism. To construct the S-matrix of a full system, we can combine the S-matrices of its individual sub-systems, which are, in the setup in Fig. 2.23, N_1-N_2 as well as N_2-S, see Fig. 2.25. For these sub-systems, we can provide the individual S-matrices. For N_1-N_2, it is

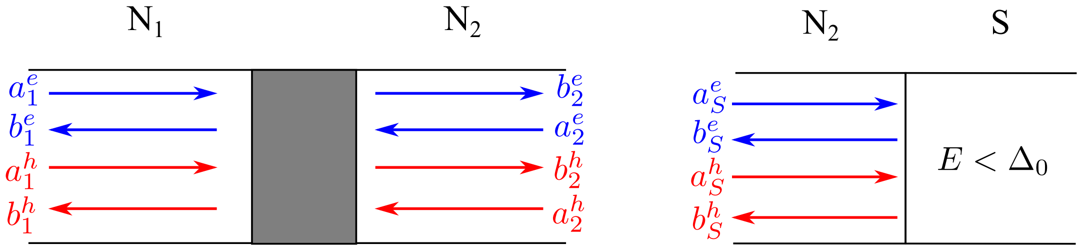

(a) N_1-N_2 junction **(b)** N_2-S junction

Fig. 2.25: Individual sub-systems of the setup in Fig. 2.23.

$$\begin{pmatrix} b_1^e \\ b_2^e \\ b_1^h \\ b_2^h \end{pmatrix} = \begin{pmatrix} r_{11}^e & t_{21}^e & 0 & 0 \\ t_{12}^e & r_{22}^e & 0 & 0 \\ 0 & 0 & r_{11}^h & t_{21}^h \\ 0 & 0 & t_{12}^h & r_{22}^h . \end{pmatrix} \begin{pmatrix} a_1^e \\ a_2^e \\ a_1^h \\ a_2^h \end{pmatrix}, \tag{2.96}$$

where the electron and hole blocks are decoupled due to the absence of superconducting order, while we obtain

$$\begin{pmatrix} b_S^e \\ b_S^h \end{pmatrix} = \begin{pmatrix} r_{ee} & r_{he} \\ r_{eh} & r_{hh} \end{pmatrix} \begin{pmatrix} a_S^e \\ a_S^h \end{pmatrix}. \tag{2.97}$$

in the N_2-S sub-system. With these, we are able to obtain the elements $s_{ee/eh/he/hh}$ of the full S-matrix in Eq. (2.94). To do so, we relate the incoming and outgoing states in N_2 in sub-system **(a)** to those in sub-system **(b)** and identify $a_S^{e/h} = b_2^{e/h}$, $b_S^{e/h} = a_2^{e/h}$, $a^{e/h} = a_1^{e/h}$ and $b^{e/h} = b_1^{e/h}$. This allows to eliminate $a_2^{e/h}$, and $b_2^{e/h}$, and we are left with a system of equations which we can rewrite in the exact form of Eq. (2.94). This yields $s_{ee/eh/he/hh}$, expressed by the matrix elements in Eqs. (2.96) and (2.97). Since this is a simple algebraic procedure, we do not give the explicit result here.

In the next step, we make the following assumptions: (i) we consider $E = 0$, (ii) the electrochemical potential is much larger than the excitation energy and the order parameter, $\mu \gg E, \Delta_0$, and (iii) the disorder does not feature magnetic order. This simplifies the matrices in Eqs. (2.96) and (2.97) significantly [66]. The electron block in Eq. (2.96) is symmetric, the hole block is simply the complex conjugate of the electron block and we have $r_{ee} = r_{hh} = 0$ and $r_{eh} = r_{he} = -i$ in Eq. (2.97). Note that this is true for all modes. With this, we obtain

$$s_{eh} = -\frac{i\,|t_{12}^e|^2}{1 + |r_{11}^e|^2}, \tag{2.98}$$

and thus

$$G_{NS} = \frac{4e^2}{\hbar} \frac{T^2}{(2-T)^2}, \tag{2.99}$$

where $T = |t_{12}^e|^2 = 1 - |r_{11}^e|^2$ is the transmission coefficient of the N_1-N_2 junction. The latter corresponds to the system in Fig. 2.23 when the order parameter is zero, i.e., the normal-state transmission. We have thus expressed the NS conductance in terms of the transmission coefficient of the same system when S is not in the superconducting state.

2.7.2 Transfer to our setup featuring FSM

The question arises if we obtain the same or a similar relation as in Eq. (2.99) if the problem features FSM. Considering the left interface of the setup in Fig. 2.1, this yields a system as sketched in Fig. 2.26, where FSM is schematically illustrated by the different widths of the domains. We face several issues if we want to apply the methodology in the previous section. First of all, in our work, we assumed the normal metal to be clean, i.e., the disorder, as well as FSM, occur exactly at the interface between

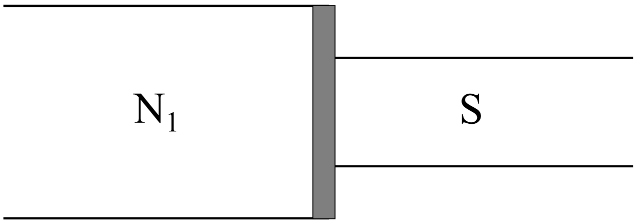

Fig. 2.26: Sketch of the left interface in Fig. 2.1. The horizontal axis corresponds to position, while the vertical axis shall illustrate the extend of the Fermi surface in each domain.

N and S. Then, however, the normal state transmission (in the sub-system N_1) is simply unity and we cannot relate the latter to G_{NS}. Secondly, the number of sub-systems is unity in this example, and the argumentation above is not applicable. In order to obtain a relation comparable to that in Eq. (2.99), this requires a minor argumentative detour.

Let us consider a system as illustrated in Fig. 2.27. Here, we have a setup comparable to Fig. 2.23, where the interface between N_2 and S is perfectly clean and we can assume Andreev reflection to be the only process to occur (under the Andreev approximation at $E = 0$). Here, the disordered region (gray) takes both FSM and the interface barrier into account and we can apply the methodology of the previous section, which yields Eq. (2.99). This is not surprising since we made no assumption on the nature of the disorder in Fig. 2.23 (except for the absence of magnetic order). The remaining problem is that Fig. 2.27 does not yet correspond to the system in Fig. 2.26. To resolve this, we may perform the limit $L \to x_0^+$, which yields the desired setup and Eq. (2.99) remains valid.

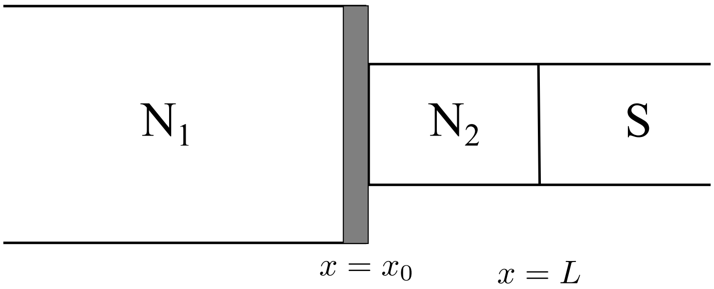

Fig. 2.27: Sketch of the auxiliary system. The horizontal axis corresponds to position, while the vertical axis shall illustrate the extend of the Fermi surface in each domain.

Our results in Sec. 2.5 confirm this relation. Considering the normal-state transmission coefficient, *cf.* Eq. (2.66),

$$T_N \equiv T(\theta_l) = \frac{4r\cos\theta_l\cos\theta_r}{4rZ^2 + (r\cos\theta_l + \cos\theta_r)^2}\Theta(\theta_c - |\theta_l|), \tag{2.100}$$

as well as the one for $\Delta_0 > 0$ and $E = 0$, *cf.* Eq. (2.72)

$$T_S \equiv T(E=0,\theta_l) = \frac{8r^2\cos^2\theta_l\cos^2\theta_r}{(4rZ^2 + r^2\cos^2\theta_l + \cos^2\theta_r)^2}\Theta(\theta_c - |\theta_l|), \tag{2.101}$$

we can convince ourselves that the relation

$$T_S(E=0,\theta_l) = \frac{2\,T_N(\theta_l)^2}{(2 - T_N(\theta_l))^2} \tag{2.102}$$

holds accordingly. Note that the factor 2 here is absorbed into the factor 4 in Eq. (2.95), where we express the differential conductance in terms of the transmission coefficient. This relation apparently holds for all modes (when $E = 0$ and $\mu \gg E, \Delta_0$).

Unfortunately, the expression for the zero-bias resistance R_0 as introduced by Kastalsky [65] for 1D systems becomes rather complicated in planar junctions featuring FSM. Defining R_0, the normal-state resistance R_N and the *limiting normal resistance of a highly transmissive contact* R_N^0 (as denoted by Kastalsky) as

$$R_0 = G_{NS}^{-1}, \qquad R_N = G_{NN'}^{-1}, \qquad R_N^0 = G_{NN'}^{-1}\big|_{Z=0}, \tag{2.103}$$

respectively, we obtain from Eqs. (2.100) to (2.102)

$$R_0 = \frac{\left(R_N\,(r\cos\theta_l + \cos\theta_r)^2 - 2rR_N^0\cos\theta_l\cos\theta_r\right)^2}{2rR_N^0\cos\theta_l\cos\theta_r\,(r\cos\theta_l + \cos\theta_r)^2}\Theta\left(\theta_c - |\theta_l|\right). \tag{2.104}$$

If we only consider the perpendicular mode θ_l (or if θ_c is rather small due to a large FSM), this expression simplifies to

$$\lim_{\theta_l \to 0} R_0 = \frac{\left(R_N \left(1+r\right)^2 - 2rR_N^0\right)^2}{2r\left(1+r\right)^2 R_N^0}, \tag{2.105}$$

which further reduces to

$$\lim_{r \to 1} \lim_{\theta_l \to 0} R_0 = \frac{\left(2R_N - R_N^0\right)^2}{2R_N^0} \tag{2.106}$$

for a homogeneous setup. Consistently, Eq. (2.106) corresponds to the relation as introduced by Kastalsky.

2.8 Conclusion

The experimental measurements of pronounced excess currents in planar metal-semiconductor-metal Josephson junctions with apparently intermediate to high interface transparencies and their agreement with theoretical predictions and calculations based on the BTK formalism have long been a rather counter-intuitive observation. On the one hand, the interfaces between the samples are not of the constriction or orifice type, whereas on the other hand, the apparently high transparency rules out the possibility of the system being in the tunneling regime. Both conditions would justify the assumption of the metals acting like local equilibrium reservoirs, which is a crucial ingredient for BTK (or, more generally, the Landauer formalism) to be applicable. A possible way out of this, for instance, is the assumption of generally opaque interfaces with a small number of penetrable 'pinholes', where incident electrons have a high chance to be transmitted (or Andreev reflected), which would partially explain the observation of such excess currents. However, such a phenomenon has not been observed yet and is probably difficult to probe.

In this chapter, we argue that a substantial FSM between the metals and the semiconductor provides the necessary preconditions such that the assumption of local equilibria left and right of the scattering region (here, the metals N or S) is justified. By means of one of the interfaces in Fig. 2.1, we illustrate how the discrepancy between the Fermi surfaces (in the dispersion) of the metals and the semiconductor performs as a directional filter for electrons approaching the interfaces from the asymptotic regions (i.e., the metals). Only those particles featuring a mode (i.e., the angle of incidence in a planar junction where the y-direction is translational invariant) that exists in both the metal and the semiconductor can be transmitted across the junction, while all the other modes are reflected at the interface and do not contribute to the transport in the system. For large FSM, only a small fraction of electrons with an angle of incidence close to zero can be attributed to these propagating modes, and we argue that then, the metals are in equilibrium since the perturbation in their Fermi distribution functions is sufficiently small. This allows to apply a bias over the junction by setting the metals to different chemical potentials. The effect is apparently even stronger if we assume the planar semiconductor to be in contact with 3D metals.

At hand of the rather simple quasi-free electron Hamiltonian we model such a single NS-interface where FSM is induced by different effective masses and study its electronic properties, where we also include a possible interface barrier. We find that the transmission coefficient for electrical current T features a sharp cut-off between the propagating and the reflected states, as expected due to FSM. And while a large mismatch reduces the transmission for perpendicular incidence, T increases as we increase the angle of incidence and reaches a maximum (which can be approximately equal to the number of channels in the system if the barrier is weak enough) before it vanishes at the cut-off. As a consequence, even though the number of propagating modes is small for large FSM, they can contribute substantially to the transport in the system. It is, however, important to fabricate a rather clean interface, since a strong barrier suppresses the transmission severely. From the calculated differential conductance and the excess current, we show that this is sufficient to obtain results that are comparable to experimental measurements, which substantiates our claim that FSM is a suitable mechanism to explain the applicability of BTK in planar junctions.

Next, we consider the more complicated BHZ-Hamiltonian to describe the semiconductor, which is more realistic than an actual experimental setup. Here, FSM is induced not only by different effective masses but also by the Fermi velocity and the filling factor in HgTe. We observe similar mode-characteristics as before, with the distinction that increasing FSM by means of a gate voltage (which affects the filling factor in HgTe) does not immediately decrease the zero-mode transmission. As a consequence, the contributions at a given energy can be stronger, and we find pronounced excess currents even at large FSM of $r \approx 0.18$ to $r \approx 0.02$, which further support the experimental observations.

While we study single interfaces, the full system in Fig. 2.1 consists of two of them. It is, nonetheless, possible to combine two single-interface systems to a full normal metal-semiconductor-normal metal junction by means of the formalism introduced by Octavio *et al.* [57]. Finally, we show that the BTK-Kastalsky-Beenakker formula holds equally in systems featuring FSM, however, the explicit expression for the zero-bias resistance becomes rather inconvenient.

3

Influence of a chiral chemical potential on Weyl hybrid junctions

This chapter is based on the work *Influence of a chiral chemical potential on Weyl hybrid junctions* by Daniel Breunig, Song-Bo Zhang, Martin Stehno and Björn Trauzettel (Phys. Rev. B **99**, 174501 (2019)).

3.1 Motivation

Weyl semimetals are 3D topological phases that can be obtained from Dirac semimetals by breaking time-reversal or inversion symmetry in the system, and are currently a focus of the research in condensed matter physics [19, 67–70]. In the simplest case of broken TRS, WSMs feature two crossing points, denoted by *Weyl nodes*, in the Brillouin zone, see, for instance, Fig. 3.1(a). For energies close to the band crossing points, these Weyl nodes (featuring opposite chirality) appear as independent cones, separated in k-space and described by linear low-energy Weyl Hamiltonians, see Fig. 3.1(b). They are topologically protected and associated to the chiral anomaly, and therefore host numerous intriguing characteristics like Fermi arcs [71], anomalous magnetoconductance [72–77] and non-local transport [78]. Various realistic materials have been proposed theoretically [79–90] and/or confirmed in experiments as WSMs [91–96]. These topological materials are particularly interesting when combined with conventional s-wave superconductors (S), since the strong spin-orbit coupling in WSMs [19, 71] can lead to spin-triplet pairing in S and thus induce topological superconductivity [97]. The latter has been identified to host exotic physical phenomena like odd-frequency superconductivity [98–100] including the creation, transfer, and possible manipulation of equal-spin Cooper pairs (which are a key concept for superconducting spintronics [101]), as well as Majorana bound states [97]. We elaborate on the creation of equal-spin Cooper pairs in the surface states of a TI and in the absence of any magnetic order in Ref. [102] and discuss it explicitly in Chap. 4 of this Thesis.

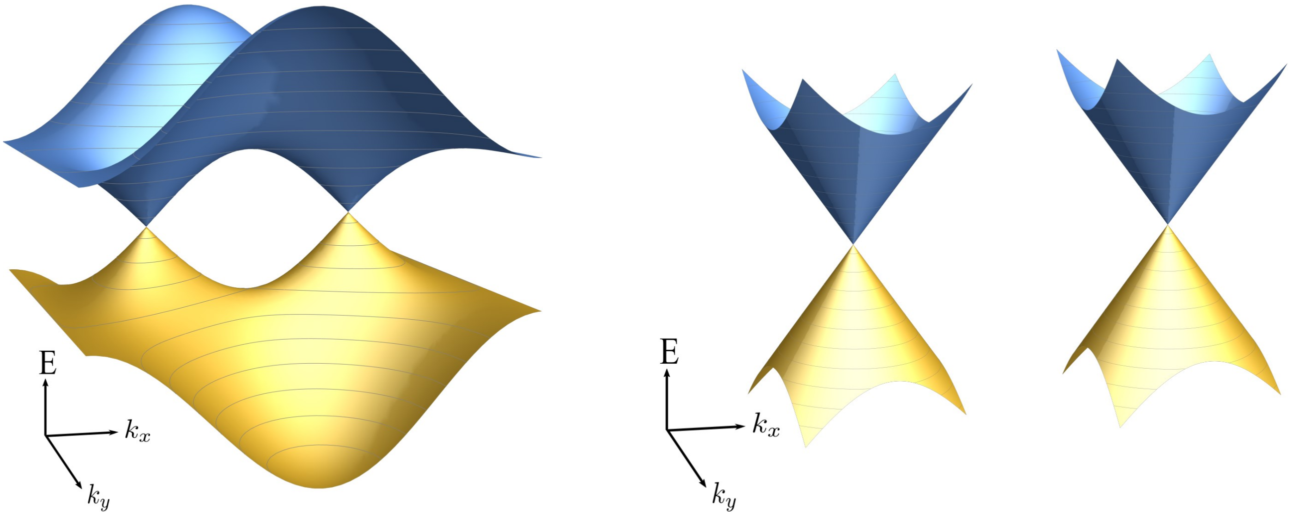

(a) Large-energy range **(b)** Low-energy range

Fig. 3.1: Dispersion of a WSM with broken time-reversal symmetry in the **(a)** large-energy and the **(b)** low-energy range. For energies close to the band crossing points, the two Weyl nodes appear as disconnected, linear cones in k-space. Here, we choose $k_z = 0$.

While the transport signatures, as well as the pairing properties in superconducting WSM heterostructures, have been studied in recent work [103–112], nearly no attention has been paid to the induced superconductivity in normal-state WSM regions. Moreover, it is usually assumed that the Weyl nodes feature the same chemical potential, which is, however, not a necessary presumption. In fact, it is possible to create an imbalance in the electron population between Weyl nodes of opposite chirality by application of parallel electric and magnetic fields [72, 113, 114], by strain deformations [115, 116] or in superlattice systems where both time-reversal and inversion symmetries are broken [117]. This imbalance is denoted by *chiral chemical potential* (CCP) and a key concept in this chapter.

An equally intriguing feature of WSMs, which is related to the anisotropy of the band structure, becomes apparent when we consider once more Fig. 3.1(a). Here, the Weyl nodes are separated in k_x-direction, which is, in principle, a convenient choice of the coordinate system. This is adequate in a homogeneous setup, while in heterostructures, the axis separating the Weyl nodes in real space does not necessarily coincide with the interface normal, but may include an angle. The question arises on how this alignment of the Weyl nodes in k-space (given by the crystalline lattice in real space) affects the transport and the pairing in hybrid systems based on WSMs.

In this chapter, we study the local and non-local differential conductance as well as the proximity effect in TRS broken Weyl semimetal-superconductor-semimetal (NSN) junctions subject to CCP and different alignments of the Weyl nodes with respect to the interface. We apply BTK theory [27] to calculate the transport signatures and the Scattering State Approach to derive the anomalous Green function [118, 119], from which we obtain the pairing amplitudes. In particular, we focus on the emergence of equal-spin pairing in the normal-state WSMs even far away from the interfaces, which leads, for appropriate angles and CCP, to a net spin polarization. The latter is opposite in the two asymptotic domains, giving the junction a dipole character which may present an intriguing feature for application in superconducting spintronics.

The remainder of this chapter is structured as follows. In Sec. 3.2, we present the formalism and additional methods to determine the retarded Green function, from which we extract the anomalous part and thus the pairing amplitudes. Sec. 3.3 gives an overview of the NSN system, the underlying Hamiltonians as well as the derivation of the eigenstates and scattering states. The results are shown and discussed in detail in Sec. 3.4, where we first approach the transport properties in the junction by means of the local and non-local conductance, followed by the pairing amplitudes. Our main focus lies on the effect of CCP and the angle between the axis separating the Weyl nodes and the interface normal. Sec. 3.5 concludes this chapter.

This work has partially been published as a regular article in the journal *Physical Review B* [120]. Similarities in the text are unavoidable. The copyright (2021) belongs to the American Physical Society. All licenses to use the content in this Thesis have been obtained. Reprinted or adapted figures are distinctly marked.

3.2 Concepts and methods

The concepts and methods introduced in this section have been elaborated in detail in Ref. [121]. Here, we provide a general overview due to the importance for the evaluation of the superconducting pairing amplitudes but do not give detailed derivations.

3.2.1 The anomalous Green function

In order to study the proximity effect in the normal-state WSMs by means of the superconducting pairing amplitudes, we need to derive an explicit expression of the anomalous Green function. This quantity is a sub-matrix of the retarded Green function, the latter representing the inverse operator of the Hamiltonian of a system. Considering a spinful 3D material and s-wave superconductivity, let us assume the Hamiltonian is written in the basis $\left(c_\uparrow(\boldsymbol{k}), c_\downarrow(\boldsymbol{k}), c_\uparrow^\dagger(-\boldsymbol{k}), c_\downarrow^\dagger(-\boldsymbol{k})\right)^T$, where $c_\sigma^\dagger(\boldsymbol{k})$ is the creation operator of an electron with spin σ and momentum $\hbar\boldsymbol{k}$. Then, the retarded Green function is of the general form

$$\mathcal{G}(\boldsymbol{r},\boldsymbol{r}',E) = \begin{pmatrix} \mathcal{G}_{ee}(\boldsymbol{r},\boldsymbol{r}',E) & \mathcal{G}_{eh}(\boldsymbol{r},\boldsymbol{r}',E) \\ \mathcal{G}_{he}(\boldsymbol{r},\boldsymbol{r}',E) & \mathcal{G}_{hh}(\boldsymbol{r},\boldsymbol{r}',E) \end{pmatrix}, \tag{3.1}$$

which is naturally a function of two coordinates r and r' in real space[1]. Here, G_{ee} and G_{hh} are the electron-electron and the hole-hole block, respectively, from which one obtains the spectral function and

---

[1] In heterostructures with spatially varying parameters, at least one element of the momentum operator is not a good quantum number and we cannot simply consider the Hamiltonian in k-space.

the density of states. In contrast, G_{eh} and G_{he} are the anomalous parts of the retarded Green function, implicitly incorporating information about the pairing amplitudes. They are manifestly related by the intrinsic BdG particle-hole symmetry and it suffices to consider only one of them. From the basis introduced above, we see that these blocks have a spin structure of the form (here illustrated by means of $\mathcal{G}_{eh}$)

$$\mathcal{G}_{eh}(\boldsymbol{r},\boldsymbol{r}',E)=\begin{pmatrix} G_{eh}^{\uparrow\uparrow}(\boldsymbol{r},\boldsymbol{r}',E) & G_{eh}^{\uparrow\downarrow}(\boldsymbol{r},\boldsymbol{r}',E) \\ G_{eh}^{\downarrow\uparrow}(\boldsymbol{r},\boldsymbol{r}',E) & G_{eh}^{\downarrow\downarrow}(\boldsymbol{r},\boldsymbol{r}',E) \end{pmatrix}. \tag{3.2}$$

It is a common convention to introduce the rotated anomalous Green function, which is given by

$$\mathcal{F}(\boldsymbol{r},\boldsymbol{r}',E)=-i\mathcal{G}(\boldsymbol{r},\boldsymbol{r}',E)s_y=\begin{pmatrix} G_{eh}^{\uparrow\downarrow}(\boldsymbol{r},\boldsymbol{r}',E) & -G_{eh}^{\uparrow\uparrow}(\boldsymbol{r},\boldsymbol{r}',E) \\ G_{eh}^{\downarrow\downarrow}(\boldsymbol{r},\boldsymbol{r}',E) & -G_{eh}^{\downarrow\uparrow}(\boldsymbol{r},\boldsymbol{r}',E) \end{pmatrix}, \tag{3.3}$$

where $s_{0,x,y,z}$ are unit and Pauli matrices in spin space. This rotation allows for a convenient decomposition of $\mathcal{F}$ according to

$$\mathcal{F}(\boldsymbol{r},\boldsymbol{r}',E)=f_0(\boldsymbol{r},\boldsymbol{r}',E)s_0+f_{\uparrow\uparrow}(\boldsymbol{r},\boldsymbol{r}',E)\frac{s_x+is_y}{2}+f_{\downarrow\downarrow}(\boldsymbol{r},\boldsymbol{r}',E)\frac{s_x-is_y}{2}+f_z(\boldsymbol{r},\boldsymbol{r}',E)s_z, \tag{3.4}$$

where we associate f_0 to the spin-singlet pairing amplitude and $f_{\uparrow\uparrow}$, $f_{\downarrow\downarrow}$ and f_z to the equal spin-triplet and the opposite spin-triplet pairing amplitudes, respectively. With this definition, we are able to study the proximity effect in a Weyl NSN junction.

3.2.2 The Scattering State Approach for the Green function

While the (rotated) anomalous Green function is straightforwardly deduced from the retarded Green function, we still require a formalism to obtain this operator. In hybrid nanostructures described by a 1D or quasi-1D Hamiltonian, this is feasible by means of an appropriate outer product of all possible scattering states in the system, a method denoted by *The Scattering State Approach* [118,119,121].

Let us consider the system in Fig. 3.2, where two leads (gray) are connected to a scattering region (black), the latter featuring superconducting order. Then, there are four different scattering states (built from the full set of eigenstates of the underlying Hamiltonian) originated from different excitations (illustrated as points in the figures) and describing the system in its entirety from a mathematical point of view. For example, in Fig. 3.2(a), an electron is excited in the left asymptotic domain ($x<-x_0$) and approaches the interface. There, it can be reflected as an electron or a hole into the original domain, or it can be transmitted as an electron or a hole into the right asymptotic domain ($x>x_0$).

Outgoing boundary conditions

An important feature of this scattering state is the fact that it complies with *outgoing boundary conditions* [8] in the right asymptotic domain, $x\to\infty$. To see this, let us assume a homogeneous material where the left and right-movers are described by wave packages e^{-ikx} and e^{ikx}, respectively, and let k be given, for simplicity and pedagogical reasons, by $k=\sqrt{E}$, with E the energy eigenvalue. By shifting this energy infinitesimally into the positive complex plane, $E\to E+i\omega$ with $\omega\in\mathbb{R}$, this adds an imaginary term to the wavenumber as well, $k\to k+i\eta$ with $\eta\in\mathbb{R}$. We are now able to determine the behavior of the wave packages at $x\to\pm\infty$. The wave function of the left-movers and right-movers are proportional to $e^{-ikx}e^{\eta x}$ and $e^{ikx}e^{-\eta x}$, respectively, and we have

$$\lim_{x\to-\infty} e^{-ikx}e^{\eta x}=0, \qquad \lim_{x\to\infty} e^{-ikx}e^{\eta x}=\infty, \qquad \text{for left movers} \tag{3.5a}$$

$$\lim_{x\to-\infty} e^{ikx}e^{-\eta x}=\infty, \qquad \lim_{x\to\infty} e^{ikx}e^{-\eta x}=0, \qquad \text{for right movers.} \tag{3.5b}$$

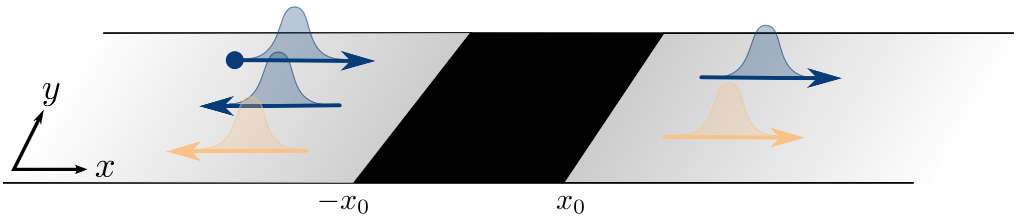

(a) $\phi_1(x)$ or $\tilde{\phi}_1(x)$. Fulfills outgoing boundary conditions at $x \to \infty$.

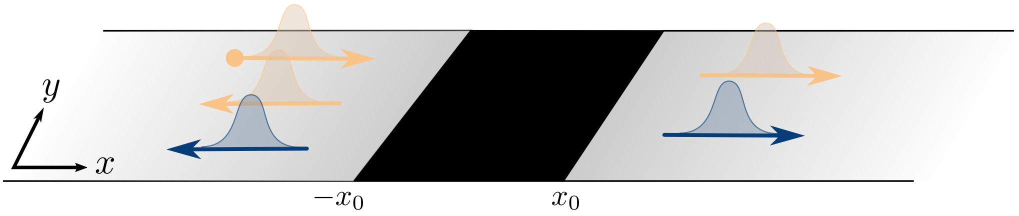

(b) $\phi_2(x)$ or $\tilde{\phi}_2(x)$. Fulfills outgoing boundary conditions at $x \to \infty$.

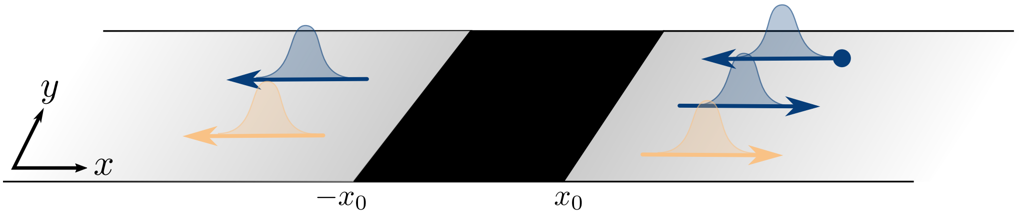

(c) $\phi_3(x)$ or $\tilde{\phi}_3(x)$. Fulfills outgoing boundary conditions at $x \to -\infty$.

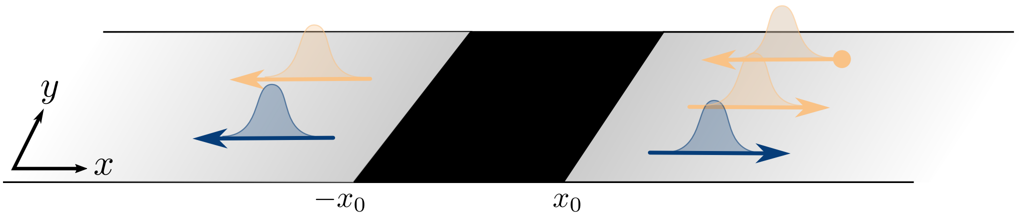

(d) $\phi_4(x)$ or $\tilde{\phi}_4(x)$. Fulfills outgoing boundary conditions at $x \to -\infty$.

Fig. 3.2: Possible scattering states in a system featuring superconducting order, but no other degrees of freedom. The gray domains represent the leads, while the black domain is the scattering region. The four states are the result of **(a)** an electron or **(b)** a hole excited in $x < -x_0$, as well as **(c)** an electron or **(d)** a hole excited in $x > x_0$, each moving towards their respective interface.

As a consequence, the left-movers converge in the asymptotic domain $x \to -\infty$, but diverge in the asymptotic domain $x \to \infty$, such that they fulfill outgoing boundary conditions in the former, but not in the latter region. Apparently, it is vice versa for the right-movers.

To transfer this concept to hybrid structures and scattering states (instead of single eigenstates), let us once more consider Fig. 3.2(a). $\phi_1(x)$ satisfies outgoing boundary conditions at $x \to \infty$, since all states in the right domain ($x > x_0$) converge in the limit $x \to \infty$ after shifting the energy into the positive complex plane. However, it does not comply with outgoing boundary conditions at $x \to -\infty$, since the right-moving electron in the domain $x < -x_0$ diverges for $x \to -\infty$. Note that we implicitly imposed outgoing boundary conditions on this scattering state when we constructed it since we assumed that a right-moving electron excited in the domain $x < -x_0$ cannot be the origin of a left-moving particle in the domain $x > x_0$. Imprinting this physical causality into the system, the scattering states automatically fulfill outgoing boundary conditions in one of the asymptotic domains.

To summarize, the scattering states $\phi_1(x)$ and $\phi_2(x)$ fulfill outgoing boundary conditions at $x \to \infty$, while for $\phi_3(x)$ and $\phi_4(x)$, it is $x \to -\infty$. This is an important concept for the Scattering State Approach, since the retarded Green function needs to satisfy these boundary conditions as well, and its construction depends crucially on the order in which we combine the scattering states.

Note that in the discussion above, the wavenumbers were given in a rather simple form. Nonetheless, the arguments hold equally for more complex expressions, and the crucial ingredient is the infinitesimal shift of the energy into the positive complex plane. It is likewise possible to add a negative imaginary contribution and construct the scattering states accordingly. However, these would then satisfy *incoming boundary conditions* from which one can construct the advanced Green function. This quantity is not relevant for this Thesis and will therefore not be further discussed.

Constructing the Green function

To construct the retarded Green function, let us consider an arbitrary 1D or quasi-1D Hamiltonian $\mathcal{H}$ of a hybrid nanostructure, obeying the Schrödinger equation

$$\underbrace{(E-\mathcal{H})}_{\equiv\mathcal{L}_x}\psi(x)=0. \tag{3.6}$$

This (system of) differential equation is represented by the hermitian operator $\mathcal{L}_x$, which is of the form

$$\mathcal{L}_x=\sum_{k=0}^{m}A_k\frac{\mathrm{d}^k}{\mathrm{d}x^k} \tag{3.7}$$

with A_k matrices or scalars, depending on the dimensionality of the system (i.e., the degrees of freedom). In a condensed mater system, we usually have $m\leq 2$, i.e., a quadratic or linear dispersion. We can solve Eq. (3.6) to obtain the eigenstates $\psi(x)$, which we use to define the full set of scattering states $\phi(x)$. With these, we are able to construct the retarded Green function according to the Scattering State Approach,

$$\mathcal{G}(x,x')=\begin{cases}\sum\limits_{i,j}\alpha_{i,j}\left(\phi_i^l(x)\otimes\tilde{\phi}_j^r(x)\right), & x<x'\\ \sum\limits_{i,j}\beta_{i,j}\left(\phi_i^r(x)\otimes\tilde{\phi}_j^l(x)\right), & x>x'\end{cases}, \tag{3.8}$$

where $\alpha_{i,j}$ and $\beta_{i,j}$ are Green function coefficients yet to be determined and $\otimes$ is the standard outer product. For two column vectors $\boldsymbol{u}=(u_1,u_2,\ldots)^T$ and $\boldsymbol{v}=(v_1,v_2,\ldots)^T$, it is defined as

$$\left(\boldsymbol{u}\boldsymbol{v}^T\right)_{ij}\equiv(\boldsymbol{u}\otimes\boldsymbol{v})_{ij}=u_iv_j. \tag{3.9}$$

Furthermore, $\phi_{i/j}^{l/r}(x)$ are scattering states of the Hamiltonian $\mathcal{H}$, where the superscripts distinguish states that comply with outgoing boundary conditions in the asymptotic domain $x\to-\infty$ (labeled l) from those that comply with outgoing boundary conditions in the asymptotic domain $x\to\infty$ (labeled r). For a Hamiltonian with multiple degrees of freedom (e.g., a BdG-Hamiltonian with electron and hole channels), there can be more than one scattering state complying with the boundary conditions in each corresponding domain. All of them need to be included in Eq. (3.8), hence the indices i and j run over all of these states.

All this holds equally for the scattering states $\tilde{\phi}_{i/j}^{l/r}(x)$, with the distinction that they are not solutions of the Hamiltonian $\mathcal{H}$, but of the transposed operator $\mathcal{H}^T$. This is a consequence of our choice of the outer product in Eq. (3.9) and results from the derivation of the Scattering State Approach [121].

To give a first example, we explicitly write the retarded Green function of the system introduced in Fig. 3.2 in terms of its scattering states, which yields

$$\mathcal{G}(x,x')=\begin{cases}\alpha_1\phi_3(x)\tilde{\phi}_1^T(x')+\alpha_2\phi_3(x)\tilde{\phi}_2^T(x')+\alpha_3\phi_4(x)\tilde{\phi}_1^T(x')+\alpha_4\phi_4(x)\tilde{\phi}_2^T(x'), & x<x'\\ \\ \beta_1\phi_1(x)\tilde{\phi}_3^T(x')+\beta_2\phi_1(x)\tilde{\phi}_4^T(x')+\beta_3\phi_2(x)\tilde{\phi}_3^T(x')+\beta_4\phi_2(x)\tilde{\phi}_4^T(x'), & x>x'\end{cases}. \tag{3.10}$$

Note that the transposed Hamiltonian results in the same qualitative scattering states as $\mathcal{H}$, while the explicit expression for the eigenstates may differ.

What remains is the calculation of the Green function coefficients $\alpha_{i,j}$ and $\beta_{i,j}$ (which we numbered consecutively in Eq. (3.10) for simplicity). This can be achieved by matching $\mathcal{G}(x,x')$ and its derivative at $x = x'$. Assuming the Hamiltonian gives rise to the differential operator in Eq. (3.7), then the $(m-1)$-st derivative of the Green function is discontinuous,

$$\frac{\mathrm{d}^{m-1}}{\mathrm{d}x^{m-1}}\mathcal{G}(x,x')\big|_{x=x'+0^+} - \frac{\mathrm{d}^{m-1}}{\mathrm{d}x^{m-1}}\mathcal{G}(x,x')\big|_{x=x'-0^+} = -A_m^{-1}, \tag{3.11}$$

while each derivative with an order less than $(m-1)$ is continuous,

$$\frac{\mathrm{d}^{k}}{\mathrm{d}x^{k}}\mathcal{G}(x,x')\big|_{x=x'+0^+} - \frac{\mathrm{d}^{k}}{\mathrm{d}x^{k}}\mathcal{G}(x,x')\big|_{x=x'-0^+} = 0, \qquad 0 \leq k < m-1. \tag{3.12}$$

With the Scattering State Approach in Eq. (3.8) and the conditions in Eqs. (3.11) and (3.12), we are now able to determine the retarded Green function of a 1D or quasi-1D Hamiltonian describing a heterostructure junction.

3.2.3 The Wronskian method

While the fundamental scattering states of the Hamiltonians $\mathcal{H}$ and $\mathcal{H}^T$ are the same, the two operators usually do not commute, i.e., can not be described by the same set of eigenstates. This results in different sets of scattering coefficients when matching the waves at the interface(s), which is unfortunate if we want an analytical expression of Eq. (3.8) in terms of one single set of scattering coefficients. Therefore, we want to express the transposed coefficients by the original ones.

A convenient method to achieve this for systems of first-order differential equations is based on Liouville's formula. The Schrödinger equation for such a system can be written in the form

$$\psi'(x) = A\psi(x), \tag{3.13}$$

where $\psi(x)$ are eigenstates of the underlying Hamiltonian and A is a matrix. If the trace of A vanishes, then Liouville's formula states that the Wronskian determinant of that system of first-order differential equations is a constant, $W(x) = W$. This is, in general, an interesting relation. Since the argument of the Wronskian determinant is a full set of solutions to a differential equation, we could, for instance, plug all the scattering states $\phi_{1,2,3,4}(x)$ in Fig. 3.2 into this quantity and evaluate it in different domains, i.e.,

$$W[\phi_1(x),\phi_2(x),\phi_3(x),\phi_4(x)]\big|_{x<-x0} = W[\phi_1(x),\phi_2(x),\phi_3(x),\phi_4(x)]\big|_{x>x0}. \tag{3.14}$$

This allows us to relate the scattering coefficients in different leads to each other, given that the system is described by a first-order differential equation.

When we want to apply this to our problem above, we face the issue that the scattering states $\phi_{1,2,3,4}(x)$ and $\tilde{\phi}_{1,2,3,4}(x)$ are, in general, not solutions to the same Hamiltonian. However, if we are able to relate the transposed Hamiltonian to the original one by a unitary transformation,

$$U\mathcal{H}^TU^\dagger = \mathcal{H}, \tag{3.15}$$

then the set $U\tilde{\phi}_{1,2,3,4}(x)$ is in fact a set of eigenfunctions of $\mathcal{H}$, and we are able to employ the Wronskian method to relate the transposed scattering coefficients to the original ones. We could, for example, evaluate the Wronskian determinant for the set $\{\phi_1(x),\phi_2(x),U\tilde{\phi}_1(x),U\tilde{\phi}_2(x)\}$ in the left and right domain of the junction and demand them to be equal, i.e.,

$$W[\phi_1(x),\phi_2(x),U\tilde{\phi}_1(x),U\tilde{\phi}_2(x)]\big|_{x<-x_0} = W[\phi_1(x),\phi_2(x),U\tilde{\phi}_1(x),U\tilde{\phi}_2(x)]\big|_{x>x_0}. \tag{3.16}$$

In the problem illustrated in Fig. 3.2, there is a total of 70 different sets with non-equal elements which can be evaluated according to this method, and we obtain an equal number of equations to solve for the transposed scattering coefficients. Note that this only works if the Schrödinger equation can be written in the form of Eq. (3.13) and if the trace of A vanishes. Else, other methods need to be employed to relate the coefficients.

With this, we conclude this section where we introduce the methods applied in the following briefly. A thorough and detailed introduction is given in [121].

3.3 Setup and Hamiltonian

The system we want to consider is a 3D NSN-junction, where the underlying material is a TRS broken WSM and the S domain is locally induced by means of a superconducting top gate and the proximity effect, see Fig. 3.3(a). We assume the left and right normal leads to be connected to voltage sources V_L and V_R, respectively, while the superconductor is grounded. The interfaces shall be located at $z_L \equiv -L_s/2$ and $z_R \equiv L_s/2$ with L_s the length of the S domain. Furthermore, the axis separating the Weyl nodes $\hat{q}_3$ in the crystalline coordinate system (described by the canonical unit vectors $(\hat{e}_1, \hat{e}_2, \hat{e}_3)$ and $(\hat{q}_1, \hat{q}_2, \hat{q}_3)$ in real and momentum space, respectively) shall include an angle α with the interface normal in the junction coordinate system (described by the canonical unit vectors $(\hat{x}, \hat{y}, \hat{z})$ and $\left(\hat{k}_x, \hat{k}_y, \hat{k}_z\right)$ in real and momentum space, respectively), see Fig. 3.3(b). Since the interfaces extend along the $x - y$ plane, the direction of this interface normal is $\hat{z}$. Finally, CCP shall be induced by setting the Weyl nodes of opposite chirality (indicated by the different colors of the cones) to different electrochemical potentials.

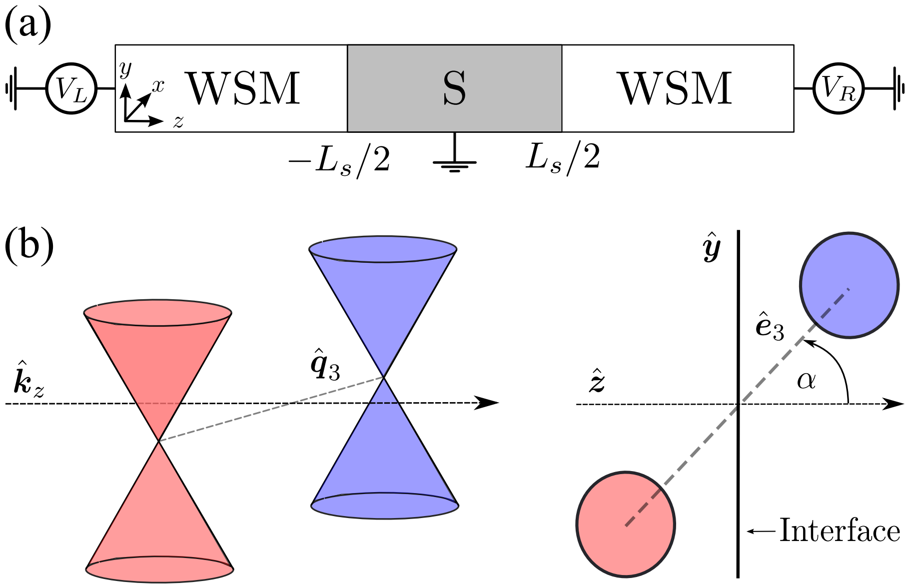

Fig. 3.3: (a) 3D WSM-S-WSM junction considered in this chapter. The interfaces extend along the $x - y$-planes, such that translational invariance is broken in $\hat{z}$-direction. The two WSM leads are connected to voltage sources V_L and V_R, respectively, while the superconductor remains grounded. (b) The axis separating the Weyl nodes $\hat{e}_3$ and the interface normal $\hat{z}$ can include an angle α in such a system. The Weyl fermions of positive and negative chirality are represented by the blue- and red-colored cones, respectively. *Reprinted figure with permission from [120]. Copyright (2021) by the American Physical Society.*

3.3.1 Low-energy Hamiltonian in the crystalline coordinate system

In order to describe the time-reversal symmetry broken WSM, we introduce a minimal model by means of the Hamiltonian

$$\mathcal{H}(\boldsymbol{q}) = \left[M_z(q_0^2 - q_3^2) - Mq^2\right] s_3 + q_1 s_1 + q_2 s_2 - \mu\, s_0, \tag{3.17}$$

which is written in the basis $(c_{\uparrow,\boldsymbol{q}}, c_{\downarrow,\boldsymbol{q}})^T$ with $c_{\sigma,\boldsymbol{q}}$ the annihilation operator of an electron with spin σ and momentum $\hbar\boldsymbol{q}$. Here, M and M_z are mass terms, μ is the electrochemical potential and $\boldsymbol{q} = (q_1, q_2, q_3)^T$ (with $q = \sqrt{q_1^2 + q_2^2}$) as well as $s_{1,2,3}$ are wavevector and Pauli matrices acting on spin space in the crystalline coordinate system, respectively. s_0 is the $(2{\times}2)$-unit matrix. As discussed above and indicated in Eq. (3.17), the Weyl nodes are separated in $\hat{q}_3$ direction and located at $\pm\boldsymbol{Q}_0 = \pm q_0\hat{q}_3$, see Fig. 3.4, where we plot the dispersion of $\mathcal{H}(\boldsymbol{q})$. This Hamiltonian features inversion symmetry, but no time-reversal symmetry, as indicated by

$$\mathcal{I}\mathcal{H}(\boldsymbol{q})\mathcal{I}^\dagger = \mathcal{H}(-\boldsymbol{q}), \qquad\qquad [\mathcal{T}, \mathcal{H}(\boldsymbol{q})] \neq 0 \tag{3.18}$$

with $I = s_z$, $\mathcal{T} = i s_y \mathcal{K}$ and $\mathcal{K}$ the operator of complex conjugation.

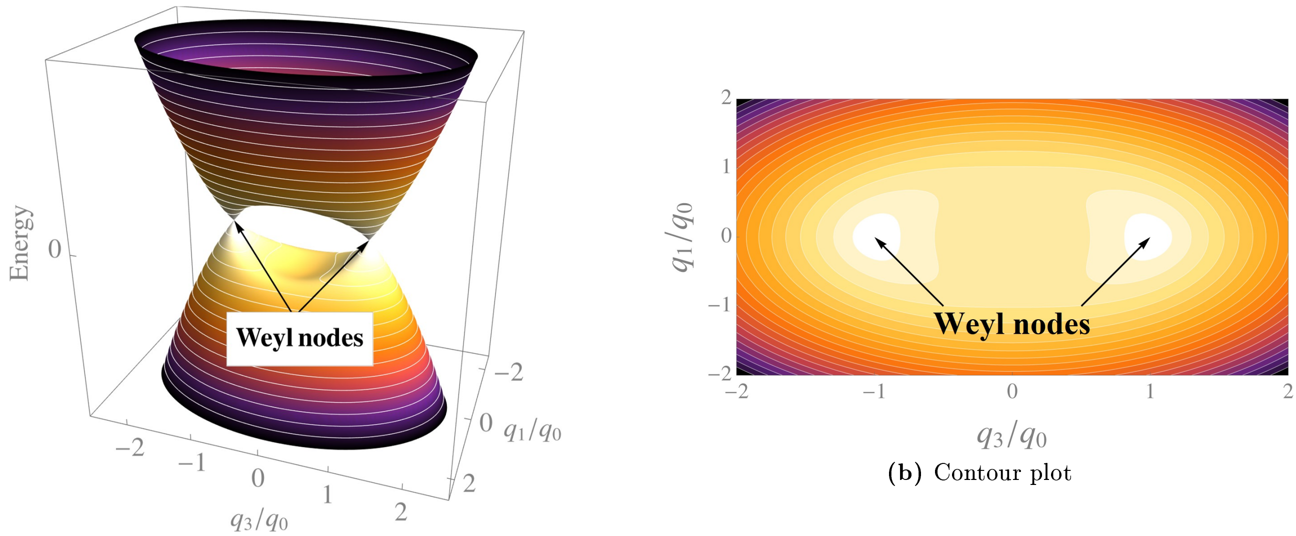

(a) 3D plot

(b) Contour plot

Fig. 3.4: **(a)** 3D and **(b)** contour plot of the energy spectrum of $\mathcal{H}(\boldsymbol{q})$ in the vicinity of the Weyl nodes at $\pm\boldsymbol{Q}_0 = \pm q_0\hat{q}_3$ and as a function of q_1 and q_3. The color indicates the absolute value of the energy (white: $E = 0$; black $|E| \gg 0$), with an equal scale in **(a)** and **(b)**. We choose $\mu = 0$, $M = M_z = 1$ and $q_2 = 0$.

BCS-like superconductivity can be realized in the system by application of the BdG formalism and artificially doubling the spectrum. Introducing the Nambu spinor $\left(c_{\uparrow,\boldsymbol{q}}, c_{\downarrow,\boldsymbol{q}}, c^\dagger_{\downarrow,-\boldsymbol{q}}, -c^\dagger_{\uparrow,-\boldsymbol{q}}\right)^T$, the BdG-Hamiltonian reads

$$\mathcal{H}_{\mathrm{BdG}}(\boldsymbol{q}) = \tau_z(q_1 s_1 + q_2 s_2 - \mu\, s_0) + \left[M_z(q_0^2 - q_3^2) - Mq^2\right]\tau_0 s_3 + \Delta\tau_x s_0, \tag{3.19}$$

with τ_0 and $\tau_{x,y,z}$ the unit matrix and Pauli matrices in Nambu space, respectively, and $\Delta(z)$ the S order parameter. Eq. (3.19) describes the full energy range of the system, whereas we are interested in the low-energy domain in the proximity of the Weyl nodes. We therefore linearize the spectrum in their vicinity and obtain for $\boldsymbol{q} \approx \boldsymbol{Q}_0$ the Hamiltonian (note that we rescale the $\hat{q}_3$-axis according to $q_3 \rightarrow q_3/(2M_z k_0)$)

$$\mathcal{H}^{+}_{\mathrm{BdG}}(\boldsymbol{q}) = \tau_z(q_1 s_1 + q_2 s_2 - \mu\, s_0) + (q_0 - q_3)\tau_0 s_3 + \Delta\tau_x s_0 \tag{3.20}$$

in the basis

$$\boldsymbol{\Psi}_{+}(\boldsymbol{q}) = \left(c_{+,\uparrow,\boldsymbol{q}}, c_{+,\downarrow,\boldsymbol{q}}, c^{\dagger}_{-,\downarrow,-\boldsymbol{q}}, -c^{\dagger}_{-,\uparrow,-\boldsymbol{q}}\right)^{T}. \tag{3.21}$$

The new indices ± of the creation and annihilation operators indicate at which node the electron is created or destroyed. Since conventional BCS s-wave pairing couples electrons and holes of opposite momentum $\hbar\boldsymbol{q}$, these states cannot stem from the same Weyl node, see Fig. 3.5. Similarly, in the basis

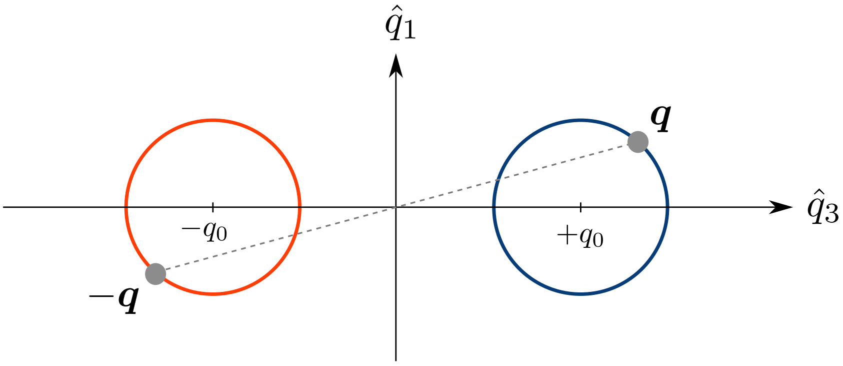

Fig. 3.5: Illustration of BCS s-wave pairing in the low energy regime of $\mathcal{H}_{\text{BdG}}(\boldsymbol{q})$. Since the order parameter couples excitations at momenta of opposite signs, $\boldsymbol{q}$ and $-\boldsymbol{q}$, these states stem from Weyl nodes of opposite chirality (blue and red). The circles are the Fermi surfaces of the low-energy Hamiltonian at a fixed energy.

$$\boldsymbol{\Psi}_{-}(\boldsymbol{q}) = \left(c_{-,\uparrow,\boldsymbol{q}}, c_{-,\downarrow,\boldsymbol{q}}, c^{\dagger}_{+,\downarrow,-\boldsymbol{q}}, -c^{\dagger}_{+,\uparrow,-\boldsymbol{q}}\right)^{T}, \tag{3.22}$$

we obtain

$$\mathcal{H}^{-}_{\text{BdG}}(\boldsymbol{q}) = \tau_z(q_1 s_1 + q_2 s_2 - \mu\, s_0) + (q_0 + q_3)\tau_0 s_3 + \Delta \tau_x s_0 \tag{3.23}$$

for $\boldsymbol{q} \approx -\boldsymbol{Q}_0$, such that the low-energy Hamiltonian for the full system is given by

$$\mathcal{H}(\boldsymbol{q}) = \sum_{\boldsymbol{q}\approx\boldsymbol{Q}_0} \boldsymbol{\Psi}^{\dagger}_{+}(\boldsymbol{q})\mathcal{H}^{+}_{\text{BdG}}(\boldsymbol{q})\boldsymbol{\Psi}_{+}(\boldsymbol{q}) + \sum_{\boldsymbol{q}\approx-\boldsymbol{Q}_0} \boldsymbol{\Psi}^{\dagger}_{-}(\boldsymbol{q})\mathcal{H}^{-}_{\text{BdG}}(\boldsymbol{q})\boldsymbol{\Psi}_{-}(\boldsymbol{q}). \tag{3.24}$$

Note that the two kernel Hamiltonians are related by inversion symmetry,

$$\mathcal{I}\mathcal{H}^{+}_{\text{BdG}}(\boldsymbol{q})\mathcal{I}^{\dagger} = \mathcal{H}^{-}_{\text{BdG}}(-\boldsymbol{q}) \tag{3.25}$$

with $\mathcal{I} = \tau_0 s_z$.

3.3.2 Transfer to the junction coordinate system

As illustrated in Fig. 3.3(b), we want to include an angle α between the axis separating the Weyl nodes and the interface normal. This can be achieved by rotating the crystalline coordinate system relatively to the junction coordinate system, for instance, by means of a rotation around the $\hat{y}$-axis,

$$\hat{R} = \begin{pmatrix} \cos\alpha & 0 & -\sin\alpha \\ 0 & 1 & 0 \\ \sin\alpha & 0 & \cos\alpha \end{pmatrix}. \tag{3.26}$$

With this, we are able to express the wavenumbers as well as the Pauli matrices acting on spin space in the junction coordinates,

$$(q_1, q_2, q_3)^{T} = \hat{R}\,(k_x, k_y, k_z)^{T}, \qquad (s_1, s_2, s_3)^{T} = \hat{R}\,(\sigma_x, \sigma_y, \sigma_z)^{T}, \tag{3.27}$$

such that the Hamiltonians $\mathcal{H}^+(\boldsymbol{q}) = \mathcal{H}^+(\hat{R}\boldsymbol{k})$ and $\mathcal{H}^-(\boldsymbol{q}) = \mathcal{H}^-(\hat{R}\boldsymbol{k})$ (we drop the subscript BdG from now on for compactness) evaluate to

$$\mathcal{H}^+ = \begin{pmatrix} -k_x\sin(2\alpha) - k_z\cos(2\alpha) - \mu & k_x\cos(2\alpha) - ik_y - k_z\sin(2\alpha) & \Delta & 0 \\ k_x\cos(2\alpha) + ik_y - k_z\sin(2\alpha) & k_x\sin(2\alpha) + k_z\cos(2\alpha) - \mu & 0 & \Delta \\ \Delta & 0 & \mu - k_z & -k_x + ik_y \\ 0 & \Delta & -k_x - ik_y & \mu + k_z \end{pmatrix} + \underline{\underline{K_0}} \tag{3.28}$$

and

$$\mathcal{H}^- = \begin{pmatrix} -\mu + k_z & k_x - ik_y & \Delta & 0 \\ k_x + ik_y & -\mu - k_z & 0 & \Delta \\ \Delta & 0 & k_x\sin(2\alpha) + k_z\cos(2\alpha) + \mu & -k_x\cos(2\alpha) + ik_y + k_z\sin(2\alpha) \\ 0 & \Delta & -k_x\cos(2\alpha) - ik_y + k_z\sin(2\alpha) & -k_x\sin(2\alpha) - k_z\cos(2\alpha) + \mu \end{pmatrix} - \underline{\underline{K_0}} \tag{3.29}$$

respectively, with

$$\underline{\underline{K_0}} = \begin{pmatrix} q_0\cos\alpha & q_0\sin\alpha & 0 & 0 \\ q_0\sin\alpha & -q_0\cos\alpha & 0 & 0 \\ 0 & 0 & q_0\cos\alpha & q_0\sin\alpha \\ 0 & 0 & q_0\sin\alpha & -q_0\cos\alpha \end{pmatrix}. \tag{3.30}$$

We move the position of the nodes, which is given by $\pm\boldsymbol{K}_0 = (q_0\sin\alpha, 0, q_0\cos\alpha)^T$ in the junction coordinate system, into the Nambu basis vectors by means of the gauge transformation in position-basis

$$\mathcal{H}^\pm \to e^{\pm i\boldsymbol{K}_0\cdot\boldsymbol{r}}\mathcal{H}^\pm e^{\mp i\boldsymbol{K}_0\cdot\boldsymbol{r}}, \tag{3.31}$$

effectively removing the terms $\underline{\underline{K_0}}$ from Eqs. (3.28) and (3.29). Moreover, we perform the unitary transformation

$$\mathcal{H}^\pm \to \hat{\mathrm{U}}_\alpha^\pm \mathcal{H}^\pm (\hat{\mathrm{U}}_\alpha^\pm)^{-1} \tag{3.32}$$

with

$$\hat{\mathrm{U}}_\alpha^\pm = \frac{1}{2}\Big[(\tau_0 \pm \tau_z)\sigma_x e^{i\alpha\sigma_y} + (\tau_0 \mp \tau_z)\sigma_0\Big], \tag{3.33}$$

which yields the simplified expressions

$$\mathcal{H}^\pm(\boldsymbol{k}) = \begin{pmatrix} k_z - \mu & k_x \pm ik_y & -\Delta\sin\alpha & \Delta\cos\alpha \\ k_x \mp ik_y & -k_z - \mu & \Delta\cos\alpha & \Delta\sin\alpha \\ -\Delta\sin\alpha & \Delta\cos\alpha & \mu - k_z & -k_x \pm ik_y \\ \Delta\cos\alpha & \Delta\sin\alpha & -k_x \mp ik_y & \mu + k_z \end{pmatrix}. \tag{3.34}$$

This provides a convenient representation of the Hamiltonians $\mathcal{H}^\pm(\boldsymbol{k})$, where the α-dependence is moved into the order parameter Δ and $\pm\boldsymbol{K}_0$ does not appear. Finally, we introduce CCP into the system by adding an inversion-symmetry breaking term

$$\mathcal{H}_\chi^\pm = \mp\chi\tau_0\sigma_0 \tag{3.35}$$

to the BdG-Hamiltonians in Eq. (3.34), which allows to modify the filling of each Weyl node. For simplicity, we assume a constant χ everywhere in the junction. To illustrate the effect of CCP, let us consider the eigenenergies for the normal-state ($\Delta = 0$) junction. The electron (e) and hole (h) bands are given by

$$E_e^+ = \pm||\boldsymbol{k}|| - \mu - \chi, \qquad E_h^+ = \pm||\boldsymbol{k}|| + \mu - \chi, \tag{3.36}$$

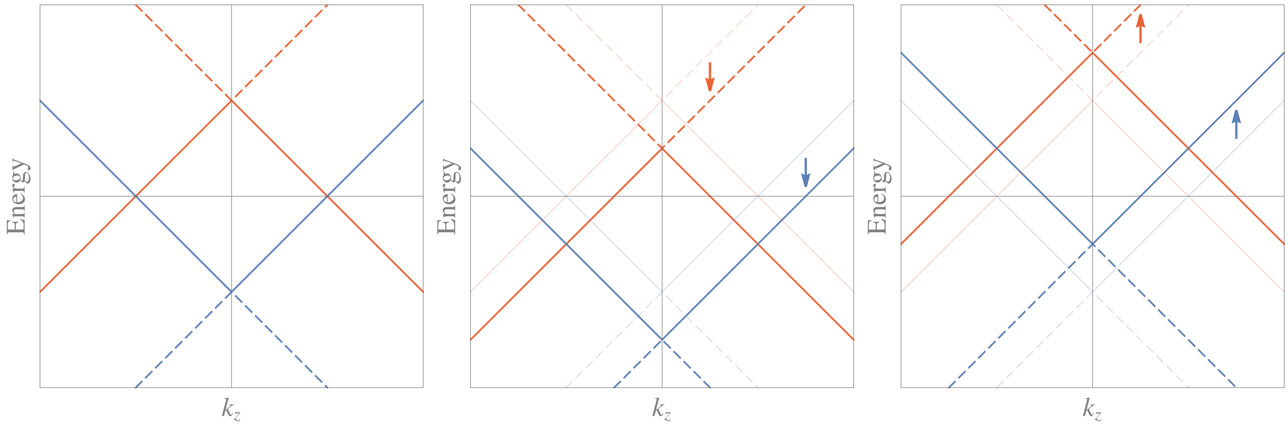

(a) $E^{+}_{e/h}$, $\chi = 0$ **(b)** $E^{+}_{e/h}$, $\chi > 0$ **(c)** $E^{+}_{e/h}$, $\chi < 0$

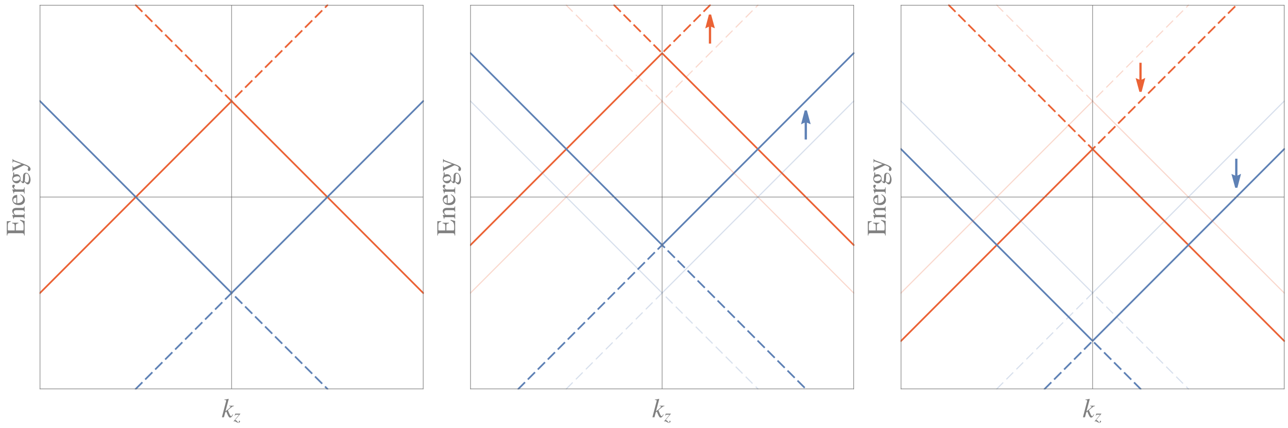

(d) $E^{-}_{e/h}$, $\chi = 0$ **(e)** $E^{-}_{e/h}$, $\chi > 0$ **(f)** $E^{-}_{e/h}$, $\chi < 0$

Fig. 3.6: Electron (blue) and hole (red) dispersion of the Hamiltonian **(a,b,c)** $\mathcal{H}^+$ and **(d,e,f)** $\mathcal{H}^-$ as a function of k_z for **(a,c)** no CCP, **(b,e)** a finite positive and a **(c,f)** a finite negative CCP. Valence bands are indicated by dashed lines, conduction bands by solid lines. We choose $k_{||} = 0$, $\alpha = 0$, $\Delta = 0$ and $\mu > 0$.

for $\mathcal{H}^+(\boldsymbol{k})$ and

$$E^{-}_{e} = \pm\,||\boldsymbol{k}|| - \mu + \chi, \qquad\qquad E^{-}_{h} = \pm\,||\boldsymbol{k}|| + \mu + \chi, \tag{3.37}$$

for $\mathcal{H}^-(\boldsymbol{k})$, where $\pm\,||\boldsymbol{k}||$ distinguishes conductance from valence bands. As we can see, χ corresponds to a shift of the energy, which is equal for the electron and hole bands of the same node, but exactly opposite for the bands of different nodes. This is shown in Fig. 3.6, where we plot the energy as a function of k_z and where we define the transverse wavenumber as

$$k_{||} = \sqrt{k_x^2 + k_y^2}. \tag{3.38}$$

For a vanishing CCP, the electron bands coincide at the $(+)$ and the $(-)$ node, as do the hole bands. For a finite and positive CCP, $\chi > 0$, both the electron and hole dispersion at the $(+)$ node are shifted to lower energies, while it is to larger ones at the $(-)$ node. The effect is exactly vise versa for a finite and negative CCP, $\chi < 0$. Note that this observation is different from tuning the electrochemical potential μ, which shifts the electron and hole bands oppositely to each other at the same node, but the same bands equally on different nodes.

Eigenstates and scattering states

To model the junction, we need to express the Hamiltonians in Eq. (3.34) in position-space, $\mathcal{H}^{\pm}(\boldsymbol{r})$, where the wave vectors are replaced by derivatives,

$$(k_x, k_y, k_z)^T \rightarrow \left(\hat{k}_x, \hat{k}_y, \hat{k}_z\right)^T = -i\left(\partial_x, \partial_y, \partial_z\right)^T . \tag{3.39}$$

The explicit position-dependence is incorporated in the electrochemical potential $\mu(z)$ and the order parameter $\Delta(z)$, which are, in accordance with Fig. 3.3, given by

$$\mu(z) = \mu_N \Theta(|z| - L_s/2) + \mu_S \Theta(L_s/2 - |z|), \tag{3.40a}$$

$$\Delta(z) = \Delta_0 \Theta(L_s/2 - |z|). \tag{3.40b}$$

Here, μ_N, μ_S, and Δ_0 are constant. This step-like model is well justified when the chemical potential μ_S in the S domain is much larger than that in the normal leads μ_N [122,123] and the order parameter Δ_0. Therefore, we assume $|\mu_S| \gg |\mu_N|, \Delta_0$ in the remainder of this chapter.

Since translational invariance is broken only in z-direction, we may perform a partial Fourier transformations in x- and y-direction (we omit a prefactor),

$$\phi(\boldsymbol{r}) = \iint \mathrm{d}x\mathrm{d}y\, \phi(z, k_x, k_y) e^{ik_x x} e^{ik_y y} \qquad \Rightarrow \qquad \mathcal{H}^{\pm}(\boldsymbol{r}) \rightarrow \mathcal{H}^{\pm}(z, k_x, k_y), \tag{3.41}$$

where k_x and k_y are actual parameters and, more importantly, good quantum numbers indexing the transverse modes. As a consequence, we have reduced the 3D Hamiltonian to a quasi-1D operator and thus simplified the problem.

The eigenstates of $\mathcal{H}^{\pm}$ in Eq. (3.41) are straightforwardly derived from the Schrödinger equation and read (note that we omit the phase factors $e^{ik_x x} e^{ik_y y}$ for brevity here)

$$\psi^{\pm}_{\underset{e}{\rightarrow}}(z) = \left(J^{\pm}_e, k_{||} e^{\mp i\theta_k}, 0, 0\right)^T e^{ik^{\pm}_e z}, \tag{3.42a}$$

$$\psi^{\pm}_{\underset{e}{\leftarrow}}(z) = \left(k_{||} e^{\pm i\theta_k}, J^{\pm}_e, 0, 0\right)^T e^{-ik^{\pm}_e z}, \tag{3.42b}$$

$$\psi^{\pm}_{\underset{h}{\rightarrow}}(z) = \left(0, 0, k_{||} e^{\mp i\theta_k}, -J^{\pm}_h\right)^T e^{ik^{\pm}_h z}, \tag{3.42c}$$

$$\psi^{\pm}_{\underset{h}{\leftarrow}}(z) = \left(0, 0, J^{\pm}_h, -k_{||} e^{\pm i\theta_k}\right)^T e^{-ik^{\pm}_h z}, \tag{3.42d}$$

where the alphanumerical indices distinguish electrons (e) from holes (h), the arrows indicate right ($\rightarrow$) and left ($\leftarrow$) movers, i.e., the sign of the associated group velocity with respect to the z-axis, and the superscripts label the nodes. The wavenumbers are given by

$$k^{\pm}_e = \zeta^{\pm}_e \sqrt{(E + \mu_N \pm \chi)^2 - k^2_{||}}, \qquad k^{\pm}_h = \zeta^{\pm}_h \sqrt{(E - \mu_N \pm \chi)^2 - k^2_{||}}, \tag{3.43}$$

where

$$\zeta^{\pm}_e = \mathrm{sgn}\left(E + \mu_N \pm \chi + k_{||}\right), \qquad \zeta^{\pm}_h = \mathrm{sgn}\left(E - \mu_N \pm \chi + k_{||}\right) \tag{3.44}$$

differentiate if the particle stems from the valence or the conduction band for a given energy E. Moreover, we define

$$J^{\pm}_e = k^{\pm}_e + E + \mu_N \pm \chi, \qquad J^{\pm}_h = k^{\pm}_h + E - \mu_N \pm \chi, \tag{3.45}$$

and $\theta_k = \arg\left(k_y/k_x\right)$. $k_{||}$ is introduced in Eq. (3.38).

The eigenstates in the superconductor are, without further approximations, rather complicated and extensive. For a heavily doped S domain, $|\mu_S| \gg |\mu_N|, \Delta_0$, however, it is valid to assume that all excitations show quasi-perpendicular ($k_{||} \approx 0$) transmission into the superconductor. In this regime, we can approximate the eigenstates rather conveniently as

$$\psi_1^{\pm}(z) = \left(J_S^{\pm}, 0, -\Delta_0 \sin\alpha, 0\right)^T e^{ik_S^{\pm} z} e^{i\mu_S z}, \tag{3.46a}$$

$$\psi_2^{\pm}(z) = \left(-\Delta_0 \sin\alpha, 0, J_S^{\pm}, 0\right)^T e^{-ik_S^{\pm} z} e^{i\mu_S z}, \tag{3.46b}$$

$$\psi_3^{\pm}(z) = \left(0, \Delta_0 \sin\alpha, 0, J_S^{\pm}\right)^T e^{ik_S^{\pm} z} e^{-i\mu_S z}, \tag{3.46c}$$

$$\psi_4^{\pm}(z) = \left(0, J_S^{\pm}, 0, \Delta_0 \sin\alpha\right)^T e^{-ik_S^{\pm} z} e^{-i\mu_S z}, \tag{3.46d}$$

where

$$k_S^{\pm} = \sqrt{(E \pm \chi)^2 - \Delta_0^2 \sin^2\alpha}, \qquad J_S^{\pm} = k_S^{\pm} + E \pm \chi. \tag{3.47}$$

Intriguingly, from these expressions, we find that the order parameter is modified by the angle α, such that we can define an effective potential

$$\tilde{\Delta}_0 = \Delta_0 \left|\sin\alpha\right|, \tag{3.48}$$

which even vanishes for $\alpha = 0$ and $\alpha = \pm\pi$, i.e., when the axis separating the nodes and the interface normal are parallel or anti-parallel. From this, we can expect interesting features in the angle-dependence of the transport properties and the proximity-effect.

We are now able to construct the full set of scattering states associated to the Hamiltonians in Eq. (3.41), which are eight in total and read

$$\phi_{1/2}^{\pm}(z) = \begin{cases} \psi^{\pm}_{\overrightarrow{e/h}}(z) + a^{\pm}_{1/2}\psi^{\pm}_{\overleftarrow{h/e}}(z) + b^{\pm}_{1/2}\psi^{\pm}_{\overleftarrow{e/h}}(z), & z < z_L \\ \sum\limits_{i=1}^{4} s^{\pm}_{i,1/2}\psi_i^{\pm}(z), & z_L < z < z_R \\ c^{\pm}_{1/2}\psi^{\pm}_{\overrightarrow{e/h}}(z) + d^{\pm}_{1/2}\psi^{\pm}_{\overrightarrow{h/e}}(z), & z > z_R \end{cases}, \tag{3.49a}$$

$$\phi_{3/4}^{\pm}(z) = \begin{cases} c^{\pm}_{3/4}\psi^{\pm}_{\overleftarrow{e/h}}(z) + d^{\pm}_{3/4}\psi^{\pm}_{\overleftarrow{h/e}}(z), & z < z_L \\ \sum\limits_{i=1}^{4} s^{\pm}_{i,3/4}\psi_i^{\pm}(z), & z_L < z < z_R \\ \psi^{\pm}_{\overleftarrow{e/h}}(z) + a^{\pm}_{3/4}\psi^{\pm}_{\overrightarrow{h/e}}(z) + b^{\pm}_{3/4}\psi^{\pm}_{\overrightarrow{e/h}}(z), & z > z_R \end{cases}. \tag{3.49b}$$

The coefficients $a_l^{\pm}, b_l^{\pm}, c_l^{\pm}$ and $d_l^{\pm}$, $l \in \{1,2,3,4\}$, are associated to Andreev reflection, normal reflection, electron co-tunneling and crossed Andreev reflection, respectively, while $s_{i,l}^{\pm}$ are scattering coefficients in the S domain. As illustrated in Fig. 3.2, $\phi_{1/2}^{\pm}(z)$ describes the scattering state based on an electron/hole excited in the asymptotic domain $z < z_L$, while $\phi_{3/4}^{\pm}(z)$ describes the scattering state based on an electron/hole excited in the asymptotic domain $z > z_R$.

Transposed eigenstates and scattering states

With the definitions so far, we are able to amply characterize the transport properties in the system. Nonetheless, if we want to study the proximity effect, i.e., the superconducting pairing amplitudes, it is necessary to determine the scattering states of the transposed system Hamiltonians, as elaborated in Sec. 3.2. When we perform the transposition $\left[\mathcal{H}^{\pm}(\boldsymbol{r}, k_x, k_y)\right]^T$, we need to be aware of the fact that $\hat{k}_z$ is an operator, i.e., in addition to transposing the matrix, we have

$$\hat{k}_z^T = -\hat{k}_z. \tag{3.50}$$

Moreover, the phase factors feature a different sign to that of the normal Hamiltonian and are given by $e^{-ik_x x}e^{-ik_y y}$. With this, we obtain the eigenstates

$$\tilde{\psi}^{\pm}_{\underrightarrow{e}}(z) = \left(k_{||}e^{\mp i\theta_k}, J^{\pm}_e, 0, 0\right)^T e^{ik^{\pm}_e z}, \tag{3.51a}$$

$$\tilde{\psi}^{\pm}_{\underleftarrow{e}}(z) = \left(J^{\pm}_e, k_{||}e^{\pm i\theta_k}, 0, 0\right)^T e^{-ik^{\pm}_e z}, \tag{3.51b}$$

$$\tilde{\psi}^{\pm}_{\underrightarrow{h}}(z) = \left(0, 0, J^{\pm}_h, -k_{||}e^{\mp i\theta_k}\right)^T e^{ik^{\pm}_h z}, \tag{3.51c}$$

$$\tilde{\psi}^{\pm}_{\underleftarrow{h}}(z) = \left(0, 0, k_{||}e^{\pm i\theta_k}, -J^{\pm}_h\right)^T e^{-ik^{\pm}_h z}, \tag{3.51d}$$

in the WSM leads and

$$\tilde{\psi}^{\pm}_1(z) = \left(0, J^{\pm}_S, 0, \Delta_0 \sin\alpha\right)^T e^{ik^{\pm}_S z}e^{i\mu_S z}, \tag{3.52a}$$

$$\tilde{\psi}^{\pm}_2(z) = \left(0, \Delta_0 \sin\alpha, 0, J^{\pm}_S\right)^T e^{-ik^{\pm}_S z}e^{i\mu_S z}, \tag{3.52b}$$

$$\tilde{\psi}^{\pm}_3(z) = \left(-\Delta_0 \sin\alpha, 0, J^{\pm}_S, 0\right)^T e^{ik^{\pm}_S z}e^{-i\mu_S z}, \tag{3.52c}$$

$$\tilde{\psi}^{\pm}_4(z) = \left(J^{\pm}_S, 0, -\Delta_0 \sin\alpha, 0\right)^T e^{-ik^{\pm}_S z}e^{-i\mu_S z}, \tag{3.52d}$$

in the S domain. Finally, the transposed scattering states are given by

$$\tilde{\phi}^{\pm}_{1/2}(z) = \begin{cases} \tilde{\psi}^{\pm}_{\underrightarrow{e/h}}(z) + \tilde{a}^{\pm}_{1/2}\tilde{\psi}^{\pm}_{\underleftarrow{h/e}}(z) + \tilde{b}^{\pm}_{1/2}\tilde{\psi}^{\pm}_{\underleftarrow{e/h}}(z), & z < z_L \\ \sum\limits_{i=1}^{4} \tilde{s}^{\pm}_{i,1/2}\tilde{\psi}^{\pm}_i(z), & z_L < z < z_R\ , \\ \tilde{c}^{\pm}_{1/2}\tilde{\psi}^{\pm}_{\underrightarrow{e/h}}(z) + \tilde{d}^{\pm}_{1/2}\tilde{\psi}^{\pm}_{\underrightarrow{h/e}}(z), & z > z_R \end{cases} \tag{3.53a}$$

$$\tilde{\phi}^{\pm}_{3/4}(z) = \begin{cases} \tilde{c}^{\pm}_{3/4}\tilde{\psi}^{\pm}_{\underleftarrow{e/h}}(z) + \tilde{d}^{\pm}_{3/4}\tilde{\psi}^{\pm}_{\underleftarrow{h/e}}(z), & z < z_L \\ \sum\limits_{i=1}^{4} \tilde{s}^{\pm}_{i,3/4}\tilde{\psi}^{\pm}_i(z), & z_L < z < z_R\ . \\ \tilde{\psi}^{\pm}_{\underleftarrow{e/h}}(z) + \tilde{a}^{\pm}_{3/4}\tilde{\psi}^{\pm}_{\underrightarrow{h/e}}(z) + \tilde{b}^{\pm}_{3/4}\tilde{\psi}^{\pm}_{\underrightarrow{e/h}}(z), & z > z_R \end{cases} \tag{3.53b}$$

The scattering coefficients can be determined by means of the conditions derived in the previous chapter, *cf.* Eqs. (2.5) and (2.14). As it turns out, the second equation is naturally satisfied and we are left with the continuity of the waves at the interfaces, i.e.,

$$\lim_{\varepsilon\to 0}\left(\phi^{\pm}_l(z_L - \varepsilon) - \phi^{\pm}_l(z_L + \varepsilon)\right) = 0, \quad \text{and} \quad \lim_{\varepsilon\to 0}\left(\phi^{\pm}_l(z_R - \varepsilon) - \phi^{\pm}_l(z_R + \varepsilon)\right) = 0, \tag{3.54a}$$

$$\lim_{\varepsilon\to 0}\left(\tilde{\phi}^{\pm}_l(z_L - \varepsilon) - \tilde{\phi}^{\pm}_l(z_L + \varepsilon)\right) = 0, \quad \text{and} \quad \lim_{\varepsilon\to 0}\left(\tilde{\phi}^{\pm}_l(z_R - \varepsilon) - \tilde{\phi}^{\pm}_l(z_R + \varepsilon)\right) = 0. \tag{3.54b}$$

We are now prepared to study the transport properties and the proximity effect in the WSM/S/WSM junction.

3.4 Results

In the following, we study quantities that depend, in general, on the transverse wave vector $\boldsymbol{k}_{||}$. Experimentally, single modes are hard to realize, which is why we consider the sum over all possible modes $\sum_{\boldsymbol{k}_{||}}$ instead. In the continuum limit, we express this sum by an integral

$$\sum_{\boldsymbol{k}_{||}} \to \frac{L_x L_y}{(2\pi)^2} \int\limits_0^{2\pi} \int\limits_0^{\kappa} \mathrm{d}k_{||}\mathrm{d}\theta_k\, k_{||}, \tag{3.55}$$

where we parameterize the transverse wave vector in polar coordinates by $k_{||}e^{i\theta_k}$ with $k_{||} = \sqrt{k_x^2 + k_y^2}$ and $\theta_k = \arg(k_y/k_x)$. Here, L_x and L_y are the extend of the junction in x- and y-direction, respectively. These quantities are not relevant for us, since we are going to consider normalized observables only. Moreover, κ is the radius of the Fermi surface at a given energy in k-space and depends on the incident particle. For an electron or a hole at node ±, it is given by

$$\kappa \equiv \kappa_e^{\pm}(E) = |E + \mu \pm \chi| \,, \tag{3.56a}$$

$$\kappa \equiv \kappa_h^{\pm}(E) = |E - \mu \pm \chi| \,, \tag{3.56b}$$

respectively.

In this section, we first consider the transport features in the junction, followed by an analysis of the pairing amplitudes.

3.4.1 Transport characteristics

For the transport properties, we are particularly interested in the differential conductance. In an NSN-junction, one can measure both the local $G_{LL} \equiv \partial I_L/\partial V_L\big|_{V_R=0}$ and the non-local $G_{LR} \equiv \partial I_R/\partial V_L\big|_{V_R=0}$ conductance, where $I_{L(R)}$ is the current measured in the domain $z < z_L$ $(z > z_R)$ and V_L means that a bias is applied to the left lead, while the right lead remains grounded, $V_R = 0$. Due to the spatial symmetry of the problem, these quantities are equivalent to G_{RR} and G_{RL}, respectively, and we only consider the case where a bias is applied to the left lead. Assuming the junction is connected to equilibrium reservoirs at $z \to \pm\infty$, the local and non-local differential conductance at zero temperature are given by [27,31,32]

$$G_{LL,l}^{\pm}(eV) \equiv \sum_{\boldsymbol{k}_{||}} G_{LL,l}^{\pm}(eV, \boldsymbol{k}_{||}) = \frac{2e^2}{h} \sum_{\boldsymbol{k}_{||}} \left[1 + A_l^{\pm}(eV, \boldsymbol{k}_{||}) - B_l^{\pm}(eV, \boldsymbol{k}_{||})\right] , \tag{3.57a}$$

$$G_{LR,l}^{\pm}(eV) \equiv \sum_{\boldsymbol{k}_{||}} G_{LR,l}^{\pm}(eV, \boldsymbol{k}_{||}) = \frac{2e^2}{h} \sum_{\boldsymbol{k}_{||}} \left[C_l^{\pm}(eV, \boldsymbol{k}_{||}) - D_l^{\pm}(eV, \boldsymbol{k}_{||})\right] . \tag{3.57b}$$

Here, the index $l \in \{1, 2, 3, 4\}$ associates the conductance to the corresponding scattering state in Eq. (3.49), while A_l, B_l, C_l and D_l are probability amplitudes for Andreev reflection (AR), normal reflection (NR), electron or hole co-tunneling (CO) as well as crossed Andreev reflection (CAR), respectively. Notice that AR increases the local differential conductance, while CAR reduces its non-local counterpart. These amplitudes are related to the scattering coefficients by

$$A_l^{\pm}(eV, \boldsymbol{k}_{||}) = j_l^{\pm} \left|a_l^{\pm}\right|^2 , \qquad B_l^{\pm}(eV, \boldsymbol{k}_{||}) = \left|b_l^{\pm}\right|^2 , \tag{3.58a}$$

$$C_l^{\pm}(eV, \boldsymbol{k}_{||}) = \left|c_l^{\pm}\right|^2 , \qquad D_l^{\pm}(eV, \boldsymbol{k}_{||}) = j_l^{\pm} \left|d_l^{\pm}\right|^2 , \tag{3.58b}$$

where j_l is the ratio of the probability currents of the incoming and outgoing particle and reads

$$j_l = \begin{cases} \frac{J_h^{\pm}}{J_e^{\pm}} \frac{\mathrm{Re}(k_h^{\pm})}{k_e^{\pm}}, & l = 1, 3 \\ \frac{J_e^{\pm}}{J_h^{\pm}} \frac{\mathrm{Re}(k_e^{\pm})}{k_h^{\pm}}, & l = 2, 4 \end{cases} . \tag{3.59}$$

Since the scattering coefficients are rather extensive in an NSN-junction, we do not provide them explicitly here and evaluate the sum in Eq. (3.57) numerically. We now consider the α and χ-dependence separately by explicitly calculating $G_{LL,1}^{\pm}(eV)$ and $G_{LR,1}^{\pm}(eV)$. All other conductances are related to these quantities by spatial inversion or particle-hole symmetry (in the sense of BdG), and we need not consider them separately. The index is thus dropped in the following for the sake of clarity.

Angular dependence of the differential conductance

For now, we set $\chi = 0$, i.e., the system features no CCP. The angle between the axis separating the Weyl nodes and the interface normal α enters the problem in terms of an effective superconducting gap, *cf.* Eq. (3.48). Apparently, $\tilde{\Delta}_0$ is maximal for $\alpha = \pm\pi/2$ and vanishes for $\alpha \in \{0, \pm\pi\}$. We see this in Fig. 3.7, where we plot the normalized conductance ($G^0_{LL/LR}$ is the corresponding normal-state conductance) as a function of the bias voltage for a length $L_s = \xi = v_F/\Delta_0$ of the S domain. Note that v_F is the Fermi velocity of the particles, which is unity since we rescaled the $\hat{q}_3$-axis, *cf.* Eq. (3.20).

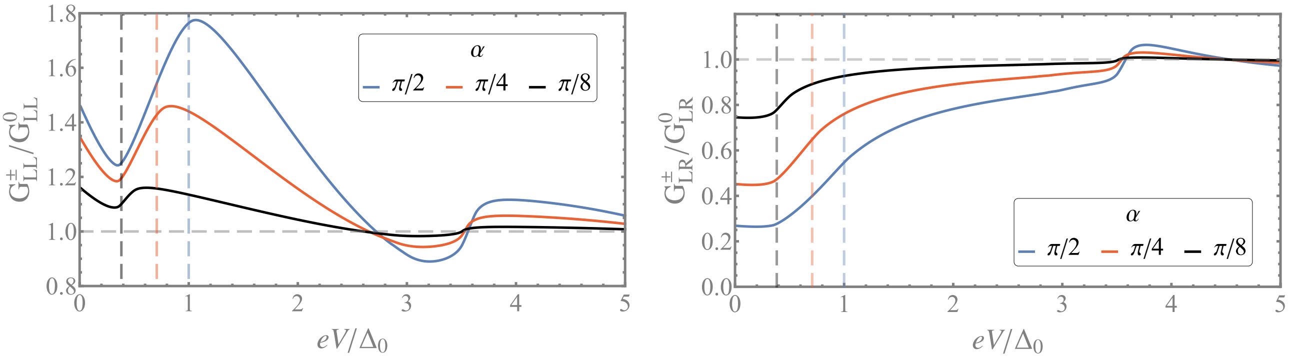

(a) Local differential conductance

(b) Non-local differential conductance

Fig. 3.7: **(a)** Local and **(b)** non-local conductance as a function of eV for different angles α. At $\alpha = \pi/2$, $\tilde{\Delta}_0$ is maximal, which strongly promotes AR and CAR. As a consequence, $G^{\pm}_{LL}$ is largest and $G^{\pm}_{LR}$ is smallest at these angles. The normal-state conductance is indicated by the horizontal gray, dashed line. The value of $\tilde{\Delta}_0$ for the listed angles is indicated by the vertical, dashed lines in the corresponding color. We choose $\mu_S = 10^6\,\Delta_0$, $\mu_N = 10^3\,\Delta_0$, $\chi = 0$ and $L = \xi$. *Reprinted figure with permission from [120]. Copyright (2021) by the American Physical Society.*

The local conductance decreases from its zero-bias value and reaches a minimum at subgap energies, after which it increases again and reaches a maximum for energies close to the effective gap, $eV = \tilde{\Delta}_0$. Nonetheless, $G^{\pm}_{LL}$ exceeds its normal-state value for $eV \approx \tilde{\Delta}_0$ due to the strong contributions from AR. The oscillatory behavior can be observed at supragap energies as well, whereas the amplitude is significantly decreased when the normal-state conductance is approached at large biases $eV \gg \tilde{\Delta}_0$.

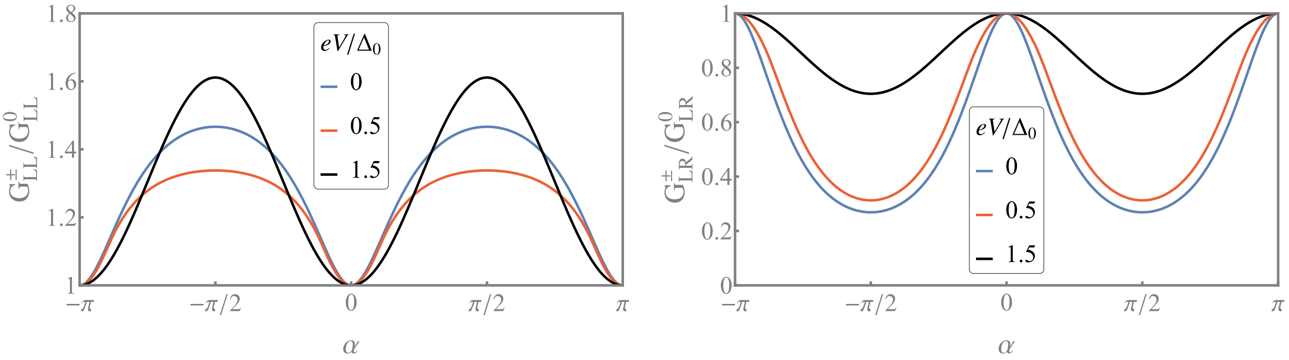

(a) Local differential conductance

(b) Non-local differential conductance

Fig. 3.8: **(a)** Local and **(b)** non-local conductance as a function of α for different biases eV. Both observables are π-periodic functions. We choose $\mu_S = 10^6\,\Delta_0$, $\mu_N = 10^3\,\Delta_0$, $\chi = 0$ and $L = \xi$.

In contrast, the non-local conductance is rather flat and noticeably below the normal-state conductance for subgap energies, and quickly approaches the former for biases above $\tilde{\Delta}_0$. The reason for this is that CAR decreases $G^{\pm}_{LR}$, see Eq. (3.57), which is suppressed only for biases $eV \gg \tilde{\Delta}_0$. Furthermore, the oscillations are hardly observable in contrast to $G^{\pm}_{LL}$.

The effect of the angle α becomes apparent in both figures. While $G^{\pm}_{LL}$ is largest and $G^{\pm}_{LR}$ smallest for $\alpha = \pi/2$ (i.e., when $\tilde{\Delta}_0 = \Delta_0$) due to the strong effect of the electron-hole conversion processes, the local conductance is generally reduced and the non-local conductance is generally increased when we decrease ($\alpha \to 0$) or increase ($\alpha \to \pi$) the angle from $\alpha = \pi/2$. At $\alpha = 0$ or $\alpha = \pm\pi$, the effective gap vanishes completely, such that $G^{\pm}_{LL}$ and $G^{\pm}_{LR}$ do not deviate from the normal-state conductance. We can comprehend this explicitly from Fig. 3.8, where we plot the differential conductance as a function of the angle α. We find that at $\alpha = 0$ and $\alpha = \pm\pi$, both $G^{\pm}_{LL}$ and $G^{\pm}_{LR}$ coincide with their normal-state values since $A^{\pm}_1 = D^{\pm}_1 = 0$, while $G^{\pm}_{LL}$ is maximal and $G^{\pm}_{LR}$ minimal at $\alpha = \pm\pi/2$, where AR and CAR are strongest. The periodicity of both functions,

$$G^{\pm}_{LL/LR}(eV, \alpha) = G^{\pm}_{LL/LR}(eV, \alpha \pm \pi) \tag{3.60}$$

corresponds to the periodicity of the effective superconducting gap, $\tilde{\Delta}_0(\alpha) = \tilde{\Delta}_0(\alpha \pm \pi)$. The effect of the angle α on the order parameter is thus directly transferable to the differential conductance in the system.

Finally, we show the observables as functions of both the angle α and the bias voltage eV in the contour plots in Fig. 3.9. This figure confirms once more that the angular dependence of the differential conductance is independent of the energy and follows that of the effective gap $\tilde{\Delta}_0$ (green, dashed lines). The oscillatory behavior, which stems from interference effects in the junction, is noticeable rather in $G^{\pm}_{LL}/G^{0}_{LL}$ than in $G^{\pm}_{LR}/G^{0}_{LL}$ and depends on the length of the S domain L_s. At large biases $eV \gg \tilde{\Delta}_0$, both quantities approach their normal-state value due to the decay of the AR and CAR probabilities.

These findings are consistent with the observations on a Weyl NS junction [103] and extend the problem to a Weyl NSN setup as illustrated in Fig. 3.3(a). Note that the conductance from the states at the (+) node is equal to that at the (−) node since no CCP is present. The full differential conductance of the system is thus simply twice the conductances shown in this section.

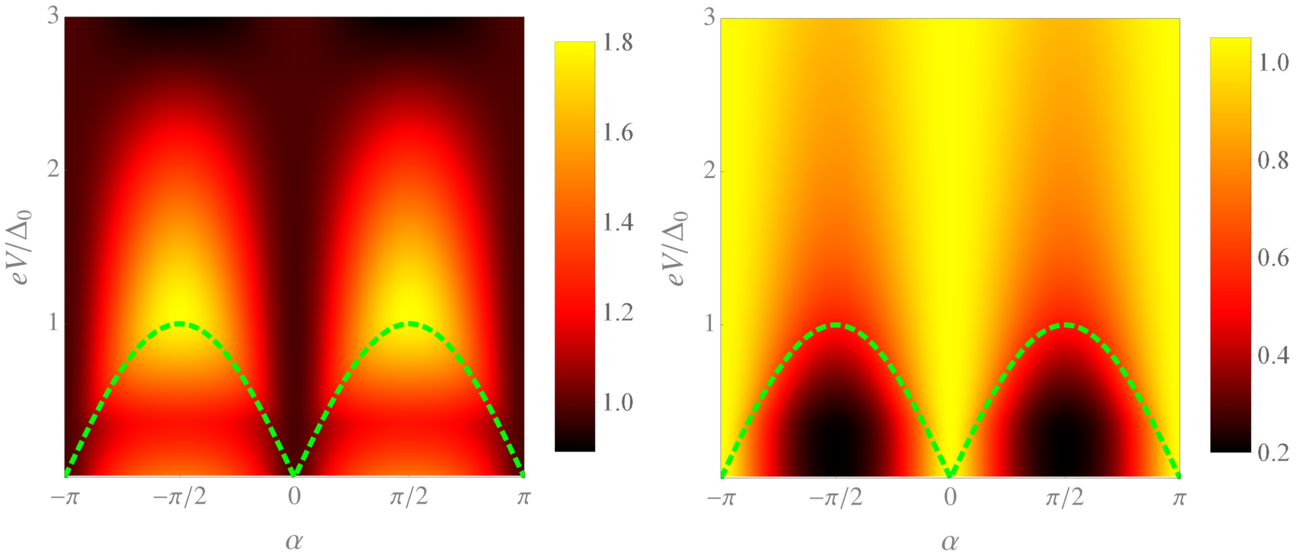

(a) $G^{\pm}_{LL}/G^{0}_{LL}$ **(b)** $G^{\pm}_{LR}/G^{0}_{LR}$

Fig. 3.9: Contour plot of the normalized **(a)** local and **(b)** non-local differential conductance as a function of eV and α. The green, dashed line represents the angular dependency of the effective superconducting gap $\tilde{\Delta}_0$. We choose $\mu_S = 10^6\,\Delta_0$, $\mu_N = 10^3\,\Delta_0$, $\chi = 0$ and $L = \xi$. *Reprinted figure with permission from [120]. Copyright (2021) by the American Physical Society.*

CCP dependence of the differential conductance

The dependence of the transport properties on a finite CCP is rather differently. As we have shown in the context of Fig. 3.6, $\chi > 0$ shifts the dispersion at the $(+)$ and $(-)$ node towards opposite energies, which enters the conductance in terms of an energy shift $eV \to eV \pm \chi$. We illustrate this in Fig. 3.10,

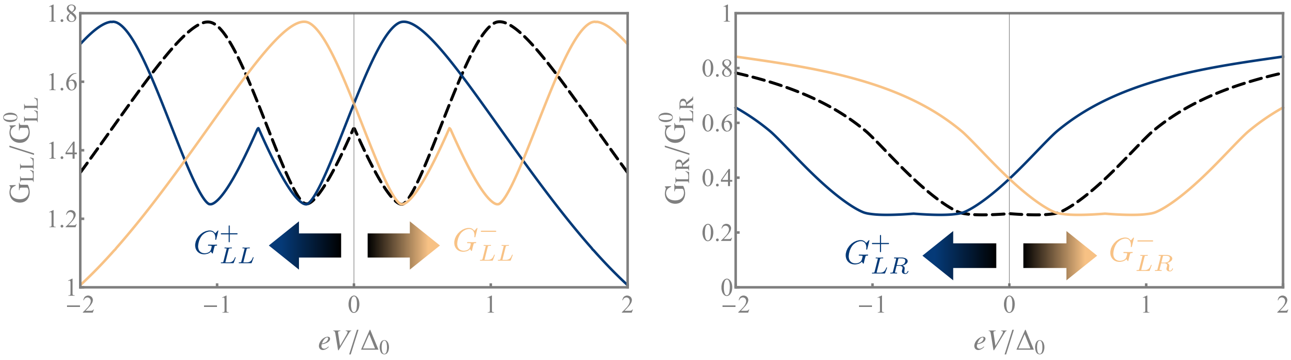

(a) Local conductance **(b)** Non-local conductance

Fig. 3.10: **(a)** Local and **(b)** non-local conductance as a function of eV for a finite and positive CCP $\chi = 0.7\,\Delta_0$. The conductances derived from $\mathcal{H}^+$ and $\mathcal{H}^-$, $G^+_{LL/LR}$ (blue curve) and $G^-_{LL/LR}$ (orange curve) are shifted oppositely along the eV-axis and relatively to the conductance for a system with no CCP (black, dashed curve). We choose $\mu_S = 10^6\,\Delta_0$, $\mu_N = 10^3\,\Delta_0$, $\alpha = \pi/2$ and $L = \xi$. *Reprinted figure with permission from [120]. Copyright (2021) by the American Physical Society.*

where we additionally consider hole excitations at negative biases and set $\alpha = \pi/2$, i.e., $\tilde{\Delta}_0 = \Delta_0$. Due to the intrinsic BdG particle-hole symmetry, we have

$$G^{\pm}_{LL/LR}(eV) = G^{\pm}_{LL/LR}(-eV) \tag{3.61}$$

when no CCP is present. This symmetry is broken when χ is finite, see the blue and orange curves. Then, $G^+_{LL/LR}$ is shifted to negative and $G^-_{LL/LR}$ to positive energies. Additionally, the symmetry in Eq. (3.61) is no longer given if we consider one node only, since the symmetry axis is shifted. Instead, we now have

$$G^+_{LL/LR}(eV - \chi) = G^+_{LL/LR}(-eV - \chi), \qquad G^-_{LL/LR}(eV + \chi) = G^-_{LL/LR}(-eV + \chi), \tag{3.62}$$

or, more generally,

$$G^+_{LL/LR}(eV) = G^-_{LL/LR}(-eV), \tag{3.63}$$

as can be seen in Fig. 3.10. This is clear since CCP does not affect the conductance qualitatively, except for the opposite shift in the bias at different nodes.

It is, however, surprising that the BdG particle-hole symmetry appears to be broken, as indicated by Eq. (3.62), which should not be possible in the BdG framework. We can resolve this by reminding ourselves that $\mathcal{H}^{\pm}$ are merely blocks of the total Hamiltonian $\mathcal{H}_{\text{BdG}}$ in Eq. (3.20), and not independent BdG Hamiltonians. The contribution from both Weyl nodes to the total conductances is plotted in Fig. 3.11 for a vanishing (black dashed curve) and a finite, positive (red, solid curve) CCP. We therefore introduce the full local and non-local differential conductance as

$$G^{\Sigma}_{LL}(eV) \equiv G^+_{LL}(eV) + G^-_{LL}(eV), \tag{3.64a}$$
$$G^{\Sigma}_{LR}(eV) \equiv G^+_{LR}(eV) + G^-_{LR}(eV), \tag{3.64b}$$

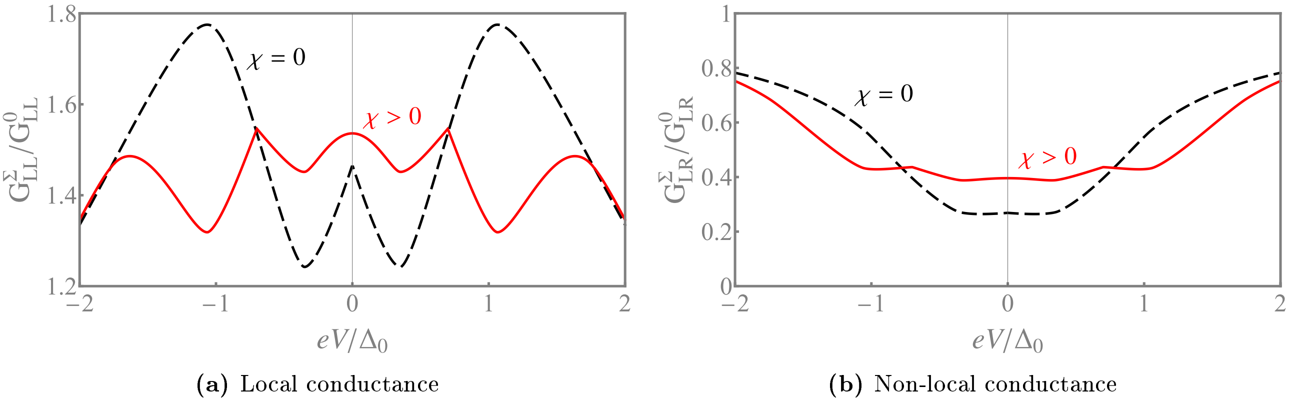

(a) Local conductance **(b)** Non-local conductance

Fig. 3.11: Full **(a)** local and **(b)** non-local conductance as a function of eV for a finite and positive CCP $\chi = 0.7\,\Delta_0$. Considering the contributions from both Weyl nodes, this restores the axial symmetry around $eV = 0$. We choose $\mu_S = 10^6\,\Delta_0$, $\mu_N = 10^3\,\Delta_0$, $\alpha = \pi/2$ and $L = \xi$. *Reprinted figure with permission from [120]. Copyright (2021) by the American Physical Society.*

The full differential conductance $G^{\Sigma}_{LL/LR}$ does not deviate from $G^{\pm}_{LL/LR}$ for $\chi = 0$[2], while for $\chi > 0$, the intrinsic BdG particle-hole symmetry is restored,

$$G^{\Sigma}_{LL/LR}(eV) = G^{\Sigma}_{LL/LR}(-eV), \tag{3.65}$$

which can directly be seen from Eqs. (3.62) and (3.63). Furthermore, we find that a finite CCP increases the oscillations in G^{Σ}_{LL} , while it flattens the valley in G^{Σ}_{LR} even more (both compared to $\chi = 0$). At large biases $|eV| \gg \chi$, the full conductance approaches its value without CCP.

Finally, we consider the dependence of the full zero-bias conductance on the CCP in Fig. 3.12. Apparently, the curves are identical to the bias-dependent plots without CCP in Fig. 3.11. In fact, the expressions in Eqs. (3.61) to (3.64) allow us to identify the relation

$$G^{\Sigma}_{LL/LR}(eV = 0, \chi) = G^{\Sigma}_{LL/LR}(eV, \chi = 0), \tag{3.66}$$

i.e., the CCP-dependence of the conductance at zero bias is equal to the bias-dependence of the conductance at a vanishing CCP. As a consequence, CCP leads to the same local and non-local differential

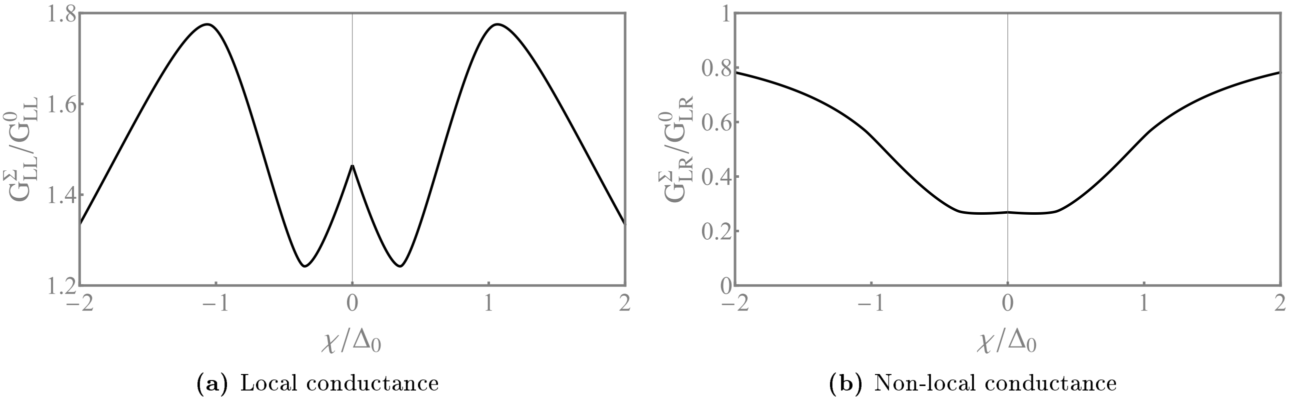

(a) Local conductance **(b)** Non-local conductance

Fig. 3.12: Full **(a)** local and **(b)** non-local conductance as a function of χ at $eV = 0$. The curves are equivalent to those in Fig. 3.11 for $\chi = 0$. We choose $\mu_S = 10^6\,\Delta_0$, $\mu_N = 10^3\,\Delta_0$, $\alpha = \pi/2$ and $L = \xi$. *Reprinted figure with permission from [120]. Copyright (2021) by the American Physical Society.*

---

[2] Note that here, even though we add both contributions together, the quantitative results are equal. This is due to the normalization, since the normal-state conductances are added up as well.

conductances when no bias is applied, as we find it in a system with no CCP and a finite eV. The application of a uniform, parallel electromagnetic field or a strain deformation can therefore be used to control the transport in the junction since CCP plays a similar role as the bias. Note that a finite, negative χ shifts $G^{\pm}$ oppositely in the examples and figures above, but has no effect on G^{Σ}.

With this, we conclude our analysis of the transport characteristics in the Weyl NSN junction and next address the proximity effect.

3.4.2 Pairing amplitudes

Anomalous Green function

In order to obtain the pairing amplitudes based on which we study the proximity effect, we first need to derive the anomalous Green function according to the Scattering State Approach introduced in Sec. 3.2.2. The scattering states in Eqs. (3.49) and (3.53) are labeled in accordance with those in Fig. 3.2, such that the ansatz in Eq. (3.10) is directly applicable. The Green function for the NSN-junction thus reads (note that we drop the superscript ± on the right-hand side of this expression for the sake of clarity. All coefficients and scattering states are understood to include this index.)

$$\mathcal{G}^{\pm}(z,z') = \begin{cases} \alpha_1\phi_3(z)\tilde{\phi}_1^T(z') + \alpha_2\phi_3(z)\tilde{\phi}_2^T(z') + \alpha_3\phi_4(z)\tilde{\phi}_1^T(z') + \alpha_4\phi_4(z)\tilde{\phi}_2^T(z'), & z < z' \\ \\ \beta_1\phi_1(z)\tilde{\phi}_3^T(z') + \beta_2\phi_1(z)\tilde{\phi}_4^T(z') + \beta_3\phi_2(z)\tilde{\phi}_3^T(z') + \beta_4\phi_2(z)\tilde{\phi}_4^T(z'), & z > z' \end{cases}, \tag{3.67}$$

and we obtain the coefficients $\alpha_l^{\pm}$ and $\beta_l^{\pm}$ according to Eq. (3.11), which evaluates to

$$\mathcal{G}^{\pm}(z,z')\big|_{z=z'+0^+} - \mathcal{G}^{\pm}(z,z')\big|_{z=z'-0^+} = -i\tau_3\sigma_3, \tag{3.68}$$

for the Hamiltonians in Eq. (3.34). Since the latter are linear in k_z, the discontinuity appears in the Green functions themselves.

In order to simplify the expression obtained from Eq. (3.67), it is convenient to replace the transposed scattering coefficients by means of their normal counterparts. As introduced in Sec. 3.2.3, the Wronskian method is a practical formalism to achieve this. We can convince ourselves that the transposed and the normal Hamiltonians are related by the transformation

$$\sigma_x \left[\mathcal{H}^{\pm}(\alpha)\right]^T \sigma_x = \mathcal{H}^{\pm}(-\alpha), \tag{3.69}$$

such that the transformed scattering states $\sigma_x\tilde{\phi}_l^{\pm}(z)|_{\alpha\to-\alpha}$ are eigenstates of the original Hamiltonians $\mathcal{H}^{\pm}$ as well. Therefore, we can construct the Wronskian determinant for all possible combinations of (each four) of the transposed and normal scattering states and demand its identity when evaluated in the domains $z < z_L$ and $z > z_R$. This yields 70 equations from which we can determine the transposed scattering coefficients, and we obtain

$$\tilde{a}_l^{\pm}(\alpha) = -a_l^{\pm}(-\alpha), \quad \tilde{b}_l^{\pm}(\alpha) = b_l^{\pm}(-\alpha), \quad \tilde{c}_l^{\pm}(\alpha) = c_l^{\pm}(-\alpha), \quad \tilde{d}_l^{\pm}(\alpha) = -d_l^{\pm}(-\alpha), \quad \forall_l. \tag{3.70}$$

At this point, we relate the transposed scattering coefficients at an angle α to the corresponding normal scattering coefficients at an angle $-\alpha$. We can resolve this by the fact that the coefficients related to AR and CAR are directly proportional to the effective order parameter,

$$a_l^{\pm} \propto \Delta_0 \sin\alpha, \qquad d_l^{\pm} \propto \Delta_0 \sin\alpha, \tag{3.71}$$

while $\tilde{\Delta}_0$ enters the coefficients solely in second order elsewise. The coefficients related to NR and CO do not feature such a direct proportionality, but only second order entries of the effective gap. As a consequence, we have

$$a_l^{\pm}(-\alpha) = -a_l^{\pm}(\alpha), \quad b_l^{\pm}(-\alpha) = b_l^{\pm}(\alpha), \quad c_l^{\pm}(-\alpha) = c_l^{\pm}(\alpha), \quad d_l^{\pm}(-\alpha) = -d_l^{\pm}(\alpha), \quad \forall_l, \tag{3.72}$$

and Eq. (3.70) reduces to

$$\tilde{a}_l^{\pm} = a_l^{\pm}, \qquad \tilde{b}_l^{\pm} = b_l^{\pm}, \qquad \tilde{c}_l^{\pm} = c_l^{\pm}, \qquad \tilde{d}_l^{\pm} = d_l^{\pm}, \qquad \forall_l, \tag{3.73}$$

i.e., the transposed and normal scattering coefficients are equal. With this, we obtain the Green function coefficients as

$$\alpha_1^{\pm} = -\frac{i}{2J_e^{\pm}k_e^{\pm}}\frac{c_4^{\pm}}{c_3^{\pm}c_4^{\pm} - d_3^{\pm}d_4^{\pm}} = \beta_1^{\pm}, \tag{3.74a}$$

$$\alpha_2^{\pm} = \frac{i}{2J_h^{\pm}k_h^{\pm}}\frac{d_4^{\pm}}{c_3^{\pm}c_4^{\pm} - d_3^{\pm}d_4^{\pm}} = \beta_2^{\pm}, \tag{3.74b}$$

$$\alpha_3^{\pm} = \frac{i}{2J_e^{\pm}k_e^{\pm}}\frac{d_3^{\pm}}{c_3^{\pm}c_4^{\pm} - d_3^{\pm}d_4^{\pm}} = \beta_3^{\pm}, \tag{3.74c}$$

$$\alpha_4^{\pm} = -\frac{i}{2J_h^{\pm}k_h^{\pm}}\frac{c_3^{\pm}}{c_3^{\pm}c_4^{\pm} - d_3^{\pm}d_4^{\pm}} = \beta_4^{\pm}. \tag{3.74d}$$

Note that, if we plug Eq. (3.74) into (3.68), not all equations automatically evaluate to be true (the system is overdetermined). Instead, we obtain an additional set of relations which are required such that Eq. (3.68) is satisfied, namely

$$a_2^{\pm} = \frac{J_h^{\pm}k_h^{\pm}}{J_e^{\pm}k_e^{\pm}}a_1^{\pm}, \qquad a_4^{\pm} = \frac{J_h^{\pm}k_h^{\pm}}{J_e^{\pm}k_e^{\pm}}a_3^{\pm}. \tag{3.75}$$

Those are usually denoted by *detailed balance relations* [119] and are related to the intrinsic BdG particle-hole symmetry.

Since the full expression of the Green function is rather extensive, and since we are primarily interested in the anomalous part, we do not give $\mathcal{G}^{\pm}(z,z')$ explicitly here, but restrict ourselves to the expressions of the pairing amplitudes. First, however, we need to reverse the unitary transformation applied to $\mathcal{H}^{\pm}$, *cf.* Eq. (3.32), such that we work in the correct basis (else, the assignment of the spin would be ill defined),

$$\mathcal{G}^{\pm}(z,z') \to (\hat{\mathrm{U}}_{\alpha}^{\pm})^{-1}\mathcal{G}^{\pm}(z,z')\hat{\mathrm{U}}_{\alpha}^{\pm}. \tag{3.76}$$

We are now able to extract the pairing amplitudes according to the decomposition

$$\mathcal{F}(z,z') = f_0(z,z')\sigma_0 + f_{\uparrow\uparrow}(z,z')\frac{\sigma_x + i\sigma_y}{2} + f_{\downarrow\downarrow}(z,z')\frac{\sigma_x - i\sigma_y}{2} + f_z(z,z')\sigma_z, \tag{3.77}$$

which is based on Eq. (3.4). In this chapter, we are interested in the local amplitudes, where $z = z'$, such that all quantities depend on one spatial variable only in the following. Moreover, the energy is – in agreement with the usual convention – expressed in terms of the frequency ω, and θ_k is given as an argument to explicitly distinguish single-mode amplitudes from the full ones (introduced later in this chapter). With this, the pairing amplitudes for the NSN-junction and the Hamiltonian $\mathcal{H}^{+}$ are given by

$$f_0^{+}(\theta_k, z) = \frac{i a_1^{+}}{4J_e^{+}k_e^{+}}\left[\left(J_e^{+}J_h^{+} + k_{||}^2 e^{2i\theta_k}\right)\sin\alpha - \left(J_e^{+} - J_h^{+}\right)k_{||}e^{i\theta_k}\cos\alpha\right]e^{-i\left(k_e^{+}+k_h^{+}\right)z}, \tag{3.78a}$$

$$f_{\uparrow\uparrow}^{+}(\boldsymbol{k}_{||}, z) = -\frac{iJ_h^{+}a_1^{+}}{4J_e^{+}k_e^{+}}\left(k_{||}e^{i\theta_k}\sin\alpha - J_e^{+}\cos\alpha\right)e^{-i\left(k_e^{+}+k_h^{+}\right)z}, \tag{3.78b}$$

$$f_{\downarrow\downarrow}^{+}(\boldsymbol{k}_{||}, z) = -\frac{ik_{||}e^{i\theta_k}a_1^{+}}{4J_e^{+}k_e^{+}}\left(J_e^{+}\sin\alpha + k_{||}e^{i\theta_k}\cos\alpha\right)e^{-i\left(k_e^{+}+k_h^{+}\right)z}, \tag{3.78c}$$

$$f_z^{+}(\boldsymbol{k}_{||}, z) = -\frac{i a_1^{+}}{4J_e^{+}k_e^{+}}\left[\left(J_e^{+}J_h^{+} - k_{||}^2 e^{2i\theta_k}\right)\sin\alpha + \left(J_e^{+} + J_h^{+}\right)k_{||}e^{i\theta_k}\cos\alpha\right]e^{-i\left(k_e^{+}+k_h^{+}\right)z}, \tag{3.78d}$$

if $z \leq z_L$ (i.e., the left lead), and

$$f_0^+(\boldsymbol{k}_{||}, z) = \frac{ia_3^+}{4J_e^+ k_e^+}\left[\left(J_e^+ J_h^+ + k_{||}^2 e^{-2i\theta_k}\right)\sin\alpha + \left(J_e^+ - J_h^+\right) k_{||} e^{-i\theta_k}\cos\alpha\right] e^{i\left(k_e^+ + k_h^+\right)z}, \tag{3.79a}$$

$$f_{\uparrow\uparrow}^+(\boldsymbol{k}_{||}, z) = -\frac{ik_{||}e^{-i\theta_k} a_3^+}{4J_e^+ k_e^+}\left(J_e^+ \sin\alpha - k_{||} e^{-i\theta_k}\cos\alpha\right) e^{i\left(k_e^+ + k_h^+\right)z}, \tag{3.79b}$$

$$f_{\downarrow\downarrow}^+(\boldsymbol{k}_{||}, z) = -\frac{iJ_h^+ a_3^+}{4J_e^+ k_e^+}\left(k_{||}e^{-i\theta_k} \sin\alpha + J_e^+\cos\alpha\right) e^{i\left(k_e^+ + k_h^+\right)z}, \tag{3.79c}$$

$$f_z^+(\boldsymbol{k}_{||}, z) = \frac{ia_3^+}{4J_e^+ k_e^+}\left[\left(J_e^+ J_h^+ - k_{||}^2 e^{-2i\theta_k}\right)\sin\alpha - \left(J_e^+ + J_h^+\right) k_{||} e^{-i\theta_k}\cos\alpha\right] e^{i\left(k_e^+ + k_h^+\right)z}, \tag{3.79d}$$

if $z \geq z_R$ (i.e., the right lead). For the Hamiltonian describing the other node $\mathcal{H}^-$, they are

$$f_0^-(\boldsymbol{k}_{||}, z) = \frac{ia_1^-}{4J_e^- k_e^-}\left[\left(J_e^- J_h^- + k_{||}^2 e^{-2i\theta_k}\right)\sin\alpha - \left(J_e^- J_h^-\right) k_{||} e^{-i\theta_k}\cos\alpha\right] e^{-i\left(k_e^- + k_h^-\right)z}, \tag{3.80a}$$

$$f_{\uparrow\uparrow}^-(\boldsymbol{k}_{||}, z) = \frac{ik_{||}e^{-i\theta_k} a_1^-}{4J_e^- k_e^-}\left(J_h^- \sin\alpha - k_{||} e^{-i\theta_k}\cos\alpha\right) e^{-i\left(k_e^- + k_h^-\right)z}, \tag{3.80b}$$

$$f_{\downarrow\downarrow}^-(\boldsymbol{k}_{||}, z) = \frac{ia_1^-}{4k_e^-}\left(k_{||}e^{-i\theta_k} \sin\alpha + J_h^-\cos\alpha\right) e^{-i\left(k_e^- + k_h^-\right)z}, \tag{3.80c}$$

$$f_z^-(\boldsymbol{k}_{||}, z) = -\frac{ia_1^-}{4J_e^- k_e^-}\left[\left(J_e^- J_h^- k_{||}^2 e^{-2i\theta_k}\right)\sin\alpha - \left(J_e^- + J_h^-\right) k_{||} e^{-i\theta_k}\cos\alpha\right] e^{-i\left(k_e^- + k_h^-\right)z}, \tag{3.80d}$$

if $z \leq z_L$ (i.e., the left lead), and

$$f_0^-(\boldsymbol{k}_{||}, z) = \frac{ia_3^-}{4J_e^- k_e^-}\left[\left(J_e^- J_h^- + k_{||}^2 e^{2i\theta_k}\right)\sin\alpha + \left(J_e^- J_h^-\right) k_{||} e^{i\theta_k}\cos\alpha\right] e^{i\left(k_e^- + k_h^-\right)z}, \tag{3.81a}$$

$$f_{\uparrow\uparrow}^-(\boldsymbol{k}_{||}, z) = \frac{ia_3^-}{4k_e^-}\left(k_{||}e^{i\theta_k} \sin\alpha - J_h^-\cos\alpha\right) e^{i\left(k_e^- + k_h^-\right)z}, \tag{3.81b}$$

$$f_{\downarrow\downarrow}^-(\boldsymbol{k}_{||}, z) = \frac{ik_{||}e^{i\theta_k} a_3^-}{4J_e^- k_e^-}\left(J_h^- \sin\alpha + k_{||} e^{i\theta_k}\cos\alpha\right) e^{i\left(k_e^- + k_h^-\right)z}, \tag{3.81c}$$

$$f_z^-(\boldsymbol{k}_{||}, z) = \frac{ia_3^-}{4J_e^- k_e^-}\left[\left(J_e^- J_h^- k_{||}^2 e^{2i\theta_k}\right)\sin\alpha + \left(J_e^- + J_h^-\right) k_{||} e^{i\theta_k}\cos\alpha\right] e^{i\left(k_e^- + k_h^-\right)z}, \tag{3.81d}$$

if $z \geq z_R$ (i.e., the right lead). Note that all amplitudes are proportional to the scattering coefficient related to AR, which illustrates that the proximity effect is mediated by Andreev reflections in the junction. Interestingly, it is possible to relate the amplitudes of the same Hamiltonian, but in different domains to each other. Considering the relation between the Andreev reflection coefficients,

$$a_3^{\pm}(\theta_k, \alpha) = -a_1^{\pm}(-\theta_k, -\alpha), \qquad a_4^{\pm}(\theta_k, \alpha) = -a_2^{\pm}(-\theta_k, -\alpha) \tag{3.82}$$

we find for $|z| \geq L_s/2$

$$f_0^{\pm}(\theta_k, \alpha, z) = f_0^{\pm}(-\theta_k, -\alpha, -z), \tag{3.83a}$$

$$f_{\uparrow\uparrow}^{\pm}(\theta_k, \alpha, z) = f_{\downarrow\downarrow}^{\pm}(-\theta_k, -\alpha, -z), \tag{3.83b}$$

$$f_z^{\pm}(\theta_k, \alpha, z) = -f_z^{\pm}(-\theta_k, -\alpha, -z). \tag{3.83c}$$

This means that every amplitude at any position $z = -|z_0| \leq z_L$ in the left lead corresponds to its spin-flipped counterpart in the right lead at $z = |z_0| \geq z_L$, with opposite angles α and θ_k. Eqs. (3.82) and (3.83) are the consequence of a symmetry of the Hamiltonians $\mathcal{H}^{\pm}$ given by

$$\sigma_x H^{\pm}(\theta_k, \alpha, k_z)\sigma_x = -H^{\pm}(-\theta_k, -\alpha, -k_z). \tag{3.84}$$

This is related to the spin-momentum coupling in the WSM and shows that the Hamiltonians are invariant (up to a sign) under a spin-flip and simultaneous inversion of the momentum $(k_x, k_y, k_z)^T$ and angle α. We do not expect that the scattering state ϕ_1, *cf.* Fig. 3.2(a), yields different observables than ϕ_3, *cf.* Fig. 3.2(c), due to the spatial parity of the junction (rotating the junction by π in real space transfers one scattering state into the other, with inverted angle α as well as momentum, and thus spin).

To follow the proceeding in the previous section, we consider the contribution from all modes indexed by $\boldsymbol{k}_{||}$, instead of single modes, and focus furthermore on the modulus of the quantities. We thus introduce the full pairing amplitudes as

$$f_s^{\pm}(z) \equiv \left| \sum_{\boldsymbol{k}_{||}} f_s^{\pm}(\boldsymbol{k}_{||}, z) \right|, \qquad s \in \{0, \uparrow\uparrow, \downarrow\downarrow, z\}. \tag{3.85}$$

In the continuum limit, we replace the sum by an integral, *cf.* Eq. (3.55). As a normalization factor, we introduce the quantity f_0^0, which is the singlet amplitude at the interfaces ($z = z_L$ or $z = z_R$) at zero energy and an angle of $\pi/2$,

$$f^0 \equiv f_0^{\pm}(z = z_{L/R})\big|_{\omega=0}^{\alpha=\pi/2}. \tag{3.86}$$

We evaluate the pairing amplitudes numerically and discuss the results in the following.

Angular dependence of the pairing amplitudes

Assuming no CCP in the junction, $\chi = 0$, we first consider the frequency dependence of the pairing amplitudes at a fixed angle α between the axis separating the Weyl nodes and the interface normal.

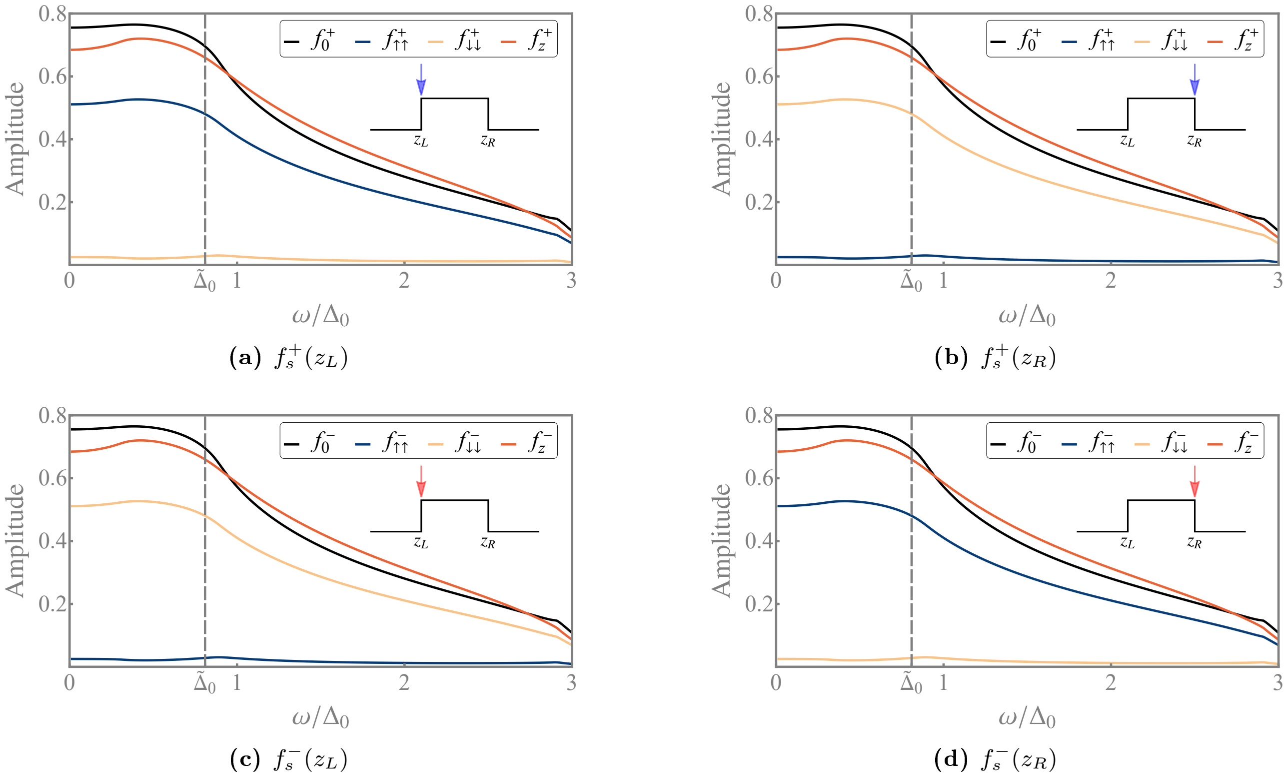

(a) $f_s^+(z_L)$ **(b)** $f_s^+(z_R)$

(c) $f_s^-(z_L)$ **(d)** $f_s^-(z_R)$

Fig. 3.13: Frequency-dependence of the pairing amplitudes for **(a,b)** $\mathcal{H}^+$ and **(c,d)** $\mathcal{H}^-$ at the **(a,c)** left ($z = z_L$) and the **(b,d)** right ($z = z_R$) interface. The gray, dashed line indicates the effective order parameter $\tilde{\Delta}_0$. We choose $\mu_S = 10^6\,\Delta_0$, $\mu_N = 10^3\,\Delta_0$, $\chi = 0$, $\alpha = \pi/3$ and $L = \xi$.

The results are shown in Fig. 3.13, where we choose $\alpha = \pi/3$. Note that, for clarity, some of the following figures include an inset which illustrates where in the junction and for which Hamiltonian we evaluate the amplitudes, indicated by an arrow (blue arrow: $\mathcal{H}^+$, red arrow: $\mathcal{H}^-$, black arrow: position only).

At subgap energies, all amplitudes show a rather flat dependence on ω and vary weakly, while they quickly decay for $\omega > \tilde{\Delta}_0$. This is reasonable since the probability for Andreev reflection, to which these amplitudes are related, decreases for energies larger than the effective order parameter as well. Note that the singlet and the opposite-spin triplet amplitude, $f_0^+(z)$ and $f_z^+(z)$, are quantitatively and qualitatively comparable. Moreover, their behavior does not change considering different positions or nodes. The symmetries of the equal-spin pairing amplitudes, $f_{\uparrow\uparrow}^+(z)$ and $f_{\downarrow\downarrow}^+(z)$, indicated in Eq. (3.83) can be observed as well,

$$f_{\uparrow\uparrow}^{\pm}(z_L) = f_{\downarrow\downarrow}^{\pm}(z_R), \qquad\qquad f_{\downarrow\downarrow}^{\pm}(z_L) = f_{\uparrow\uparrow}^{\pm}(z_R). \tag{3.87}$$

Note that, for $\mathcal{H}^+$ and the left interface, $z = z_L$, the spin-up amplitude $f_{\uparrow\uparrow}^{\pm}(z_L)$ is comparable in its magnitude to $f_0^+(z)$ and $f_z^+(z)$, while $f_{\downarrow\downarrow}^{\pm}(z_L)$ nearly vanishes. At the right interface, $z = z_L$, it is exactly vise versa. The same holds for $\mathcal{H}^-$, only that the spin directions are exchanged at the interfaces. Intriguingly, we find that the equal-spin amplitudes of $\mathcal{H}^+$ at each interface corresponds to their spin-flipped counterparts of $\mathcal{H}^-$,

$$f_{\uparrow\uparrow}^{\pm}(z_L) = f_{\downarrow\downarrow}^{\mp}(z_L), \qquad\qquad f_{\downarrow\downarrow}^{\pm}(z_R) = f_{\uparrow\uparrow}^{\mp}(z_R). \tag{3.88}$$

Upon further consideration, this observation is, however, reasonable. Since the two equal-spin amplitudes of the same Hamiltonian differ significantly in their magnitudes, this would lead to a spin polarization of the Cooper pairs (which is related to the pairing amplitudes) in the WSM leads. We do not expect this in the absence of, e.g., an electromagnetic field, such that the equal amplitudes of

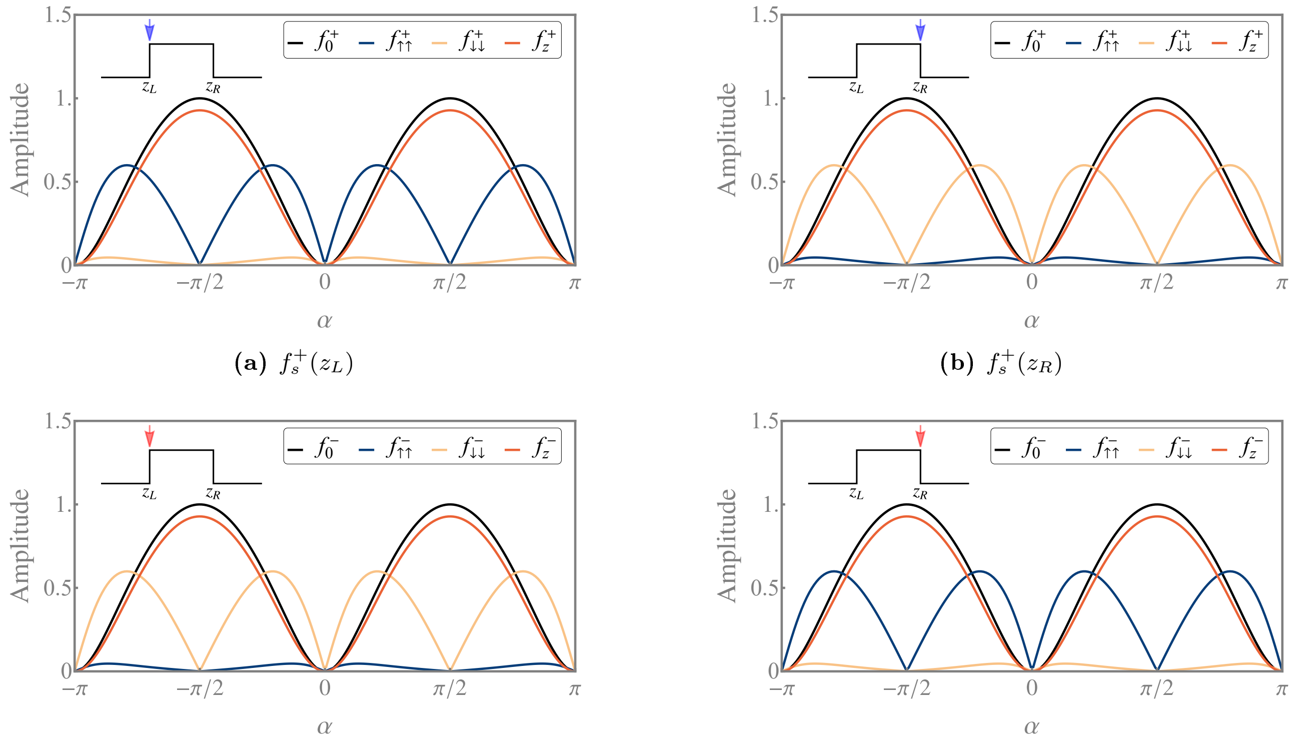

(a) $f_s^+(z_L)$

(b) $f_s^+(z_R)$

(c) $f_s^-(z_L)$

(d) $f_s^-(z_R)$

Fig. 3.14: Angular dependence of the pairing amplitudes for **(a,b)** $\mathcal{H}^+$ and **(c,d)** $\mathcal{H}^-$ at the **(a,c)** left ($z = z_L$) and the **(b,d)** right ($z = z_R$) interface. We choose $\mu_S = 10^6\,\Delta_0$, $\mu_N = 10^3\,\Delta_0$, $\chi = 0$, $\omega = 0$ and $L = \xi$.

opposite spin from the other Hamiltonian compensate this polarization. As we will see, this can be lifted if a CCP is present.

Next, we consider the angular dependence of the amplitudes for a fixed frequency ω in Fig. 3.14. Here, we observe the same dependencies of the amplitudes at different interfaces and nodes as indicated in Eqs. (3.87) and (3.88), which is to be expected. Furthermore, we see the same effects of the effective gap $\tilde{\Delta}_0$ in the pairing amplitudes as we did for the differential conductance. At $\alpha = 0$ and $\alpha = \pm\pi$, the effective order parameter vanishes, as does the proximity effect in the WSM leads. The singlet and opposite-spin triplet equally feature maxima at $\alpha = \pm\pi/2$, where $\tilde{\Delta}_0$ is maximal. The equal-spin triplet amplitudes, however, vanish at these angles. To understand this behavior, we need to consider the single-mode amplitudes $f^{+}_{\uparrow\uparrow}(\boldsymbol{k}_{||}, z)$ and $f^{+}_{\downarrow\downarrow}(\boldsymbol{k}_{||}, z)$ and their dependence on θ_k. We illustrate this in Fig. 3.15, where we plot the real and imaginary parts of $f^{+}_{\uparrow\uparrow}(\boldsymbol{k}_{||}, z)$ as a function of the angle of incidence and for a fixed $k_{||}$. When $\alpha \notin \{0, \pm\pi/2, \pm\pi\}$, then we obtain the polar plot in Fig. 3.15(b). The real and imaginary parts are asymmetric around the axes, such that the integration over all modes yields a finite value. Instead, at $\alpha = \pm\pi/2$, the real and imaginary parts are perfectly symmetric around the real and imaginary axes, respectively, such that the contributions cancel themselves and result in a vanishing full amplitude, see Fig. 3.15(a). The reason behind this observation is that, while the Hamiltonians, in general, do not feature a C_2 symmetry with respect to the $\hat{z}$-axis, this is not true when the axis separating the Weyl nodes includes an angle $\alpha = \pm\pi/2$ with the interface normal, where we have

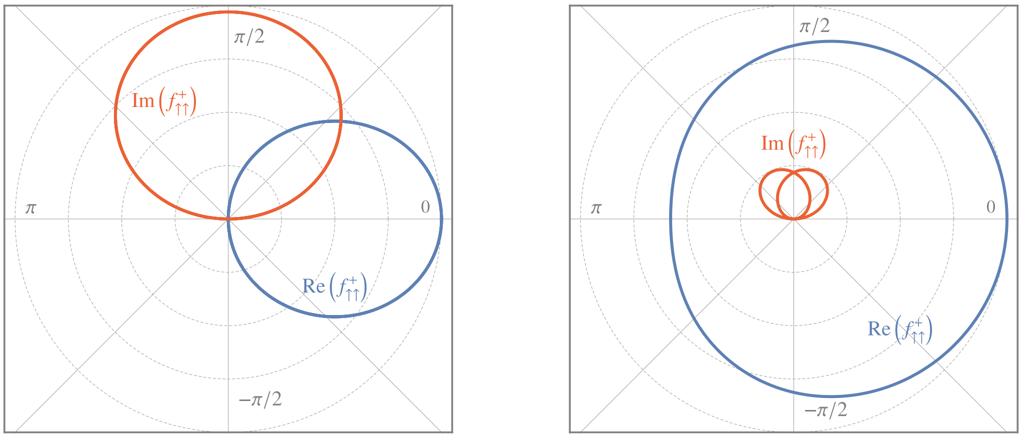

(a) $\alpha = \pi/2$ **(b)** $\alpha = \pi/4$

Fig. 3.15: Dependence of the real and imaginary parts of $f^{+}_{\uparrow\uparrow}(\boldsymbol{k}_{||}, z)$ on the angle of incidence θ_k for a finite $k_{||}$ at **(a)** $\alpha = \pi/2$ and **(b)** $\alpha = \pi/4$. At $\alpha = \pm\pi/2$, the Hamiltonians $\mathcal{H}^{\pm}$ obey a C_2-symmetry, such that the sum of the real and imaginary parts over all modes θ_k vanishes.

$$C_2 \mathcal{H}^{\pm}(k_x, k_y, k_z) C_2^{-1} = \mathcal{H}^{\pm}(-k_x, -k_y, k_z), \qquad C_2 = i\sigma_z. \tag{3.89}$$

Thus, the full equal-spin amplitudes vanish at exactly these angles. Note that the π-periodicity and the symmetry

$$f^{\pm}_{s}(\alpha) = f^{\pm}_{s}(\pi \pm \alpha) \tag{3.90}$$

that we observe in the differential conductance is present in the pairing amplitudes as well.

So far, we have considered the pairing amplitudes directly at the interfaces $z = z_L$ and $z = z_R$. To obtain an intuition of the spatial dependence, we plot the prominent equal-spin triplet amplitudes in each lead ($f^{+}_{\uparrow\uparrow} = f^{-}_{\downarrow\downarrow}$ for $z \leq z_L$ and $f^{-}_{\uparrow\uparrow} = f^{+}_{\downarrow\downarrow}$ for $z \geq z_R$) as a function of z in Fig. 3.16. For finite energies, the amplitudes decays as $|z|$ is increased, such that the proximity effect, mediated by Andreev reflection, is present only over a short distance away from the interfaces, but does not extend to the bulk WSM leads. This is physically reasonable, since we do not expect S order in the asymptotic

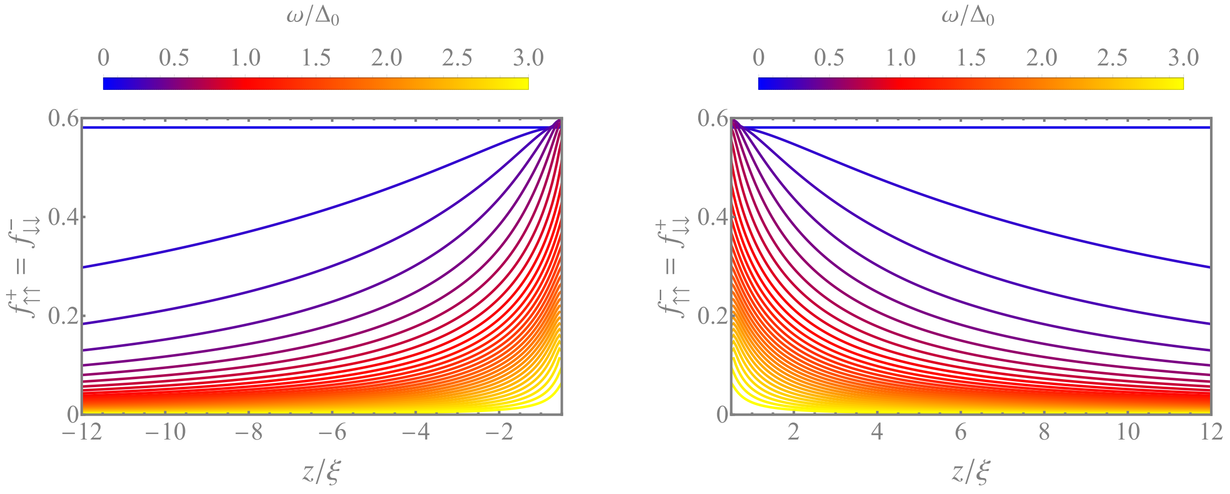

(a) $z \leq z_L$ **(b)** $z \geq z_R$

Fig. 3.16: Spatial dependence of the prominent equal-spin amplitudes in the **(a)** left and **(b)** right WSM lead for different choices of the frequency ω. We choose $\mu_S = 10^6\,\Delta_0$, $\mu_N = 10^3\,\Delta_0$, $\chi = 0$, $\alpha = \pi/4$ and $L = \xi$. *Reprinted figure with permission from [120]. Copyright (2021) by the American Physical Society.*

domains $z \ll z_L$ and $z \gg z_R$ of a material without a superconducting potential. At $\omega = 0$, however, the amplitudes do not decay and extend deep into the bulk, which is due to electron-hole degeneracy at this energy, *cf.* Fig. 3.6(a,d). These features are characteristic for all pairing amplitudes and are encoded in the exponential term

$$f_s^{\pm}(z \leq z_L) \propto e^{-i\left(k_e^{\pm}+k_h^{\pm}\right)z}, \qquad f_s^{\pm}(z \geq z_R) \propto e^{i\left(k_e^{\pm}+k_h^{\pm}\right)z}, \tag{3.91}$$

in Eqs. (3.78) to (3.81), which describes the exponential suppression of $f_s^{\pm}(z)$ in the asymptotic domains. However, from Eqs. (3.43) and (3.44), we see that $k_e^{\pm} = -k_h^{\pm}$ at $\omega = 0$ when no CCP is present, and thus the exponential term evaluates to unity at this frequency. Nonetheless, this is a consequence of the assumption that we work in the thermodynamic limit of zero temperature, $\mathrm{T} = 0\,\mathrm{K}$, such that the amplitudes decay even at $\omega = 0$ [124].

To conclude this section, we show the pairing amplitudes associated with the Hamiltonian $\mathcal{H}^+$ at the left interface $z = z_L$ and as a function of both the frequency ω and the angle between the axis separating the Weyl nodes and the interface normal α in the density plot in Fig. 3.17. We clearly see the decay of $f_s^+(z)$ for energies larger than the effective gap $\tilde{\Delta}_0$, which is due to the reduced probability for AR. Furthermore, the amplitudes show the same π-periodicity and symmetry with respect to α as the transport properties, see Eq. (3.90). f_0^+ and f_z^+ follow the $|\sin\alpha|$ dependence of the effective superconducting gap $\tilde{\Delta}_0$, while $f_{\uparrow\uparrow}^+$ and $f_{\downarrow\downarrow}^+$ feature additional roots at $\alpha = \pm\pi/2$ due to the restoration of a C_2-symmetry, *cf.* Eq. (3.89). The amplitudes at the other interface and/or associated to the Hamiltonian $\mathcal{H}^-$ are indicated by Fig. 3.17 as well, considering the relations in Eqs. (3.83), (3.87) and (3.88).

CCP dependence of the pairing amplitudes

Fig. 3.16 indicates that the farther away from the interfaces the amplitudes are considered, the stronger they decay with the frequency ω. This is illustrated by the black dashed lines in Fig. 3.18, which show the expected peak-like behavior around $\omega = 0$ at $z = -5\,\xi$. As we have mentioned before, $f_{\uparrow\uparrow}^+$ and $f_{\downarrow\downarrow}^-$ ($f_{\downarrow\downarrow}^+$ and $f_{\uparrow\uparrow}^-$) are equal in the left (right) domain, and no spin-polarization occurs. This scenario changes if we introduce CCP to the system. As it is the case for the differential conductance associated to $\mathcal{H}^+$ and $\mathcal{H}^-$, the pairing amplitudes remain quantitatively and qualitatively the same, except that they are shifted oppositely in the frequency, $\omega \to \omega \pm \chi$, see the colored curves in Fig. 3.18. For a

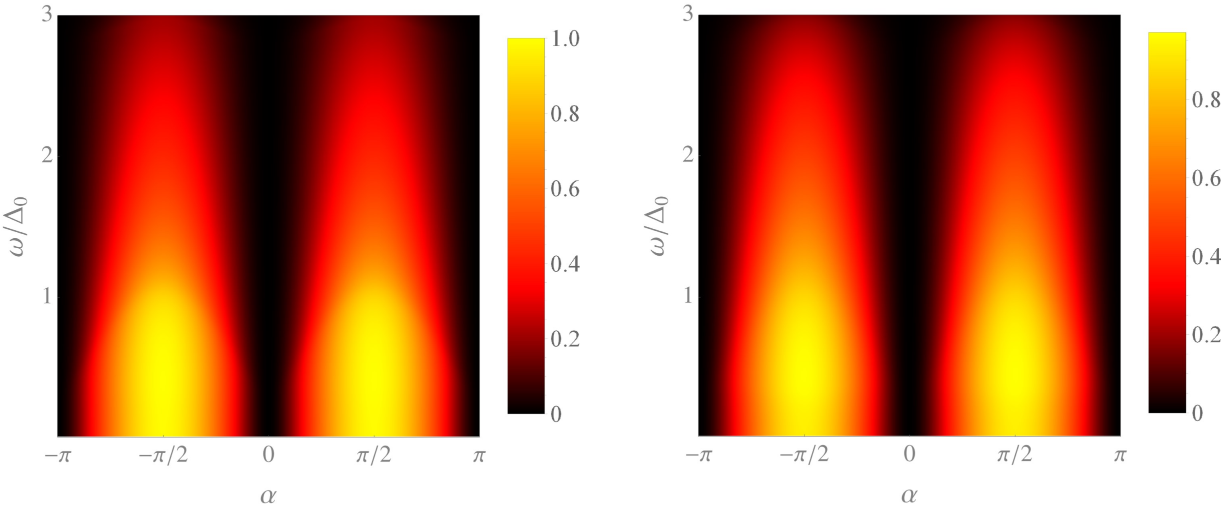

(a) $f_0^+(z_L)$ **(b)** $f_z^+(z_L)$

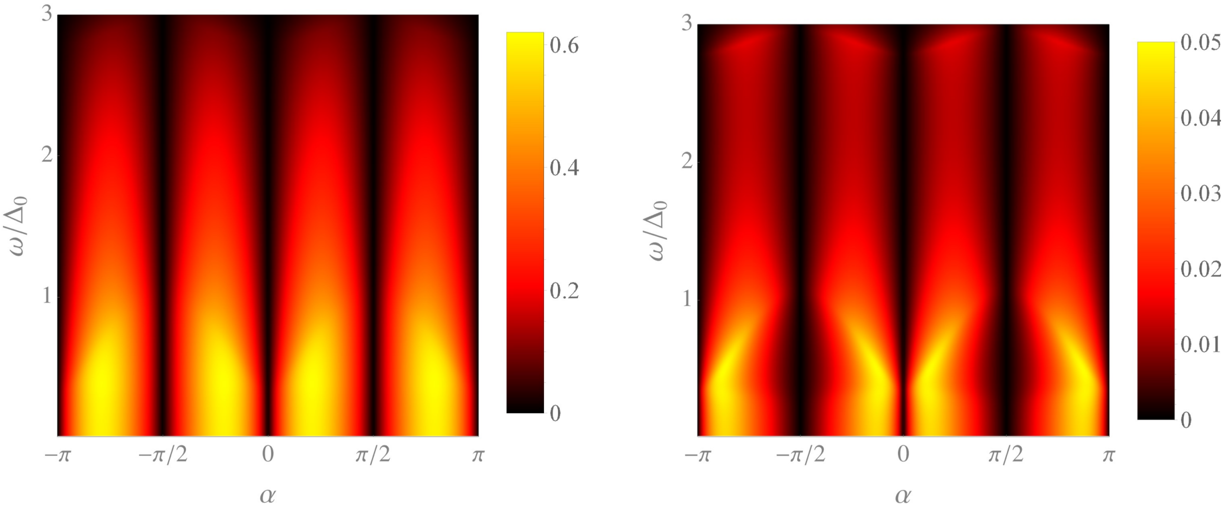

(c) $f_{\uparrow\uparrow}^+(z_L)$ **(d)** $f_{\downarrow\downarrow}^+(z_L)$

Fig. 3.17: Density plot of the amplitudes $f_s^+(z_L)$ at the left interface as a function of ω and α. We choose $\mu_S = 10^6\,\Delta_0$, $\mu_N = 10^3\,\Delta_0$, $\chi = 0$ and $L = \xi$. *Reprinted figure with permission from [120]. Copyright (2021) by the American Physical Society.*

positive χ, the peaks of $f_{\uparrow\uparrow}^+$ and $f_{\downarrow\downarrow}^+$ are now located at $\omega = -\chi$, while it is $\omega = \chi$ for $f_{\uparrow\uparrow}^-$ and $f_{\downarrow\downarrow}^-$. This has an interesting consequence. Since $f_{\downarrow\downarrow}^+(z < z_L)$ and $f_{\uparrow\uparrow}^-(z > z_R)$ as well as $f_{\uparrow\uparrow}^-(z < z_L)$ and $f_{\downarrow\downarrow}^+(z > z_R)$ remain negligible, a finite CCP means that the equal-spin amplitudes associated with one Weyl node are no longer compensated by their counterparts associated to the opposite node. This indicates a possible Cooper pair spin-polarization in the WSM leads. To substantiate this claim, we introduce a quantitative spin-polarization by assigning a positive sign to the ↑↑ amplitudes and a negative sign to the ↓↓ amplitudes. Explicitly,

$$S_L = \tau_z \begin{pmatrix} f_{\uparrow\uparrow}^+(z) \\ f_{\downarrow\downarrow}^-(z) \end{pmatrix} = f_{\uparrow\uparrow}^+(z) - f_{\downarrow\downarrow}^-(z), \text{ for } z \leq z_L, \tag{3.92a}$$

$$S_R = \tau_z \begin{pmatrix} f_{\uparrow\uparrow}^-(z) \\ f_{\downarrow\downarrow}^+(z) \end{pmatrix} = f_{\uparrow\uparrow}^-(z) - f_{\downarrow\downarrow}^+(z), \text{ for } z \geq z_R, \tag{3.92b}$$

in the left and right WSM lead, respectively. We plot these quantities in Fig. 3.19. As we can see, the polarization is extremal at $\omega = \pm\chi$, but with opposite sign, i.e., the Cooper pairs in $z \leq z_L$ are

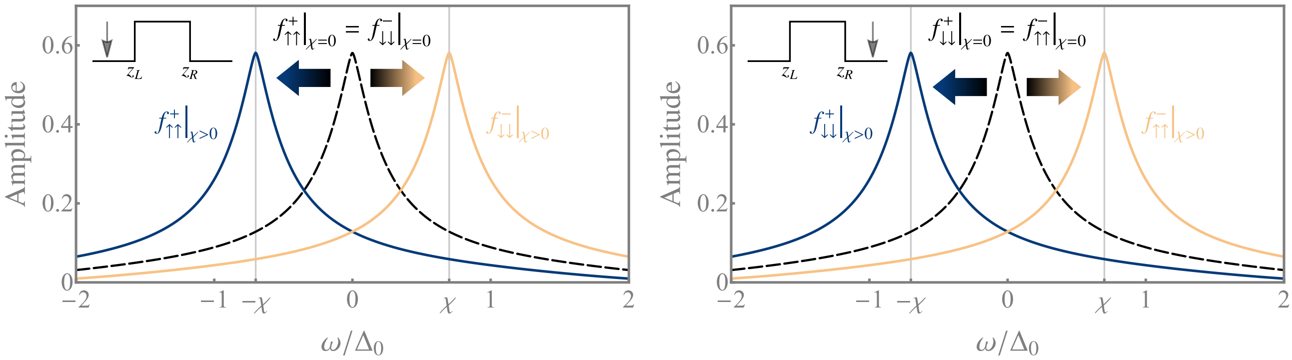

(a) $z = -5\xi$ **(b)** $z = 5\xi$

Fig. 3.18: Frequency dependence of the prominent equal-spin amplitudes in **(a)** the left and **(b)** the right WSM for no (black, dashed curve) and a finite, positive CCP (colored curves). The amplitudes associated with $\mathcal{H}^+$ are shifted to negative frequencies, those with $\mathcal{H}^-$ to positive frequencies. We choose $\mu_S = 10^6\,\Delta_0$, $\mu_N = 10^3\,\Delta_0$, $\alpha = \pi/4$, $L = \xi$ and $\chi = 0.7\,\Delta_0$ for the finite CCP. *Reprinted figure with permission from [120]. Copyright (2021) by the American Physical Society.*

predominantly $\uparrow\uparrow$ -polarized at $\omega = -\chi$ and $\downarrow\downarrow$ -polarized at $\omega = \chi$. This polarization decreases quickly as we move away from these energies. In particular, it vanishes at $\omega = 0$ for any choice of χ and naturally for $|\omega| \gg \chi$. Intriguingly, the polarization at any energy is exactly opposite in the left and the right WSM lead, such that the system features a dipole character if CCP is induced. From Fig. 3.16, we can conclude that the peak becomes narrower the farther away from the interfaces we evaluate the pairing amplitudes. As discussed above, this only holds true at zero temperature.

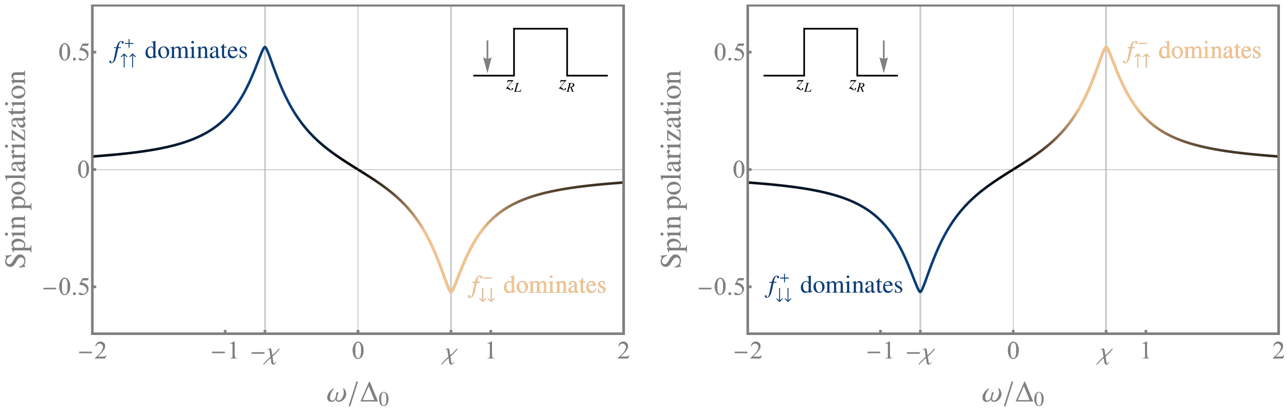

(a) $z = -5\xi$ **(b)** $z = 5\xi$

Fig. 3.19: Spin polarization **(a)** S_L in the left and **(b)** S_R in the right WSM lead as a function of ω. Due to the finite CCP, the system features a distinct polarization at $\omega \approx \pm\chi$, which is opposite left and right of the superconductor. We choose $\mu_S = 10^6\,\Delta_0$, $\mu_N = 10^3\,\Delta_0$, $\alpha = \pi/4$, $L = \xi$ and $\chi = 0.7\,\Delta_0$. *Reprinted figure with permission from [120]. Copyright (2021) by the American Physical Society.*

In Fig. 3.20, we study the dependence of the spin-polarization as a function of CCP for two choices of the frequency ω. The figures are qualitatively identical to those in Fig. 3.19 – for illustrative purposes, we choose the fixed frequencies differently than the CCP in the previous figure, to explicitly show that the peaks always occur under the condition $|\omega| = |\chi|$. For a positive frequency, we observe a $\uparrow\uparrow$ - polarization at $\chi = -\omega$ and a $\downarrow\downarrow$ - polarization at $\chi = \omega$ in the domain $z \leq z_L$, while it is exactly vice versa for a negative frequency. At zero-excitation, $\omega = 0$, the polarization vanishes for all choices of CCP, as it is the case for the frequency dependence when no CCP is present. The situation is exactly opposite in the domain $z \geq z_R$.

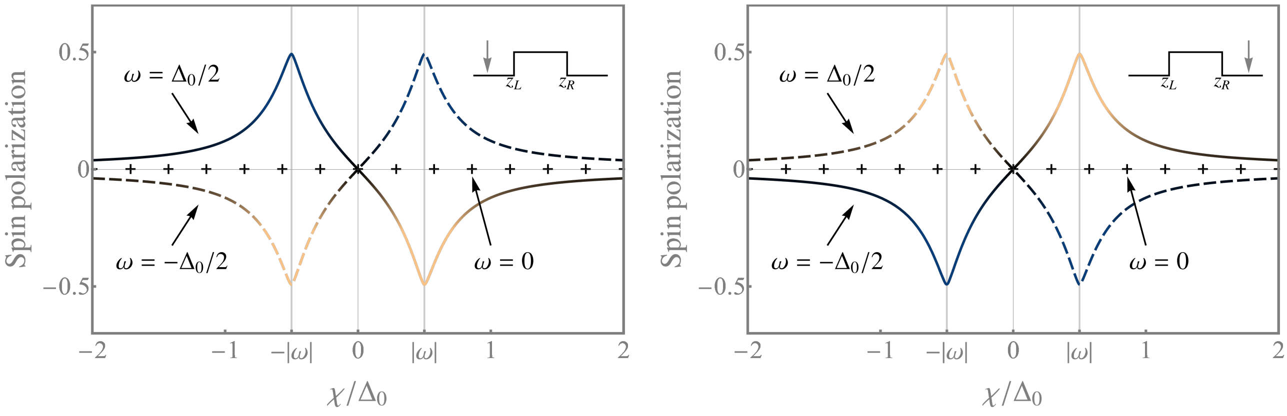

(a) $z = -5\xi$ **(b)** $z = 5\xi$

Fig. 3.20: Spin polarization **(a)** S_L in the left and **(b)** S_R in the right WSM lead as a function of χ. Due to the finite CCP, the system features a distinct polarization at $\omega \approx \pm\chi$, which is opposite left and right of the superconductor. We choose $\mu_S = 10^6\,\Delta_0$, $\mu_N = 10^3\,\Delta_0$, $\alpha = \pi/4$ and $L = \xi$. *Reprinted figure with permission from [120]. Copyright (2021) by the American Physical Society.*

The features above, as well as those observed in the differential conductance, suggest the interchangeability of the energy/frequency and CCP, which is apparent considering Eq. (3.35) – CCP directly affects the eigenenergies of the Hamiltonians $\mathcal{H}^{\pm}$. Consequently, we can control the spin-polarization and thus the dipole character in the junction by variation of either the frequency or CCP. Nonetheless, the fixed quantity needs to be finite. Otherwise, the pairing amplitudes $f^+_{\uparrow\uparrow}(z)$ and $f^+_{\downarrow\downarrow}(z)$ in the domain $z \leq z_L$ as well as $f^+_{\downarrow\downarrow}(z)$ and $f^+_{\uparrow\uparrow}(z)$ in the domain $z \geq z_R$ would be pairwise equal, effectively canceling S_L and S_R.

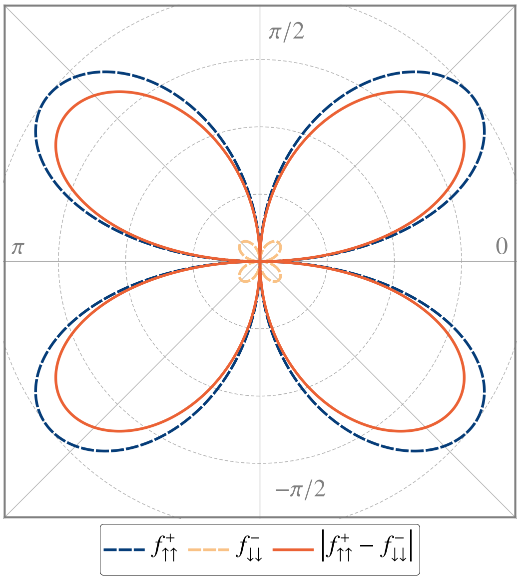

Fig. 3.21: Angular dependence of the spin polarization $|S_{L/R}|$ at $\chi = -\omega = 0.7\,\Delta_0$ and $|z| = 5\xi$. We choose $\mu_S = 10^6\,\Delta_0$, $\mu_N = 10^3\,\Delta_0$, $\alpha = \pi/4$ and $L = \xi$. *Reprinted figure with permission from [120]. Copyright (2021) by the American Physical Society.*

The angular dependence of the spin-polarization is illustrated in Fig. 3.21, where we show only the modulus of $S_{L/R}$, since this is equal on both sides of the superconductor in the NSN-junction. The polarization vanishes naturally at $\alpha \in \{0, \pm\pi\}$, where the effective order parameter is zero, and at $\alpha = \pm\pi/2$ due to the restoration of the C_2-symmetry, *cf.* Eq. (3.89). The maxima occur in the proximity of $\alpha \approx \pm\pi/4$ and $\alpha \approx \pm 3\pi/4$. These observations are in accordance with the features found in the context of Figs. 3.14 and 3.17, and show that the spin-polarization is affected by the orientation of the interface normal with respect to the axis separating the Weyl nodes.

As a last remark, we mention that a uniform CCP across the junction as introduced in Eq. (3.35) is not required to obtain qualitatively similar results as discussed in this section, nor might it be experimentally favorable. If CCP is induced by electromagnetic fields, this breaks down superconductivity if the field strength is too large, so one is inclined to apply the fields only to the WSM leads, i.e.,

$$\chi(z) = \chi\Theta(|z| - L_s/2). \tag{3.93}$$

In fact, this affects the pairing amplitudes, and thus the spin-polarization, only slightly. As we can see in Fig. 3.22, the characteristics are basically the same, except for a certain skewness of the peaks. Their location, however, is not affected and still at $|\omega| = |\chi|$, as is the fact that no polarization emerges if either the frequency or the CCP is zero.

With this, we conclude our analysis ot the TRS broken WSM NSN-junction.

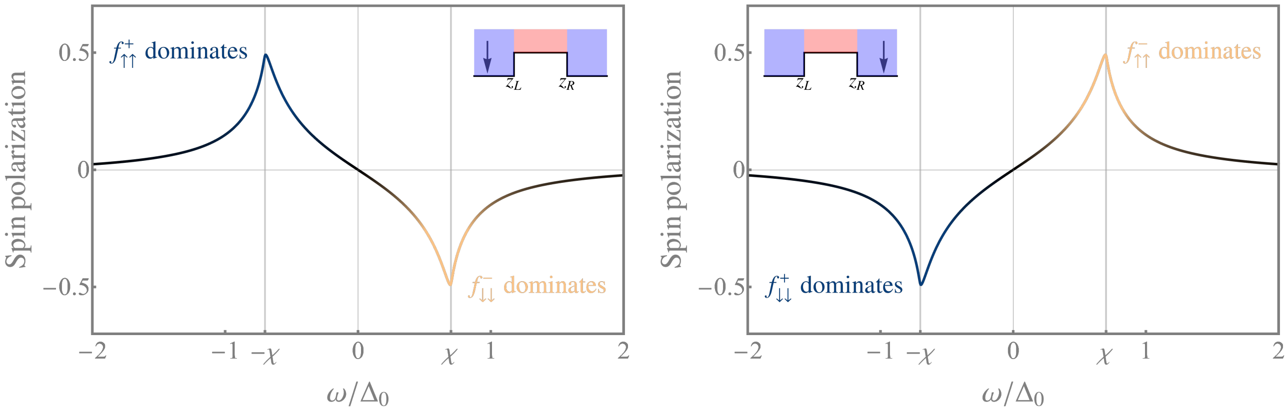

(a) $z = -5\xi$ **(b)** $z = 5\xi$

Fig. 3.22: Spin polarization **(a)** S_L in the left and **(b)** S_R in the right WSM lead as a function of ω in a junction with spatially varying CCP. The blue domains in the inset feature a finite CCP, while in the red domain, it shall be zero. We choose $\mu_S = 10^6\,\Delta_0$, $\mu_N = 10^3\,\Delta_0$, $\alpha = \pi/4$, $L = \xi$ and $\chi = 0.7\,\Delta_0$ for the finite CCP. *Reprinted figure with permission from [120]. Copyright (2021) by the American Physical Society.*

3.5 Conclusion

In this chapter, we study an NSN-junction where the underlying material is a TRS broken Weyl semimetal and conventional superconductivity is induced by means of the proximity effect due to a top electrode on the central domain. We choose a model where the WSM features two nodes of opposite chirality in the Brillouin zone, and consider explicitly the linear low-energy Hamiltonians in the proximity of these band crossing points. In general, the line along which these nodes are separated in k-space can include an angle α with the interface normal in a heterostructure. Moreover, a chiral chemical potential may be induced by the application of parallel electromagnetic fields or a strain deformation, which oppositely shifts the dispersion of the two nodes. Based on this setup, we study local and non-local differential conductance in the system, as well as the proximity effect into the WSM leads by means of the anomalous Green function, from which we extract the pairing amplitudes.

The orientation of the Weyl nodes with respect to the interface normal affects the superconducting order in the S domain, leading to an effective gap that depends on the angle according to $\tilde{\Delta}_0 = \Delta_0\,|\sin\alpha|$. As a consequence, the order parameter is diminished from its initial value Δ_0 if the angle deviates from $\alpha = \pm\pi/2$ and even vanishes for $\alpha \in \{0, \pm\pi\}$, effectively canceling the coupling of electrons and holes in S. As a consequence, the probabilities for Andreev reflection as well as crossed

Andreev reflection are zero at these angles. This characteristics is directly observable in the differential conductance as well as the pairing amplitudes. Local and non-local conductance are maximal and minimal, respectively, at $\alpha = \pm\pi/2$, which is an indicator for predominant electron-hole conversion processes in the scattering problem, while both quantities attain their normal-state values as we approach the angles $\alpha \in \{0, \pm\pi\}$. Since the pairing amplitudes, and the anomalous Green function in general, are mediated by Andreev reflection, they feature the same characteristics as the transport properties, and we observe a similar angle dependence. Nonetheless, the equal-spin amplitudes $f^{\pm}_{\uparrow\uparrow/\downarrow\downarrow}$ additionally vanish at $\alpha = \pm\pi/2$ for any choice of the position in the WSM leads, instead of reaching their maxima there. This is due to a restoration of the C_2-symmetry of the low-energy Hamiltonians, which is broken for arbitrary $\alpha \neq \pm\pi/2$. Notably, the equal-spin amplitudes associated to the same node differ significantly in their magnitudes. While one is comparable to the singlet and opposite-spin amplitudes, the other is approximately zero. The predominant amplitude depends on its associated Weyl node, as well as on the domain (left or right of the superconductor).

Particularly interesting features can be observed if a CCP is introduced into the system. For $\chi = 0$, the quantities derived for the two Hamiltonians $\mathcal{H}^{\pm}$ are equal to each other, up to a spin-flip in the pairing amplitudes. And while the equal-spin triplets associated with the same node differ strongly, each is equal to its spin-flipped counterpart at the other node. Therefore, we do not expect a spin-polarization in the absence of CCP. A finite χ, however, moves the band structures at the two nodes in opposite directions, and thus shifts the energy/frequency dependence of all quantities oppositely, $eV \rightarrow eV \pm \chi$ and $\omega \rightarrow \omega \pm \chi$. Not only does this alter the local and non-local conductances, but also creates an effective Cooper pair spin-polarization in the WSM leads. Since the latter is opposite left and right of the central superconducting domain, the junction displays a dipole character. Furthermore, we show that the spin-polarization is tunable by varying the frequency ω or CCP, such that is theoretically possible to switch the orientation of the dipole. These characteristics might prove valuable for applications in spintronics, if experimentally realizable. Finally, we illustrate that the equal-spin amplitudes, and thus the spin-polarization, are extremal for angles in the proximity of $\alpha \approx \pm\pi/4$ and $\alpha \approx \pm 3\pi/4$. Consequently, the axis separating the Weyl nodes should neither be aligned with the interface normal nor stand perpendicular to it, since in both cases, the equal-spin pairing amplitudes vanish.

4

Creation of spin-triplet Cooper Pairs in the absence of magnetic ordering

This chapter is based on the work *Creation of Spin-Triplet Cooper Pairs in the Absence of Magnetic Ordering* by Daniel Breunig, Pablo Burset and Björn Trauzettel (Phys. Rev. Lett. **120**, 037701 (2018)).

4.1 Motivation

The famous *Datta-Das transistor*, also denoted by *spin field-effect transistor*, is a famous device in spintronics that employs the electron spin to store information, instead of its charge [125]. It is based on materials with strong spin-orbit coupling and a desirable setup since electronic switching can be implemented faster than magnetic switching. The concept is contemporary to this day, and still under further development [126]. For superconducting spintronics, however – and to the best of our knowledge – no similar device has been proposed that does not include magnetic components, like, e.g., spin valves [127–135]. The on-demand creation of equal-spin Cooper pairs in the absence of magnetic order would thus be a fascinating concept for an application in this field. Intriguingly, the surface states of 3D TIs provide such a material featuring strong spin-orbit coupling and linear dispersions in the proximity of the band crossing points (denoted by *Dirac points*). In this work, we propose a bipolar setup performing as a device that enables the creation of out-of -equilibrium, equal-spin Cooper pairs in a superconductor (S) sandwiched between two normal TI leads. In particular, we assume the underlying material to be the surface state of a 3D TI, where an S top electrode induces a superconducting gap in a locally confined region by means of the proximity effect, see Fig. 4.1. The leads left (L) and right (R) of the S domain shall be connected to voltage sources V_L and V_R, respectively, which can be tuned independently, while the superconductor remains grounded. Moreover, we assume that each domain features distinct carrier densities (electrochemical potentials), which is realizable by means of gating technology [136]. As we will show, the primary mechanism which is responsible for the creation of equal-spin Cooper pairs is *crossed Andreev reflection*, a scattering process in which an electron approaching the S domain in one lead is transmitted as a hole into the other lead, as illustrated in Fig. 4.1.

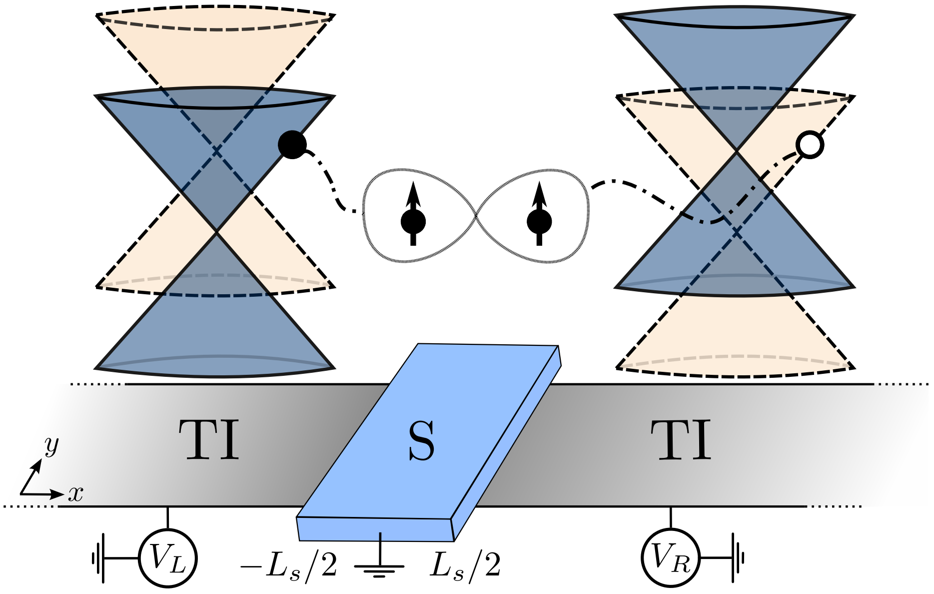

Fig. 4.1: TI-S-TI junction considered in this work. A top electrode induces superconductivity into the system, which enables scattering processes converting incident electrons to reflected or transmitted holes. A crossed Andreev reflection process, which creates an equal-spin Cooper pair in S is illustrated. In the proximity of the Dirac points, the leads feature relativistic (linear) dispersions, where the solid blue and the dashed orange cones represent electrons and holes, respectively. *Reprinted figure with permission from [102]. Copyright (2021) by the American Physical Society.*

The bipolar setup has been studied in detail for graphene by Cayssol [123] and requires the electrochemical potentials in L and R to feature the same magnitude, but opposite signs, i.e., one TI region is of the n-type, and the other of the p-type. Here, the spin degree of freedom played no role due to the negligible spin-orbit coupling in graphene (the isospin degree of freedom stems from the two sublattices), while in our setup, featuring 3D TIs, the latter effect is rather strong. In combination with superconducting order, this yields intriguing physics [137], like odd-frequency pairing in the superconductor [56, 138–141] or the appearance of Majorana bound states [142–144], due to the breaking of spin-rotational invariance by strong spin-orbit coupling. This is possible due to the emergence of unconventional superconductivity [145], even if the proximity-induced order is only of the s-wave type. And while spin-triplet states can be equally induced by proximity to a magnetic insulator [146–153], interfacing surface states of TIs with superconductors currently seems more feasible from the experimental side. The system we propose should therefore be realizable.

As has been proposed for graphene [123] and common semiconductors [154], the bipolar setup allows to completely suppress local Andreev reflection as well as co-tunneling from one lead into the other for an appropriate choice of the bias. In the following chapter, we show that this equally applies to our TI setup and, moreover, suppresses non-local spin-singlet pairing in the system. As a consequence, the TI-S-TI junction acts as a spin-triplet filter and pumps equal-spin Cooper pairs into the superconductor.

This chapter is structured as follows. In Sec. 4.2, we introduce the junction, the corresponding Hamiltonian, and the choice of parameters that results in the bipolar setup. Furthermore, we determine the eigenstates in each domain and define the full set of scattering states. The results are presented in Sec. 4.3. Here, we first consider the transport properties by means of the local and non-local differential conductance, followed by an analysis of the proximity effect in the TI leads via the anomalous Green function. Finally, we determine the spin polarization of the Cooper pairs and estimate its effect when applying a bias to the junction. A methodical section is not included, since the underlying concepts have been elucidated in the previous chapters (wave matching conditions in Sec. 2.3 and the anomalous Green function as well as the concept of outgoing boundary conditions in Sec. 3.2).

This work has partially been published as a letter in the journal *Physical Review Letters* [102]. Similarities in the text are unavoidable. The copyright (2021) belongs to the American Physical Society. All licenses to use the content in this Thesis have been obtained. Reprinted or adapted figures are distinctly marked.

4.2 Setup and Hamiltonian

4.2.1 Definitions and preliminary calculations

The TI-S-TI system we want to consider is illustrated in Fig. 4.1 and corresponds to a 2D NSN-junction, which shall be described by the Dirac Hamiltonian. In the basis $(c_{\uparrow,\boldsymbol{k}}, c_{\downarrow,\boldsymbol{k}})^T$, where $c^\dagger_{\sigma,\boldsymbol{k}}$ is the creation operator of an electron with spin σ and wave vector $\boldsymbol{k} = (k_x, k_y)^T$, the Bloch Hamiltonian reads

$$H_0(\boldsymbol{k}) = v_f\,(k_x s_x + k_y s_y) - \mu, \tag{4.1}$$

where s_0 and $s_{x,y,z}$ are unit and Pauli matrices in spin space, v_f is the Fermi velocity and μ the electrochemical potential. Equation (4.1) is the projection of the TI bulk Hamiltonian [60] onto one surface. Introducing s-wave superconductivity into the system, we can write the full BdG Hamiltonian in the basis $\left(c_{\uparrow,\boldsymbol{k}}, c_{\downarrow,\boldsymbol{k}}, c^\dagger_{\uparrow,-\boldsymbol{k}}, c^\dagger_{\downarrow,-\boldsymbol{k}}\right)^T$ as

$$\mathcal{H}_{\mathrm{BdG}}(\boldsymbol{k}) = \begin{pmatrix} H_0(\boldsymbol{k}) & i\Delta s_y \\ -i\Delta s_y & -H_0^*(-\boldsymbol{k}) \end{pmatrix} = v_f\,(k_x s_x + k_y \tau_z s_y) - \mu\,\tau_z s_0 - \Delta \tau_y s_y, \tag{4.2}$$

where τ_0 and $\tau_{x,y,z}$ are unit and Pauli matrices in Nambu space and Δ is the superconducting order parameter. Note that, contrary to Ref. [123], the spin matrices act on the actual spin of the particles, and not on the sublattice isospin degree of freedom. In the following, we set $v_f = 1$ for simplicity.

To model the NSN-junction in accordance with Fig. 4.1, we choose the electrochemical and superconducting potentials to be position-dependent,

$$\mu(x) = \mu_l \Theta(x_L - x) + \mu_s \Theta(L_s - |x|) + \mu_r \Theta(x - x_R), \tag{4.3a}$$

$$\Delta(x) = \Delta_0 \Theta(L_s - |x|), \tag{4.3b}$$

where we define $x_L = -L_s/2$ and $x_R = L_s/2$. As a consequence, the S gap is finite only in the domain $-L_s/2 \leq x \leq L_s/2$, while it is zero in the leads. This step-wise definition of the potentials is valid if the wave vector in the S domain is much larger than that in L and R [66,123]. The BdG Hamiltonian is now position-dependent, $\mathcal{H}_{\text{BdG}}(\boldsymbol{r})$ with $\boldsymbol{r} = (x, y)^T$, such that the wave numbers are replaced by operators

$$(k_x, k_y)^T \rightarrow \left(\hat{k}_x, \hat{k}_y\right)^T = -i\left(\partial_x, \partial_y\right)^T, \tag{4.4}$$

where $\partial_{x(y)}$ is the partial derivative in the $x(y)$-variable. We therefore need to solve the Schrödinger equation

$$\mathcal{H}_{\text{BdG}}(\boldsymbol{r})\phi(\boldsymbol{r}) = E\phi(\boldsymbol{r}) \tag{4.5}$$

with E the energy eigenvalues. The potentials in Eq. (4.3), however, break translational invariance only along the x-axis, such that we may perform a partial Fourier transformation and obtain

$$\phi(\boldsymbol{r}) = \int \mathrm{d}k_y\, \phi(x, k_y) e^{i k_y y} \qquad \Rightarrow \qquad \mathcal{H}_{\text{BdG}}(\boldsymbol{r}) \rightarrow \mathcal{H}_{\text{BdG}}(x, k_y). \tag{4.6}$$

Here, k_y is a real parameter and a good quantum number indexing the transverse modes. The eigenvalues of this Hamiltonian are given by

$$E_e^{l/r} = \pm||\boldsymbol{k}|| - \mu_{l/r}, \qquad E_h^{l/r} = \pm||\boldsymbol{k}|| + \mu_{l/r} \tag{4.7}$$

in the bulk TIs and

$$E_{eq}^s = \pm\sqrt{\left(||\boldsymbol{k}|| - \mu_s\right)^2 + \Delta_0^2}, \qquad E_{hq}^{l/r} = \pm\sqrt{\left(||\boldsymbol{k}|| + \mu_s\right)^2 + \Delta_0^2} \tag{4.8}$$

in S, where the superscripts label the domain and the subscripts distinguish electrons (e) from holes (h) and electron-like (eq) from hole-like (hq) quasiparticles. The sign ± differentiates valence and conduction bands.

Eigenstates and scattering states

In order to derive the transport properties and the pairing amplitudes via the anomalous Green function, we need to define the eigenstates in each region, and subsequently the corresponding scattering states. In the normal leads, they are given, in a mixed energy-position representation, by

$$\psi_{e,l/r}^{+}(x) = \left(1, \frac{k_e^{l/r} + i k_y}{E + \mu_{l/r}}, 0, 0\right)^T e^{i k_e^{l/r} x} = \left(1, e^{i\theta_e^{l/r}}, 0, 0\right)^T e^{i\kappa_e^{l/r} \cos\theta_e^{l/r} x}, \tag{4.9a}$$

$$\psi_{e,l/r}^{-}(x) = \left(\frac{k_e^{l/r} + i k_y}{E + \mu_{l/r}}, -1, 0, 0\right)^T e^{-i k_e^{l/r} x} = \left(e^{i\theta_e^{l/r}}, -1, 0, 0\right)^T e^{-i\kappa_e^{l/r} \cos\theta_e^{l/r} x}, \tag{4.9b}$$

$$\psi_{h,l/r}^{+}(x) = \left(0, 0, \frac{k_h^{l/r} + i k_y}{E - \mu_{l/r}}, 1\right)^T e^{i k_h^{l/r} x} = \left(0, 0, e^{i\theta_h^{l/r}}, 1\right)^T e^{i\kappa_h^{l/r} \cos\theta_h^{l/r} x}, \tag{4.9c}$$

$$\psi_{h,l/r}^{-}(x) = \left(0, 0, 1, -\frac{k_h^{l/r} + i k_y}{E - \mu_{l/r}}\right)^T e^{-i k_h^{l/r} x} = \left(0, 0, 1, -e^{i\theta_h^{l/r}}\right)^T e^{-i\kappa_h^{l/r} \cos\theta_h^{l/r} x}, \tag{4.9d}$$

while in the superconductor, they read

$$\psi^{+}_{eq}(x) = \left(u, \frac{k_{eq} + ik_y}{\Omega + \mu_s} u, -\frac{k_{eq} + ik_y}{\Omega + \mu_s} v, v\right)^T e^{ik_{eq}x} = \left(u, e^{i\theta_{eq}} u, -e^{i\theta_{eq}} v, v\right)^T e^{i\kappa_{eq}\cos\theta_{eq} x}, \tag{4.10a}$$

$$\psi^{-}_{eq}(x) = \left(\frac{k_{eq} + ik_y}{\Omega + \mu_s} u, -u, v, \frac{k_{eq} + ik_y}{\Omega + \mu_s} v\right)^T e^{-ik_{eq}x} = \left(e^{i\theta_{eq}} u, -u, v, e^{i\theta_{eq}} v\right)^T e^{-i\kappa_{eq}\cos\theta_{eq} x}, \tag{4.10b}$$

$$\psi^{+}_{hq}(x) = \left(v, \frac{k_{hq} \pm ik_y}{\Omega + \mu_s} v, -\frac{k_{hq} \pm ik_y}{\Omega + \mu_s} u, u\right)^T e^{ik_{hq}x} = \left(v, e^{i\theta_{hq}} v, -e^{i\theta_{hq}} u, u\right)^T e^{i\kappa_{hq}\cos\theta_{hq} x}, \tag{4.10c}$$

$$\psi^{-}_{hq}(x) = \left(\frac{k_{hq} + ik_y}{\Omega + \mu_s} v, -v, u, \frac{k_{hq} + ik_y}{\Omega + \mu_s} u\right)^T e^{-ik_{hq}x} = \left(e^{i\theta_{hq}} v, -v, u, e^{i\theta_{hq}} u\right)^T e^{-i\kappa_{hq}\cos\theta_{hq} x}. \tag{4.10d}$$

The superscripts indicate the group velocity with respect to the x-axis and thus distinguish right $(+)$ from left $(-)$ movers, while the subscripts are explained in the context of the eigenvalues above. Note that we omit the phase factor $e^{ik_y y}$ for convenience. Here, the wave vectors are given by

$$k_e^{l/r} = \operatorname{sgn}\left(E + \mu_{l/r} + |k_y|\right) \sqrt{\left(E + \mu_{l/r}\right)^2 - k_y^2}, \tag{4.11a}$$

$$k_h^{l/r} = \operatorname{sgn}\left(E - \mu_{l/r} + |k_y|\right) \sqrt{\left(E - \mu_{l/r}\right)^2 - k_y^2}, \tag{4.11b}$$

$$k_{eq/hq} = \sqrt{\left(\Omega \pm \mu_{l/r}\right)^2 - k_y^2}, \tag{4.11c}$$

with the BCS coefficients

$$u^2 = \frac{1}{2}\left(1 + \frac{\Omega}{E}\right) = 1 - v^2 \tag{4.12}$$

and

$$\Omega = \begin{cases} \operatorname{sgn}(E)\sqrt{E^2 - \Delta_0^2}, & |E| > \Delta_0 \\ i\sqrt{\Delta_0^2 - E^2}, & |E| < \Delta_0 \end{cases}. \tag{4.13}$$

For the angular representation (the right most expressions in Eqs. (4.9) and (4.10)), we have

$$\kappa_e^{l/r} = \left|E + \mu_{l/r}\right|, \qquad \kappa_h^{l/r} = \left|E - \mu_{l/r}\right|, \qquad \kappa_{eq/hq} = \left|\Omega \pm \mu_s\right|, \tag{4.14}$$

as well as

$$\theta^{l/r}_{e/h} = \arcsin\left(\frac{k_y}{\kappa^{l/r}_{e/h}}\right), \qquad \theta_{eq/hq} = \arcsin\left(\frac{k_y}{\kappa_{eq/hq}}\right). \tag{4.15}$$

Note that this representation is only valid if the corresponding wavenumbers are real valued. It does not describe the evanescent states appropriately.

We are now able to define the full set of scattering states in the system. Since the underlying system, a quasi-1D NSN heterojunction, is the same as in Chap. 3, we choose the definitions in accordance with Fig. 3.2, such that we have

$$\phi_{1/2}(x) = \begin{cases} \psi^{+}_{e/h}(x) + a_{1/2}\psi^{-}_{h/e}(x) + b_{1/2}\psi^{-}_{e/h}(x), & x < x_L \\ s_{1/2,1}\,\psi^{+}_{eq}(x) + s_{1/2,2}\,\psi^{-}_{eq}(x) + s_{1/2,3}\,\psi^{+}_{hq}(x) + s_{1/2,4}\,\psi^{-}_{hq}(x), & x_L < x < x_R \\ c_{1/2}\psi^{+}_{e/h}(x) + d_{1/2}\psi^{+}_{h/e}(x), & x > x_R \end{cases}, \tag{4.16a}$$

$$\phi_{3/4}(x) = \begin{cases} c_{3/4}\psi^{-}_{e/h}(x) + d_{3/4}\psi^{-}_{h/e}(x), & x < x_L \\ s_{3/4,1}\,\psi^{+}_{eq}(x) + s_{3/4,2}\,\psi^{-}_{eq}(x) + s_{3/4,3}\,\psi^{+}_{hq}(x) + s_{3/4,4}\,\psi^{-}_{hq}(x), & x_L < x < x_R \\ \psi^{-}_{e/h}(x) + a_{3/4}\psi^{+}_{h/e}(x) + b_{3/4}\psi^{+}_{e/h}(x), & x > x_R \end{cases}. \tag{4.16b}$$

$\phi_{1(2)}$ describes the scattering event corresponding to an electron excited in $L(R)$ and moving towards the superconductor, while it is a hole excited in $L(R)$ when we consider $\phi_{3(4)}$. This takes all solutions of the Schrödinger equation that comply with outgoing boundary conditions into account, *cf.* Sec. 3.2.2. The scattering coefficient are related to local Andreev reflection (LAR, a_l), normal reflection (NR, b_l), electron or hole co-tunneling (CO, c_l) and crossed Andreev reflection (CAR, d_l), where $l \in \{1,2,3,4\}$. They can be calculated by means of the wave matching conditions introduced in Sec. 2.3. Since $\mathcal{H}_{\mathrm{BdG}}(\boldsymbol{k})$ in Eq. (4.2) represents a Dirac Hamiltonian, k_x appears in first order only, i.e., the effective mass terms vanish and Eq. (2.14) naturally evaluates to be true. This leaves us with the continuity condition of the waves at the interfaces,

$$\lim_{\varepsilon\to 0^+}\left[\phi_l(x_L-\varepsilon)-\phi_l(x_L+\varepsilon)\right]=0, \qquad \lim_{\varepsilon\to 0^+}\left[\phi_l(x_R-\varepsilon)-\phi_l(x_R+\varepsilon)\right]=0. \tag{4.17}$$

The probability amplitudes of the scattering processes above are given by the square moduli of the corresponding coefficients, multiplied by the normalized probability current associated with the states in Eq. (4.9), which can be calculated according to Eq. (2.20). They read

$$R_{eh}^{l/r}(E,k_y)=\Theta\left(\kappa_h^{l/r}-|k_y|\right)\frac{\cos\theta_h^{l/r}}{\cos\theta_e^{l/r}}\left|a_{1/3}\right|^2, \quad R_{ee}^{l/r}(E,k_y)=\left|b_{1/3}\right|^2, \tag{4.18a}$$

$$T_{ee}^{l/r}(E,k_y)=\Theta\left(\kappa_e^{r/l}-|k_y|\right)\frac{\cos\theta_e^{r/l}}{\cos\theta_e^{l/r}}\left|c_{1/3}\right|^2, \quad T_{eh}^{l/r}(E,k_y)=\Theta\left(\kappa_h^{r/l}-|k_y|\right)\frac{\cos\theta_h^{r/l}}{\cos\theta_e^{l/r}}\left|d_{1/3}\right|^2, \tag{4.18b}$$

for an electron excited in L/R and

$$R_{he}^{l/r}(E,k_y)=\Theta\left(\kappa_e^{l/r}-|k_y|\right)\frac{\cos\theta_e^{l/r}}{\cos\theta_h^{l/r}}\left|a_{2/4}\right|^2, \quad R_{hh}^{l/r}(E,k_y)=\left|b_{2/4}\right|^2, \tag{4.19a}$$

$$T_{hh}^{l/r}(E,k_y)=\Theta\left(\kappa_h^{r/l}-|k_y|\right)\frac{\cos\theta_h^{r/l}}{\cos\theta_h^{l/r}}\left|c_{2/4}\right|^2, \quad T_{he}^{l/r}(E,k_y)=\Theta\left(\kappa_e^{r/l}-|k_y|\right)\frac{\cos\theta_e^{r/l}}{\cos\theta_h^{l/r}}\left|d_{2/4}\right|^2, \tag{4.19b}$$

for a hole excited in L/R. The first and second indices in the subscripts of the probability amplitudes represent the incident and reflected/transmitted particles, respectively, while the superscripts indicate from which domain the incident particle originates. The Heaviside step functions $\Theta(\cdot)$ make sure that the probability amplitudes are zero if the corresponding scattered particle is described by an evanescent wave (i.e, its probability current vanishes). Note that, in writing Eqs. (4.18) and (4.19), we assume that k_y is chosen in such a way that the incident particle is always a propagating mode with a finite probability current.

Transposed eigenstates and scattering states

The Scattering State Approach requires both the normal as well as the transposed scattering states of the system to determine the retarded Green function. We therefore transpose the Hamiltonian in Eq. (4.6) (note that $\hat{k}_x^T=-\hat{k}_x$) and obtain the corresponding eigenstates as

$$\tilde{\psi}_{e,l/r}^{+}(x)=\left(1,-\frac{k_e^{l/r}+ik_y}{E+\mu_{l/r}},0,0\right)^T e^{ik_e^{l/r}x}=\left(1,-e^{i\theta_e^{l/r}},0,0\right)^T e^{i\kappa_e^{l/r}\cos\theta_e^{l/r}x}, \tag{4.20a}$$

$$\tilde{\psi}_{e,l/r}^{-}(x)=\left(\frac{k_e^{l/r}+ik_y}{E+\mu_{l/r}},1,0,0\right)^T e^{-ik_e^{l/r}x}=\left(e^{i\theta_e^{l/r}},1,0,0\right)^T e^{-i\kappa_e^{l/r}\cos\theta_e^{l/r}x}, \tag{4.20b}$$

$$\tilde{\psi}_{h,l/r}^{+}(x)=\left(0,0,\frac{k_h^{l/r}+ik_y}{E-\mu_{l/r}},-1\right)^T e^{ik_h^{l/r}x}=\left(0,0,e^{i\theta_h^{l/r}},-1\right)^T e^{i\kappa_h^{l/r}\cos\theta_h^{l/r}x}, \tag{4.20c}$$

$$\tilde{\psi}_{h,l/r}^{-}(x)=\left(0,0,1,\frac{k_h^{l/r}+ik_y}{E-\mu_{l/r}}\right)^T e^{-ik_h^{l/r}x}=\left(0,0,1,e^{i\theta_h^{l/r}}\right)^T e^{-i\kappa_h^{l/r}\cos\theta_h^{l/r}x}, \tag{4.20d}$$

in L and R, while in S, they read

$$\tilde{\psi}^{+}_{eq}(x) = \left(u, -\frac{k_{eq}+ik_y}{\Omega+\mu_s}u, \frac{k_{eq}+ik_y}{\Omega+\mu_s}v, v\right)^T e^{ik_{eq}x} = \left(u, -e^{i\theta_{eq}}u, e^{i\theta_{eq}}v, v\right)^T e^{i\kappa_{eq}\cos\theta_{eq}x}, \tag{4.21a}$$

$$\tilde{\psi}^{-}_{eq}(x) = \left(\frac{k_{eq}+ik_y}{\Omega+\mu_s}u, u, -v, \frac{k_{eq}+ik_y}{\Omega+\mu_s}v\right)^T e^{-ik_{eq}x} = \left(e^{i\theta_{eq}}u, u, -v, e^{i\theta_{eq}}v\right)^T e^{-i\kappa_{eq}\cos\theta_{eq}x}, \tag{4.21b}$$

$$\tilde{\psi}^{+}_{hq}(x) = \left(v, -\frac{k_{hq}\pm ik_y}{\Omega+\mu_s}v, \frac{k_{hq}\pm ik_y}{\Omega+\mu_s}u, u\right)^T e^{ik_{hq}x} = \left(v, -e^{i\theta_{hq}}v, e^{i\theta_{hq}}u, u\right)^T e^{i\kappa_{hq}\cos\theta_{hq}x}, \tag{4.21c}$$

$$\tilde{\psi}^{-}_{hq}(x) = \left(\frac{k_{hq}+ik_y}{\Omega+\mu_s}v, v, -u, \frac{k_{hq}+ik_y}{\Omega+\mu_s}u\right)^T e^{-ik_{hq}x} = \left(e^{i\theta_{hq}}v, v, -u, e^{i\theta_{hq}}u\right)^T e^{-i\kappa_{hq}\cos\theta_{hq}x}. \tag{4.21d}$$

The definitions of the subscripts and superscripts as well as those of the wavenumbers, the angles and the BCS coefficients are equal to the ones defined in the context of the normal eigenstates above. Again, we omit the phase factor $e^{-ik_y y}$, which has the opposite sign of its normal pendant. With these definitions, we obtain the transposed scattering states as

$$\tilde{\phi}_{1/2}(x) = \begin{cases} \tilde{\psi}^{+}_{e/h}(x) + \tilde{a}_{1/2}\tilde{\psi}^{-}_{h/e}(x) + \tilde{b}_{1/2}\tilde{\psi}^{-}_{e/h}(x), & x < x_L \\ \tilde{s}_{1/2,1}\,\tilde{\psi}^{+}_{eq}(x) + \tilde{s}_{1/2,2}\,\tilde{\psi}^{-}_{eq}(x) + \tilde{s}_{1/2,3}\,\tilde{\psi}^{+}_{hq}(x) + \tilde{s}_{1/2,4}\,\tilde{\psi}^{-}_{hq}(x), & x_L < x < x_R\ , \\ \tilde{c}_{1/2}\tilde{\psi}^{+}_{e/h}(x) + \tilde{d}_{1/2}\tilde{\psi}^{+}_{h/e}(x), & x > x_R \end{cases} \tag{4.22a}$$

$$\tilde{\phi}_{3/4}(x) = \begin{cases} \tilde{c}_{3/4}\tilde{\psi}^{-}_{e/h}(x) + \tilde{d}_{3/4}\tilde{\psi}^{-}_{h/e}(x), & x < x_L \\ \tilde{s}_{3/4,1}\,\tilde{\psi}^{+}_{eq}(x) + \tilde{s}_{3/4,2}\,\tilde{\psi}^{-}_{eq}(x) + \tilde{s}_{3/4,3}\,\tilde{\psi}^{+}_{hq}(x) + \tilde{s}_{3/4,4}\,\tilde{\psi}^{-}_{hq}(x), & x_L < x < x_R\ . \\ \tilde{\psi}^{-}_{e/h}(x) + \tilde{a}_{3/4}\tilde{\psi}^{+}_{h/e}(x) + \tilde{b}_{3/4}\tilde{\psi}^{+}_{e/h}(x), & x > x_R \end{cases} \tag{4.22b}$$

It is straightforward to derive similar wave matching conditions and probability amplitudes as in Eqs. (4.17) - (4.19). This is, however, not necessary, since we are able to express the transposed scattering coefficients in terms of the normal ones by means of a unitary transformation which relates the transposed Hamiltonian to the original one, see Sec. 4.3.2.

4.2.2 The bipolar setup

By means of state-of-the-art gating technology [136], the carrier density in L and R shall be tuned in such a way that the system features a bipolar setup, see Fig. 4.2. In our model, this means that the electrochemical potentials in L and R feature the same moduli, but opposite signs, $\mu_L = -\mu_R \equiv \mu$. Without loss of generality, we choose $\mu > 0$ and, additionally, to lie inside the S gap, $\mu < \Delta_0$. As a consequence, the band structures in L and R are identical, with the exception that the particle nature is inverted, i.e., the electron band in L corresponds to the hole band in R, and vice versa. A closer inspection of Fig. 4.2(a) reveals furthermore that the Dirac points of the hole dispersion in L and the electron dispersion in R lie at exactly the same energy, $E = \mu$. This has an interesting effect on the possible scattering processes which we can observe at this particular excitation energy. An electron excited in L at $E = \mu$ and approaching the interface ① can be reflected back as an electron (NR) into the same lead ② or transmitted as a hole (CAR) into the other lead R ③, since, for both scattering events, a corresponding state is available (note that, since the system is translational invariant in y-direction, k_y is conserved in a scattering event). Reflection as a hole into the same lead (LAR) and transmission as an electron into R (CO), however, are severely suppressed at this energy in a 2D TI-S-TI junction. This is due to the fact that at the Dirac points, a partial gap emerges as soon as k_y is finite, i.e., when the incident electron approaches the interface under a finite angle of incidence θ^l_e, see Fig. 4.2(b). From the Heaviside step functions in Eq. (4.18) and the definition of κ^l_h and κ^r_e in Eq. (4.14), we see that

$$R^l_{eh}(E=\mu, k_y) = T^l_{ee}(E=\mu, k_y) = 0 \qquad \forall\,|k_y| > 0, \tag{4.23}$$

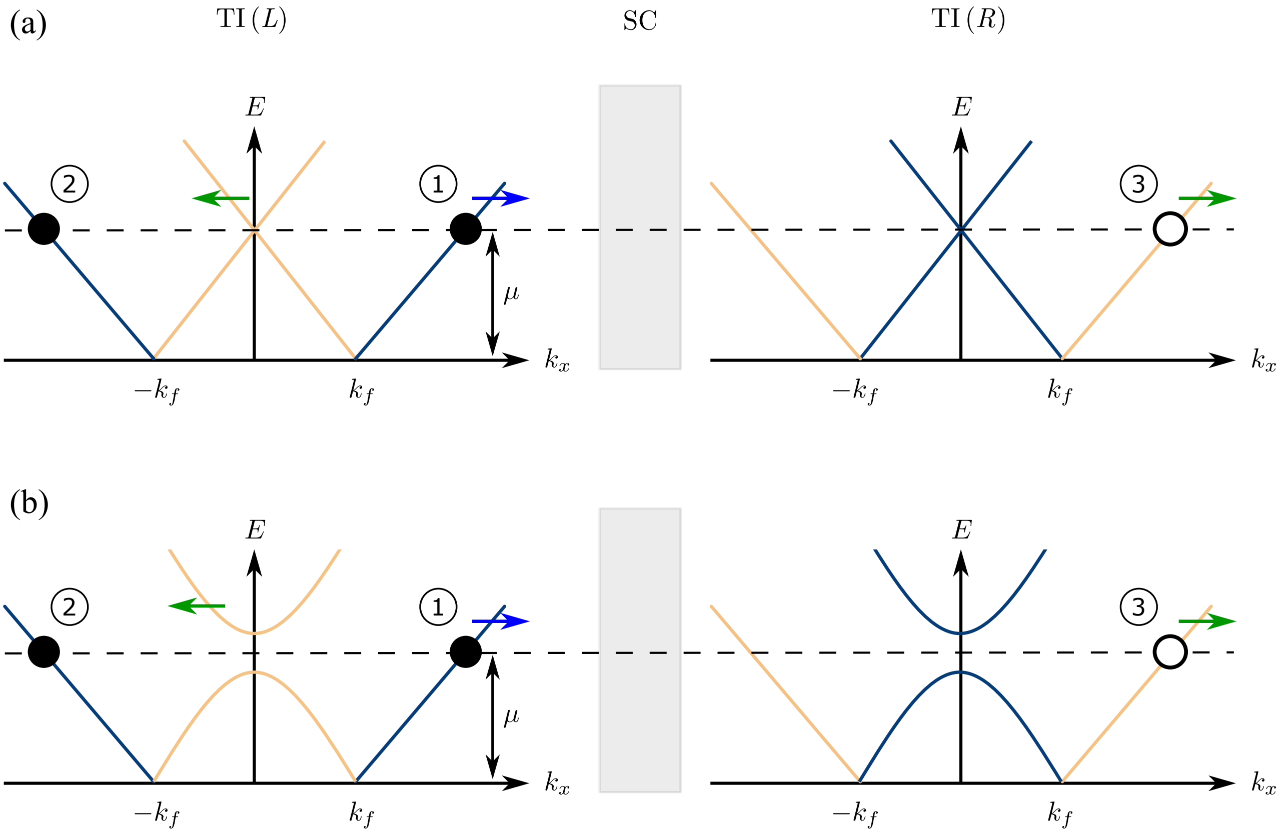

Fig. 4.2: Illustration of the bipolar setup. By choosing $\mu_L = -\mu_R \equiv \mu$, the electron band (blue) in L corresponds to the hole band (orange) in R and vice versa. At $E = \mu$, LAR and CO vanish in the 2D junction, since we hit the Dirac points where the partial gap, induced by a finite transverse mode k_y, emerges. The gray area represents the S domain, while the blue and green arrows indicate the spin of the electrons forming the Cooper pairs, *cf.* Sec. 4.3.3. We choose **(a)** $k_y = 0$ and **(b)** $|k_y| > 0$. *Reprinted figure with permission from [102]. Copyright (2021) by the American Physical Society.*

such that LAR and CO vanish for all modes except for perpendicular incidence, $k_y = 0$. In the following, we integrate over all available modes at a given energy when we consider the differential conductance or the pairing amplitudes, such that one single mode, $k_y = 0$, has no effect on the result. Consequently, we expect LAR and CO to vanish in a 2D junction in the bipolar setup at $E = \mu$. Moreover, the only process creating Cooper pairs in the superconductor is CAR, which results in a net spin polarization in S at the *sweet spot*, $E = \mu$. We elucidate this and further interesting results in the following section.

4.3 Results

We follow our proceeding in the previous chapters and consider the sum over all modes k_y when studying the differential conductance and the proximity effect in the junction, since single modes are a difficult task in an experimental setup. The system is infinite in y-direction, such that we express this sum by an integral in the large L_y limit,

$$\sum_{k_y} \to \frac{L_y}{2\pi} \int_{-\kappa}^{\kappa} \mathrm{d}k_y, \tag{4.24}$$

where L_y is the width of the junction. κ is the natural cut-off of the modes k_y and depends on the scattering process, as indicated by the step functions in Eq. (4.18). They are explicitly defined in Eq. (4.14).

In this section, we first consider the transport properties of the junction, followed by an analysis of the proximity effect at hand of the pairing amplitudes. Finally, we study the spin polarization of the Cooper pairs created in LAR and CAR processes and show that the bipolar setup is an intriguing regime for the formation of equal-spin Cooper pairs.

4.3.1 Transport characteristics

We put the system into the bipolar regime, $\mu_L = -\mu_R = \mu$, and assume that the junction is connected to equilibrium reservoirs at $x \to \pm\infty$. Then, we can employ the extended BTK formalism [27, 32, 33, 155, 156] to calculate the local and non-local conductance. To this end, we apply a voltage to the left lead, $V_L > 0$, while we keep the right lead grounded, $V_R = 0$. Therefore, we assume that an electron is excited in L, which is described by the scattering state $\phi_1(x)$ in Eq. (4.16). With the definitions in Eq. (4.18), we obtain (we omit the superscript l in the following for the sake of clarity)

$$G_{LL}(eV_L, k_y) \equiv \frac{\partial I_L}{\partial V_L}(eV_L, k_y)\Big|_{V_R=0} = \frac{2e^2}{h}\left[1 - R_{ee}(eV_L, k_y) + R_{eh}(eV_L, k_y)\right], \tag{4.25a}$$

$$G_{LR}(eV_L, k_y) \equiv \frac{\partial I_R}{\partial V_L}(eV_L, k_y)\Big|_{V_R=0} = \frac{2e^2}{h}\left[T_{ee}(eV_L, k_y) - T_{eh}(eV_L, k_y)\right], \tag{4.25b}$$

where G_{LL} corresponds to the local conductance (voltage applied to lead L, current measured in lead L) and G_{LR} to the non-local conductance (voltage applied to lead L, current measured in lead R). Considering the Andreev processes, we can see that LAR increases G_{LL}, while CAR reduces G_{LR}. Furthermore, the local and non-local conductances coincide when the system is in the normal state ($\Delta_0 = 0$), i.e., $R_{eh} = T_{eh} = 0$, as we can see from probability current conservation,

$$R_{ee}(eV_L, k_y) + R_{eh}(eV_L, k_y) + T_{ee}(eV_L, k_y) + T_{eh}(eV_L, k_y) = 1, \tag{4.26}$$

such that we obtain

$$G_{LL}(eV_L, k_y)|_{\Delta_0=0} = \underbrace{\frac{2e^2}{h}\left[1 - R_{ee}(eV_L, k_y)\right]}_{\equiv G_0(eV_L, k_y)} = \frac{2e^2}{h}T_{ee}(eV_L, k_y) = G_{LR}(eV_L, k_y)|_{\Delta_0=0}. \tag{4.27}$$

$G_0(eV_L, k_y)$ corresponds to the normal-state conductance of the system. As discussed before, we refrain from studying single modes and consider the full local and non-local conductances,

$$G_{LL}(eV_L) \equiv \sum_{k_y} G_{LL}(eV_L, k_y), \qquad G_{LR}(eV_L) \equiv \sum_{k_y} G_{LR}(eV_L, k_y), \tag{4.28}$$

and express the sum by means of the integral introduced in Eq. (4.24). Then, we obtain the probability amplitudes in Fig. 4.3(a), where we choose L_s to be approximately equal to the coherence length in S, $L_s = 1.1\xi$ with $\xi = v_f/\Delta_0$. This plot confirms the discussion in Sec. 4.2.2. Both LAR and CO decrease quickly from their zero-bias value and vanish completely at $eV_L = \mu$, where the energy lies at the Dirac points of the hole band in L and the electron band in R. For larger biases, LAR attains a finite value again but vanishes at $eV_L \gg \Delta_0$. CO, instead, increases steadily and attains a comparable probability to NR in the large bias limit, where both quantities attain their normal-state equivalents. This becomes apparent in Fig. 4.3, where we plot the local, non-local, and normal-state differential conductance. Note that, usually, it is a common convention to normalize G_{LL} and G_{LR} with respect to G_0. Here, however, the normal-state conductance vanishes at $eV_L = \mu$, *cf.* Eq. (4.27), and normalizing to this quantity would create an artificial singularity. Therefore, we normalize to the total number of modes at a given energy,

$$\mathcal{N} = \int_{-\kappa_e}^{\kappa_e} \mathrm{d}k_y = 2\kappa_e, \tag{4.29}$$

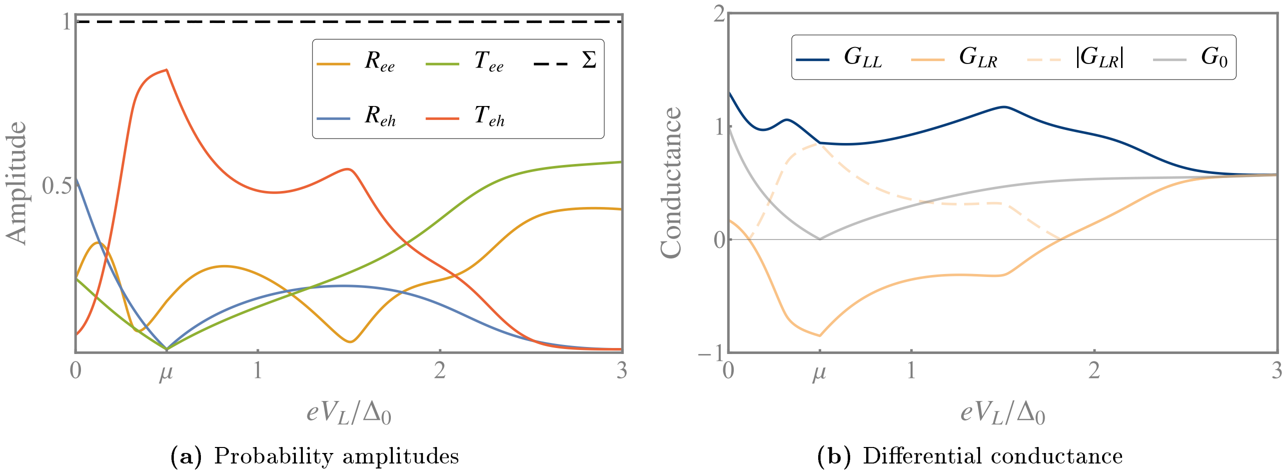

(a) Probability amplitudes **(b)** Differential conductance

Fig. 4.3: **(a)** Probability amplitudes and **(b)** differential conductance of the junction as a function of the bias V_L and averaged over all modes k_y. At $eV_L = \mu$, LAR and CO vanish in the bipolar setup. As a consequence, G_{LL} and G_{LR} are equal at this energy. The black, dashed curve represents the sum of all amplitudes and confirms probability current conservation. We choose $\mu_s = 10\,\Delta_0$, $\mu = 0.5\,\Delta_0$ and $L_s = 1.1\xi$. *Reprinted figure with permission from [102]. Copyright (2021) by the American Physical Society.*

which corresponds to the mode-averaged values of the quantities mentioned above.

Intriguingly, the moduli of the local and non-local conductance coincide at $eV_L = \mu$ in the bipolar setup, as can be seen from

$$G_{LL}(eV_L = \mu) = \frac{2e^2}{h}\left[1 - R_{ee}(eV_L, k_y)\right] = -\frac{2e^2}{h} T_{eh}(eV_L, k_y) = -G_{LR}(eV_L = \mu), \tag{4.30}$$

which is a direct consequence of the absence of LAR and CO and the equation of continuity, Eq. (4.26). This is rather interesting, since, usually, the magnitude of the non-local conductance is smaller than its local counterpart. Furthermore, CAR is rather pronounced in the subgap-regime and for biases in the proximity of the Dirac points. As we will see later in the chapter, this is an important ingredient for the creation of equal-spin Cooper pairs in S.

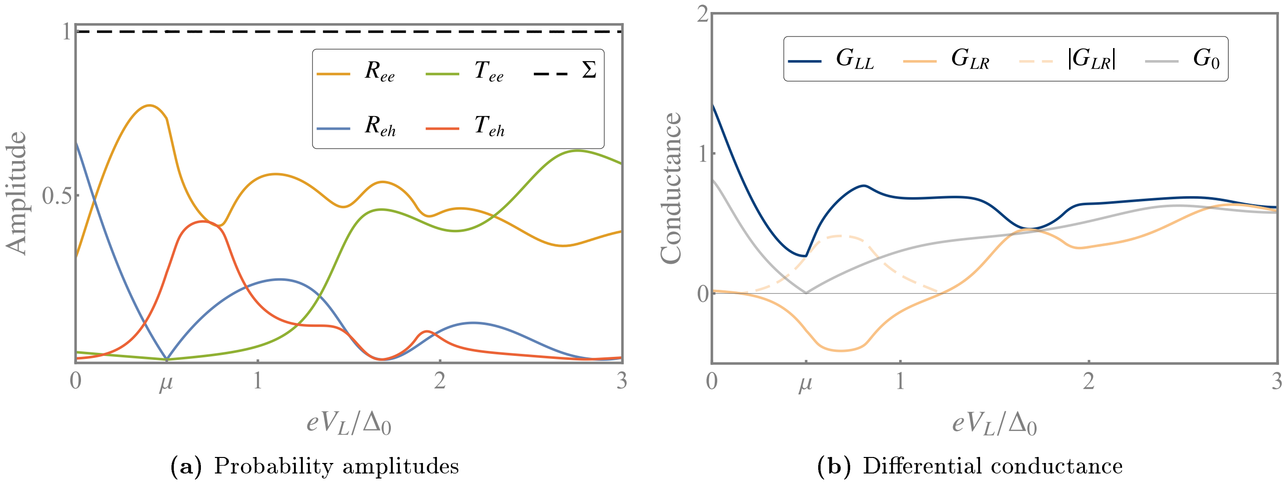

(a) Probability amplitudes **(b)** Differential conductance

Fig. 4.4: **(a)** Probability amplitudes and **(b)** differential conductance of the junction as a function of the bias V_L and averaged over all modes k_y. At $eV_L = \mu$, LAR and CO vanish in the bipolar setup. We choose $\mu_s = 10\,\Delta_0$, $\mu = 0.5\,\Delta_0$ and $L_s = 2.3\xi$. *Reprinted figure with permission from [102]. Copyright (2021) by the American Physical Society.*

Nonetheless, this effect is dependent on the length of the superconductor. As we can see in Fig.

4.4(a), where we choose a different length, $L_s = 2.3\xi$, LAR and CO vanish at $eV_L = \mu$ and behave similarly to Fig. 4.3(a), except for more pronounced oscillations due to quasiparticle interactions in S. CAR, however, is no longer the predominant process in the subgap regime, which is compensated by a stronger probability for NR. As a consequence, if we compare 4.3(b) and 4.4(b), the local and non-local differential conductance are diminished for biases in the proximity of the Dirac points, *cf.* Eq. (4.30).

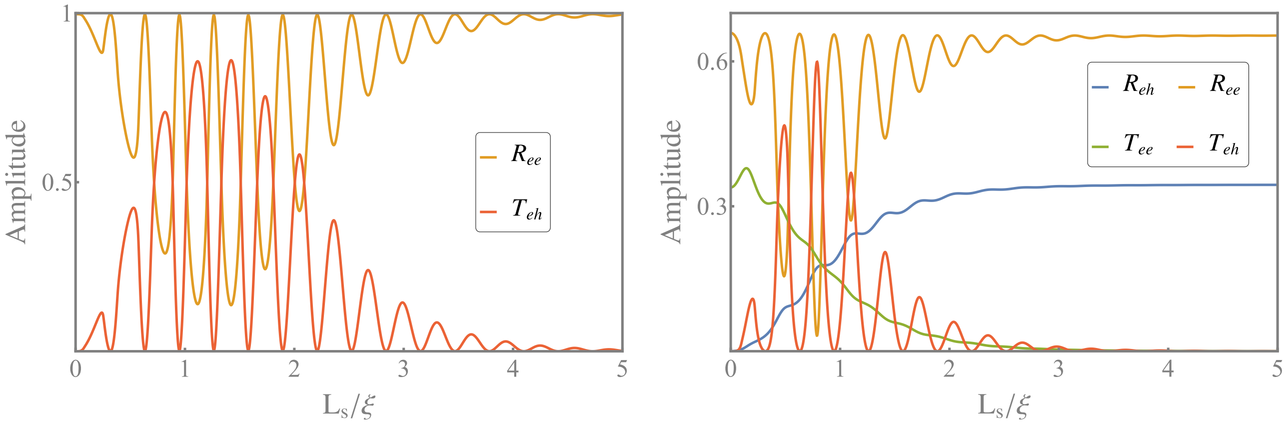

(a) $eV_L = \mu$ **(b)** $eV_L = \Delta_0/5$

Fig. 4.5: Length dependence of the probability amplitudes **(a)** at the Dirac point $eV_L = \mu$ and **(b)** away from the Dirac point. When the length of the S domain is increased from zero, CAR increases at first, reaches a maximum and vanishes if L_s exceeds ξ notably. This is superposed by a strong oscillation, such that CAR vanishes at certain lengths. We choose $\mu_s = 10\,\Delta_0$ and $\mu = 0.5\,\Delta_0$. *Reprinted figure with permission from [102]. Copyright (2021) by the American Physical Society.*

To obtain an insight into the length dependence of CAR, we plot the probability amplitudes as a function of L_s in Fig. 4.5. Considering a bias $eV_L = \mu$, CAR and NR are the only processes that occur, see 4.5(a). We find that T_{eh} follows a curve similar to a Gaussian function, in the sense that the probability grows as L_s is increased from zero, reaches a maximum after which it decreases again and vanishes when the S domain becomes exceedingly large for transmission to occur. This is superposed by a strong, periodical oscillation[1] such that at certain lengths, NR becomes unity and CAR vanishes. At $L_s \approx 1.1\xi$, however, it reaches a maximum and exceeds NR significantly, which explains the strong contribution of CAR in Fig. 4.3. When we move away from the Dirac points, we observe a similar behavior, with the distinction that LAR and CO are finite as well, see 4.5(b). These amplitudes feature the same oscillation but do not follow a Gaussian curve. As is the case for CAR, CO vanishes as the S domain becomes too extensive. NR and LAR approach a constant value in this limit, corresponding to R_{ee} and R_{eh} in a pure NS junction.

With this, we conclude our analysis of the transport properties and advance to the analysis of the proximity effect in the junction.

4.3.2 Pairing amplitudes

Derivation of the retarded Green function

Before we are able to study the pairing amplitudes, we need to derive the retarded Green function of the system. Due to the translational invariance in y-direction, which allowed us to Fourier transform the eigenfunctions and reduce the Hamiltonian to a quasi-1D operator, *cf.* Eq. (4.6), we can simplify the spatial dependence of this quantity in advance and obtain

$$\mathcal{G}(\boldsymbol{r}, \boldsymbol{r}') = \mathcal{G}(x, x', y, y') = \mathcal{G}(x, x', k_y) e^{ik_y(y-y')}. \tag{4.31}$$

---

[1] At $eV_L = \mu$, the minima occur approximately at $L_s/\xi = (n+1/2)\pi\Delta_0/\mu_s$ with $n \in \mathbb{N}$, as discussed in [123]. However, the summation over the modes leads to a slight shift.

In the following, we evaluate all quantities at the same position, $y = y'$, such that this phase factor evaluates to unity.

We follow the Scattering State Approach introduced in Sec. 3.2.2 and make the ansatz

$$\mathcal{G}(x, x', k_y) = \begin{cases} \alpha_1 \phi_3(x) \tilde{\phi}_1^T(x') + \alpha_2 \phi_3(x) \tilde{\phi}_2^T(x') + \alpha_3 \phi_4(x) \tilde{\phi}_1^T(x') + \alpha_4 \phi_4(x) \tilde{\phi}_2^T(x'), & x < x' \\ \\ \beta_1 \phi_1(x) \tilde{\phi}_3^T(x') + \beta_2 \phi_1(x) \tilde{\phi}_4^T(x') + \beta_3 \phi_2(x) \tilde{\phi}_3^T(x') + \beta_4 \phi_2(x) \tilde{\phi}_4^T(x'), & x > x' \end{cases} \tag{4.32}$$

for the retarded Green function, where the scattering states in Eqs. (4.16) and (4.22) are in accordance with the definitions in Fig. 3.2. Since $\mathcal{H}_{\mathrm{BdG}}$ is linear in $\hat{k}_x$, the discontinuity arises in the Green function itself, such that Eq. (3.11) evaluates to

$$\mathcal{G}(x, x', k_y)\big|_{x = x' + 0^+, k_y} - \mathcal{G}(x, x', k_y)\big|_{x = x' - 0^+} = -i \tau_0 s_x. \tag{4.33}$$

Before we evaluate this equation, it is rather useful to express the transposed scattering coefficients by means of the normal ones. Fortunately, the transposed and the normal Hamiltonian are related by a straightforward unitary transformation, given by

$$\mathcal{U}_T \left[\mathcal{H}_{\mathrm{BdG}}(x, k_y)\right]^T \mathcal{U}_T^\dagger = \mathcal{H}_{\mathrm{BdG}}(x, k_y), \qquad\qquad \mathcal{U}_T = \tau_z s_z. \tag{4.34}$$

With this, we can employ the Wronskian method, *cf.* Sec. 3.2.3, and obtain a system of equations from which we can derive the desired relations. This yields

$$\tilde{a}_l = -a_l, \qquad \tilde{b}_l = b_l, \qquad \tilde{c}_l = c_l, \qquad \tilde{d}_l = -d_l, \qquad l \in \{1, 2, 3, 4\}, \tag{4.35}$$

i.e., the scattering coefficients associated to processes conserving the particle type are identical, while the remaining coefficients change their sign.

At this point, we want to mention another symmetry of the Hamiltonian, which inverses the sign of k_y, i.e., the angle of incidence/reflection/transmission. We can show that the Hamiltonian at $-k_y$ is related to that at k_y by the unitary transformation

$$\mathcal{U}_{k_y} \mathcal{H}_{\mathrm{BdG}}(x, -k_y) \mathcal{U}_{k_y}^\dagger = \mathcal{H}_{\mathrm{BdG}}(x, k_y), \qquad\qquad \mathcal{U}_{k_y} = \tau_z s_x. \tag{4.36}$$

We are again able to employ the Wronskian method and obtain a system of equations which allows us to relate the scattering coefficients at $-k_y$ to those at k_y. This yields

$$a_{1/3}(-k_y) = e^{i\left(\theta_h^{l/r} - \theta_e^{l/r}\right)} a_{1/3}(k_y), \qquad a_{2/4}(-k_y) = e^{i\left(\theta_e^{l/r} - \theta_h^{l/r}\right)} a_{2/4}(k_y), \tag{4.37a}$$

$$b_{1/3}(-k_y) = -b_{1/3}(k_y), \qquad b_{2/4}(-k_y) = -b_{2/4}(k_y), \tag{4.37b}$$

$$c_{1/3}(-k_y) = e^{i\left(\theta_e^{r/l} - \theta_e^{l/r}\right)} c_{1/3}(k_y), \qquad c_{2/4}(-k_y) = e^{i\left(\theta_h^{r/l} - \theta_h^{l/r}\right)} c_{2/4}(k_y), \tag{4.37c}$$

$$d_{1/3}(-k_y) = -e^{i\left(\theta_h^{r/l} - \theta_e^{l/r}\right)} d_{1/3}(k_y), \qquad d_{2/4}(-k_y) = -e^{i\left(\theta_e^{r/l} - \theta_h^{l/r}\right)} d_{2/4}(k_y), \tag{4.37d}$$

We find that each scattering coefficient is modified by a phase which is determined by the difference between the angle of incidence (of the incoming particle) and the angle of reflection/transmission (of the scattered particle). As we will show, those are useful relations to understand the behavior of certain elements of the anomalous Green function when summing over all modes.

Reducing $\mathcal{G}(x, x', k_y)$ by means of Eq. (4.35), we are able to determine the Green function coefficients from Eq. (4.33) and obtain

$$\alpha_1 = -\frac{i\,e^{-i\theta_e^l}}{2\cos\left(\theta_e^l\right)}\frac{c_4}{c_3c_4-d_3d_4} = -\frac{i\,e^{-i\theta_e^r}}{2\cos\left(\theta_e^r\right)}\frac{c_2}{c_1c_2-d_1d_2} = \beta_1, \tag{4.38a}$$

$$\alpha_2 = \frac{i\,e^{-i\theta_h^l}}{2\cos\left(\theta_h^l\right)}\frac{d_4}{c_3c_4-d_3d_4} = -\frac{i\,e^{-i\theta_e^r}}{2\cos\left(\theta_e^r\right)}\frac{d_1}{c_1c_2-d_1d_2} = -\beta_2, \tag{4.38b}$$

$$\alpha_3 = \frac{i\,e^{-i\theta_e^l}}{2\cos\left(\theta_e^l\right)}\frac{d_3}{c_3c_4-d_3d_4} = -\frac{i\,e^{-i\theta_h^r}}{2\cos\left(\theta_h^r\right)}\frac{d_2}{c_1c_2-d_1d_2} = -\beta_3, \tag{4.38c}$$

$$\alpha_4 = -\frac{i\,e^{-i\theta_h^l}}{2\cos\left(\theta_h^l\right)}\frac{c_3}{c_3c_4-d_3d_4} = -\frac{i\,e^{-i\theta_h^r}}{2\cos\left(\theta_h^r\right)}\frac{c_1}{c_1c_2-d_1d_2} = \beta_4, \tag{4.38d}$$

where the left and right expressions are derived by evaluating Eq. (4.33) in the domains $x < x_L$ and $x > x_R$, respectively. Since the Green function coefficients are independent of the position, evaluating them in one of the domains would, in general, suffice. For convenient analytic expression of the corresponding pairing amplitudes in L and R, however, it is necessary to calculate them in both domains.

Note that, with the coefficients in Eq. (4.38), not all equations in Eq. (4.33) evaluate to be true (the system is overdetermined). We obtain the detailed balance relations between the scattering coefficients associated to LAR when we demand the latter system of equations to be satisfied, which are given by

$$a_2 = -e^{i\left(\theta_h^l-\theta_e^l\right)}\frac{\cos\theta_h^l}{\cos\theta_e^l}a_1, \qquad a_4 = -e^{i\left(\theta_h^r-\theta_e^r\right)}\frac{\cos\theta_h^r}{\cos\theta_e^r}a_3. \tag{4.39}$$

With the above, we obtain an analytical expression of the retarded Green function. We do not present it explicitly here, but focus on its anomalous part and express it in terms of the pairing amplitudes. As elucidated in Sec. 3.2.1, we rotate the anomalous Green function,

$$\mathcal{F}(x,x',k_y) = -is_yG_{eh}(x,x',k_y), \tag{4.40}$$

and decompose it with respect to the Pauli matrices in spin space,

$$\mathcal{F}(x,x',k_y) = f_0(x,x',k_y)s_0 + f_{\uparrow\uparrow}(x,x',k_y)\frac{s_x+is_y}{2} + f_{\downarrow\downarrow}(x,x',k_y)\frac{s_x-is_y}{2} + f_z(x,x',k_y)s_z. \tag{4.41}$$

This equation provides the desired quantities to study the proximity effect. Before we proceed, let us introduce new variables in position space to better illustrate where the pairing amplitudes are evaluated. We define $x_l \equiv x \leq x_L$ as well as $x_r \equiv x \geq x_R$, which label an arbitrary position in L and R, respectively, for clarity and ease of notation. Contrary to x_L and x_R, these are not fixed values.

Local pairing amplitudes

First, we consider the local amplitudes, where both coordinates lie in the same lead[2]. In L, we have

$$f_0(x_l,x_l',\omega,k_y) = \cos\left(\frac{\theta_e^l+\theta_h^l}{2}\right)\frac{i\,e^{-i/2\left(\theta_e^l-\theta_h^l\right)}}{2\cos\theta_e^l}e^{-i\left(k_e^lx_l+k_h^lx_l'\right)}a_1, \tag{4.42a}$$

$$f_{\uparrow\uparrow}(x_l,x_l',\omega,k_y) = \frac{i\,e^{-i\left(\theta_e^l-\theta_h^l\right)}}{2\cos\theta_e^l}e^{-i\left(k_e^lx_l+k_h^lx_l'\right)}a_1, \tag{4.42b}$$

$$f_{\downarrow\downarrow}(x_l,x_l',\omega,k_y) = \frac{i}{2\cos\theta_e^l}e^{-i\left(k_e^lx_l+k_h^lx_l'\right)}a_1, \tag{4.42c}$$

$$f_z(x_l,x_l',\omega,k_y) = \sin\left(\frac{\theta_e^l+\theta_h^l}{2}\right)\frac{e^{-i/2\left(\theta_e^l-\theta_h^l\right)}}{2\cos\theta_e^l}e^{-i\left(k_e^lx_l+k_h^lx_l'\right)}a_1. \tag{4.42d}$$

---

[2] In contrast to the previous chapter, 'local' does not mean that x and x' are identical, but are located in the same domain. We explicitly mention the case $x = x'$ in what follows.

For the same reason that we have introduced the relations in Eq. (4.37), let us consider an alternative decomposition of the anomalous Green function,

$$\mathcal{F}(x,x',k_y) = f_0(x,x',k_y)s_0 + f_x(x,x',k_y)s_x + f_y(x,x',k_y)s_y + f_z(x,x',k_y)s_z, \tag{4.43}$$

which provides two additional amplitudes f_x and f_y. Since the Pauli matrices are a complete basis of the vector space of complex (2×2)-matrices, these quantities contain no new information. Instead, they are related to $f_{\uparrow\uparrow}$ and $f_{\downarrow\downarrow}$ by

$$f_{\uparrow\uparrow/\downarrow\downarrow} = f_x \mp i f_y, \tag{4.44}$$

and additionally aid in understanding certain properties of the pairing amplitudes. For $x, x' \leq x_L$, they read

$$f_x(x_l,x_l',\omega,k_y) = \cos\left(\frac{\theta_e^l - \theta_h^l}{2}\right) \frac{i\, e^{-i/2\left(\theta_e^l - \theta_h^l\right)}}{2\cos\theta_e^l} e^{-i\left(k_e^l x_l + k_h^l x_l'\right)} a_1, \tag{4.45a}$$

$$f_y(x_l,x_l',\omega,k_y) = \sin\left(\frac{\theta_e^l - \theta_h^l}{2}\right) \frac{i\, e^{-i/2\left(\theta_e^l - \theta_h^l\right)}}{2\cos\theta_e^l} e^{-i\left(k_e^l x_l + k_h^l x_l'\right)} a_1. \tag{4.45b}$$

We obtain similar expressions R, namely

$$f_0(x_r,x_r',\omega,k_y) = -\cos\left(\frac{\theta_e^r + \theta_h^r}{2}\right) \frac{i\, e^{-i/2\left(\theta_e^r - \theta_h^r\right)}}{2\cos\theta_e^r} e^{i\left(k_e^r x_r + k_h^r x_r'\right)} a_3, \tag{4.46a}$$

$$f_x(x_r,x_r',\omega,k_y) = \cos\left(\frac{\theta_e^r - \theta_h^r}{2}\right) \frac{i\, e^{-i/2\left(\theta_e^r - \theta_h^r\right)}}{2\cos\theta_e^r} e^{i\left(k_e^r x_r + k_h^r x_r'\right)} a_3 \tag{4.46b}$$

$$f_y(x_r,x_r',\omega,k_y) = -\sin\left(\frac{\theta_e^r - \theta_h^r}{2}\right) \frac{i\, e^{-i/2\left(\theta_e^r - \theta_h^r\right)}}{2\cos\theta_e^r} e^{i\left(k_e^r x_r + k_h^r x_r'\right)} a_3 \tag{4.46c}$$

$$f_z(x_r,x_r',\omega,k_y) = \sin\left(\frac{\theta_e^r + \theta_h^r}{2}\right) \frac{e^{-i/2\left(\theta_e^r - \theta_h^r\right)}}{2\cos\theta_e^l} e^{i\left(k_e^r x_r + k_h^r x_r'\right)} a_3, \tag{4.46d}$$

$$f_{\uparrow\uparrow}(x_r,x_r',\omega,k_y) = \frac{i}{2\cos\theta_e^r} e^{i\left(k_e^r x_r + k_h^r x_r'\right)} a_3, \tag{4.46e}$$

$$f_{\downarrow\downarrow}(x_r,x_r',\omega,k_y) = \frac{i\, e^{-i\left(\theta_e^r - \theta_h^r\right)}}{2\cos\theta_e^r} e^{i\left(k_e^r x_r + k_h^r x_r'\right)} a_3. \tag{4.46f}$$

Notice that both sets are directly proportional to the scattering coefficients related to LAR in each lead, a_1 and a_3. This illustrates that the proximity effect, i.e., the superconducting order *leaking* into the normal-state TIs, is mediated by (local) Andreev reflection, creating a Cooper pair in the process. Furthermore, we find that $f_s(x_l, x_l', k_y)$ vanishes if $x_l \to -\infty$ or/and $x_l' \to -\infty$ when we shift the frequency into the positive complex plane. The retarded Green function thus satisfies outgoing boundary conditions in this domain, which is consistent with our discussion in Sec. 3.2.2. This is true for the amplitudes $f_s(x_r, x_r', k_y)$ as well, i.e., they vanish as $x_r \to \infty$ or/and $x_r' \to \infty$.

Non-local pairing amplitudes

Next, we study the non-local amplitudes across the superconductor. When $x < x_L$ and $x' > x_R$, we have

$$\begin{aligned}
f_0(x_l, x_r, \omega, k_y) &= \sin\left(\frac{\theta_e^l - \theta_h^r}{2}\right) \frac{e^{-i/2\left(\theta_e^l - \theta_h^r\right)}}{2\cos\theta_e^l} e^{-i\left(k_e^l x_l - k_h^r x_r\right)} d_1, && \text{(4.47a)}\\
f_x(x_l, x_r, \omega, k_y) &= -\sin\left(\frac{\theta_e^l + \theta_h^r}{2}\right) \frac{e^{-i/2\left(\theta_e^l - \theta_h^r\right)}}{2\cos\theta_e^l} e^{-i\left(k_e^l x_l - k_h^r x_r\right)} d_1, && \text{(4.47b)}\\
f_y(x_l, x_r, \omega, k_y) &= \cos\left(\frac{\theta_e^l + \theta_h^r}{2}\right) \frac{e^{-i/2\left(\theta_e^l - \theta_h^r\right)}}{2\cos\theta_e^l} e^{-i\left(k_e^l x_l - k_h^r x_r\right)} d_1, && \text{(4.47c)}\\
f_z(x_l, x_r, \omega, k_y) &= \cos\left(\frac{\theta_e^l + \theta_h^r}{2}\right) \frac{e^{-i/2\left(\theta_e^l - \theta_h^r\right)}}{2\cos\theta_e^l} e^{-i\left(k_e^l x_l - k_h^r x_r\right)} d_1, && \text{(4.47d)}\\
f_{\uparrow\uparrow}(x_l, x_r, \omega, k_y) &= -\frac{i\, e^{-i\theta_e^l}}{2\cos\theta_e^l} e^{-i\left(k_e^l x_l - k_h^r x_r'\right)} d_1, && \text{(4.47e)}\\
f_{\downarrow\downarrow}(x_l, x_r, \omega, k_y) &= \frac{i\, e^{i\theta_h^r}}{2\cos\theta_e^l} e^{-i\left(k_e^l x_l - k_h^r x_r'\right)} d_1, && \text{(4.47f)}
\end{aligned}$$

whereas they read

$$\begin{aligned}
f_0(x_r, x_l, \omega, k_y) &= \sin\left(\frac{\theta_e^r - \theta_h^l}{2}\right) \frac{e^{-i/2\left(\theta_e^r - \theta_h^l\right)}}{2\cos\theta_e^r} e^{i\left(k_e^r x_r - k_h^l x_l\right)} d_3, && \text{(4.48a)}\\
f_x(x_r, x_l, \omega, k_y) &= \sin\left(\frac{\theta_e^r + \theta_h^l}{2}\right) \frac{e^{-i/2\left(\theta_e^r - \theta_h^l\right)}}{2\cos\theta_e^r} e^{i\left(k_e^r x_r - k_h^l x_l\right)} d_3, && \text{(4.48b)}\\
f_y(x_r, x_l, \omega, k_y) &= \cos\left(\frac{\theta_e^r + \theta_h^l}{2}\right) \frac{e^{-i/2\left(\theta_e^r - \theta_h^l\right)}}{2\cos\theta_e^r} e^{i\left(k_e^r x_r - k_h^l x_l\right)} d_3, && \text{(4.48c)}\\
f_z(x_r, x_l, \omega, k_y) &= \cos\left(\frac{\theta_e^r - \theta_h^l}{2}\right) \frac{e^{-i/2\left(\theta_e^r - \theta_h^l\right)}}{2\cos\theta_e^r} e^{i\left(k_e^r x_r - k_h^l x_l\right)} d_3, && \text{(4.48d)}\\
f_{\uparrow\uparrow}(x_r, x_l, \omega, k_y) &= -\frac{i\, e^{i\theta_h^l}}{2\cos\theta_e^r} e^{i\left(k_e^r x_r - k_h^l x_l\right)} d_3, && \text{(4.48e)}\\
f_{\downarrow\downarrow}(x_r, x_l, \omega, k_y) &= \frac{i\, e^{-i\theta_e^r}}{2\cos\theta_e^r} e^{i\left(k_e^r x_r - k_h^l x_l\right)} d_3, && \text{(4.48f)}
\end{aligned}$$

if $x > x_R$ and $x' < x_L$. This kind of pairing, also creating Cooper pairs in S, is dependent on the scattering coefficients associated to CAR, and we see that the proximity-effect is solely carried by Andreev reflections – either in the same lead, or from one lead to the other. The non-local amplitudes satisfy outgoing boundary conditions, as well, as can be seen when we shift the energy into the positive complex plane and perform the limits $x_l \to -\infty$ and $x_r \to \infty$.

Numerical evaluation

Similar to the transport characteristics, we do not consider the dependence of the amplitudes on single modes, but calculate the sum over all k_y. We therefore define the full amplitudes

$$f_s(x, x', \omega) \equiv \left|\sum_{k_y} f_s(x, x', \omega, k_y)\right|, \qquad s \in \{0, x, y, z, \uparrow\uparrow, \downarrow\downarrow\} \tag{4.49}$$

and replace the sum by an integral, *cf.* Eq. (4.24). Doing so, this reveals that f_y and f_z vanish when we add up the contributions from all modes, i.e.,

$$\sum_{k_y} f_y(x, x', \omega, k_y) = \sum_{k_y} f_z(x, x', \omega, k_y) = 0, \tag{4.50}$$

independent of the choice of the parameters and, in particular, x and x'. This is due to a point-symmetry of these quantities with respect to k_y and can be seen explicitly by the application of Eq. (4.37). We obtain

$$f_y(x, x', \omega, -k_y) = f_y(x, x', \omega, k_y), \qquad f_z(x, x', \omega, -k_y) = f_z(x, x', \omega, k_y). \tag{4.51}$$

Therefore, the amplitudes cancel themselves pairwise at modes k_y and $-k_y$, such that, in total, they vanish. This has an interesting effect on the full equal-spin pairing amplitudes, which can be seen from Eq. (4.44). Since f_y vanishes, while f_x remains finite, this means that these two quantities are equal,

$$f_{\uparrow\uparrow}(x, x', \omega) = f_{\downarrow\downarrow}(x, x', \omega), \tag{4.52}$$

independent of the choice of the parameters.

Let us now consider explicit results. As in the previous section, we focus on the bipolar domain $\mu_l = -\mu_r \equiv \mu$. As a reference, we define

$$f^0 \equiv f_0(-L_s/2, -L_s/2, 0), \tag{4.53}$$

i.e., the singlet-amplitude directly at the left interface and at the Fermi energy of the superconductor, $E = 0$ (in the BdG framework). This serves as a normalization factor for all quantities presented below. Moreover, all plots provide an inset illustrating where the amplitudes are evaluated, where the origin and the head of the arrows indicate x and x', respectively.

We show the pairing amplitudes in Fig. 4.6, where we use the same values for the electrochemical potentials as in the previous section and set $L = 1.1\xi$. Moreover, we evaluate them directly at the interfaces.

The plots confirm the properties derived above. Due to its symmetry with respect to k_y, f_z vanishes for all frequencies and independently of the choice of x and x'. For the same reason, the equal-spin triplet amplitudes are identical, locally and non-locally. We furthermore observe how the amplitudes are affected by the bipolar setup – except for $f_s(x_L, x_R, \omega)$, all quantities vanish at $\omega = \mu$. This can be explained individually, while all stems from the fact that the energy now lies at the Dirac points:

- $f_s(x_l, x_l, \omega = \mu)$ vanishes since LAR is not possible, completely suppressing the proximity effect at this frequency.
- $f_s(x_r, x_r, \omega = \mu)$ vanishes since no states are available in R for an electron to be excited, which equally suppresses LAR and thus the proximity effect.
- $f_s(x_r, x_l, \omega = \mu)$ vanishes since no states are available for CAR processes, suppressing this non-local proximity-effect.

Solely $f_s(x_l, x_r, \omega = \mu)$ remains finite at $\omega = \mu$, which is apparent since both an electron state in L as well as a hole state in R exist. Apparently, the bipolar setup affects the pairing amplitudes in the same way as the transport properties.

Intriguingly, we find that the non-local singlet pairing amplitudes vanish completely for all choices of ω. This is not due to a symmetry with respect to k_y, i.e., it is not the contributions from each mode which cancel themselves out, but another interesting feature of the bipolar setup. Since the hole dispersion in R corresponds to the electron dispersion in L (and vice versa), the angle under which the electron approaches the interface is the same as the angle of the transmitted hole moving away from the interface, $\theta_e^{l/r} = \theta_h^{r/l}$, *cf.* Eqs. (4.14) and (4.15). As a consequence, the single-mode singlet amplitudes

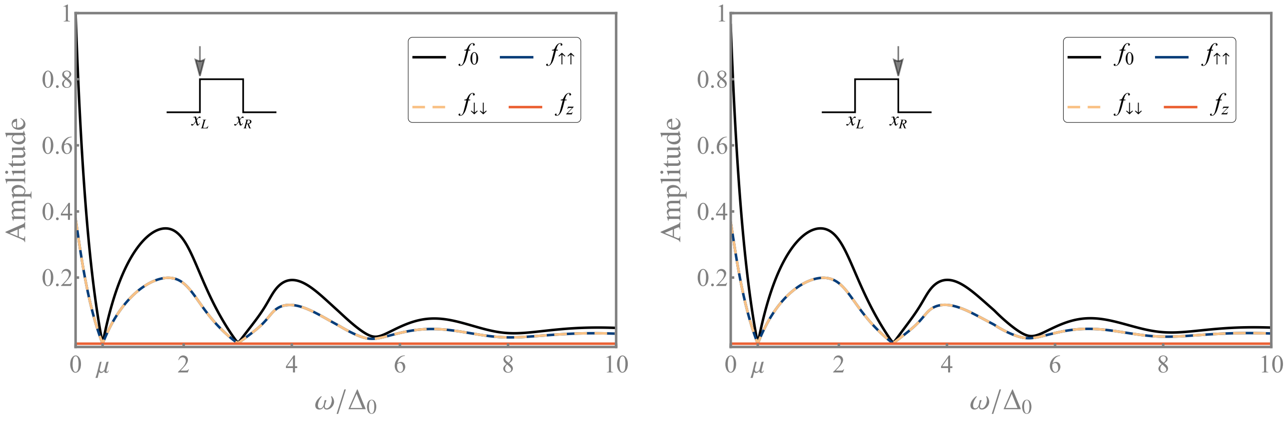

(a) $f_s(x_L, x_L, \omega)$ **(b)** $f_s(x_R, x_R, \omega)$

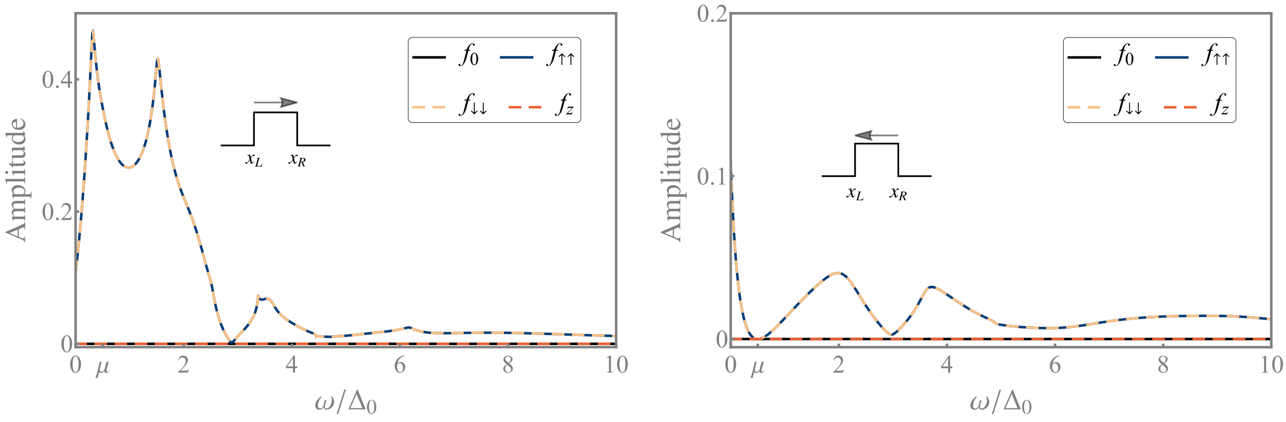

(c) $f_s(x_L, x_R, \omega)$ **(d)** $f_s(x_R, x_L, \omega)$

Fig. 4.6: Full pairing amplitudes as a function of ω in the bipolar setup at **(a)** the left interface and **(b)** the right interface as well as non-locally from **(c)** the left to the right and **(d)** the right to the left interface. f_z vanishes due to its point-symmetry in k_y, while the non-local singlet amplitudes vanish globally in the bipolar setup. All quantities are normalized to f^0. We choose $\mu_s = 10\,\Delta_0$, $\mu = 0.5\Delta_0$ and $L_s = 1.1\xi$. *Reprinted figure with permission from [102]. Copyright (2021) by the American Physical Society.*

in Eqs. (4.47) and (4.48) evaluate to zero in the bipolar setup and for any choice of the parameters. This means that non-local singlet pairing is completely suppressed, which strongly promotes equal-spin triplet pairing across the junction. In combination with the strong contributions of CAR, this is the second building block in the formation of equal-spin Cooper pairs in S, as we will show shortly.

Before we proceed, let us discuss the position-dependence of the pairing amplitudes, which we plot in Fig. 4.7. Here, we evaluate the local amplitudes at the same position, $x_{l/r} = x'_{l/r}$. In contrast, for the non-local amplitudes, we fix one location to x_L or x_R (dependent on the interface which is approached by the incident particle) and vary the other. Apparently, all amplitudes decay as we move away from the interfaces into the bulk TIs, which is consistent with the Green function obeying outgoing boundary conditions. As a consequence, the proximity-effect occurs in the proximity of the interfaces and vanishes in the asymptotic domains $x \to \pm\infty$. The value at the interface, *cf.* Fig. 4.6, as well as the rate at which the amplitudes decrease, depend on the frequency ω, such that for energies $\omega \approx 0$, the local amplitudes reach far into the bulk. This is not the case for the non-local amplitudes.

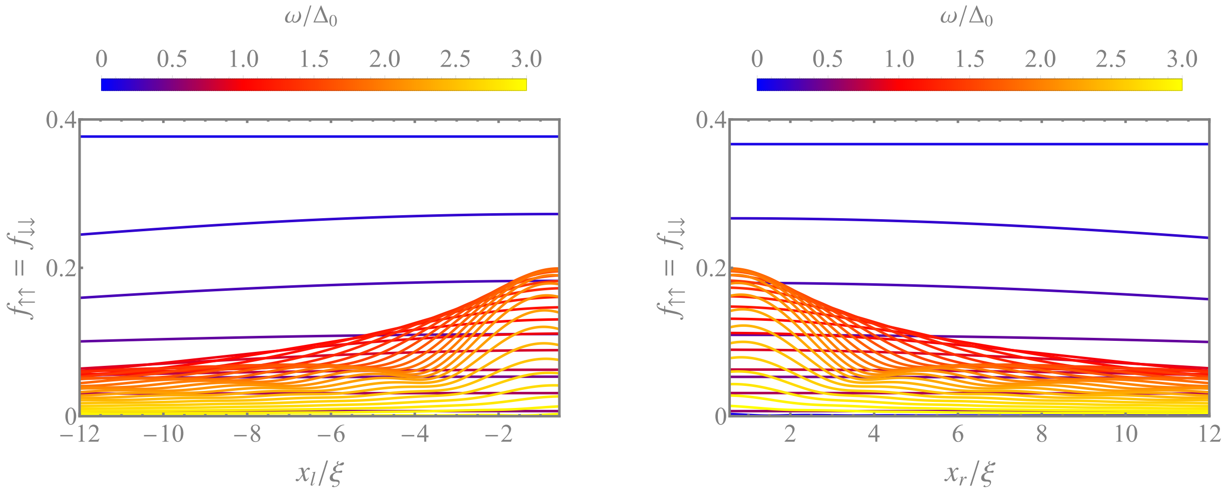

(a) $f_s(x_l, x_l, \omega)$ **(b)** $f_s(x_r, x_r, \omega)$

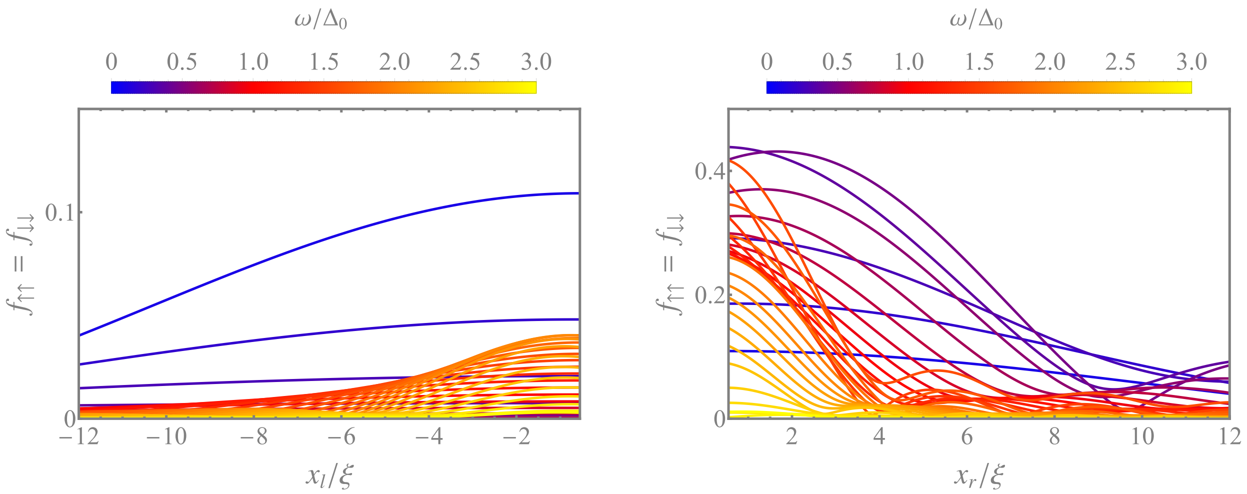

(c) $f_s(x_l, x_R, \omega)$ **(d)** $f_s(x_L, x_r, \omega)$

Fig. 4.7: Position-dependence of the equal-spin pairing amplitudes for different choices of the frequency for **(a)** $x_l = x_l'$, **(b)** $x_r = x_r'$, **(c)** $x_R = L_s/2$ and **(d)** $x_L = -L_s/2$. All quantities are normalized to f^0. We choose $\mu_s = 10\,\Delta_0$, $\mu = 0.5\Delta_0$ and $L_s = 1.1\xi$.

We can understand this from the position-dependent factors,

$$f_s(x_l, x_l, \omega, k_y) \propto e^{-i\left(k_e^l + k_h^l\right)x_l}, \tag{4.54a}$$

$$f_s(x_r, x_r, \omega, k_y) \propto e^{i\left(k_e^r + k_h^r\right)x_r}, \tag{4.54b}$$

$$f_s(x_l, x_R, \omega, k_y) \propto e^{-i\left(k_e^l x_l - k_h^r x_R\right)}, \tag{4.54c}$$

$$f_s(x_L, x_r, \omega, k_y) \propto e^{i\left(k_e^r x_r - k_h^l x_L\right)}. \tag{4.54d}$$

At $\omega = 0$, the wavenumbers of electrons and holes in the same lead are identical but differ in their signs, $k_e^{l/r} = -k_h^{l/r}$, such that they cancel each other and evaluate the exponential terms to unity. As a consequence, the amplitudes are not position-dependent at this energy and extend deep into the bulk. This is, of course, only true at zero temperature [124]. This cannot be achieved for the non-local pairing amplitudes, which are position-dependent at any energy.

Let us now proceed to the final part of this section, where we analyze the spin of the Cooper pairs created in a scattering event.

4.3.3 Spin injection

So far, we have observed two rather peculiar effects in TI-S-TI junctions in the bipolar setup, $\mu_l = -\mu_r \equiv \mu$, with $0 < \mu < \Delta_0$. (1) Due to the vanishing of LAR and CO for energies at the Dirac points, CAR governs the transport in the subgap-regime for an appropriate length of the S domain, *cf.* Figs. 4.3 to 4.5, while (2) opposite-spin triplet and non-local spin-singlet pairing are completely suppressed in such a system. This suggests a polarization of the Cooper pair net spin created in a LAR or CAR scattering process. The aim of this section is to elaborate and quantify this polarization.

Net spin pumped into the superconductor

The total spin of a Cooper pair created in either a LAR or CAR scattering event is determined by the spin of its building blocks. These are the incident electron as well as the additional electron removed from the Fermi sea, the latter leaving behind a hole state in the TI lead, see Fig. 4.8. We can calculate the spin of a given eigenstate by means of the BdG operator

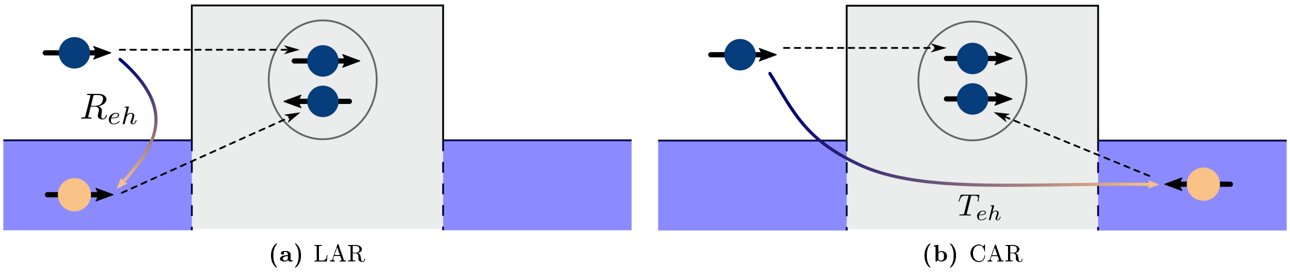

(a) LAR **(b)** CAR

Fig. 4.8: Illustration of the processes resulting in the emergence of Cooper pairs in the superconductor (gray), **(a)** local Andreev reflection with probability R_{eh} and **(b)** crossed Andreev reflection with probability T_{eh}. The incident as well as an additional electron from the Fermi sea (blue) in one of the TI leads are added to the condensate, leaving behind a hole. The arrows indicate the x-component of the spin according to Eq. (4.57).

$$\hat{S}_{\text{BdG}} = \frac{\hbar}{2} \begin{pmatrix} \boldsymbol{\sigma} & 0 \\ 0 & -\boldsymbol{\sigma}^* \end{pmatrix}, \tag{4.55}$$

with the vector of Pauli matrices in spin space

$$\boldsymbol{\sigma} = (s_x, s_y, s_z)^T . \tag{4.56}$$

$\hat{S}_{\text{BdG}}$ measures the spin of the incident electron and the reflected/transmitted hole correctly, and we obtain a spin texture as illustrated in Fig. 4.9(a). However, since we assume that the Fermi sea has zero angular momentum before the scattering process, the latter is not identical to the spin of the electron that is removed from the Fermi sea. Instead, we argue that the hole which emerges in a LAR or CAR process has the exact opposite spin of the second electron which is used to create the Cooper pair. As a consequence, we introduce an additional spin operator,

$$\hat{S}_{\text{CP}} = \frac{\hbar}{2} \begin{pmatrix} \boldsymbol{\sigma} & 0 \\ 0 & \boldsymbol{\sigma}^* \end{pmatrix}, \tag{4.57}$$

which assigns the opposite spin to a hole state, and denote it by *Cooper pair spin operator*. The spin texture of this operator is illustrated in Fig. 4.9(b) for LAR and in 4.9(c) for CAR. With this, we are able to determine the correct net spin in a scattering event. Defining $\langle\hat{S}\rangle$ and $\langle\hat{S}\rangle_{\text{LAR}}$ as the spin expectation values for the incident and the removed electron in L, respectively, we obtain

$$\langle\hat{S}\rangle_l \equiv \langle\hat{S}\rangle + \langle\hat{S}\rangle_{\text{LAR}} \tag{4.58}$$

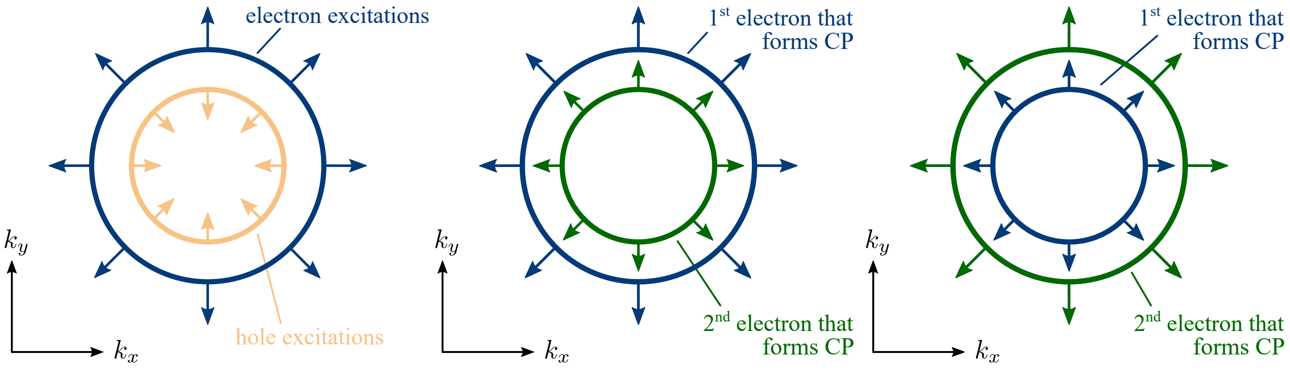

(a) $\hat{S}_{\mathrm{BdG}}$ **(b)** $\hat{S}_{\mathrm{CP}}$ (local) **(c)** $\hat{S}_{\mathrm{CP}}$ (non-local)

Fig. 4.9: Spin texture of the electron (blue) and hole (orange) states at a given excitation energy $E > \mu$ in the bipolar setup. Since the electron removed from the Fermi sea features the opposite spin of the reflected/transmitted hole, the spin texture in **(a)** is not accurate if we want to describe the full spin of the Cooper pair. Instead, we need to calculate its spin (green) from $\hat{S}_{\mathrm{CP}}$, such that we obtain the accurate **(b)** local and **(c)** non-local spin texture. *Reprinted figure with permission from [102]. Copyright (2021) by the American Physical Society.*

as the total spin of a Cooper pair created in a (local) LAR process. Introducing furthermore $\langle\hat{S}\rangle_{\mathrm{CAR}}$ as the spin expectation value of the removed electron in R, this yields the total spin of a Cooper pair created in a (non-local) CAR process,

$$\langle\hat{S}\rangle_{nl} \equiv \langle\hat{S}\rangle + \langle\hat{S}\rangle_{\mathrm{CAR}} \,. \tag{4.59}$$

Explicitly, we have

$$\langle\hat{S}\rangle \equiv \langle\psi^{+}_{e,l}(x)|\,\hat{S}_{\mathrm{CP}}\,|\psi^{+}_{e,l}(x)\rangle = \frac{\hbar}{2\,(E+\mu_l)}\left(k^l_e, k_y, 0\right)^T = \frac{\hbar}{2}\left(\cos\theta^l_e, \xi^l_e\sin\theta^l_e, 0\right)^T , \tag{4.60a}$$

$$\langle\hat{S}\rangle_{\mathrm{LAR}} \equiv \langle\psi^{-}_{h,l}(x)|\,\hat{S}_{\mathrm{CP}}\,|\psi^{-}_{h,l}(x)\rangle = \frac{\hbar}{2\,(E-\mu_l)}\left(-k^l_h, k_y, 0\right)^T = \frac{\hbar}{2}\left(-\cos\theta^l_h, \xi^l_h\sin\theta^l_h, 0\right)^T , \tag{4.60b}$$

$$\langle\hat{S}\rangle_{\mathrm{CAR}} \equiv \langle\psi^{+}_{h,r}(x)|\,\hat{S}_{\mathrm{CP}}\,|\psi^{+}_{h,r}(x)\rangle = \frac{\hbar}{2\,(E-\mu_r)}\,(k^r_h, k_y, 0)^T = \frac{\hbar}{2}\left(\cos\theta^r_h, \xi^r_h\sin\theta^l_h, 0\right)^T , \tag{4.60c}$$

with

$$\xi^l_e = \operatorname{sgn}\left(E+\mu_l\right), \qquad \xi^{l/r}_h = \operatorname{sgn}\left(E-\mu_{l/r}\right). \tag{4.61}$$

We find that all expectation values feature no component in z-direction, which is clear since the system is purely 2D and $\mathcal{H}_{\mathrm{BdG}}$ does not couple to this spin projection. Furthermore, in the bipolar setup, $\langle\hat{S}\rangle$ and $\langle\hat{S}\rangle_{CAR}$ are identical and we have perfect equal-spin pairing, while $\langle\hat{S}\rangle$ and $\langle\hat{S}\rangle_{LAR}$ show antiparallel alignment in the x-component. The latter is, in fact, the relevant spin projection, since the y-component is point-symmetric in k_y and thus vanishes when we sum over all modes. We therefore focus on the first element in the following. Finally, we note that the norm of each expectation value evaluates to $\hbar/2$, as to be expected for fermions.

The above provides an appropriate quantification of the Cooper pair net spin in a LAR or CAR process. However, since these scattering events occur only with a certain probability, it is not sufficient to describe the spin pumped into the superconductor for a given applied bias. Therefore, we assign a weight to the local and non-local Cooper pair spin, given by the probabilities of LAR and CAR, respectively, averaged over all modes k_y. This defines the *nonequilibrium net spin pumped into the S domain*,

$$\boldsymbol{\mathcal{S}} \equiv R_{\mathrm{LAR}}\,\langle\hat{S}\rangle_l + T_{\mathrm{CAR}}\,\langle\hat{S}\rangle_{nl} \,, \tag{4.62}$$

where, for the situation illustrated in Fig. 4.8, we have (we drop the superscripts for the sake of clarity)

$$R_{\text{LAR}} = R_{eh}, \qquad\qquad T_{\text{CAR}} = T_{eh}. \tag{4.63}$$

With the definitions above, we find that $\boldsymbol{\mathcal{S}}$ is manifestly bounded. While its y-component vanishes for all choices of the parameters, the total spin of the Cooper pairs can attain values $-1 \leq \langle \hat{S} \rangle_{l/nl} \leq 1$, and we therefore have

$$0 \leq |\boldsymbol{\mathcal{S}}_x| \leq R_{\text{LAR}} + T_{\text{CAR}} \leq 1. \tag{4.64}$$

The last inequality is a consequence of probability current conservation.

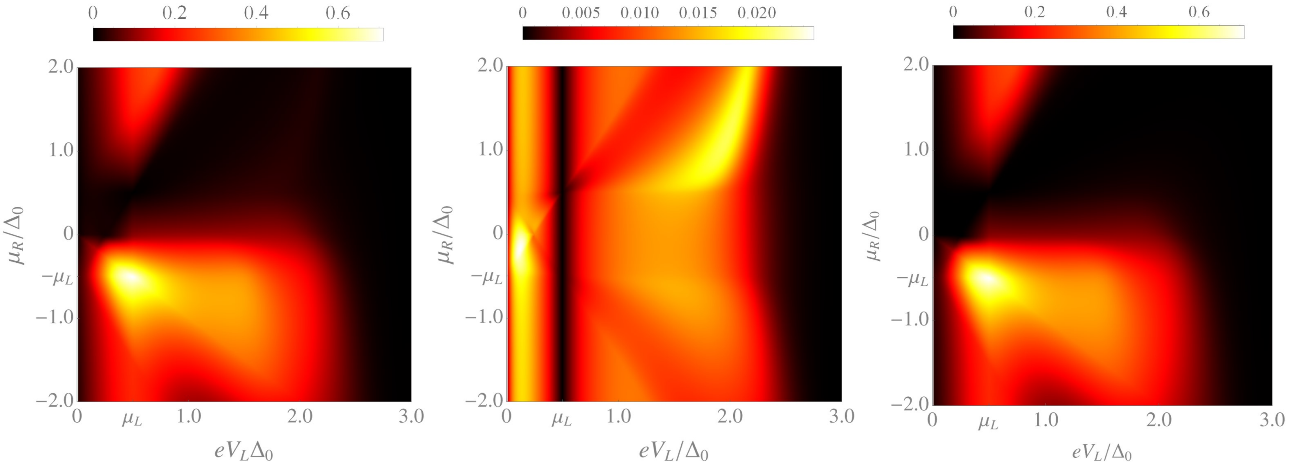

(a) $\hat{S}_{\text{BdG}}$ **(b)** $\hat{S}_{\text{CP}}$ (local) **(c)** $\hat{S}_{\text{CP}}$ (non-local)

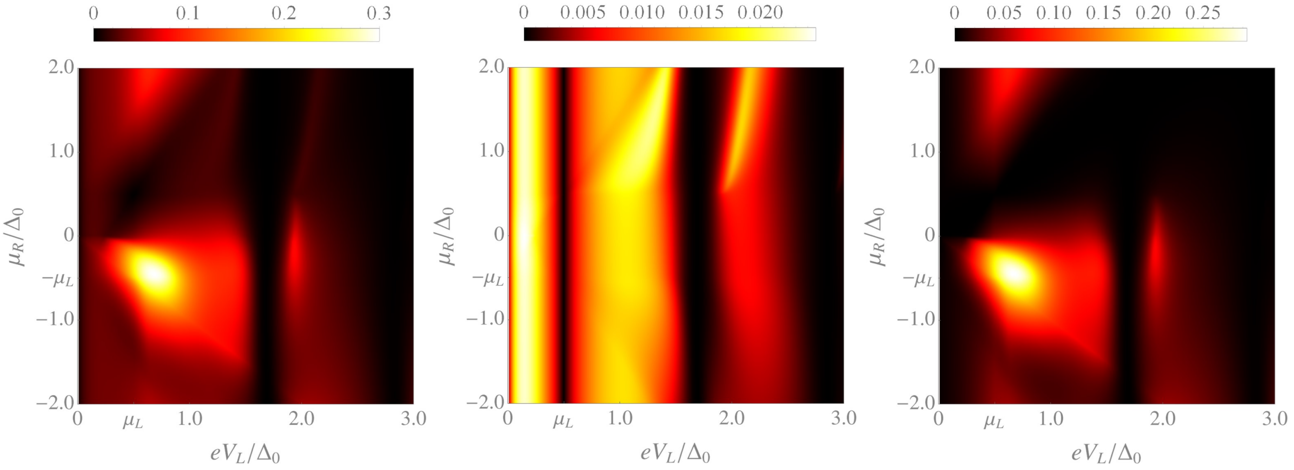

(d) $\hat{S}_{\text{BdG}}$ **(e)** $\hat{S}_{\text{CP}}$ (local) **(f)** $\hat{S}_{\text{CP}}$ (non-local)

Fig. 4.10: Nonequilibrium net spin pumped into the S domain as a function of eV_L and μ_r. We consider **(a,d)** the full quantity as well as its **(b,e)** local and **(c,f)** non-local contributions. We choose $\mu_s = 10\,\Delta_0$, $\mu_l = \Delta_0/2$ and **(a-c)** $L_s = 1.1\xi$ **(d-f)** $L_s = 2.3\xi$. *Reprinted figure with permission from [102]. Copyright (2021) by the American Physical Society.*

Let us now study this quantity. From Eq. (4.62) and our discussion above, we can expect strong contributions from the non-local pairing terms. The reasoning is, on the one hand, that the spin of the incident and the removed electron are equal in the bipolar setup and comparable in its alignment if we deviate from it. Furthermore, CAR has strong contributions in the subgap-regime for appropriate choices of the length L_s. In contrast, for the local parts, both spin projections are nearly antiparallel, and LAR is severely suppressed since the Dirac point of the hole band in L falls into the energy range $0 \leq E \leq \Delta_0$. This is exactly what we find in Fig. 4.10(a-c), where we present a contour plot of

$\boldsymbol{\mathcal{S}}_x$ as a function of both the applied bias eV_L and the electrochemical potential in the right TI, μ_r. The local contributions are, in fact, rather small and deviate up to a magnitude from their non-local counterparts. At $eV_L = \mu_l$, they vanish for all choices of μ_r, since we hit the Dirac point in the hole band structure.

Intriguingly, we find a peak at $eV_L = -\mu_r = \mu_l$, i.e., when we hit the *sweet spot* $eV_L = \mu$ in the bipolar setup, $\mu_l = -\mu_r = \mu$. This is a consequence of the strong contributions of CAR in this system and follows the curve of this transport characteristic, *cf.* Fig. 4.3, which equally features a maximum at the sweet spot. This becomes even more apparent in Fig. 4.11(a), where we show the bias dependence of the net spin pumped into the S domain for distinct choices of μ_r. In fact, the bipolar setup provides the strongest yield if we tune the bias into the proximity of the Dirac points in the hole dispersion in L. Moreover, we find that, at the sweet spot, CAR is, in fact, the only process that pumps Cooper pairs into the superconductor, resulting in the perfect creation of equal-spin Cooper pairs. And even though LAR contributes to $\boldsymbol{\mathcal{S}}_x$ if the bias deviates from $eV_L = \mu$, this contribution is rather small.

As we have shown, CAR is sensitive to the length of the S domain, *cf.* Fig. 4.5, and can be diminished or even suppressed for certain choices. We illustrate this in Fig. 4.10(d-f), where we choose the same length as in Fig. 4.4. Here, CAR is no longer the predominant process, and the maximum is shifted away from the sweet spot. We observe the same features in the net spin $\boldsymbol{\mathcal{S}}_x$. Even though the significant contributions stem from non-local pairing, the maximum is approximately half of that in Fig. 4.10(a-c) and shifted to slightly larger biases. As before, the curve follows the probability for CAR, *cf.* Fig. 4.4, which can be clearly seen in Fig. 4.11(b). Apparently, for this choice of the length, the bipolar setup is not the optimal choice. However, it yet provides a strong contribution to the net spin pumped into the S domain for biases in the proximity of the sweet spot.

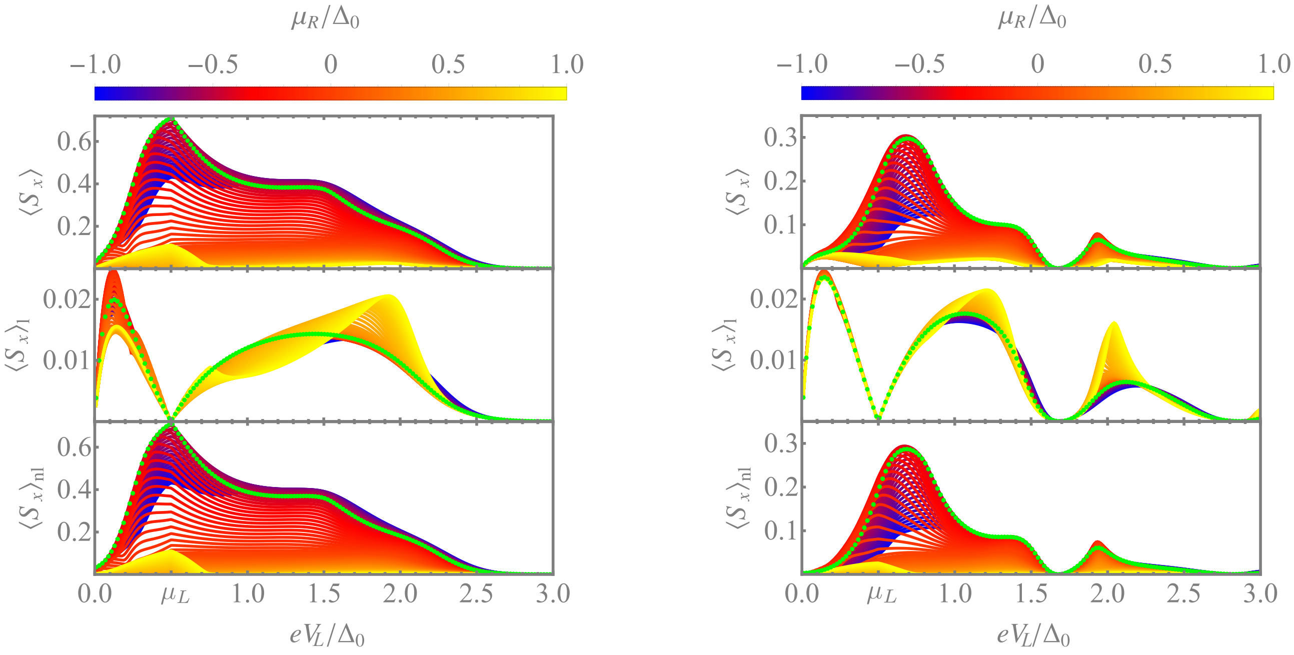

(a) $L_s = 1.1\xi$ **(b)** $L_s = 2.3\xi$

Fig. 4.11: (Top) Full nonequilibrium net spin pumped into the S domain as well as its **(middle)** local and **(bottom)** non-local contributions as a function of eV_L for various choices of μ_r. The bipolar setup is represented by the green dotted line. We choose $\mu_s = 10\,\Delta_0$, and $\mu_l = \Delta_0/2$.

Estimated effect

We assume that Cooper pairs are only created in the central superconductor when a bias is applied to the junction, which is why we denote it by the *nonequilibrium* net spin pumped into the S domain. We now want to estimate the effect of this pumping when the bias voltage is varied over a certain energy range, $\delta eV_l > \delta E > 0$. Therefore, we sum the contributions of $\boldsymbol{\mathcal{S}}$ over all wavenumbers k_x and k_y that fall into this domain, i.e.,

$$\boldsymbol{\mathcal{S}}_{\mathrm{est}} \equiv \sum_{k_x,k_y} \boldsymbol{\mathcal{S}}(k_x,k_y) \rightarrow \frac{A}{(2\pi)^2} \iint \mathrm{d}k_x \mathrm{d}k_y \boldsymbol{\mathcal{S}}(k_x,k_y) = \frac{A}{(2\pi)^2} \iint \mathrm{d}E \mathrm{d}k_y \left(\frac{\partial E}{\partial k_x}\right)^{-1} \boldsymbol{\mathcal{S}}(E,k_y), \quad (4.65)$$

where $A = L_x L_y$ is the area of the junction. We plot this quantity as a function of the electrochemical potential and different choices of the length L_s in Fig. 4.12, where we increase the voltage from zero to a value slightly above μ_l and to a voltage corresponding to the S order parameter Δ_0. In the former case, we can see that the bipolar setup is a favorable choice since we observe clear peaks at $\mu_r = -\mu_l$, particularly at $L_s = 1.1\xi$. This is due to the fact that, for most of the choices of the length (except for those at which CAR vanishes), CAR increases quickly in the proximity of the Dirac point of the hole band in L, *cf.* Figs. 4.3 and 4.4. In the latter case, the bipolar setup is yet favorable, while some peaks appear at lower μ_r. This stems from the shift of the CAR peak if the length is not optimal. Note that, independent of L_s, the effect nearly vanishes at $\mu_r = \mu_l$, i.e., when the TIs are identical in the electrochemical potential. Then, the Dirac points of both hole band structures in L and R lie at the same energy, such that LAR and CAR are severely suppressed and only a negligible number of Cooper pairs is pumped into the superconductor.

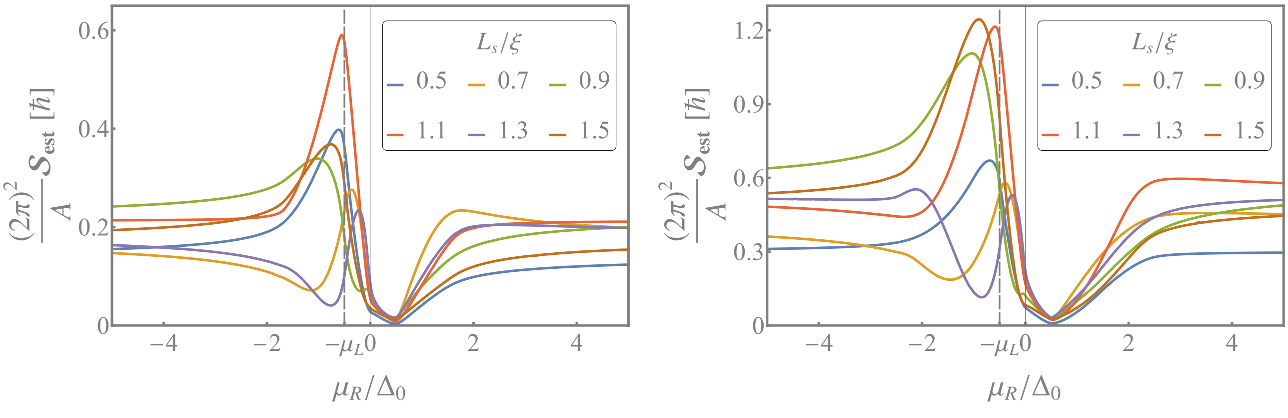

(a) $eV_L = 0$ to $eV_L = 0.6\,\Delta_0$ **(b)** $eV_L = 0$ to $eV_L = \Delta_0$

Fig. 4.12: Estimated spin pumped into the S domain as a function of μ_r for a bias increased from $eV_L = 0$ to **(a)** $0.6\,\Delta_0$ and **(c)** Δ_0. We choose $\mu_s = 10\,\Delta_0$ and $\mu_l = \Delta_0/2$. *Reprinted figure with permission from [102]. Copyright (2021) by the American Physical Society.*

4.4 Conclusion

In this chapter, we study the transport properties and the proximity effect in an NSN-junction where the underlying material is the 2D surface state of a 3D topological insulator with strong spin-orbit coupling. The central S domain is induced by means of a superconducting top electrode, separating the left and right TI regions in such a way that the carrier density can each be modified by the application of a gate voltage. In particular, we choose the system to be in the bipolar setup, where the electrochemical potentials in both leads have the same magnitude, but opposite signs. As a consequence, and for our choice of the parameters, the Dirac points of the hole band in the left lead and the electron band in the right lead lie at exactly the same energy, which we tune to fall inside the S gap of the central domain.

This has an interesting effect on the transport properties. LAR and CO are completely suppressed when we choose a bias that corresponds to the energy of the Dirac points, since in a 2D setup, a finite mode index opens a partial gap in the dispersion at $E = \mu$. If this energy lies inside the gap of the superconductor, both transport processes are rather unpronounced in the subgap-regime. Instead, NR and CAR govern the transport. For an appropriate length of the S domain, which does not exceed the superconducting coherence length ξ significantly, CAR even occurs with prominent probability, which is a rather unusual observation. As a consequence, the non-local differential conductance becomes comparable to its local counterpart for biases in the proximity of the Dirac points and even coincides with it at $eV_L = \mu$.

Another intriguing consequence of the bipolar setup is the suppression of any kind of non-local spin-singlet pairing across the junction. This is true for any mode k_y and due to the fact that this amplitude is proportional to the difference of the angles of the incident electron and the transmitted hole, $f_0 \propto \sin\left(\theta_e^l - \theta_h^r\right)$, which are identical in the bipolar setup. In contrast, the non-local equal-spin amplitudes are rather pronounced, which is related to the strong CAR contributions in such a system. Notably, f_z is suppressed locally and non-locally for all choices of the parameter when we consider the sum over all modes indexed by k_y.

Both effects mentioned above indicate significant equal-spin triplet pairing in the superconductor, and we introduce a quantity that determines the *nonequilibrium net spin pumped into the S domain* to study the Cooper pair spin polarization. To this end, we add the spin expectation value of the incident electron and that of the electron removed from the Fermi sea in a LAR and CAR process, respectively, weigh them by their respective, averaged probability, and consider the sum of both quantities. Considering the contributions from all modes indexed by k_y, this cancels the y-component of the net spin, such that only the x-component remains finite. We show that, in fact, a strong Cooper pair spin polarization can be observed in such a TI-S-TI junction. In particular, the bipolar setup is a favorable choice, since the peak of the nonequilibrium net spin appears at or in close proximity to the sweet spot $eV_L = \mu$, depending on the length of the superconductor. Moreover, this setup is experimentally easy to detect, since the local and non-local differential conductance coincide when the bias corresponds to the energy at the Dirac points.

To summarize, we propose the nanostructure presented in this chapter as a device for applications in spintronics, where equal-spin Cooper pairs can be created and manipulated by means of electrical switching and in the absence of magnetic ordering. This is possible due to the strong spin-orbit coupling in TIs and the associated breaking of spin-rotational invariance. As has been shown, Cooper pairs pumped into a superconductor can lead to long-range spin accumulation [157, 158], and we suggest measuring this effect by means of a Hall probe or a local superconducting quantum interference device. This requires a second superconductor connected to the central domain of the TI-S-TI junction [159–161].

5

Summary and outlook

In this Thesis, we employ scattering theory and associated concepts to study the transport properties and pairing amplitudes in mesoscopic heterojunctions where the underlying samples feature topological order. Materials like TIs and WSMs – in all their realizations – have been predicted and realized in the early 2000s and 2010s, respectively, and host a plethora of intriguing and fascinating physical phenomena. Among those are relativistic, linear surface states, pronounced spin-momentum locking in transport, Fermi surface arcs, the chiral anomaly, and anomalous magnetoconductance. Moreover, if we consider hybrid junctions featuring (local) superconducting order, this leads to the observation of Andreev bound states carrying superconducting currents in Josephson junctions or even the hypothetical emergence of Majorana bound states. Seldom has a concept captured both experimental and theoretical condensed matter physics like it is the case for topological materials. With this work, we want to provide a small contribution to this tremendous field by analyzing observable transport features as well as the peculiar proximity effect in distinct hybrid junctions of topological materials and superconductors.

In Chap. 2 we start quite generally with N'NN' or SNS junctions of non-topological materials that differ distinctly in their band structures. To this end, we extend the well-known wave matching conditions for 1D and quasi-1D hybrid junctions in scattering theory to more complex settings. Here, we assume that the materials, that are brought into contact, may exhibit unequal effective masses, Fermi velocities, and potentials of any kind and are thus rather distinct. Furthermore, we give a more general formula for the corresponding probability current density. This disparity in the band structures results in FSM, a situation where, for instance, an electron state described by a certain set of quantum numbers in one domain has no corresponding state in another domain and the transfer from one to the other is thus limited. In our context, this is the mode index k_y. Hence, an electron incident from a material with a large Fermi surface cannot penetrate a material with a smaller Fermi surface if its angle of incidence exceeds a certain critical angle. FSM thus acts as a directional filter in k-space and at the interfaces, effectively promoting normal reflection. We argue that a significant mismatch between the materials justifies the assumption of equilibrium reservoirs left and right of the scattering region if two of such interfaces are set in series in a hybrid junction. This allows the application of a bias across the junction and is a crucial requirement for the applicability of BTK theory in order to calculate the transport properties by means of the scattering formalism. We show that even though only a small portion of incident particles feature corresponding modes to be transmitted across the junction – and thus contribute to the differential conductance and the current in the system – these states can do so with prominent probabilities. In fact, we pinpoint distinct angles at which the transmission coefficient for electrical current can attain values up to its maximum. A crucial ingredient for this observation are clean interfaces, such that the barrier parameter, describing impurities or oxide layers between the materials, does not exceed a certain critical barrier strength. If this is fulfilled, strong currents can be expected in experiments. More interestingly, we observe similar characteristics if the leads feature superconducting order. The additional hole channel increases the transport coefficient and thus the differential conductance up to twice their normal-state counterpart, which may lead to pronounced excess currents in the system. Unfortunately, superconductivity also leads to a greater sensitivity of the transport properties to the barrier strength, such that a clean interface becomes even more important. In the next step, we replace the central scattering domain – which was a metal or semiconductor described by a generic quadratic Hamiltonian – with a HgTe QW, given by the more complex BHZ model. Despite the noticeable difference in the band structures, we observe the same features in the transport properties as in the simple model before. In fact, the differential conductance is even increased for the HgTe sample, since FSM is not only induced by different effective masses, but also by varying filling factors. As a consequence, we observe pronounced excess currents in S-HgTe-S junctions, where S denotes a superconductor. The results are qualitatively similar to those observed in Ref. [41] and theoretically described in Ref. [40]. Moreover, we find a justification on why BTK theory is applicable in such 2D (or even 3D) junctions, even though no spatial constrictions are given, this being FSM. The mismatch in the band structures thus directly affects the interface properties in heterojunctions of distinctly different materials. A simple experimental setup in which this can be tested is a N'NN' or SNS junction where a gate voltage is applied to the leads. Since a shift of the dispersion in energy directly affects FSM, the effect should be observable in transport measurements.

While the first chapter is rather technical and touches them only slightly, Chap. 3 puts an emphasis on topological materials. In particular, we study a system where the underlying sample is a TRS broken WSM with two Weyl nodes in the Brillouin zone. The latter are separated along a certain axis in momentum space, which is an indicator of the anisotropy of the dispersion. In a hybrid system, this has an interesting effect - the axis can include an angle with the normal of an interface between two materials. Moreover, CCP can be induced by the application of parallel electric and magnetic fields or by strain deformation, meaning that the filling factor differs at the two Weyl nodes. We analyze the effect of both parameters on the transport characteristics as well as on the pairing amplitudes in the normal-state WSM domains. The effect of the angle between the axis separating the Weyl nodes and the interface normal is well captured in the effective order parameter $\tilde{\Delta}_0 = \Delta_0 \, |\sin\alpha|$. For a perpendicular orientation, $\alpha = \pm\pi/2$, $\tilde{\Delta}_0$ is identical to Δ_0, resulting in the strongest contributions by Andreev processes to the differential conductances, which are maximal in this case. This is equally true for the opposite-spin pairing amplitudes, which are directly related to LAR and CAR. The equal-spin amplitudes, however, vanish when we sum over all modes due to the restoration of a C_2-symmetry of the BdG-Hamiltonian at these angles. For $\alpha \in \{0, \pm\pi\}$, the effective gap is zero and all particle-conversion processes are completely suppressed, as is the proximity effect (independent of the mode). Only NR and CO are observable under these circumstances. The equal-spin pairing amplitudes are maximal for angles in the proximity of $\alpha \approx \pm\pi/4$ and $\alpha \approx \pm 3\pi/4$. For intermediate angles, the curves are comparable and depend primarily on the strength of $\tilde{\Delta}_0$. More intriguing features can be observed when CCP is induced into the system. While for the transport, the effect solely corresponds to a shift in the bias, the consequence of CCP is richer for the pairing amplitudes. In its absence, the effect is such that each Weyl node favors a different spin polarization in the leads (e.g., $f_{\uparrow\uparrow}$ in the left and $f_{\downarrow\downarrow}$ in the right lead). However, it is exactly the opposite for the other Weyl node, such that no total spin polarization remains. This situation changes if CCP is finite and the nodes of opposite chirality feature different filling factors. Since the pairing amplitudes are shifted in opposite directions (on the frequency axis), this results in a net spin polarization of the Cooper pairs leaking into the normal leads. Since the predominant equal-spin amplitude in each WSM is different, the junction assumes a dipole character. We thus propose this system as an interesting device for applications in superconducting spintronics. Finally, we remark that, since both quantities enter the Hamiltonian similarly, the differential conductance and the proximity effect can be tuned by both the applied bias/frequency as well as CCP.

The focus in the last chapter, Chap. 4, lies equally on NSN-junctions, with the distinction that here, the underlying material is the 2D surface state of a 3D TI where superconductivity is induced by the proximity effect. This separation due to S allows for independent gating of the normal-state TI leads, and we consider the particular case of a bipolar setup. We assume that the magnitude of the electrochemical potentials is equal left and right of the superconductor, while the sign is opposite. As a consequence, the electron (hole) band in one domain corresponds to the hole (electron) band in the other domain (except for the particle nature), as do the associated Dirac points. Choosing the electrochemical potential to lie inside the superconducting gap and tuning the bias to the Dirac nodes, this results in a situation where an incident electron cannot undergo LAR nor CO, but solely NR and CAR due to the partial gap that emerges at the Dirac points in 2D junctions. Intriguingly, this leads to overall small contributions of LAR and CO in the subgap-regime, resulting in a non-local differential conductance which is comparable to its local counterpart for biases $eV \approx \mu$. This observation is rather unusual since the latter is commonly more pronounced than the former. The length of the S domain, however, is a crucial factor since CAR can be completely suppressed for a certain choice of L_s. For the proximity effect, the bipolar setup is an equally fascinating choice. Any kind of spin-singlet pairing across the junction is completely suppressed, independent of the energy or the mode. And since the mode-averaged opposite-spin triplet vanishes, the non-local equal spin amplitudes are enhanced for this choice of parameters. This, in combination with the strong CAR contributions in the subgap-transport, suggests a significant spin polarization of the Cooper pair created in a scattering event in such a bipolar NSN-junction. We introduce a quantity to estimate the effect, the *nonequilibrium* *net spin polarization of Cooper pairs pumped into the S domain*, and evaluate it averaged over all incident modes k_y. While the y- and z-components vanish, the x-projection of the Cooper pair net spin remains finite and can attain noticeable values for the appropriate choice of parameters. Even though the length of the superconducting domain is a crucial factor and needs to be chosen in such a way that CAR does not vanish, the bipolar setup is, in general, a favorable choice to obtain a significant amount of equal-spin Cooper pairs created in the superconductor. Intriguingly, this is feasible due to the strong spin-orbit coupling and the associated breaking of spin-rotational invariance in TIs and does not require the application of magnetic fields. The effect should be measurable by means of a Hall probe or a superconducting quantum interference device in the proximity of the central S domain.

Herewith, we conclude this Thesis. As an outlook, we remark that the junctions we consider are assumed to extend infinitely along the axes perpendicular to the interface normal. This suggests studying FSM, transport properties, and proximity effect in finite-size materials with open boundary conditions in these, up to now, translational invariant directions. The question remains on how strongly the dipole character of the WSM junction or the formation of equal-spin Cooper pairs in the 2D surface state are affected under these circumstances. Tight-binding or finite-difference calculations are particularly interesting considering FSM, since these allow us to introduce a mismatch into the system, as well as to (numerically) analyze distinct features of the interfaces themselves. This does not only include different shapes or alignments of the latter, but also rather exotic properties like the before-mentioned pinholes in 2D interfaces. Those are assumed to be generally opaque, except for certain spots where transmission from one domain into the other is possible. We expect exciting results from such studies and do not rule out even more intriguing setups or extensions for future research in this field.

References

[1] R. Feynman, R. B. Leighton, and M. Sands. *The Feynman Lectures on Physics, Vol. II: the Electromagnetic Field.* Addison-Wesley, Reading, Massachusetts (1965).

[2] W. Nolting. *Grundkurs Theoretische Physik 3: Elektrodynamik.* Springer, Berlin, Deutschland (2013).

[3] D. J. Griffiths. *Introduction to electrodynamics (4th ed.).* Pearson, Boston, Massachusetts (2013).

[4] P. Drude. *Zur Elektronentheorie der Metalle.* Annalen der Physik **306**, 566–613 (1900).

[5] P. Drude. *Zur Elektronentheorie der Metalle; II. Teil. Galvanomagnetische und thermomagnetische Effecte.* Annalen der Physik **308**, 369–402 (1900).

[6] A. Sommerfeld. *Zur Elektronentheorie der Metalle auf Grund der Fermischen Statistik.* Zeitschrift für Physik **47**, 1–32 (1928).

[7] E. Schrödinger. *An Undulatory Theory of the Mechanics of Atoms and Molecules.* Phys. Rev. **28**, 1049–1070 (1926).

[8] S. Datta. *Electronic Transport in Mesoscopic Systems.* Cambridge Studies in Semiconductor Physics and Microelectronic Engineering. Cambridge University Press (1995).

[9] E. H. Hall. *On a New Action of the Magnet on Electric Currents.* American Journal of Mathematics **2**, 287–292 (1879).

[10] L. D. Landau. *Diamagnetism of metals.* Zeitschrift für Physik **64**, 629–637 (1930).

[11] B. Volkov and O. Pankratov. *Two-dimensional massless electrons in an inverted contact.* JETP Letters **42** (1985).

[12] O. Pankratov, S. Pakhomov, and B. Volkov. *Supersymmetry in heterojunctions: Band-inverting contact on the basis of* $Pb_{1\text{-}x}Sn_xTe$ *and* $Hg_{1\text{-}x}Cd_xTe$. Solid State Communications **61**, 93–96 (1987).

[13] C. L. Kane and E. J. Mele. *Quantum Spin Hall Effect in Graphene.* Phys. Rev. Lett. **95**, 226801 (2005).

[14] B. A. Bernevig and S.-C. Zhang. *Quantum Spin Hall Effect.* Phys. Rev. Lett. **96**, 106802 (2006).

[15] M. König, S. Wiedmann, C. Brune, A. Roth, H. Buhmann, L. W. Molenkamp, X.-L. Qi, and S.-C. Zhang. *Quantum Spin Hall Insulator State in HgTe Quantum Wells.* Science **318**, 766–770 (2007).

[16] M. Vergniory, L. Elcoro, C. Felser, N. Regnault, B. Bernevig, and Z. Wang. *A complete catalogue of high-quality topological materials.* Nature **566**, 480–485 (2019).

[17] S. M. Young, S. Zaheer, J. C. Y. Teo, C. L. Kane, E. J. Mele, and A. M. Rappe. *Dirac Semimetal in Three Dimensions.* Phys. Rev. Lett. **108**, 140405 (2012).

[18] B. Yan and C. Felser. *Topological Materials: Weyl Semimetals.* Annual Review of Condensed Matter Physics **8**, 337–354 (2017).

[19] N. P. Armitage, E. J. Mele, and A. Vishwanath. *Weyl and Dirac semimetals in three-dimensional solids.* Rev. Mod. Phys. **90**, 015001 (2018).

[20] S.-Y. Xu, I. Belopolski, N. Alidoust, M. Neupane, G. Bian, C. Zhang, R. Sankar, G. Chang, Z. Yuan, C.-C. Lee, S.-M. Huang, H. Zheng, J. Ma, D. S. Sanchez, B. Wang, A. Bansil, F. Chou, P. P. Shibayev, H. Lin, S. Jia, and M. Z. Hasan. *Discovery of a Weyl fermion semimetal and topological Fermi arcs.* Science **349**, 613–617 (2015).

[21] A. A. Soluyanov, D. Gresch, Z. Wang, Q. Wu, M. Troyer, X. Dai, and B. Bernevig. *Type-II Weyl semimetals.* Nature **527**, 495 – 498 (2015).

[22] D. van Delft and P. Kes. *The discovery of superconductivity.* Physics Today **63**, 38–43 (2010).

[23] W. Meissner and R. Ochsenfeld. *Ein neuer Effekt bei Eintritt der Supraleitfähigkeit.* Naturwissenschaften **21**, 787–788 (1933).

[24] J. Bardeen, L. N. Cooper, and J. R. Schrieffer. *Microscopic Theory of Superconductivity.* Phys. Rev. **106**, 162–164 (1957).

[25] A. F. Andreev. *The Thermal Conductivity of the Intermediate State in Superconductors.* JETP **19**, 1228 (1964).

[26] A. K. Saxena. *High–temperature superconductors.* Springer–Verlag, Berlin, Germany (2012).

[27] G. E. Blonder, M. Tinkham, and T. M. Klapwijk. *Transition from metallic to tunneling regimes in superconducting microconstrictions: Excess current, charge imbalance, and supercurrent conversion.* Phys. Rev. B **25**, 4515–4532 (1982).

[28] Y. Imry and R. Landauer. *Conductance viewed as transmission.* Reviews of Modern Physics **71**, S306–S312 (1999).

[29] E. Scheer, N. Agraït, J. C. Cuevas, A. L. Yeyati, B. Ludoph, A. Martín-Rodero, G. Rubio Bollinger, J. M. v. Ruitenbeek, and C. Urbina. *The signature of chemical valence in the electrical conduction through a single-atom contact.* Nature **394**, 154–157 (1998).

[30] C. Beenakker and H. van Houten. *Quantum Transport in Semiconductor Nanostructures.* In H. Ehrenreich and D. Turnbull, eds., *Semiconductor Heterostructures and Nanostructures*, vol. 44 of *Solid State Physics*. Academic Press (1991).

[31] C. J. Lambert, V. C. Hui, and S. J. Robinson. *Multi-probe conductance formulae for mesoscopic superconductors.* Journal of Physics: Condensed Matter **5**, 4187–4206 (1993).

[32] M. P. Anantram and S. Datta. *Current fluctuations in mesoscopic systems with Andreev scattering.* Phys. Rev. B **53**, 16390–16402 (1996).

[33] J. Linder and A. Sudbø. *Tunneling conductance in s- and d-wave superconductor-graphene junctions: Extended Blonder-Tinkham-Klapwijk formalism.* Phys. Rev. B - Condens. Matter Mater. Phys. **77**, 1–14 (2008).

[34] D. Breunig, S.-B. Zhang, B. Trauzettel, and T. M. Klapwijk. *Directional electron filtering at a superconductor-semiconductor interface.* Phys. Rev. B **103**, 165414 (2021).

[35] L. Fu, C. L. Kane, and E. J. Mele. *Topological Insulators in Three Dimensions.* Phys. Rev. Lett. **98**, 106803 (2007).

[36] J. Wiedenmann, E. Bocquillon, R. S. Deacon, S. Hartinger, O. Herrmann, T. M. Klapwijk, L. Maier, C. Ames, C. Brüne, C. Gould, A. Oiwa, K. Ishibashi, S. Tarucha, H. Buhmann, and L. Molenkamp. *4π periodic Josephson supercurrent in HgTe-based topological Josephson junctions.* Nat. Commun. **7**, 1–7 (2015).

[37] C. Beenakker and H. Van Houten. *Josephson current through a superconducting quantum point contact shorter than the coherence length.* Phys. Rev. Lett. **66**, 3056–3059 (1991).

[38] Y. Nazarov and Y. M. Blanter. *Quantum Transport. Introduction to Nanoscience.* Cambridge University Press, Cambridge (2009).

[39] J. B. Oostinga, L. Maier, P. Schüffelgen, D. Knott, C. Ames, C. Brüne, G. Tkachov, H. Buhmann, and L. W. Molenkamp. *Josephson Supercurrent through the Topological Surface States of Strained Bulk HgTe.* Phys. Rev. X **3**, 021007 (2013).

[40] D. K. Efetov and K. B. Efetov. *Crossover from retro to specular Andreev reflections in bilayer graphene.* Phys. Rev. B **94**, 075403 (2016).

[41] D. Efetov, L. Wang, C. Handschin, K. Efetov, J. Shuang, R. Cava, T. Taniguchi, K. Watanabe, J. Hone, C. Dean, and P. Kim. *Specular interband Andreev reflections at van der Waals interfaces between graphene and NbSe2.* Nat. Phys. **12**, 328–332 (2016).

[42] V. E. Calado, S. Goswami, G. Nanda, M. Diez, A. R. Akhmerov, K. Watanabe, T. Taniguchi, T. M. Klapwijk, and L. M. Vandersypen. *Ballistic Josephson junctions in edge-contacted graphene.* Nat. Nanotechnol. **10**, 761–764 (2015).

[43] I. V. Borzenets, F. Amet, C. T. Ke, A. W. Draelos, M. T. Wei, A. Seredinski, K. Watanabe, T. Taniguchi, Y. Bomze, M. Yamamoto, S. Tarucha, and G. Finkelstein. *Ballistic Graphene Josephson Junctions from the Short to the Long Junction Regimes.* Phys. Rev. Lett. **117**, 1–5 (2016).

[44] M. Büttiker. *Absence of backscattering in the quantum Hall effect in multiprobe conductors.* Phys. Rev. B **38**, 9375–9389 (1988).

[45] A. Stone and A. Szafer. *What is measured when you measure a resistance?–The Landauer formula revisited.* IBM Journal of Research and Development **32**, 384–412 (1988).

[46] G. E. Blonder and M. Tinkham. *Metallic to tunneling transition in Cu-Nb point contacts.* Phys. Rev. B **27**, 112–118 (1983).

[47] M. Büttiker, Y. Imry, R. Landauer, and S. Pinhas. *Generalized many-channel conductance formula with application to small rings.* Phys. Rev. B **31**, 6207–6215 (1985).

[48] R. Landauer. *Electrical transport in open and closed systems.* Zeitschrift für Physik-Condensed Matter **68**, 217–228 (1987).

[49] R. Landauer. *Resistance of planar barriers.* Phys. Rev. B **52**, 11225–11230 (1995).

[50] Z. Radović, V. Paltoglou, N. Lazarides, and N. Flytzanis. *Resonant effects in ballistic Josephson junctions.* Eur. Phys. J. B **69**, 229–236 (2009).

[51] E. Bocquillon, R. S. Deacon, J. Wiedenmann, P. Leubner, T. M. Klapwijk, C. Brüne, K. Ishibashi, H. Buhmann, and L. Molenkamp. *Gapless Andreev bound states in the quantum spin Hall insulator HgTe.* Nat. Nanotechnol. **12**, 137–143 (2016).

[52] K. Bendias, S. Shamim, O. Herrmann, A. Budewitz, P. Shekhar, P. Leubner, J. Kleinlein, E. Bocquillon, H. Buhmann, and L. Molenkamp. *High Mobility HgTe Microstructures for Quantum Spin Hall effect studies.* Nanoletters **18**, 4831–4836 (2018).

[53] C. T. Ke, C. M. Moehle, F. K. de Vries, C. Thomas, S. Metti, C. R. Guinn, R. Kallaher, M. Lodari, G. Scappucci, T. Wang, and et al. *Ballistic superconductivity and tunable π–junctions in InSb quantum wells.* Nat. Commun. **10** (2019).

[54] J. Davies and J. Davies. *The Physics of Low-dimensional Semiconductors: An Introduction.* Cambridge University Press (1998).

[55] N. Horing. *Quantum Statistical Field Theory: An Introduction to Schwinger's Variational Method with Green's Function Nanoapplications, Graphene and Superconductivity.* International series of monographs on physics. Oxford University Press (2017).

[56] F. Crépin, P. Burset, and B. Trauzettel. *Odd-frequency triplet superconductivity at the helical edge of a topological insulator.* Phys. Rev. B **92**, 100507 (2015).

[57] M. Octavio, M. Tinkham, G. E. Blonder, and T. M. Klapwijk. *Subharmonic energy-gap structure in superconducting constrictions.* Phys. Rev. B **27**, 6739–6746 (1983).

[58] P. de Gennes. *Superconductivity of Metals and Alloys.* Perseus Books Group, 2. revised edn. (1999).

[59] J. F. Cochran and D. E. Mapother. *Superconducting Transition in Aluminum.* Phys. Rev. **111**, 132–142 (1958).

[60] B. A. Bernevig, T. L. Hughes, and S.-C. Zhang. *Quantum Spin Hall Effect and Topological Phase Transition in HgTe Quantum Wells.* Science **314**, 1757–1761 (2006).

[61] C. Liu and S. Zhang. *Models and Materials for Topological Insulators.* Contemporary Concepts of Condensed Matter Science **6**, 59–89 (2013).

[62] A. I. Kiselev, L. A. Akashev, and V. I. Kononenko. *Effective electron mass in melts of aluminum, cerium, and Al-3 at.% Ce binary system.* Technical Physics **49**, 302–305 (2004).

[63] J. Song, H. Liu, J. Liu, Y.-X. Li, R. Joynt, Q.-f. Sun, and X. C. Xie. *Quantum interference in topological insulator Josephson junctions.* Phys. Rev. B **93**, 195302 (2016).

[64] M. Kjaergaard, F. Nichele, H. J. Suominen, M. P. Nowak, M. Wimmer, A. R. Akhmerov, J. A. Folk, K. Flensberg, J. Shabani, C. J. Palmstrøm, and et al. *Quantized conductance doubling and hard gap in a two-dimensional semiconductor–superconductor heterostructure.* Nat. Commun. **7** (2016).

[65] A. Kastalsky, A. W. Kleinsasser, L. H. Greene, R. Bhat, F. P. Milliken, and J. P. Harbison. *Observation of pair currents in superconductor-semiconductor contacts.* Phys. Rev. Lett. **67**, 3026–3029 (1991).

[66] C. W. J. Beenakker. *Quantum transport in semiconductor-superconductor microjunctions.* Phys. Rev. B **46**, 12841–12844 (1992).

[67] P. Hosur and X. Qi. *Recent developments in transport phenomena in Weyl semimetals.* C. R. Phys. **14**, 857 (2013).

[68] A. M. Turner and A. Vishwanath. *Chapter 11 - Beyond Band Insulators: Topology of Semimetals and Interacting Phases.* In M. Franz and L. Molenkamp, eds., *Topological Insulators*, vol. 6 of *Contemporary Concepts of Condensed Matter Science*, pp. 293–324. Elsevier (2013).

[69] B. A. Bernevig. *It's been a Weyl coming.* Nat. Phys. **11**, 698 (2015).

[70] A. A. Burkov. *Topological semimetals.* Nat. Mater. **15**, 1145 (2016).

[71] X. Wan, A. M. Turner, A. Vishwanath, and S. Y. Savrasov. *Topological semimetal and Fermi-arc surface states in the electronic structure of pyrochlore iridates.* Phys. Rev. B **83**, 205101 (2011).

[72] H. B. Nielsen and M. Ninomiya. *The Adler-Bell-Jackiw anomaly and Weyl fermions in a crystal.* Phys. Lett. B **130**, 389 (1983).

[73] A. A. Zyuzin and A. A. Burkov. *Topological response in Weyl semimetals and the chiral anomaly.* Phys. Rev. B **86**, 115133 (2012).

[74] D. T. Son and B. Z. Spivak. *Chiral anomaly and classical negative magnetoresistance of Weyl metals.* Phys. Rev. B **88**, 104412 (2013).

[75] A. A. Burkov. *Chiral Anomaly and Diffusive Magnetotransport in Weyl Metals.* Phys. Rev. Lett. **113**, 247203 (2014).

[76] H.-Z. Lu, S.-B. Zhang, and S.-Q. Shen. *High-field magnetoconductivity of topological semimetals with short-range potential.* Phys. Rev. B **92**, 045203 (2015).

[77] S.-B. Zhang, H.-Z. Lu, and S.-Q. Shen. *Linear magnetoconductivity in an intrinsic topological Weyl semimetal.* New J. Phys. **18**, 053039 (2016).

[78] S. A. Parameswaran, T. Grover, D. A. Abanin, D. A. Pesin, and A. Vishwanath. *Probing the Chiral Anomaly with Nonlocal Transport in Three-Dimensional Topological Semimetals.* Phys. Rev. X **4**, 031035 (2014).

[79] A. A. Burkov and L. Balents. *Weyl Semimetal in a Topological Insulator Multilayer.* Phys. Rev. Lett. **107**, 127205 (2011).

[80] G. B. Halász and L. Balents. *Time-reversal invariant realization of the Weyl semimetal phase.* Phys. Rev. B **85**, 035103 (2012).

[81] M. Hirayama, R. Okugawa, S. Ishibashi, S. Murakami, and T. Miyake. *Weyl Node and Spin Texture in Trigonal Tellurium and Selenium.* Phys. Rev. Lett. **114**, 206401 (2015).

[82] H. M. Weng, C. Fang, Z. Fang, B. A. Bernevig, and X. Dai. *Weyl Semimetal Phase in Noncentrosymmetric Transition-Metal Monophosphides.* Phys. Rev. X **5**, 011029 (2015).

[83] S. M. Huang, S. Y. Xu, I. Belopolski, C. C. Lee, G. Chang, B. K. Wang, N. Alidoust, G. Bian, M. Neupane, C. Zhang, S. Jia, A. Bansil, H. Lin, and M. Z. Hasan. *A Weyl Fermion semimetal with surface Fermi arcs in the transition metal monopnictide TaAs class.* Nat. Commun. **6**, 7373 (2015).

[84] T. Rauch, S. Achilles, J. Henk, and I. Mertig. *Spin chirality tuning and topological semimetals in strained* $HgTe_xS_{1-x}$. Phys. Rev. Lett. **114**, 236805 (2015).

[85] J. Ruan, S.-K. Jian, H. Yao, H. Zhang, S.-C. Zhang, and D. Xing. *Symmetry-protected ideal Weyl semimetal in HgTe-class materials.* Nat. Commun. **7**, 11136 (2016).

[86] J. Ruan, S.-K. Jian, D. Zhang, H. Yao, H. Zhang, S.-C. Zhang, and D. Xing. *Ideal Weyl Semimetals in the Chalcopyrites* $CuTlSe_2$, $AgTlTe_2$, $AuTlTe_2$, *and* $ZnPbAs_2$. Phys. Rev. Lett. **116**, 226801 (2016).

[87] Z. Wang, M. G. Vergniory, S. Kushwaha, M. Hirschberger, E. V. Chulkov, A. Ernst, N. P. Ong, R. J. Cava, and B. A. Bernevig. *Time-Reversal-Breaking Weyl Fermions in Magnetic Heusler Alloys.* Phys. Rev. Lett. **117**, 236401 (2016).

[88] Y. J. Jin, R. Wang, Z. J. Chen, J. Z. Zhao, Y. J. Zhao, and H. Xu. *Ferromagnetic Weyl semimetal phase in a tetragonal structure.* Phys. Rev. B **96**, 201102 (2017).

[89] H. Yang, Y. Sun, Y. Zhang, W.-J. Shi, S. S. P. Parkin, and B. Yan. *Topological Weyl semimetals in the chiral antiferromagnetic materials Mn 3 Ge and Mn 3 Sn.* New J. Phys. **19**, 015008 (2017).

[90] G. Chang, B. Singh, S.-Y. Xu, G. Bian, S.-M. Huang, C.-H. Hsu, I. Belopolski, N. Alidoust, D. S. Sanchez, H. Zheng, H. Lu, X. Zhang, Y. Bian, T.-R. Chang, H.-T. Jeng, A. Bansil, H. Hsu, S. Jia, T. Neupert, H. Lin, and M. Z. Hasan. *Magnetic and noncentrosymmetric Weyl fermion semimetals in the RAlGe family of compounds ($R =$ rare earth).* Phys. Rev. B **97**, 041104 (2018).

[91] S. Y. Xu, I. Belopolski, N. Alidoust, M. Neupane, G. Bian, C. L. Zhang, R. Sankar, G. Q. Chang, Z. J. Yuan, C. C. Lee, S. M. Huang, H. Zheng, J. Ma, D. S. Sanchez, B. K. Wang, A. Bansil, F. C. Chou, P. P. Shibayev, H. Lin, S. Jia, and M. Z. Hasan. *Discovery of a Weyl fermion semimetal and topological Fermi arcs.* Science **349**, 613 (2015).

[92] L. X. Yang, Z. K. Liu, Y. Sun, H. Peng, H. F. Yang, T. Zhang, B. Zhou, Y. Zhang, Y. F. Guo, M. Rahn, D. Prabhakaran, Z. Hussain, S.-K. Mo, C. Felser, B. Yan, and Y. L. Chen. *Weyl semimetal phase in the non-centrosymmetric compound TaAs.* Nat. Phys. **11**, 728–732 (2015).

[93] B. Q. Lv, H. M. Weng, B. B. Fu, X. P. Wang, H. Miao, J. Ma, P. Richard, X. C. Huang, L. X. Zhao, G. F. Chen, Z. Fang, X. Dai, T. Qian, and H. Ding. *Experimental Discovery of Weyl Semimetal TaAs.* Phys. Rev. X **5**, 031013 (2015).

[94] B. Q. Lv, N. Xu, H. M. Weng, J. Z. Ma, P. Richard, X. C. Huang, L. X. Zhao, G. F. Chen, C. E. Matt, F. Bisti, V. N. Strocov, J. Mesot, Z. Fang, X. Dai, T. Qian, M. Shi, and H. Ding. *Observation of Weyl nodes in TaAs.* Nat. Phys. **11**, 724 (2015).

[95] S. Y. Xu, N. Alidoust, I. Belopolski, Z. Yuan, G. Bian, T. R. Chang, H. Zheng, V. N. Strocov, D. S. Sanchez, G. Chang, C. Zhang, D. Mou, Y. Wu, L. Huang, C. C. Lee, S. M. Huang, B. Wang, A. Bansil, H. T. Jeng, T. Neupert, A. Kaminski, H. Lin, S. Jia, and M. Zahid Hasan. *Discovery of a Weyl fermion state with Fermi arcs in niobium arsenide.* Nat. Phys. **11**, 294 (2015).

[96] N. Xu, H. M. Weng, B. Q. Lv, C. E. Matt, J. Park, F. Bisti, V. N. Strocov, D. Gawryluk, E. Pomjakushina, K. Conder, N. C. Plumb, M. Radovic, G. Autes, O. V. Yazyev, Z. Fang, X. Dai, T. Qian, J. Mesot, H. Ding, and M. Shi. *Observation of Weyl nodes and Fermi arcs in tantalum phosphide.* Nat. Commun. **7** (2016).

[97] L. Fu and C. L. Kane. *Superconducting Proximity Effect and Majorana Fermions at the Surface of a Topological Insulator.* Phys. Rev. Lett. **100**, 096407 (2008).

[98] P. Burset, B. Lu, G. Tkachov, Y. Tanaka, E. M. Hankiewicz, and B. Trauzettel. *Superconducting proximity effect in three-dimensional topological insulators in the presence of a magnetic field.* Phys. Rev. B **92**, 205424 (2015).

[99] M. Sato and Y. Ando. *Topological superconductors: a review.* Rep. Prog. Phys. **80**, 076501 (2017).

[100] C. Fleckenstein, N. T. Ziani, and B. Trauzettel. *Conductance signatures of odd-frequency superconductivity in quantum spin Hall systems using a quantum point contact.* Phys. Rev. B **97**, 134523 (2018).

[101] J. Linder and J. W. Robinson. *Superconducting spintronics.* Nat. Phy. **11**, 307 (2015).

[102] D. Breunig, P. Burset, and B. Trauzettel. *Creation of Spin-Triplet Cooper Pairs in the Absence of Magnetic Ordering.* Phys. Rev. Lett. **120**, 037701 (2018).

[103] W. Chen, L. Jiang, R. Shen, L. Sheng, B. G. Wang, and D. Y. Xing. *Specular Andreev reflection in inversion-symmetric Weyl semimetals.* Europhys. Lett. **103**, 27006 (2013).

[104] S. Uchida, T. Habe, and Y. Asano. *Andreev Reflection in Weyl Semimetals.* J. Phys. Soc. Jpn. **83**, 064711 (2014).

[105] U. Khanna, A. Kundu, S. Pradhan, and S. Rao. *Proximity-induced superconductivity in Weyl semimetals.* Phys. Rev. B **90**, 195430 (2014).

[106] N. Bovenzi, M. Breitkreiz, P. Baireuther, T. E. O'Brien, J. Tworzydło, I. Adagideli, and C. W. J. Beenakker. *Chirality blockade of Andreev reflection in a magnetic Weyl semimetal.* Phys. Rev. B **96**, 035437 (2017).

[107] A. Chen, D. I. Pikulin, and M. Franz. *Josephson current signatures of Majorana flat bands on the surface of time-reversal-invariant Weyl and Dirac semimetals.* Phys. Rev. B **95**, 174505 (2017).

[108] S.-B. Zhang, F. Dolcini, D. Breunig, and B. Trauzettel. *Appearance of the universal value* e^2/h *of the zero-bias conductance in a Weyl semimetal-superconductor junction.* Phys. Rev. B **97**, 041116 (2018).

[109] K. A. Madsen, E. J. Bergholtz, and P. W. Brouwer. *Josephson effect in a Weyl SNS junction.* Phys. Rev. B **95**, 064511 (2017).

[110] S.-B. Zhang, J. Erdmenger, and B. Trauzettel. *Chirality Josephson Current Due to a Novel Quantum Anomaly in Inversion-Asymmetric Weyl Semimetals.* Phys. Rev. Lett. **121**, 226604 (2018).

[111] M. Alidoust. *Self-biased current, magnetic interference response, and superconducting vortices in tilted Weyl semimetals with disorder.* Phys. Rev. B **98**, 245418 (2018).

[112] S. Uddin, W. Duan, J. Wang, Z. Ma, and J.-F. Liu. *Chiral anomaly induced oscillations in the Josephson current in Weyl semimetals.* Phys. Rev. B **99**, 045426 (2019).

[113] K. Fukushima, D. E. Kharzeev, and H. J. Warringa. *Chiral magnetic effect.* Phys. Rev. D **78**, 074033 (2008).

[114] Q. Li, D. E. Kharzeev, C. Zhang, Y. Huang, I. Pletikosic, A. V. Fedorov, R. D. Zhong, J. A. Schneeloch, G. D. Gu, and T. Valla. *Chiral magnetic effect in* $ZrTe_5$. Nat. Phys. **12**, 550 (2016).

[115] Z. Song, J. Zhao, Z. Fang, and X. Dai. *Detecting the chiral magnetic effect by lattice dynamics in Weyl semimetals.* Phys. Rev. B **94**, 214306 (2016).

[116] A. Cortijo, D. Kharzeev, K. Landsteiner, and M. A. H. Vozmediano. *Strain-induced chiral magnetic effect in Weyl semimetals.* Phys. Rev. B **94**, 241405 (2016).

[117] A. A. Zyuzin, S. Wu, and A. A. Burkov. *Weyl semimetal with broken time reversal and inversion symmetries.* Phys. Rev. B **85**, 165110 (2012).

[118] W. L. McMillan. *Theory of Superconductor—Normal-Metal Interfaces.* Phys. Rev. **175**, 559–568 (1968).

[119] S. Kashiwaya and Y. Tanaka. *Tunnelling effects on surface bound states in unconventional superconductors.* Rep. Prog. Phys. **63**, 1641 (2000).

[120] D. Breunig, S.-B. Zhang, M. Stehno, and B. Trauzettel. *Influence of a chiral chemical potential on Weyl hybrid junctions.* Phys. Rev. B **99**, 174501 (2019).

[121] D. Breunig. *Scattering State Approach for the Classification of Superconducting Order Parameters: Application to 3D TI Hybrid Structures.* Master's thesis, University of Würzburg (2016).

[122] C. W. J. Beenakker. *Three "Universal" Mesoscopic Josephson Effects.* Springer, Berlin (1992).

[123] J. Cayssol. *Crossed Andreev Reflection in a Graphene Bipolar Transistor.* Phys. Rev. Lett. **100**, 147001 (2008).

[124] J. Cayao, C. Triola, and A. Black-Schaffer. *Odd-frequency superconducting pairing in one-dimensional systems.* Eur. Phys. J Spec. Top. **229**, 545–575 (2020).

[125] S. Datta and B. Das. *Electronic analog of the electro-optic modulator.* Appl. Phys. Lett. **56** (1990).

[126] P. Chuang, S.-C. Ho, L. W. Smith, F. Sfigakis, M. Pepper, C.-H. Chen, J.-C. Fan, J. P. Griffiths, I. Farrer, H. E. Beere, and et al. *All-electric all-semiconductor spin field-effect transistors.* Nature Nanotechnology **10**, 35–39 (2014).

[127] S. Takahashi, H. Imamura, and S. Maekawa. *Spin Imbalance and Magnetoresistance in Ferromagnet/Superconductor/Ferromagnet Double Tunnel Junctions.* Phys. Rev. Lett. **82**, 3911–3914 (1999).

[128] Y. V. Fominov, A. A. Golubov, and M. Y. Kupriyanov. *Triplet proximity effect in FSF trilayers.* JETP Letters **77**, 510–515 (2003).

[129] K. Halterman, P. H. Barsic, and O. T. Valls. *Odd Triplet Pairing in Clean Superconductor/Ferromagnet Heterostructures.* Phys. Rev. Lett. **99**, 127002 (2007).

[130] Y. V. Fominov, A. A. Golubov, T. Y. Karminskaya, M. Y. Kupriyanov, R. G. Deminov, and L. R. Tagirov. *Superconducting triplet spin valve.* JETP Letters **91**, 308–313 (2010).

[131] P. V. Leksin, N. N. Garif'yanov, I. A. Garifullin, Y. V. Fominov, J. Schumann, Y. Krupskaya, V. Kataev, O. G. Schmidt, and B. Büchner. *Evidence for Triplet Superconductivity in a Superconductor-Ferromagnet Spin Valve.* Phys. Rev. Lett. **109**, 057005 (2012).

[132] L. Y. Zhu, Y. Liu, F. S. Bergeret, J. E. Pearson, S. G. E. te Velthuis, S. D. Bader, and J. S. Jiang. *Unanticipated Proximity Behavior in Ferromagnet-Superconductor Heterostructures with Controlled Magnetic Noncollinearity.* Phys. Rev. Lett. **110**, 177001 (2013).

[133] K. Halterman, O. T. Valls, and M. Alidoust. *Spin-Controlled Superconductivity and Tunable Triplet Correlations in Graphene Nanostructures.* Phys. Rev. Lett. **111**, 046602 (2013).

[134] N. Banerjee, C. B. Smiet, R. G. J. Smits, A. Ozaeta, F. S. Bergeret, M. G. Blamire, and J. W. A. Robinson. *Evidence for spin selectivity of triplet pairs in superconducting spin valves.* Nat Communications **5**, 3048 (2014).

[135] A. Singh, S. Voltan, K. Lahabi, and J. Aarts. *Colossal Proximity Effect in a Superconducting Triplet Spin Valve Based on the Half-Metallic Ferromagnet* $\mathrm{CrO_2}$. Phys. Rev. X **5**, 021019 (2015).

[136] J. Wiedenmann, E. Liebhaber, J. Kübert, E. Bocquillon, P. Burset, C. Ames, H. Buhmann, T. M. Klapwijk, and L. W. Molenkamp. *Transport spectroscopy of induced superconductivity in the three-dimensional topological insulator HgTe.* Phys. Rev. B **96**, 165302 (2017).

[137] J. Linder, Y. Tanaka, T. Yokoyama, A. Sudbø, and N. Nagaosa. *Unconventional Superconductivity on a Topological Insulator.* Phys. Rev. Lett. **104**, 067001 (2010).

[138] T. Yokoyama. *Josephson and proximity effects on the surface of a topological insulator.* Phys. Rev. B **86**, 075410 (2012).

[139] A. M. Black-Schaffer and A. V. Balatsky. *Odd-frequency superconducting pairing in topological insulators.* Phys. Rev. B **86**, 144506 (2012).

[140] P. Burset, B. Lu, G. Tkachov, Y. Tanaka, E. M. Hankiewicz, and B. Trauzettel. *Superconducting proximity effect in three-dimensional topological insulators in the presence of a magnetic field.* Phys. Rev. B **92**, 205424 (2015).

[141] J. Cayao and A. M. Black-Schaffer. *Odd-frequency superconducting pairing and subgap density of states at the edge of a two-dimensional topological insulator without magnetism.* Phys. Rev. B **96**, 155426 (2017).

[142] L. Fu and C. L. Kane. *Superconducting Proximity Effect and Majorana Fermions at the Surface of a Topological Insulator.* Phys. Rev. Lett. **100**, 096407 (2008).

[143] J. Nilsson, A. R. Akhmerov, and C. W. J. Beenakker. *Splitting of a Cooper Pair by a Pair of Majorana Bound States.* Phys. Rev. Lett. **101**, 120403 (2008).

[144] Y. Tanaka, T. Yokoyama, and N. Nagaosa. *Manipulation of the Majorana Fermion, Andreev Reflection, and Josephson Current on Topological Insulators.* Phys. Rev. Lett. **103**, 107002 (2009).

[145] G. Tkachov and E. M. Hankiewicz. *Spin-helical transport in normal and superconducting topological insulators.* physica status solidi (b) **250**, 215–232 (2013).

[146] P. A. Frigeri, D. F. Agterberg, A. Koga, and M. Sigrist. *Superconductivity without Inversion Symmetry:* MnSi *versus* $\mathrm{CePt_3Si}$. Phys. Rev. Lett. **92**, 097001 (2004).

[147] P. A. Frigeri, D. F. Agterberg, A. Koga, and M. Sigrist. *Erratum: Superconductivity without Inversion Symmetry:* MnSi *versus* $\mathrm{CePt_3Si}$ *[Phys. Rev. Lett. 92, 097001 (2004)].* Phys. Rev. Lett. **93**, 099903 (E) (2004).

[148] A. G. Mal'shukov and C. S. Chu. *Spin Hall effect in a Josephson contact.* Phys. Rev. B **78**, 104503 (2008).

[149] P. Burset, F. Keidel, Y. Tanaka, N. Nagaosa, and B. Trauzettel. *Transport signatures of superconducting hybrids with mixed singlet and chiral triplet states.* Phys. Rev. B **90**, 085438 (2014).

[150] C. R. Reeg and D. L. Maslov. *Proximity-induced triplet superconductivity in Rashba materials.* Phys. Rev. B **92**, 134512 (2015).

[151] F. Konschelle, I. V. Tokatly, and F. S. Bergeret. *Theory of the spin-galvanic effect and the anomalous phase shift* φ_0 *in superconductors and Josephson junctions with intrinsic spin-orbit coupling.* Phys. Rev. B **92**, 125443 (2015).

[152] F. S. Bergeret and I. V. Tokatly. *Manifestation of extrinsic spin Hall effect in superconducting structures: Nondissipative magnetoelectric effects.* Phys. Rev. B **94**, 180502 (2016).

[153] I. V. Bobkova and A. M. Bobkov. *Quasiclassical theory of magnetoelectric effects in superconducting heterostructures in the presence of spin-orbit coupling.* Phys. Rev. B **95**, 184518 (2017).

[154] M. Veldhorst and A. Brinkman. *Nonlocal Cooper Pair Splitting in a p***S***n Junction.* Phys. Rev. Lett. **105**, 107002 (2010).

[155] C. J. Lambert and R. Raimondi. *Phase-coherent transport in hybrid superconducting nanostructures.* Journal of Physics: Condensed Matter **10**, 901 (1998).

[156] G. Falci, D. Feinberg, and F. W. J. Hekking. *Correlated tunneling into a superconductor in a multiprobe hybrid structure.* Europhys. Lett. **54**, 255–261 (2001).

[157] M. Silaev, P. Virtanen, F. S. Bergeret, and T. T. Heikkilä. *Long-Range Spin Accumulation from Heat Injection in Mesoscopic Superconductors with Zeeman Splitting.* Phys. Rev. Lett. **114**, 167002 (2015).

[158] F. S. Bergeret, M. Silaev, P. Virtanen, and T. T. Heikkilä. *Colloquium: Nonequilibrium effects in superconductors with a spin-splitting field.* Rev. Mod. Phys. **90**, 041001 (2018).

[159] P. G. Björnsson, Y. Maeno, M. E. Huber, and K. A. Moler. *Scanning magnetic imaging of* Sr_2RuO_4. Phys. Rev. B **72**, 012504 (2005).

[160] J. R. Kirtley, C. Kallin, C. W. Hicks, E.-A. Kim, Y. Liu, K. A. Moler, Y. Maeno, and K. D. Nelson. *Upper limit on spontaneous supercurrents in* Sr_2RuO_4. Phys. Rev. B **76**, 014526 (2007).

[161] K. Sengupta and V. M. Yakovenko. *Spontaneous Spin Accumulation in Singlet-Triplet Josephson Junctions.* Phys. Rev. Lett. **101**, 187003 (2008).

Acknowledgments

First and foremost, I want to express my sincere thanks to Björn Trauzettel, who has been an exceptional professor, supervisor, and guide throughout my study and my time as a PhD candidate. The opportunity to work at his academic chair and in such an intriguing branch of theoretical physics was both an honor and a delight. Moreover, I want to thank him for his trust in me as a teaching assistant, an editor, and as a TP4-IT administrator. I am immensely grateful for everything I had the chance to learn during these years, a circumstance that would not have been possible to this extend without a doctoral advisor as committed as Björn Trauzettel. Thank you.

Furthermore, I want to thank Song-Bo Zhang. His knowledge in the field of solid-state physics, and topological materials in particular, as well as his methods to approach problems and the way he solves them have been fascinating from the very beginning. I am deeply grateful for the chance to have learned from such a skilled physicist and for all his support during my PhD. The discussions with him, both physics-related and casual, are always a highlight. Also, I am thankful to have learned the Chinese translation of one of the most important questions for a PhD student – *Nǐ yào kāfēi ma?*

In equal measure, I am very grateful to have learned from and worked with Pablo Burset, who accompanied me as a supervisor during my Master Thesis and my first years as a PhD student. His vast knowledge on superconducting order has paved my way into this intriguing field of condensed matter physics, and his proficiency in explaining complex topics and relations in a straightforward and easy-to-understand manner baffle me to this day.

A general word of thanks goes to all my colleagues at the chair of TP4. It was a pleasure to work in such a congenial and astute community – I will certainly miss the social coffee gathering after lunch, where we had many intriguing conversations. In particular, I am indebted to Nelly Meyer, Nicolas Bauer, Philipp Heilmann, Daniel Hetterich, Felix Keidel, and Ewelina Hankiewicz for their assistance on so many occasions.

Last, but not least, I want to thank my family for their ongoing, invaluable support. Suzie – I am incredibly grateful for having you by my side; for your patience; for your understanding; for your caring. It is wonderful that we walk this path together. Nicolas and Joana – I cannot express in words how proud I am of you. Seeing you grow up is the most exciting and amazing thing I have ever experienced in my life. I love the three of you very much. Thank you for being by my side.